

ABSTRACT

Title of dissertation: SPECTROSCOPY WITH LASER-COOLED
FRANCIUM AND PROGRESS ON
ATOMIC PARITY NON-CONSERVATION

Jiehang Zhang,
Doctor of Philosophy, 2015

Dissertation directed by: Professor Luis A. Orozco
Joint Quantum Institute,
University of Maryland Department of Physics
and
National Institute of Standards and Technology

Francium, the heaviest alkali, possesses a unique combination of structural simplicity and great sensitivity to effects such as atomic parity non-conservation (APNC). We report in this thesis our progress towards measuring weak-interaction physics in a low energy system: the francium atom. We have built a new generation of high-efficiency laser cooling and trapping facility at TRIUMF national laboratory in Canada. We constructed a precision science chamber and demonstrate francium atom transfer into the precision trap, where the electromagnetic field environments can be exquisitely controlled such that weak-interaction studies via optical and microwave excitations can take place. We perform laser spectroscopy measurements of the hyperfine structure and isotope shifts in a chain of francium isotopes near the neutron closed shell ($N = 126$), including both ground and isomeric nuclear states. These measurements provide a basis for benchmarking state of the art atomic theory,

as well as future nuclear structure calculations in Fr, necessary for interpreting the weak-interaction studies. These developments lay important foundations for precision parity non-conservation measurements with francium.

Spectroscopy with Laser-cooled Francium
and Progress on Atomic Parity Non-conservation

by

Jiehang Zhang

Dissertation submitted to the Faculty of the Graduate School of the
University of Maryland, College Park in partial fulfillment
of the requirements for the degree of
Doctor of Philosophy
2015

Advisory Committee:

Professor Luis A. Orozco, Chair/Advisor

Professor James V. Porto

Professor William D. Phillips

Professor Gene D. Sprouse

Professor Alice Mignerey

© Copyright by
Jiehang Zhang
2015

Dedication

To my mother.

Acknowledgments

First and foremost, I am deeply indebted to my advisor, Professor Luis A. Orozco. The Ph.D journey in physics is not a small undertaking with few challenges. Luis has taught me how to face the challenges and transform from a “kindergarten” physics student into a young science researcher. He taught me not only atomic physics, but also many things ranging from music, history, and humanity. His unique way of inspiring scientific passion and demonstrating that hard work can make things happen are of great help. His endless patience and injections of courage have been of great help during difficult times, especially through frustrations with accelerator beam-times. He has offered me the six years of PhD experience a most unique educational journey in my life.

I would like to thank all members in the Francium Parity Non-Conservation collaboration, without whom this work will not be possible. First I thank all the senior members. I am extremely lucky to have the privilege to work with so many excellent scientists. Gerald Gwinner (from Manitoba) continuously amazes me with his careful thinking of physics, exceptional teaching skills, and great sense of humor. His ability to turn serious science questions and hilarious jokes back and forth into each other, was of enormous help making it a fun journey. John Behr (from TRIUMF) is the single most passionate yet humble scientist I have ever met. His enthusiasm is only paralleled by his extreme carefulness with science. Matt Pearson (also at TRIUMF) has always been the local expert whenever we need support and resources from the accelerator facility. Eduardo Gomez (from Mexico) always has

brilliant ideas, as well as the ability to execute them. I have enjoyed immensely working out the francium trap with him. Seth Aubin (from William and Mary) has devotion and carefulness only matched by John. I remember vividly the times when we work for beamtime preparations through nights till almost dawn. Yanting Zhao (from Shanxi University in China) had been of great help during his stay in Vancouver.

Special thanks to Michael Tandecki. He joined the group as a postdoc at the same time as when we moved to Vancouver. We started in the francium room when there was no electricity. Together with John he built our part of the ion delivery beam-line with blazing speed, without which francium will never arrive. We enjoyed three years of establishing the entire lab together: managing every little piece of detail, upgrading the experimental machine to a much more modern apparatus, and being the fire fighters during beam-times to put out any emergent situation that the experiment does not work. I wish him all my best, hope that he enjoys life and family back in Belgium as a data scientist. I also thank my coworker Ph.D students Rob Collister and Kyle Shiells. Rob has helped a lot both during the first winter and the various experimental runs. He also wrote an excellent manuscript on the isotope shift paper. Kyle is diligent and has good passion for physics. During the several months we overlapped he did excellent work ranging from hefty coil winding to fixing photomultiplier tube electronics. I wish him good luck for his future choice of theoretical physics career. In no particular order, Gary Chen, Young Ho Shin, Alysa Obertas, and Michael Kossin all contributed to labwork during their stays as summer (or one semester) undergraduates or graduates. We have also obtained from

enormous help from TRIUMF local supports: the machine shop and scintillator shop have fantastic capabilities; the procurement and accounting group are excellent in ensuring that we get the equipments we need; and of course the science division for granting us beamtime to be able to do experiments with francium.

I started my PhD at Maryland, and now finally returned to the original destination. Here I have the most sincere friends ever since I first took a flight to America. I have enjoyed great friendships with my fellow PhD students in Luis's group, especially Jonathan Hoffman, Jeff Grover, Andres Cimmarusti, and Pablo Solano. They have been continuously offering me alt ruistic help, even till today. We shared so much joy and sadness, fun as well as commiserations. I cannot find words to express my gratefulness. I wish you all have the best career, either still in academia or in the industry. I thank other friends from the Joint Quantum Institute at UMD, including (but are not limited to nor in no particular order) Kristen Voigt, Sylvan Ravets, Jongmin Lee, Jared Hertzberg, Xiao (Sean) Li, Varun Vaidya, Creston Herold, and so many other people who have offered technical knowledge sharing as well as great friendship. I have enjoyed great times spent with two other physics graduates, Xinghan (Herold) Cai and Lvyuan Chen. I wish you the best and have the most confidence on your future careers, especially given all the endurances that you had to come through. I thank Chuchu Li, with whom I spent two happy years of life together.

Finally, I thank my mother, who raise me almost entirely by herself, educated me with the absolute best ways she could find, but did not have a chance to be proud for me today. I love you and hope you rest well.

I am grateful to the National Science Foundation. Its continued support of the experiment has made this work possible.

Table of Contents

List of Figures	ix
List of Abbreviations	xi
1 Introduction	1
1.1 Weak interaction manifestation at low energies.	1
1.1.1 Atomic Parity Non-conservation Hamiltonian	2
1.1.2 PNC transition amplitude and the interference technique.	4
1.2 The francium parity non-conservation (FrPNC) experiment	6
1.2.1 Heavy atom enhancements.	6
1.2.2 Tractable atomic and nuclear structure.	7
1.2.3 On-going experiments and exotic possible sources of APNC.	9
1.3 Outline of the thesis	11
2 Measurement Schemes for APNC.	13
2.1 Overview, two types of parity forbidden transitions.	14
2.2 Optical experiment	16
2.3 Microwave experiment	19
2.4 From the accelerator to the precision APNC measurement	22
3 The francium capture trap	25
3.1 Glass cell.	26
3.2 Optics and Optomechanics.	28
3.3 Neutralizer	31
3.4 Modular design of the in-vacuum assemblies.	36
3.5 Laser locking and frequency reference	36
3.6 Radioactive decays of ^{210}Fr	39
3.7 Francium 221	42
4 Precision PNC apparatus: the science chamber.	79
4.1 Science chamber requirements	80
4.1.1 Microwave experiment	80
4.1.2 Optical experiment	83

4.2	Design and Construction	84
4.2.1	Accessibility	85
4.2.2	Magnetism and ultrahigh vacuum solutions	87
4.3	The entire UHV system and peripherals	89
4.3.1	UHV system	90
4.3.2	Peripherals	93
4.4	Laser optics layout	98
4.5	Experimental control hardware and software.	100
4.6	Atom transfer.	101
5	Precision spectroscopy of the francium $D1$ line.	106
5.1	Physics case: finite nuclear size corrections.	107
5.2	Measurement techniques and systematic effects	109
5.2.1	Rapid-scanning spectroscopy.	109
5.2.2	Systematic errors	114
5.3	Hyperfine anomaly: empirical calculation and the shell model.	121
5.3.1	Hyperfine interaction: electronic wavefunction integrals	122
5.3.2	Spherical shell model nuclei: ^{207}Fr to ^{213}Fr	126
5.3.3	Nuclear g factors and spin alignment.	129
5.3.4	The Breit-Rosenthal effect	132
5.4	The Nilsson deformed nucleus, ^{209g}Fr and ^{221}Fr	135
5.4.1	^{206g}Fr nuclear ground state.	136
5.4.2	Neutron rich ^{221}Fr	138
5.5	Possible implications of the hyperfine anomaly.	140
5.5.1	Magnetic moment relationship with the anapole moment.	140
5.5.2	Neutron density and neutron skin.	142
6	Preparation work with the microwave cavity and the Optical Dipole Trap.	159
6.1	Microwave cavity.	159
6.2	Sensitivity test of Rb atoms trapped in an optical dipole trap.	165
7	Conclusion.	167
A	Mechanical drawings	169
	Bibliography	175

List of Figures

1.1	Parity non-conserving Feynman diagrams involving weak interaction in atomic systems.	3
1.2	Periodic table of atomic parity non-conservation experiments.	10
2.1	Parity allowed and parity forbidden transitions in a francium atom. . .	15
2.2	Schematic and time sequence for the optical PNC experiment.	18
2.3	Schematic and time-sequence for the anapole moment experiment. . .	21
2.4	Schematic of the francium trapping facility (FTF) at TRIUMF.	23
3.1	Picture of the glass cell for the capture trap.	27
3.2	“Exoskeleton” cage surrounding the glass cell.	30
3.3	Theoretical curve for neutral atom release fraction.	33
3.4	Vapor pressures for neutralizer candidates.	34
3.5	Modular designs for the neutralizer chamber assembly.	37
3.6	Capture display of the scanning cavity laser locking program.	38
3.7	Radioactive decay chain of ^{210}Fr	40
4.1	The science chamber: Isometric view of the 3D CAD model.	86
4.2	PNC experimental setups with the science chamber.	87
4.3	Picture of the science chamber.	91
4.4	Peripheral for the science chamber: Bias coil support.	94
4.5	Science chamber full assembly with peripherals.	95
4.6	Schematic for the main imaging system.	97
4.7	Auxiliary imaging system.	98
4.8	Trap laser branches addressing different purposes for the two MOTs. .	99
4.9	Schematic trap laser layout on the optics table.	100
4.10	Experimental control and data-acquisition system.	102
4.11	Timing sequence for atom capture and transfer into the science chamber.	103
4.12	Picture of francium atoms in the capture trap and transferred into the science chamber.	104
5.1	Physical origins of hyperfine anomaly and isotope shift.	108
5.2	Experimental setup schematics for $D1$ line spectroscopy.	110

5.3	Scan of laser sidebands in HFA and IS measurements	113
5.4	Sample data with AC Stark shift effect.	117
5.5	Lorentzian fits with and without subtraction of background	119
5.6	Shell model nucleus of ^{210}Fr	127
5.7	Neutron spin alignment with the total nuclear spin	130
5.8	Hyperfine anomalies of ^{206}Fr nuclear ground and isomeric states. . . .	133
5.9	Neutron-holes of ^{206}Fr in a deformed nucleus.	137
5.10	Hyperfine anomalies in a chain of francium isotopes ^{207}Fr to ^{221}Fr . .	139
5.11	Protons of ^{221}Fr in a deformed nucleus	141
6.1	Microwave synthesis and delivery system.	160
6.2	Photomask for producing the microwave cavity mirror with litho- graphic technique.	162
6.3	Photograph of the microwave Fabry-Perot cavity test setup.	162
6.4	Transmission measurement after the microwave passes through the cavity.	163
6.5	Measured transverse mode of the microwave cavity.	164

List of Abbreviations

AM	amplitude modulation	
AOM	acousto-optic modulator	
APC	angled physical contact	
APNC	atomic parity non-conservation	
CF	ConFlat	
DC	direct current	
EOM	electro-optic modulator	
FM	frequency modulation	
FSR	free spectral range	
FWHM	full width at half maximum	
HFA	hyperfine anomaly HFS	hyperfine structure
HV	high voltage	
HWP	half-wave plate	
IS	isotope shift	
ISAC	isotope separator and accelerator facility at TRIUMF	
JQI	Joint Quantum Institute	
MOT	magneto-optical trap	
NIST	National Institutes of Standards and Technology	
NSF	National Science Foundation	
NSD-PNC	nuclear dependent parity non-conservation	
NSI-PNC	nuclear spin-independent parity non-conservation	
PBS	polarizing beam splitter	
PCB	Printed-circuit board	
PDH	Pound-Drever-Hall	
PID	proportional-integral-differential	
PM	polarization maintaining	
PMT	photomultiplier tube	
PZT	piezo-electric transducer	
QED	quantum electrodynamics	
QWP	quarter-wave plate	
RF	radio frequency	
S/N	signal to noise ratio	
TEM	transverse electromagnetic	
TTL	transistor-transistor logic	
TRIUMF	Tri-university meson facility, Canada's national laboratory for particle and nuclear physics	
UHV	ultra-high vacuum	
VCMOT	vapor-cell magneto-optical trap	

Chapter 1: Introduction

1.1 Weak interaction manifestation at low energies.

The weak interaction has many intriguing peculiarities. It is the only interaction capable of changing the flavors of fundamental fermions, e.g. for nuclear beta-decays to be possible. It is mediated by massive (> 80 GeV) W^\pm and Z^0 bosons, and has extremely short interaction ranges. Most amazingly, it is the only interaction which violates parity symmetry: the equivalence under space coordinate reversal.

Symmetry is one of the most fascinating and fundamental properties in the universe we live in. The Nobel Prize in Physics 1957 was awarded to C. N. Yang and T. D. Lee, “for their penetrating investigation of the so-called parity laws which has led to important discoveries regarding the elementary particles”. Their realization, that the weak interaction violates parity, was an important element in the development of the Standard Model (SM) by Glashow, Weinberg, and Salam. Among other things, the Standard Model unifies the weak and electromagnetic interactions, and has survived numerous experimental tests. However, it cannot explain some of the biggest puzzles, the best examples being dark matter and dark energy. Moreover, weak-interaction parameters such as the Weinberg angle or those involved in

hardronic weak-interactions are not fully characterized.

The weak interaction couples to all fermions, which include elementary particles such as electrons, as well as composite particles such as protons and neutrons. These three types of particles are exactly what an atom is composed of. We think of the atom as electrons orbiting around the nucleus, with the electromagnetic interaction governing the electronic properties. The nucleus is a cluster of protons and neutrons, with interactions originating from the strong force. This description, though, is only complete when we also take the weak interaction into account, which can manifest itself through parity non-conservation in atomic transitions. This manifestation represents a particularly interesting category of experiments, namely atomic parity non-conservation (APNC), which lies in the low momentum exchange regime, complementary to high energy experiments. The most precise APNC experiment to date is the work carried out in Cs by the group of C. E. Wieman, with a precision of 0.35% [1].

1.1.1 Atomic Parity Non-conservation Hamiltonian

The PNC Hamiltonian can be written as [2]:

$$H = \frac{G}{\sqrt{2}} \left(-\frac{Q_W}{2} \gamma_5 + \frac{\kappa}{I} \alpha \mathbf{I} \right) \rho(\mathbf{r}), \quad (1.1)$$

where G is the Fermi constant for the weak interaction, γ_5 and α are the Dirac matrices, Q_W is the weak charge of the nucleus, κ is a dimensionless factor, and $\rho(\mathbf{r})$ is the neutron density distribution. This operator acts on the Dirac electronic

wavefunction as in our usual quantum mechanical meaning.

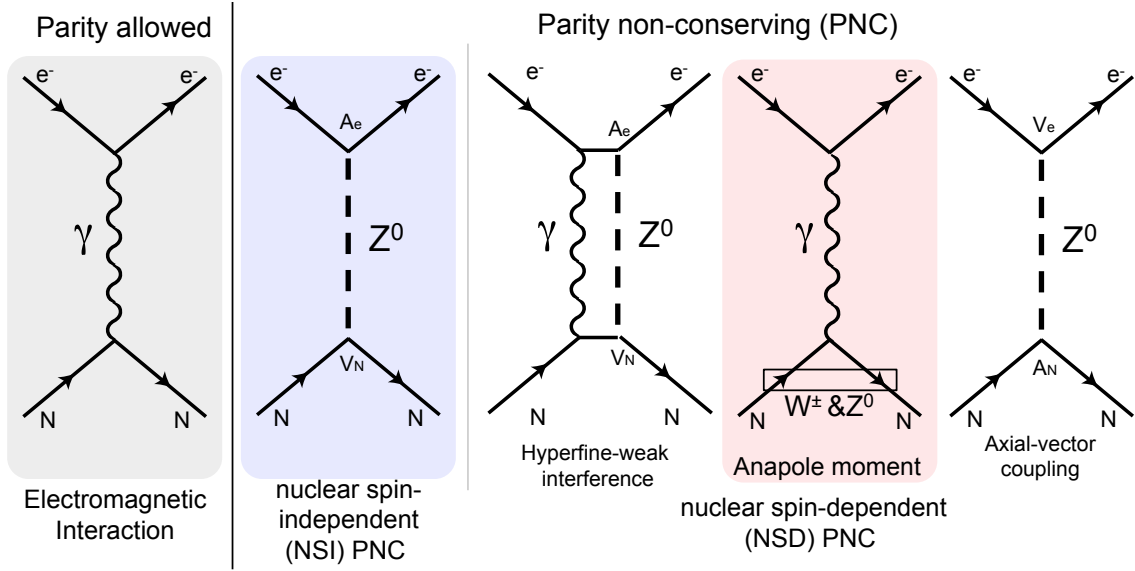


Figure 1.1: Parity non-conserving Feynman diagrams involving weak interaction in atomic systems. Photon exchanges represent electromagnetic interactions, which are parity-allowed. The W and Z bosons in the weak interaction contribute to the parity non-conserving terms, which can in turn be divided into nuclear spin independent and dependent terms, while the latter one is dominated by the anapole moment. See text for details.

Figure 1.1 shows the Feynman diagrams for the interactions between electrons and nucleons (or quarks inside of the nucleus). The left diagram showing electron-nucleon photon exchange is our familiar Coulomb interaction. The weak interaction introduces parity non-conserving terms, that can be divided into two categories corresponding to the two terms in Eq. 1.1: The largest source of APNC comes from the electron directly exchanging a Z^0 with the nucleons (second diagram in Fig. 1.1). All the nucleons add together, rendering a “bulk” effect independent of the nuclear spin, referred to as the nuclear spin-independent (NSI) PNC. The second term in Eq. 1.1 is dominated by the “anapole moment”, which is produced by weak inter-

actions within the nucleus, adding as a correction term to the Coulomb interaction (fourth diagram in 1.1). This creates a toroidal current inside of the nucleus, which produces parity violation effects that are nuclear spin-dependent (NSD-PNC). This distinction through nuclear spin dependence is important because the two effects arise from different physical origins, and the measurement methods also differ from one another. A theme with two experimental approaches will penetrate throughout this thesis, following the plans of our experimental program.

1.1.2 PNC transition amplitude and the interference technique.

So how do we detect weak neutral current interactions in atoms? The idea is to look into the electromagnetic interaction, i.e. optical or microwave transitions, for a tiny transition amplitude between levels in an atom with the same parity. We chose a transition which is forbidden by the parity selection rule, however can become slightly allowed as the weak interaction induces a mixture between opposite parity levels. The matrix element A characterizes the amplitude of a electronic transition. A parity allowed electric dipole transition between S and P electronic levels in e.g. an alkali atom, has a matrix element of the form:

$$A_{E1} = \langle S | H_{E1} | P \rangle = \langle S | \mathbf{d} \cdot \mathbf{E} | P \rangle, \quad (1.2)$$

The atomic unit for the electric dipole matrix element is ea_0 , where e denotes unit electrical charge (1.6×10^{-19} Coulomb), and a_0 the Bohr radius (0.53 Anstrom). The lowest electric dipole allowed transitions in alkali atoms typically have transition

dipole matrix elements of a few atomic units [3].

The weak-interaction mixing induced transition matrix element for transitions involving two S states is:

$$A_{\text{PNC}} = \langle S | H_{\text{PNC}} | S' \rangle, \quad (1.3)$$

where H_{PNC} is the Hamiltonian in Eq. 1.1 introduced before. This amplitude A_{PNC} is extremely small: only of the order $10^{-11}ea_0$ in Cs [1]. The anapole moment induced forbidden transition, which dominates the nuclear spin-dependent part of APNC, has a even smaller amplitude of the order $10^{-12}ea_0$ ¹. Note that the experimental observable, the transition probability, is proportional to the square of the amplitude A . It seems formidable to observe such a faint transition at all, let alone to measure it to sub-percent accuracy. Fortunately we can employ some brilliant tricks to enhance the signal by large factors.

One crucial method for improving the statistical signal to noise ratio, is the “interference technique”, which can amplify the signal by several orders of magnitude. The idea is to measure the constructive and destructive interference effects between two processes, the parity violating one, and a parity conserving one, which is larger than the parity non-conserving part. This idea is general to weak interaction experiments (see for example also the results and proposals in the medium energy sector [4]). Among the classic atomic PNC experiments, the interference technique is represented by using the (relatively) allowed M1 to interfere in early optical rotation experiments [5–7], and the Stark-interference in the Cs experiment [1]. The

¹Compare this to for example the hyperfine mixing induced ultra-narrow clock transition in ⁸⁷Sr, which has an amplitude of the order $10^{-5}ea_0$.

key is to chose a relatively allowed transition that has tunable strength, and arrange the apparatus to have handedness such that two measurements are possible with the PNC E1 transition. The total transition probability becomes:

$$|A_{\text{tot}}|^2 = |A_{\text{PC}} \pm A_{\text{PNC}}|^2 = |A_{\text{PC}}|^2 \pm 2A_{\text{PC}} \cdot A_{\text{PNC}} + |A_{\text{PNC}}|^2 \quad (1.4)$$

The last term is negligible. The interference term $A_{\text{PNC}} \cdot A_{\text{PNC}}$ effectively enhances the PNC signal by a factor of the ratio $A_{\text{Int}}/A_{\text{PNC}}$. This factor can be of the order 10^5 in the Stark-interference experiments [8]. Besides this “external” amplifying method, particular atomic systems can also have “inherent” enhancement, which is one of the main reasons for using francium.

1.2 The francium parity non-conservation (FrPNC) experiment

Francium is the heaviest alkali atom, on the bottom left corner of the periodic table (Fig. 1.2), with no stable isotopes². It possesses a unique combination of atomic and nuclear structural simplicity, with great sensitivity to effects such as APNC and possible permanent electric dipole moments due to its high nuclear charge:

1.2.1 Heavy atom enhancements.

Evaluation of the PNC matrix element introduced in Eq. 1.3 can be expressed as the product of two parts; the atomic/electronic and the nuclear. For example the

²Isotope with the longest lifetime is the 23 minutes half-life ^{223}Fr .

NSI-PNC term can be written as:

$$A_{Q_w} \propto Q_w \langle S | \gamma_5 \rho(\mathbf{r}) | S' \rangle \quad (1.5)$$

The weak charge of the nucleus Q_w comes from standard model predictions, and the rest comes from atomic theory calculation. The enhancement in heavy atoms was first pointed out by the Bouchiat [9]. The weak charge scales linearly with atomic number Z , and the S electronic wavefunction and the derivative of the P wavefunction mixed into the S and S' states contribute another Z^2 [9]. The NSI-PNC effect thus scales at least as Z^3 , with additional factors from relativistic enhancements. The anapole moment term is slightly slower, $Z^{8/3}$, which can be pictorially thought of as more of a “surface” effect rather than a “bulk” property. Cesium is an excellent atom due to these enhancements, and francium is its natural extension. Detailed calculations show that the parity non-conserving observables are about 20 times larger in Fr than in Cs [10, 11].

1.2.2 Tractable atomic and nuclear structure.

Precise theoretical calculations are crucial for extracting weak interaction physics (for example the nuclear weak charge and the anapole moment) from APNC experiments. The importance of the atomic (electronic) structure theory is seen in Eq. 1.5: extraction of Q_w from an experiment requires dividing the measurement by the atomic calculation. This demands accurate knowledge of the electronic wavefunction inside the finite extent of the nucleus. Various atomic properties of Cs

have been measured to benchmark the atomic theory calculations, such as dipole matrix elements that directly enter into the PNC calculation, and.... In the case of Cs, many direct as well as auxiliary atomic properties have been measured, for benchmarking the atomic theory. State of the art atomic theory calculations of APNC have reached unprecedented levels of precision, and are still evolving for better accuracy [12, 13]. Francium has the advantage of possessing a simple electronic structure, similar to that of Cs or any other alkali, which is a highly desirable feature when choosing an atomic system.

Besides the electronic structure, the nuclear structure also warrants great attention, especially in the case of the anapole moment. The cesium anapole result has been interpreted to constrain hadronic parity violation parameters [14–16]. However, as theorists have been pointing out, calculating the Cs nuclear polarizabilities involves great complexity [14], which complicates the extraction of the weak coupling constants.

New theories such as lattice quantum chromodynamics are recently emerging for calculating parity violation [17]. These calculations are evolving beyond a system of only a few nucleons [18, 19]. As modern experimental tools become available for studies of ground state nuclear matter properties [20], nuclear physics moves steadily towards the precision frontier [21]. This would greatly facilitate interpreting APNC measurements and extracting weak-interaction constants. Francium has advantages due to proximity to the “doubly” magic nucleus of ^{206}Pb . A chain of isotopes on the neutron-deficient side (down from ^{213}Fr with closed neutron shell) shows magnetic properties, such as the magnetic moment and the hyperfine anomaly, with significant

regularity, which will explore this in more detail in Chapter 5.

This collection of benefits from the heavy atom enhancements and tractable theories on both the atomic and nuclear sectors, makes francium the ideal laboratory for weak interaction studies in atoms.

1.2.3 On-going experiments and exotic possible sources of APNC.

Parity violation in atoms has been a long lasting tradition in precision measurements, and gained much attention in recent years. Figure 1.2 shows the periodic table, highlighting the elements involved in APNC experiments. Existing PNC measurements are roughly categorized into two types: optical rotation and Stark-interference. PNC optical rotations in vapor cells are best represented by the Tl and Pb measurements in Seattle [5,22] and the Bi measurement in Oxford [6]. Such experiments in metastable Xe and Hg with cavity-enhancement techniques have newly started [23]. The Stark-interference method is represented by the Cs experiment [1]. The group of D. Budker is actively pursuing this technique in atomic beams of Dy and Yb [24,25], where two opposite parity states are almost degenerate. Part of our plan in the FrPNC collaboration is to use this interference method, and we will give more detail in the next chapter.

Several novel experimental techniques have been proposed, including PNC frequency shift measurement in a single ion [26]. The Fortson group is pursuing this in Ba [27], and the KVI group in the Netherlands has efforts in Ra [28]. The group of D. Elliot at Purdue is revisiting APNC in Cs with two-pathway coherent

<div>H $2s_{1/2}$</div>		<div><div><div>^{210}Fr $2s_{1/2}$</div></div><div><div>Half life: 3.18 min</div><div>Atomic number: 87</div><div>Neutron number: 124</div><div>Electron configuration: [Rn] 7s1</div><div>D2 line: 718nm</div><div>D1 line: 817nm</div></div></div>																<div>He $1s_0$</div>																
<div>Li $2s_{1/2}$</div>	<div>Be $1s_0$</div>																	<div>B $2p_{1/2}$</div>	<div>C $3p_0$</div>	<div>N $4s_{3/2}$</div>	<div>O $3p_2$</div>	<div>F $2p_{3/2}$</div>	<div>Ne $1s_0$</div>											
<div>Na $2s_{1/2}$</div>	<div>Mg $1s_0$</div>																	<div>Al $2p_{1/2}$</div>	<div>Si $3p_0$</div>	<div>P $4s_{3/2}$</div>	<div>S $3p_2$</div>	<div>Cl $2p_{3/2}$</div>	<div>Ar $1s_0$</div>											
<div>K $2s_{1/2}$</div>	<div>Ca $1s_0$</div>	<div>Sc $2d_{3/2}$</div>	<div>Ti $3f_2$</div>	<div>V $4f_{3/2}$</div>	<div>Cr $7s_3$</div>	<div>Mn $6s_{5/2}$</div>	<div>Fe $5d_4$</div>	<div>Co $4f_{9/2}$</div>	<div>Ni $3f_4$</div>	<div>Cu $2s_{1/2}$</div>	<div>Zn $1s_0$</div>	<div>Ga $2p_{1/2}$</div>	<div>Ge $3p_0$</div>	<div>As $4s_{3/2}$</div>	<div>Se $3p_2$</div>	<div>Br $2p_{3/2}$</div>	<div>Kr $1s_0$</div>																	
<div>Rb $2s_{1/2}$</div>	<div>Sr $1s_0$</div>	<div>Y $2d_{3/2}$</div>	<div>Zr $3f_2$</div>	<div>Nb $6d_{1/2}$</div>	<div>Mo $7s_3$</div>	<div>Tc $6s_{5/2}$</div>	<div>Ru $5f_5$</div>	<div>Rh $4f_{9/2}$</div>	<div>Pd $1s_0$</div>	<div>Ag $2s_{1/2}$</div>	<div>Cd $1s_0$</div>	<div>In $2p_{1/2}$</div>	<div>Sn $3p_0$</div>	<div>Sb $4s_{3/2}$</div>	<div>Te $3p_2$</div>	<div>I $2p_{3/2}$</div>	<div>Xe $1s_0$</div>																	
<div>Cs $2s_{1/2}$</div>	<div>Ba $1s_0$</div>			<div>Hf $3f_2$</div>	<div>Ta $4f_{3/2}$</div>	<div>W $5d_0$</div>	<div>Re $6s_{5/2}$</div>	<div>Os $5d_4$</div>	<div>Ir $4f_{9/2}$</div>	<div>Pt $3d_3$</div>	<div>Au $2s_{1/2}$</div>	<div>Hg $1s_0$</div>	<div>Tl $2p_{1/2}$</div>	<div>Pb $3p_0$</div>	<div>Bi $4s_{3/2}$</div>	<div>Po $3p_2$</div>	<div>At $2p_{3/2}$</div>	<div>Rn $1s_0$</div>																
<div>Fr $2s_{1/2}$</div>	<div>Ra $1s_0$</div>			<div>Rf $3f_2$</div>	<div>Db $4f_{3/2}$</div>	<div>Sg $5d_0$</div>	<div>Bh $6s_{5/2}$</div>	<div>Hs $5d_4$</div>	<div>Mt $4f_{9/2}$</div>	<div>Ds $3d_3$</div>	<div>Rg $2s_{1/2}$</div>	<div>Cn $1s_0$</div>	<div>Uut $2p_{1/2}$</div>	<div>Fl $3p_0$</div>	<div>Uup $4s_{3/2}$</div>	<div>Lv $3p_2$</div>	<div>Uus $2p_{3/2}$</div>	<div>Uuo $1s_0$</div>																
																		<div>La $2d_{3/2}$</div>	<div>Ce $1g_4$</div>	<div>Pr $4i_{9/2}$</div>	<div>Nd $5i_4$</div>	<div>Pm $6h_{5/2}$</div>	<div>Sm $7f_0$</div>	<div>Eu $8s_{7/2}$</div>	<div>Gd $9d_2$</div>	<div>Tb $6h_{15/2}$</div>	<div>Dy $5i_8$</div>	<div>Ho $4i_{15/2}$</div>	<div>Er $3h_6$</div>	<div>Tm $2f_{7/2}$</div>	<div>Yb $1s_0$</div>	<div>Lu $2d_{3/2}$</div>		
																		<div>Ac $2d_{3/2}$</div>	<div>Th $3f_2$</div>	<div>Pa $4k_{11/2}$</div>	<div>U $5l_6$</div>	<div>Np $6l_{11/2}$</div>	<div>Pu $7f_0$</div>	<div>Am $8s_{7/2}$</div>	<div>Cm $9d_2$</div>	<div>Bk $6h_{15/2}$</div>	<div>Cf $5i_8$</div>	<div>Es $5i_{15/2}$</div>	<div>Fm $3h_6$</div>	<div>Md $2f_{7/2}$</div>	<div>No $1s_0$</div>	<div>Lr $2p_{1/2}$</div>		

Figure 1.2: Periodic table of atomic parity non-conservation experiments. We choose francium, the heaviest alkali at the bottom left corner. Various kinds of experimental techniques are used for measuring PNC in different atoms or molecules. See text for detailed explanations.

control [29]. The anapole moment is directly measurable with a PNC electrical dipole transition between hyperfine ground states in an alkali atom. This is the other part of the experimental program for Fr [30, 31]. The group of D. Demille at Yale is working towards measuring the anapole moment in molecules [32]. Other proposed experimental techniques include PNC frequency shifts in a neutral Fr [33], two-photon excitations in Yb [34], etc.

These experiments aim at testing weak interaction properties, and when theo-

retical calculations do not match experimental results (and [?]d that we trust both), it could indicate physics beyond our understanding. This includes physics beyond the Standard Model (SM) as well as things within the SM that are not particularly well known, such as the hadronic weak interaction. Among the things modern theories still cannot explain is dark matter/energy. Potential candidates range widely from supersymmetric particles to light cosmic fields such as that from axions. Recently the group of Flambaum has proposed that the anapole moment can constrain nucleon coupling with axion dark matter [35]. Such indirect searches for dark matter in low energy atomic systems can be complementary to direct measurements [36,37].

1.3 Outline of the thesis

The work presented in this thesis focuses on francium trapping and other advances en route towards atomic parity non-conservation. The organization is as follows: Chapter 2 outlines our experimental plans for measuring the weak charge and the anapole moment, with optical and microwave excitations respectively. Chapter 3 describes the francium trapping facility: a new generation of laser-cooling and trapping apparatus for radioactive Fr. Chapter 4 details the design and construction of the science chamber, which incorporates the two planned PNC experiments and provide the basis for exquisite electromagnetic field control. In Chapter 5 we describe the laser spectroscopy measurements along a chain of francium isotopes. Our precision hyperfine splitting measurement can provide information about the atomic nucleus, especially magnetic properties at the next to leading order. We also

measure isotope shifts which serves as a benchmark for atomic theory calculations. Chapter 6 contains some off-line developments for improving the sensitivity of our apparatus. We conclude in Chapter 7 and share some remarks for the future.

Chapter 2: Measurement Schemes for APNC.

We have introduced in Chapter 1 the effect of weak interactions in atomic systems: tiny parity forbidden electric dipole transition amplitudes. The experimental observable is an asymmetry on the transition used for the interference, as we switch the field directions which tunes this transition in and out of phase with the PNC transition. In other words, we measure the handedness of the atom with an apparatus that also handedness. The left-handed and right-handed coordinate systems are defined by the static and dynamic fields we apply.

This chapter describes the experimental plans and techniques involved. We have two experimental plans in parallel: one aimed at measuring the weak charge of the nucleus using an optical transition; the other targeted towards directly detecting the anapole moment with a microwave transition. We lay out the schemes for the two experiments: the optical one containing high-voltage DC electrodes for level mixing and a high-finesse optical power build-up cavity; the anapole one involving a microwave cavity with precise positioning of the atom cloud with an optical dipole trap (ODT). We end this chapter by presenting the requirements of the FrPNC experiment in a cyclotron accelerator facility: obtaining the francium from the radioactive atom source, collecting it into a high efficiency capture trap,

and performing the experiment in a precision trap.

2.1 Overview, two types of parity forbidden transitions.

We first examine the Fr electronic energy level structure. Fig. 2.1 shows the APNC related francium energy levels. The $D2$ (used for laser cooling) and $D1$ lines have wavelengths of about 817nm and 718nm, respectively, which represent the lowest, parity-allowed, electric dipole (E1) transitions from the ground state. The $8S$ excited state is parity even, as is the ground state, and thus it is forbidden to have any E1 transitions between the two with only electromagnetic interactions¹. The hyperfine ground states are also forbidden to have E1 transitions among one another, and the first allowed one is the magnetic dipole (M1) transition. The upper hyperfine state has practically infinite lifetime.

¹Note that although this E1 transition from the ground state is forbidden, the $8S$ level is still a short-lived state with lifetime of about 50 ns [38], because of the decay through the P manifold.

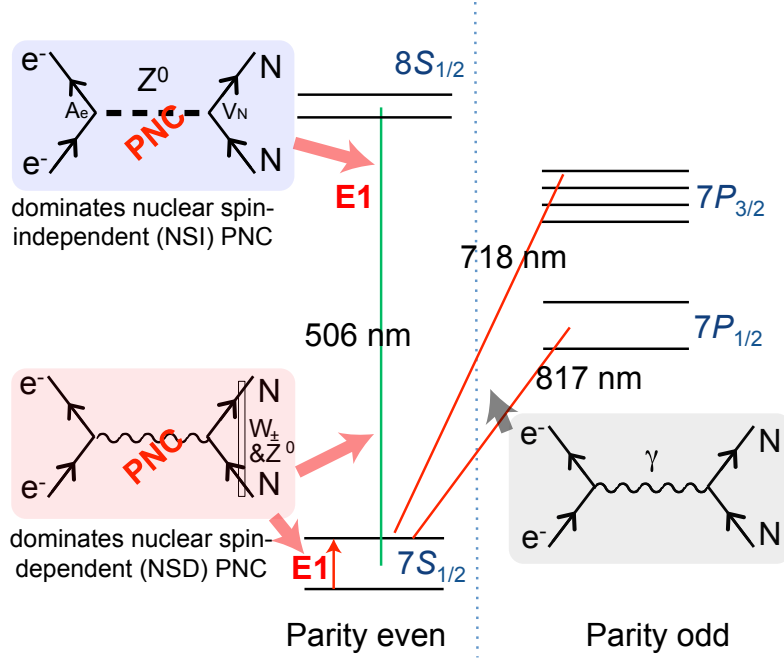


Figure 2.1: Parity allowed and parity forbidden transitions in a francium atom. Red lines between ground ($7S_{1/2}$ state in Fr) and first excited states ($7P_{1/2}$ and $7P_{3/2}$ states) denotes the electric dipole allowed $D1$ and $D2$ lines, respectively. These transitions are mediated by photon exchange between the electrons and the atomic nucleus. Within the parity even manifold, the optical transition between $7S_{1/2}$ and $8S_{1/2}$ and the microwave transition between the hyperfine ground states, are electric dipole forbidden but has small amplitudes due to the weak interaction mixing. They are dominated by the weak charge of the nucleus and the anapole moment, respectively.

When we take weak interaction effects into account (Feynman diagrams on the left in Fig. 2.1), there exist small admixtures of P states into the S states.

We need not emphasize again how small these amplitudes are. To obtain a good signal to noise ratio and counteract the disadvantage of the scarcity of francium atoms, our solution is to laser cool and trap the atoms, which enables long

interrogations and high efficiency usage of the available atom source. We can estimate the statistical signal-to-noise ratio (S/N) by comparing to the Boulder Cs experiment: if we trap all the atoms from the accelerator, in 1s 10^8 atoms are in the MOT. We have 100 times longer interrogation time (a Cs atom in a beam flies through the interaction region in a few μs), and recapture for recycling the atoms 100 times. With the factor of 20 enhancement benefitting from Fr atomic and nuclear properties, we have 2 times better statistical S/N than the 10^{13} atoms/s Cs used by Wieman [8]. The pre-requisite of doing such an experiment with francium, is that the Fr atoms are captured with high efficiency, suspended in the center of an Ultra-high Vacuum (UHV) chamber, and cooled to about 100 μK above absolute zero temperature in an exquisitely controlled electromagnetic field environment. The parity non-conservation experiment will commence in either a MOT, as is the case for the optical experiment, or in a subsequent optical-dipole trap (ODT), as is required for the anapole moment experiment. These are of course experimental challenges that a large portion of this thesis deals with. Let us now examine the two proposed experimental schemes.

2.2 Optical experiment

The optical experiment aims at following Carl Wieman's footsteps, and uses a DC electric field to create the Stark mixing, for the interference with PNC transition amplitude. The Stark-interference technique is very well documented in Ref. [8], which contains extensive analysis of the systematic effects. We summarize the key

features and emphasize some specifics when applying to the laser cooled and trapped francium atoms. The total transition rate is written as:

$$P_{\text{tot}} = |A_{\text{tot}}|^2 = |A_{\text{Stark}} \pm A_{\text{PNC}}|^2 \approx A_{\text{Stark}}^2 \pm 2A_{\text{Stark}}A_{\text{PNC}} + A_{\text{PNC}}^2 \quad (2.1)$$

Figure 2.2 shows the experimental scheme. Two electrodes made out of glass has transparent indium-tin-oxide coatings on the inner side facing the atoms and anti-reflection coatings on the outside. The axis of an optical Fabry-Perot cavity lies in the horizontal direction. This cavity is needed for the power build-up to enhance the electric field amplitude and consequently the PNC signal (see Eq. 2.3), as well as suppressing systematic effects. The static magnetic field, dc electric field, and the excitation laser polarization defines the coordinate system. Each reversal of any quantity among the three, is a reversal between a left-handed apparatus and a right-handed one.

One key difference between a PNC experiment with trapped cold atoms compared to that with an atomic beam, is that the spatial separation of preparation, excitation, and detection steps of the measurement in a beam setup have to be replaced by alternating the field applied to the trapped atoms via time-sequencing. Figure 2.2 (b) shows an example timing steps for the measurement. Starting with atoms in a trap (a second stage MOT in the case of the optical PNC experiment) with precise controlled electromagnetic field environment, the state preparation involves hyperfine and Zeeman optical pumping to states with maximum m_F (e.g. $F = 9/2$, maximum $m_F = \pm 9/2$ for ^{210}Fr). We then turn on the DC electric field

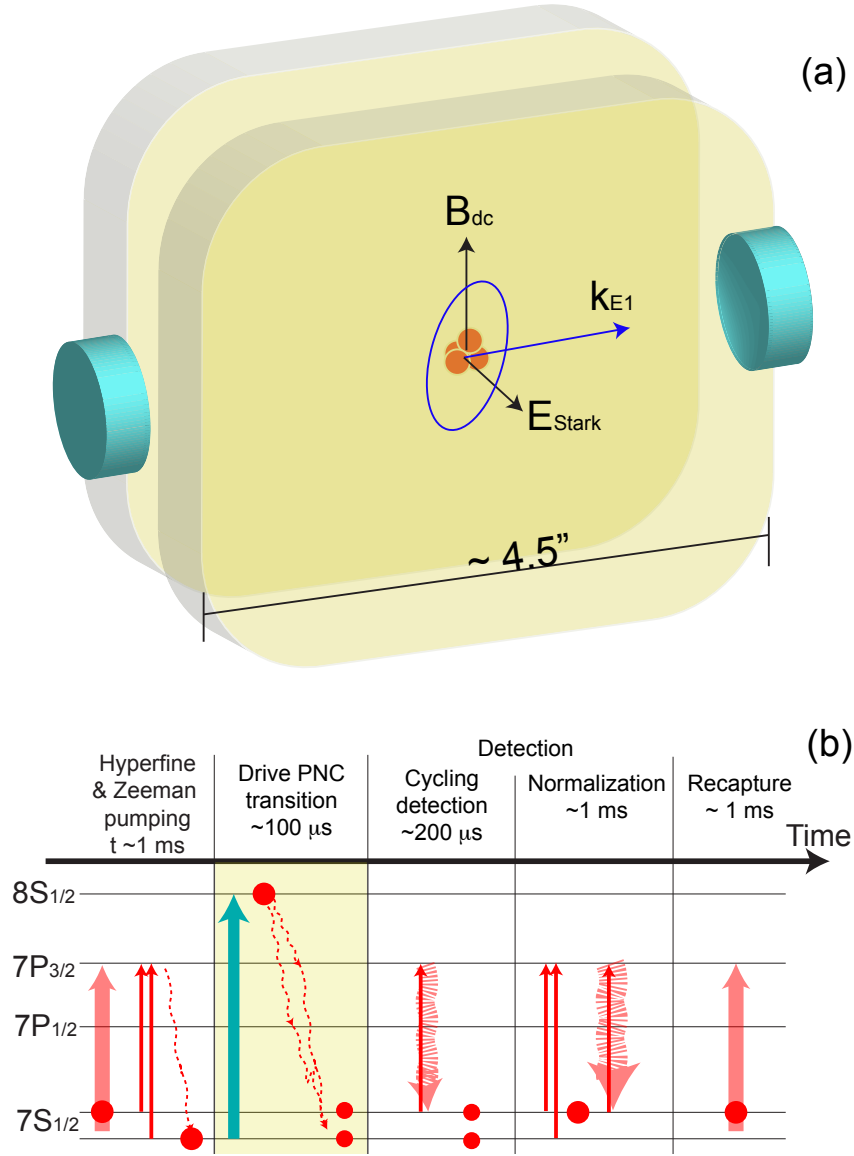


Figure 2.2: Schematic and time sequence for the optical PNC experiment. (a) Transparent electrodes provide DC electric field for Stark-induced mixing, and allows for optical access for lasers such as those from the MOT beam. A high-finesse optical cavity builds up the optical power to drive the $7S$ to $8S$ transition. The static electric and magnetic fields (black arrows), plus the laser polarization (indicate by the blue ellipse), together defines the coordinate system. (b) Example timing sequence. Thick solid red lines denote cooling/trapping and repumping laser. Thin solid lines represent optical pumping lasers. Thin and thick dashed wiggly lines indicate single photon decays and cycling transitions, respectively.

which mixes the energy levels and creates the interference, as well as the excitation laser, which drives the transition. The $8S$ excited state lifetime is short enough that the atoms will always decay via spontaneous emission. The characteristic timescale for driving the $7S$ to $8S$ transition is determined by how fast the atoms move out of the excitation optical field, and is of the order of a few $100\ \mu\text{s}$. The detection relies on measuring the population distribution between the two hyperfine levels. Fluorescence detection with the cycling transition effectively amplifies the signal by hundreds to a thousand times, ideally reaching the atomic shot noise limit with good effort in the photon collection and control of technical noise.

2.3 Microwave experiment

The microwave experiment aims at a direct measurement of the nuclear spin-dependent (NSD) PNC, which is dominated by the anapole moment in heavy atoms such as Fr. This measurement involves a transition between the hyperfine levels of the electronic ground state. Ref. [39] first proposed its application to heavy atoms. Ref. [30] details a specific measurement plan for francium.

Figure 2.3 (a) shows a schematic for the proposed anapole experiment. A microwave Fabry-Perot cavity creates a standing wave, with the electric field anti-nodes coinciding with the magnetic field nodes. Subsequent to the MOT stages, the atoms need to be transferred into an optical dipole trap (not shown in the figure), where the cloud position can be precisely located at the central one of the electric field anti-nodes. This anti-node coincides with the magnetic field node, which is

a property for a perfect standing electromagnetic wave, and is our main method to suppress the magnetic dipole allowed transition. The static magnetic field, the microwave field $E_{\mu\text{W}}$, and the microwave field $B_{\mu\text{W}}$ used for the interference, together define the handedness of the coordinate system.

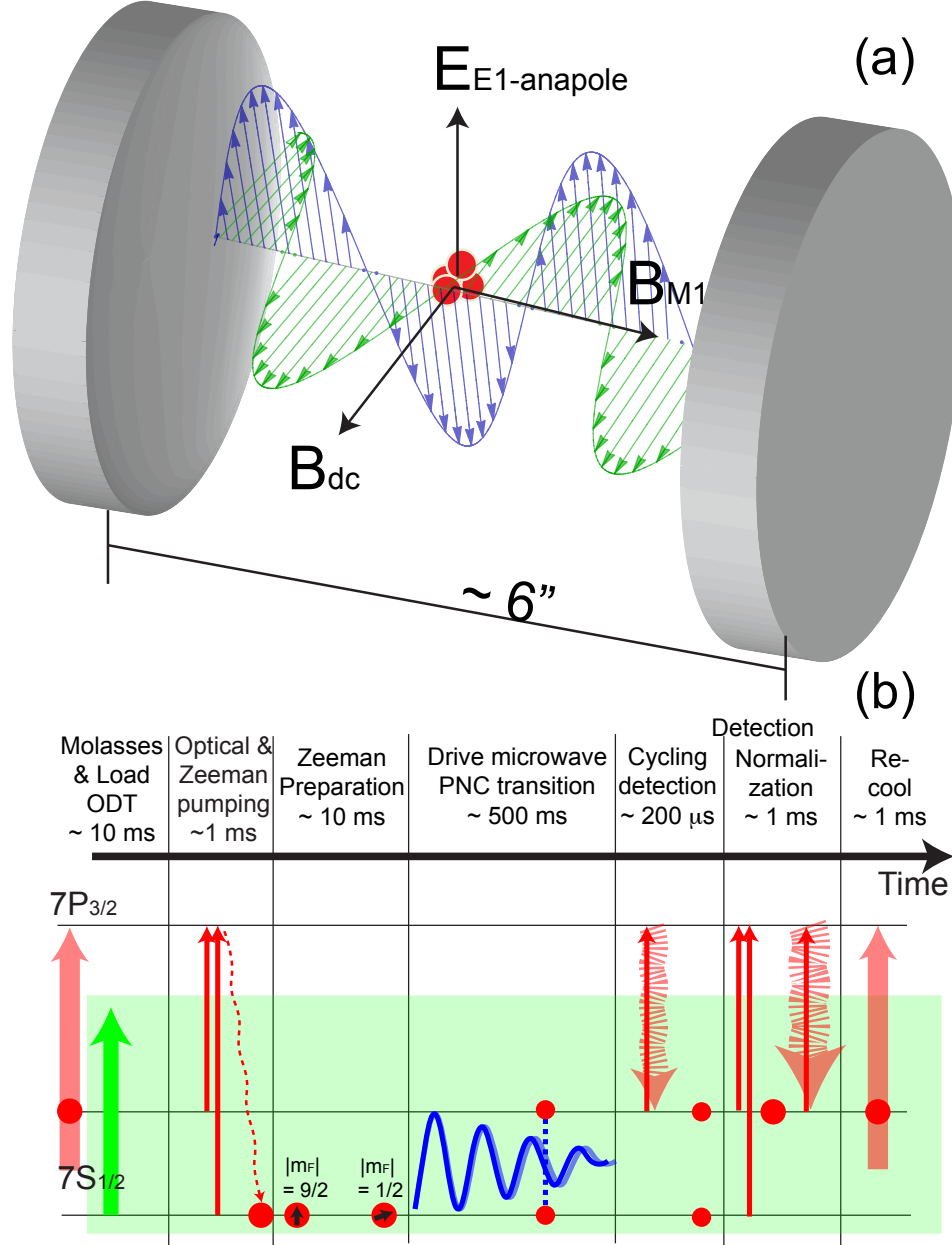


Figure 2.3: a) Schematic for the anapole moment experiment with magnetic dipole interference. A microwave cavity creates a standing wave. The atoms trapped in an optical dipole trap (ODT, not shown in the figure) have to be positioned at the center one of these anti-nodes, which is also the electrical field node. The static magnetic field, the microwave $E_{\mu W}$ field, and the interfering microwave $B_{\mu W}$ field define the handedness of the coordinate system. b) Time sequence of the measurement starting with the trapping on the optical dipole trap.

Fig. 2.3 (b) shows an example of the timing sequence for a microwave anapole experiment. State preparation involves specific Zeeman levels ², and can be achieved by coherent population trapping [40] or adiabatic fast passage [41] techniques. We then drive the E1-PNC transition with electric field from the standing microwave field inside the cavity. The interference M1 transition is driven by another microwave magnetic field (not shown in Fig. 2.3). The coherent oscillation between the two hyperfine states can be driven for many Rabi cycles, since the upper state essentially has infinite lifetime. External perturbations such as magnetic field noise or ODT Stark shift inhomogeneities will be the sources of decoherence and the limiting factors for the probe duration. Detection relies upon measuring the hyperfine states population distribution, much like that required for the optical experiment.

2.4 From the accelerator to the precision APNC measurement

We have to carry out the above experimental programs with a francium source with high enough intensity. A few rare-isotope facilities can provide a sufficient amount of francium with accelerator-based technologies. We have built the francium trapping facility at TRIUMF (TRI-University Meson Facility), Canada's national laboratory for nuclear and particle physics, where a proton beam from a cyclotron is available for bombarding uranium targets, producing a large quantity of radioactive ions including francium.

Figure 2.4 shows the schematic of the Francium Trapping Facility (FTF) at

²For example $m_F = \pm 1/2$ to $m_F = \mp 1/2$ shown in Fig. 2.3 (b), for fermionic francium isotopes such as ²¹⁰Fr.

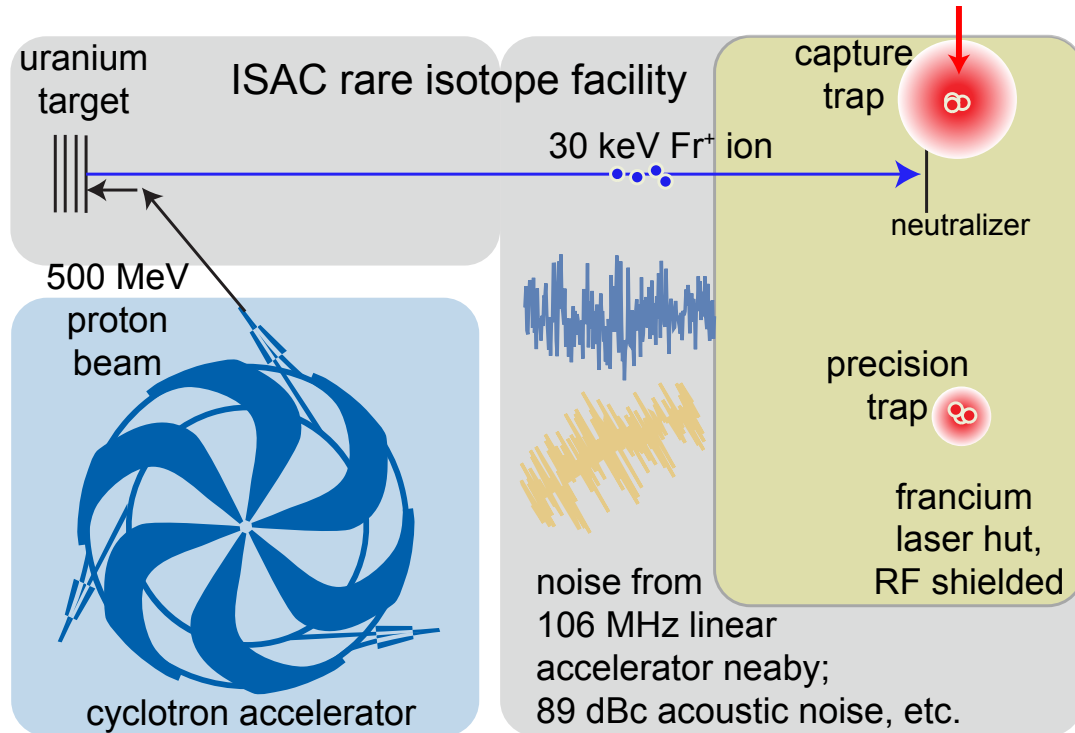


Figure 2.4: Schematic of the francium trapping facility (FTF) at TRIUMF. Not to scale. The radioactive ions are produced by up to $10\ \mu\text{A}$ of 500 MeV energy proton beam from the cyclotron accelerator, bombarding a uranium target. These ions are neutralized and laser cooled and trapped with magneto-optical trapping techniques. The cold ($100\ \mu\text{K}$) francium are then transported to a precision trap for APNC measurements. The francium laser room is a RF shielded metal hut, isolated from the noise of the hall.

TRIUMF. The main accelerator is the world's largest cyclotron, which produces up to $10\ \mu\text{A}$ of proton beam available for various physics programs. The FTF is located inside the Isotope Separator and Accelerator (ISAC) facility. We have a laser room constructed out of RF shielding materials and provides the necessary environmental control (RF, temperature, humidity, etc.). The francium beam is delivered as 30 keV energy singly charged ions. We neutralize these ions, and then cool and trap them with a high-efficiency magneto-optical trap (MOT). We then transport the collected cold atoms to a second stage trap where the electromagnetic field needs to be exquisitely controlled, necessary for weak interaction studies. The PNC experiment starts there.

Chapter 3: The francium capture trap

This chapter describes our high-efficiency magneto-optical trap. We have published two instrumentation articles, attached to the end of this chapter, on the commissioning of the capture trap in the FTF [42], and the off-line trapping of ^{221}Fr [43], respectively. The main text in this chapter is complementary, containing experimental details not present in the papers, as well as broadening the understanding on the design decisions to complete the FTF. We may recommend that the reader should first look at the two papers, which have the overall picture and the results, and then read the rest of the chapter for more details.

The francium trapping facility at TRIUMF is a unique cold atom trap in many ways. As stated before, francium has no stable isotopes and the longest half-life is only 22 minutes. The main solution is to directly connect the trapping apparatus to the accelerator beamline, and receive the singly charged Fr ions in a chamber called the neutralizer chamber. Then we use an electrical heating pulse to release the neutral Fr atoms, and trap them in a vapor-cell magneto-optical trap (VCMOT) [44]. The trap is newly constructed with design concepts based on the last version of the Stony Brook trap [45], adding various upgrades in the UHV system and neutralization technique. New features include modular design for

ease of replacing the neutralizer assembly, the offline ^{225}Ac source to obtain ^{221}Fr without proton beamtime (see section 3.7 and the second publication attached to this chapter, Ref. [43]), and a new design of the optical system for delivering the laser beams via optical fibers. We start with the glass cell.

3.1 Glass cell.

Our vapor-cell MOT is optimized for high trapping efficiency. Some key design features originate from the need to have large diameter laser beams that completely fill the cell, that ideally any atom within the volume can experience the cooling force. This is accomplished by having a cubic cell with the corners cut off (Fig. 3.1), which has major faces sized at about 2 inches, to which our laser beams can be conveniently expanded. The cube corners are efficiently utilized by having small viewports, which can be used for imaging and sending in probe laser beams.

Figure 3.1 shows a picture of the glass cell. This cell design directly descend from the one used in Stony Brook by Seth Aubin and Eduardo Gomez, built by a glass blower in Stony Brook from 2 inch and 0.5 inch optical flats and a glass viewport from Larson Electronic Glass. We were using the Stony Brook cell in the beginning, until it had problems with the glass to metal seal, presumably because of the multiple runs of dry-film coating process, which involves potassium hydroxide rinsing. This created a problem a few days before a run in 2012 and we had to seal it in-situ, with silicon-based sealant (VacSeal VGL-VS1/2). W. Kruithof from KVI in the Netherlands [46] based their radioactive Na trap cell from the thesis of

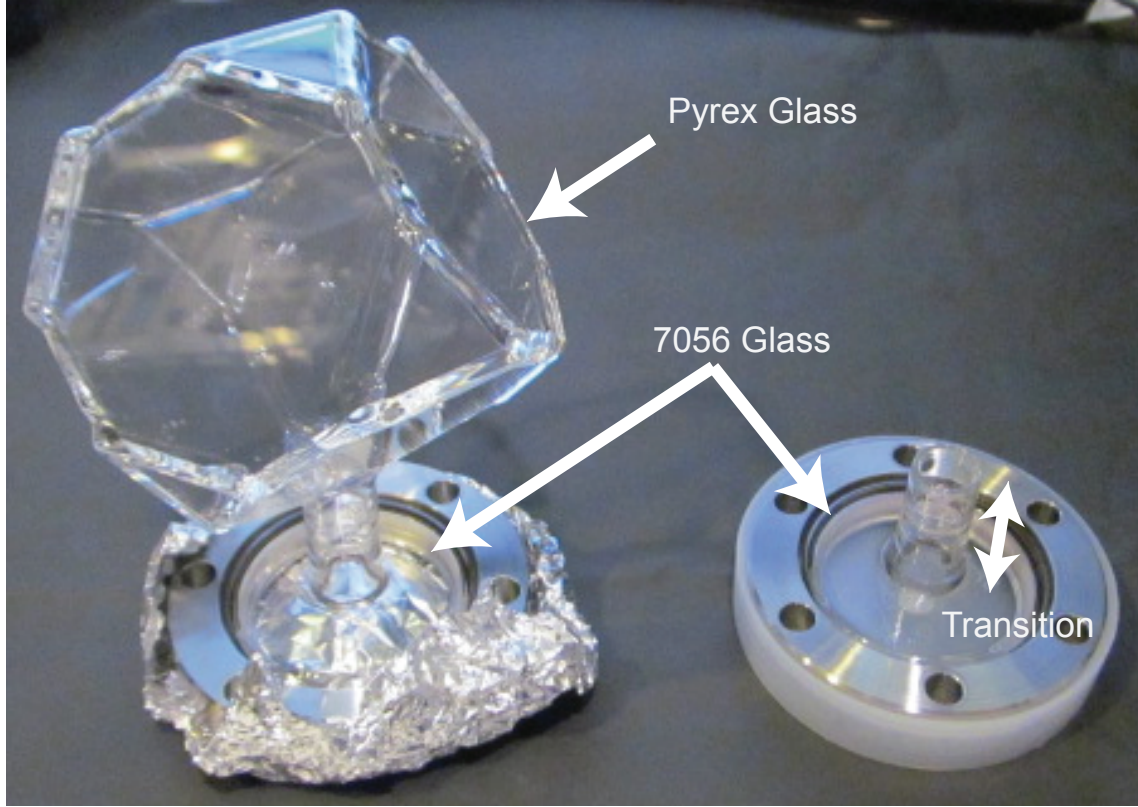


Figure 3.1: Picture of the glass cell for the capture trap. Left: complete cell. Right: 2.75” flange with glass to metal seal and glass type transition.

Seth Aubin [47]. Precision Glassblowing from Boulder, Colorado have experience building the KVI cell, so we purchased our new cells from them. Larson Electronic glass provided a flange with a glass neck: a Corning 7056 glass tube is joined to the the 2.75 inch CF flange via a Kovar seal¹, and the center includes the transition glass to Pyrex. The cell is manually assembled and torch fused from pyrex pieces cut to size, and then joined to the neck. Appendix A contains detailed dimensions.

The cell has to be coated with a “dry-film” layer, in order to prevent the released thermal atoms from sticking to the surfaces while bouncing between the

¹This metal alloy is commonly chosen to match the thermal expansion coefficient with that of Corning 7056 glass. Kovar is magnetic, as we will encounter (or avoid) in the apparatus described later in this thesis.

walls of the cell. The dry film coating has always been the “black magic” part of the capture trap, because we do not fully understand the chemistry involved, plus the beamtime availability prevent us from exploring different options and compare. We resort to a safe path with procedures established quite sometime ago [48], which uses a mixed silane called SC-77. It can be purchased from Alfa Aesar even though one cannot find it in their online catalog.² Our summer undergraduate student Alysa Obertas has re-written the coating procedure³. The cell itself does not have any anti-reflection coating on any surface, and the dry-film likely makes the transmission worse (by eye inspection) than 96% per surface, which is what we expect for uncoated glass. However it could also work in favor of us to randomize the phase in the laser wavefront, as the flatness of the glass is compromised, reducing interference effects. We are not aware of conclusive and quantitative studies to support either of these two arguments. Our typical MOT shape is reasonable, occasionally having avocado shaped deformations as seen in Fig. 8 of Ref. [42].

3.2 Optics and Optomechanics.

The trapping laser beams flooding the cell are fiber coupled and expanded to Gaussian beams of 3 cm waist ($1/e^2$ diameter). The mechanical assembly is built from Thorlabs optical-cage (mainly 60 mm cage for the large diameter optics, though small components on 15 mm cage are used immediately after the fiber output) and

²It has a short shelf-life of about 6 months, so call them and ask for quick delivery, they will do the required mixtures and ship to us in about 3 to 4 weeks.

³For internal reference, see francium Elog entry (general, thread 480). <https://elog.triumf.ca/Francium/General/480>. Log-in required.

lens-tube systems (2 inch SM2 series tubes mainly) similar to that described in the thesis of Andres Cimmarusti [49]. The optics design originates from Roger Brown from the JQI, and is a three lens construction that has excellent near diffraction limited performance (few micron resolution calculated by OSLO, compatible with the fiber mode diameter), and chromatic aberration compensation, the latter of which particularly important for switching between different alkali atom species. Based on a suggestion from Gerald Gwinner, we designed this “exoskeleton” cage for mounting the optics and the quadrupole and bias field coils, which is one of my favorite pieces machined by the shop at TRIUMF. Figure 3.2 shows the model for this exoskeleton. It not only supports the 60 mm cage system mounting with ease, but also serves as a nuclear safety barrier. It prevents people from easily accessing the glass surface with sharp tools, and breaking the delicate cell apart, e.g. by accidentally dropping a wrench. For ease of assembling, the exoskeleton is designed to be a monolithic “cup” with 5 faces, with a “lid” on the bottom. Two edges have two slots each, which clear 8-32 screws. These edges have angled surfaces that can match the orientation of the cell (vertical axis aligned with 111 axis in crystal terminology), so that the cage can be mounted to two brackets which are inturn bolted to the 2.75” flange on the bottom. Appendix B contains detailed drawings of this exoskeleton.

We would like to mention some experimental details and the reason why we made certain decisions. We use quarter wave-plates (QWP) that are true zero-order at 718 nm. Magneto-optical traps are famous for being quite forgiving for the exact light polarization. The true zero-order QWPs would have retardance proportional

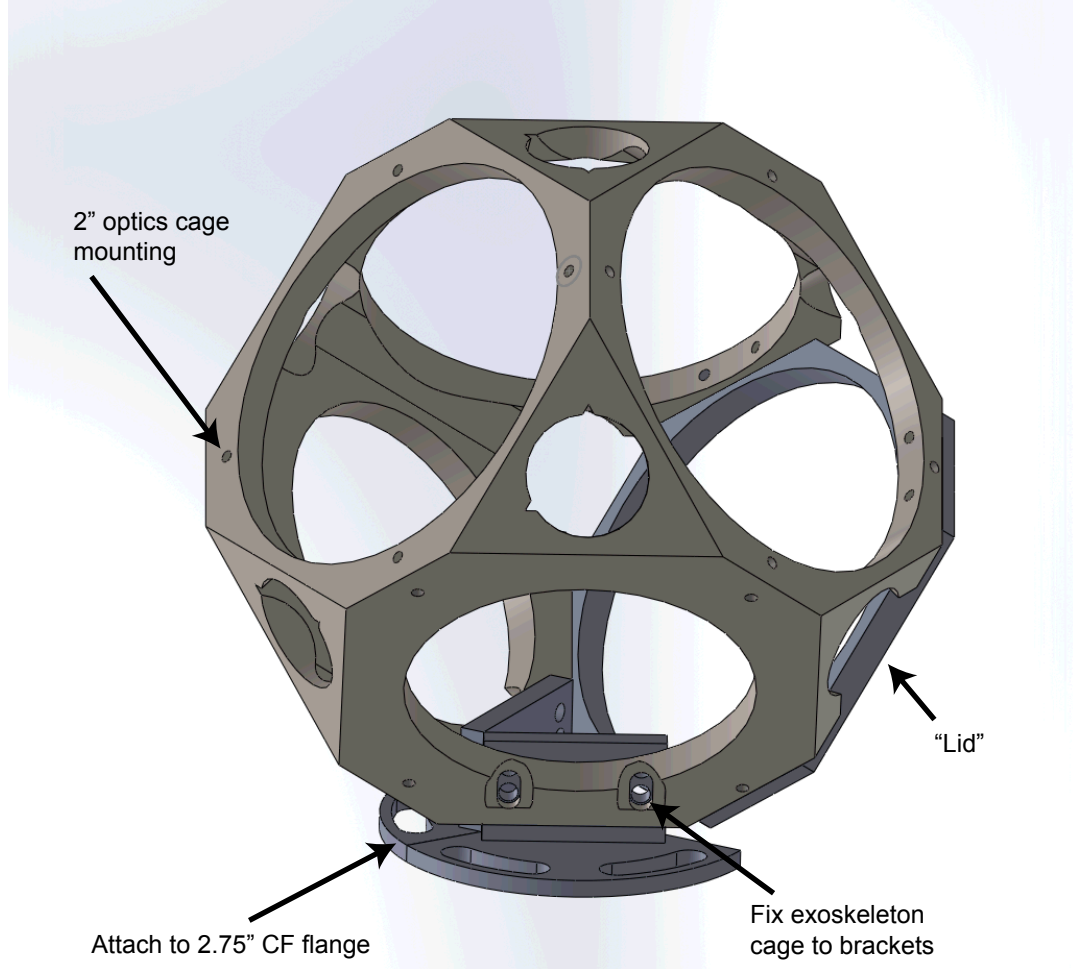


Figure 3.2: (Almost monolithic) “Exoskeleton” cage surrounding the glass cell, serving as a mounting structure for optics assembly, as well as a radiation safety caution, by protecting the cell against breakage.

to the wavelength, yielding about 0.27 waves at 780 nm instead of the ideal 0.25 waves at the design frequency. This does not pose any issues with the Rb MOT. The wide angle-tolerance of true zero-order waveplates is advantageous because we generate the circular polarization where the laser beam is still small and expanding, and avoid using large 2” waveplates. We have explored dual wavelength QWPs, and found that some of them (e.g. from Opti-source LLC) are fine, and some (e.g. from Sinocera Optics) have fast and slow axis reversed for the two wavelengths.

The use of 6 beam instead of 3 beam retro-reflected configuration, is forbidden because of two reasons: First, the space constraints on the bottom three faces of the glass cell are already tight, such that we had to insert small kinematic (KM) mounts into modified cage adaptor plates, instead of using off-the-shelf 2 inch kinematic mirror mounts. Fiber expansion optics is only possible on the top three faces. Second, the evanescent-wave fiber-splitters (Evanescent Wave, Inc. custom model based on 954P series, quotation 8914R1) has wavelength dependent ratios. Three branches output equally 33% for 718 nm light, while at 780 nm we tested the outputs to be 40%, 45%, and 10%, respectively. If we use 6 beams, the fiber splitter would inevitably create power imbalances at one of the wavelengths. This discussion is valid for the science chamber MOT as well.

3.3 Neutralizer

Francium arrives from the accelerator side as singly-charged ions with 30 keV energy. These ions are transported through the ISAC beamline with suitable ion beam optics, and directly stopped by implanting into a metal foil. This foil is heated to high temperatures to release francium as neutral atoms, and is referred to as the neutralizer. The common choice of material by several radioactive alkali-atom trapping groups [50–53] includes a few elements from Group 3 and Group 4 in the periodic table, namely yttrium (Y), zirconium (Zr) and hafnium (Hf).

The heating process significantly speeds up the diffusion and desorption [52], such that the atoms move fast within the metal and eventually out of the surface,

such that a reasonable portion of Fr atoms can be released. One key concern for choosing the neutralizer material, is that its work-function [54], which is the potential that the solid material can bind the free electron in the “electron sea”, should be lower than the ionization potential of an electron in a free Fr atom (4.07 eV).⁴ The fraction of released neutral atoms depend on the neutralizer work function through a Fermi-type function, the Saha-Langmuir equation [55]:

$$\frac{n_+}{n_0} = \frac{g_+}{g_0} \cdot \exp\left(\frac{W - E_I}{k_B T}\right), \quad (3.1)$$

where n_+/n_0 denotes the ratio of ion number density to neutral number density, g_+/g_0 is the ratio of the degeneracy of states, equal to 1/2 for alkali atoms, and E_I is the ionization energy. This results in a release fraction for neutral atoms with a Fermi distribution, plotted in Fig. 3.3 at temperature 1000 K (which determines the width of the Fermi distribution to be 0.086 eV), and the ionization energy of francium 4.07 eV [56].

The actual heating temperature depends on many parameters, including the crystal structure of the metal, the diffusion coefficient of the particular material, which for Y has been measured to be $D_{T=1000K} = (1.0 \pm 0.4) \times 10^{-14} \text{cm}^2 \text{s}^{-1}$ [52], and the threshold to avoid damage to the Dryfilm [57]. A convenient range then is 1000 K to 1200 K, at about 55% of the melting point of yttrium and zirconium, respectively.⁵ In fact this proportionality to the melting point, is a coarse rule

⁴The underlying physics of surface ionization is essentially the same, except the role of high work function metal and relatively low ionization potential of neutral atoms are reversed.

⁵Another material commonly occurring in our group discussions is Hf, which has a work-function 3.9 eV, however the melting temperature is a little too high (2506 K) for us to consider as suitable.

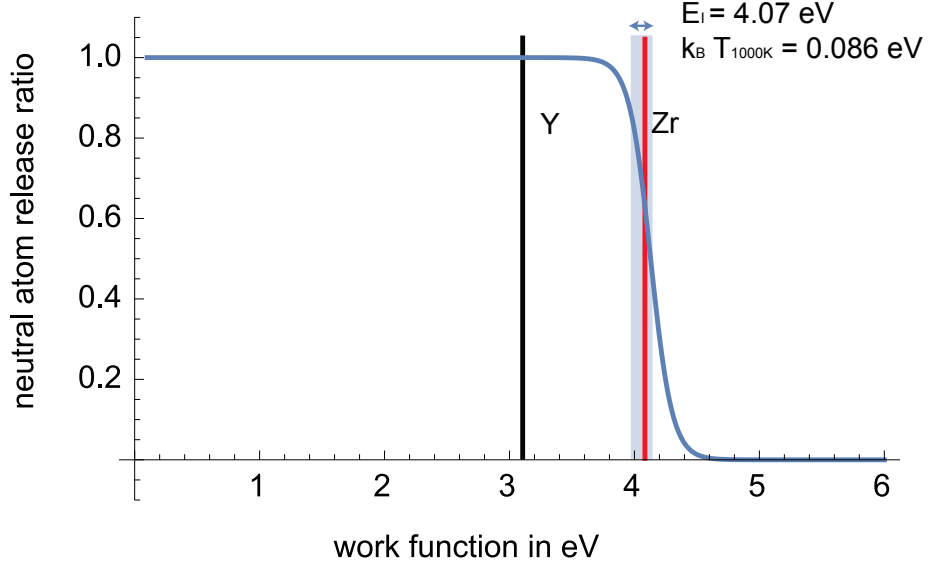


Figure 3.3: Theoretical curve for neutral atom release fraction. Yttrium and zirconium are indicated with black and red dashed lines, respectively. The gray region illustrates the center and width, determined by the ionization potential (E_I) of Fr and the heating temperature (T), respectively, of this Fermi distribution resulting from the Saha-Langmuir equation (see text).

of thumb for choosing the heating temperature, as shown in the extensive material searches performed in Ref. [50].⁶

There are several other concerns for choosing the neutralizer material:

1. It should have a low vapor pressure, such that the vacuum background is not affected too much during heating. The vapor pressure for three different metals including Y and Zr are plotted in Fig. 3.4, with reference data for the coefficients from [58], which quotes 5% uncertainty within temperature range 298 - 2500 K. As can be seen in the insert in Fig. 3.4, yttrium at 1000 K has

⁶There are of course finer details, such as the structural phase transitions of the metal that only exists in some of the materials, see Ref. [50]. The exact heating temperature is an empirically determined number. The Italian group in Ref. [52] uses 1000 K, which is also where we (conservatively) operate [42]. In Ref. [45] the quoted heating temperature in Stony Brook is at 1150 ± 150 K.

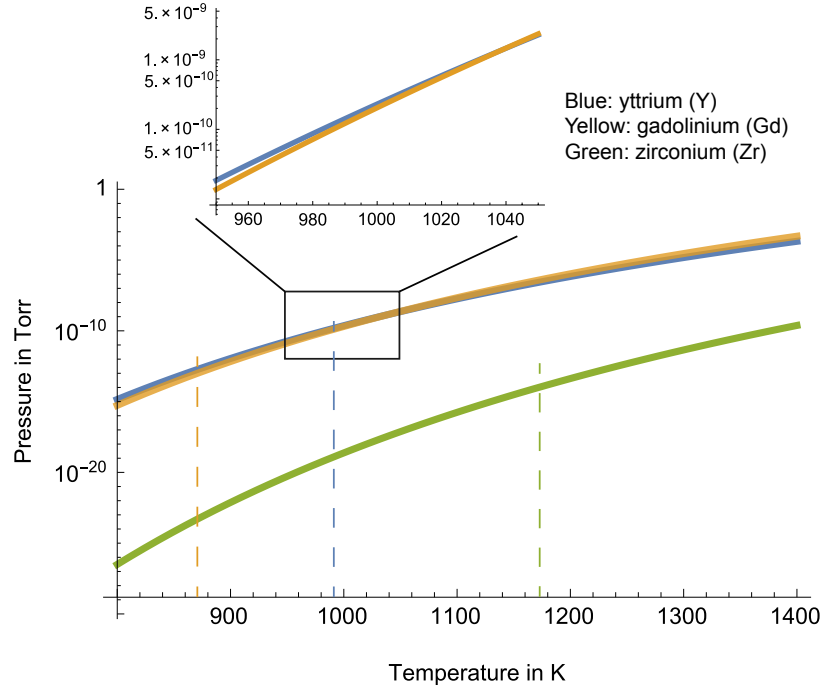


Figure 3.4: Vapor pressure [58] as a function of temperature, for three different neutralizer candidates. The dashed lines indicate 55% of their melting temperatures.

a pressure of low 10^{-10} Torr, which is visible with the ion pumps, but does not pose a significant issue for the trapping. Due to the nearly exponential dependence on the temperature, this vapor pressure quickly climbs up to 10^{-9} Torr at 1050 K. We have always operated the francium trap conservatively, gauged by the Nextorr ion pump current, because of the lack of precision control on the heating temperature.

2. The oxidation in air should be reasonably small, so that the surface layer is essentially clean metal after a few pulses of heating in UHV. Yttrium is relatively stable in air due to passivation from the thin protective oxide layer on the surface. We have observed no difference of the francium trapping with

either fresh Y foil under argon packaged, or ones that has been sitting in air for a few months before spot-welding.

3. The metal should not be too soft or brittle, for ease of handling and workability.

We have always been using spot-welding to attach the foil to its holders. This is a manual process, and it takes a lot of training and caution to make sure that the attachment is nice and even. Other methods that have been discussed include electron-beam welding, which is not suitable because the process is under low vacuum, and would result in undesirable uneven heating and/or oxidation; and high-temperature oven-brazing, which we have not yet explored.

7

Yttrium has been our neutralizer material for our francium trapping at TRIUMF so far, and was also used in the old Stony Brook trap. the latest Y foil became wrinkled after one or two beam-times, which amounts to roughly 30,000 cycles, and broke in the run in December of 2014. Some new designs are being explored with the help of Dr. Alexander Gorelov from TRINAT at TRIUMF, where Zr is used for neutralizing K. The 4.34 eV ionization energy of ^{37}K relaxes the work-function requirement, and a crystal structure phase-transition aids with the release [50]. Searching across the periodic table with the afore-mentioned requirements, a rare-earth element appears as a future possibility: gadolinium (Gd). It has a work-function of 3.2 eV and a melting point of 1585 K, is relatively stable in dry

⁷The metal foil should be bought annealed if possible, as cold-rolled foils without annealing can have brittleness or other undesirable properties. Eduardo Gomez and I have rolled yttrium with a bench-top rolling mill in Simon Fraser University Chemistry Department, and it turned out to be much darker than off-the-shelf Y foils, and is much more flammable, as we burned a few just during weighing and spot-welding.

air, and is available from Alfa Aesar as 25 micron foils (\$106 for an 1 inch square piece, catalog 12397). We have included Gd in the vapor pressure plot Fig. 3.4.

3.4 Modular design of the in-vacuum assemblies.

The new designs for Y foil heating, as well as Ta foil mechanical assembly for the offline ^{221}Fr source [43], share the feature of modularity. Their mechanical and electrical connections are all attached to a single 4.5" CF flange, which greatly facilitate assembly replacements. This is crucial for dealing with vacuum openings while residual radioactivity is still present, as we can finish the un-irradiated assembly independently before venting the vacuum system. Replacements usually takes less than one hour, though of course the preparations can take a day or two.

Figure 3.5 shows these modular designs, (a) the Y assembly, and (b) the Ac assembly. Each assembly has two 1.33" CF half-nipples welded to the 4.5" CF flange, one used for the rotational feedthrough (MDC model 670050), the other used for the electrical feedthrough. The Ac assembly only has a grounded BNC feedthrough for measuring implantation current, whereas the Y assembly has a multi-pin feedthrough that can carry up to 10 A DC current, more than enough capacity for the heating pulse.

3.5 Laser locking and frequency reference

The laser locking is a scanning transfer-cavity lock, similar to that described by an early instrumentation article [59] from Stony Brook. The original software

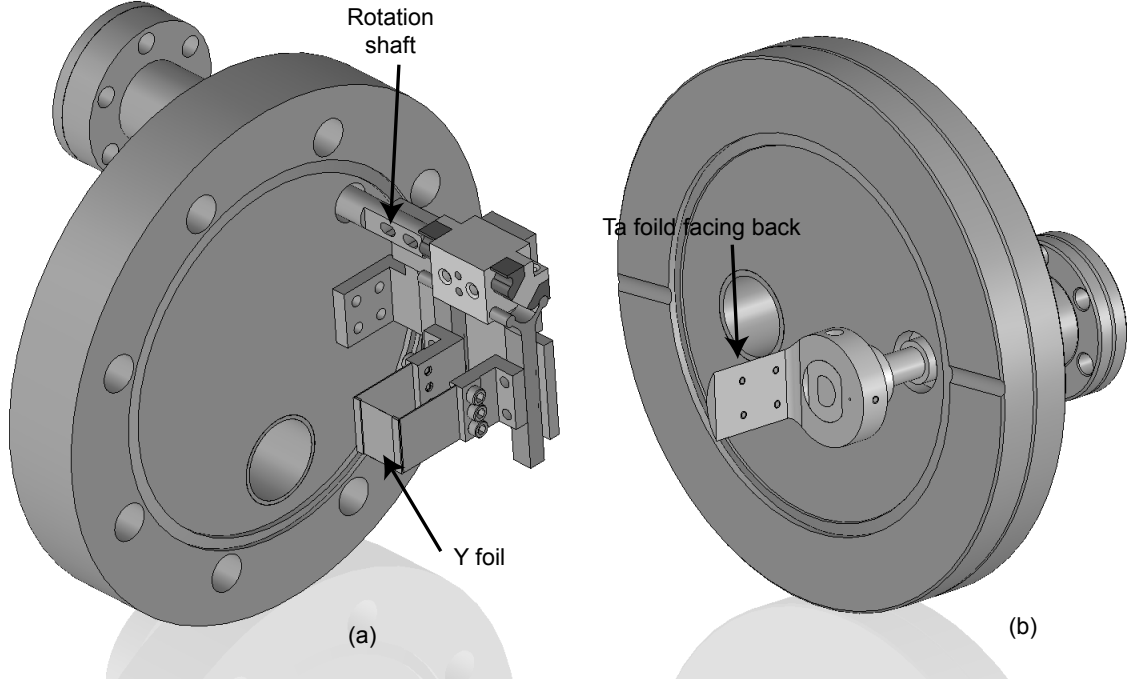


Figure 3.5: Modular designs for the neutralizer chamber assembly. The 4.5 inch CF flanges have 1.33 inch CF half nipples directly welded to it, such that mechanical rotation and electrical feedthroughs (not shown) are conveniently attached. The modularity eases with handling, which is especially important when radiation safety concern is involved. (a) Y (neutralizer) assembly. (b) Ta (source for ^{221}Fr) assembly. Clearance holes on the 4.5 inch CF flange is obviated.

was lost over the years, and the currently version is based on Labview code started by Eduardo Gomez in the summer of 2011, greatly improved by Michael Tandecki afterwards. Fig. 3.6 shows the laser locking control program. The HeNe reference laser (upper right corner, white lines) peak positions are calculated when the cavity piezo is scanned over a free spectral range (FSR, 300 MHz for a confocal cavity with 25 cm mirror spacing). The cavity is under hermetic seal built with standard UHV components, however is not pumped down under daily operations. It is locked to the HeNe by feeding back to the bias of the piezo ramp voltage, with error signal

generated from the separation of the two He-Ne peaks. Four laser channels can then be independently locked to the cavity. The computer program calculates the peak centroids, and lock the lasers by feeding back to external inputs such as the reference cavities for Ti:sapph lasers or piezos of diode lasers. A wavelength meter (we used to have a HighFinesse WS-7, 10 MHz version) reading of the laser frequency is incorporated, shown in the middle right of Fig. 3.6.

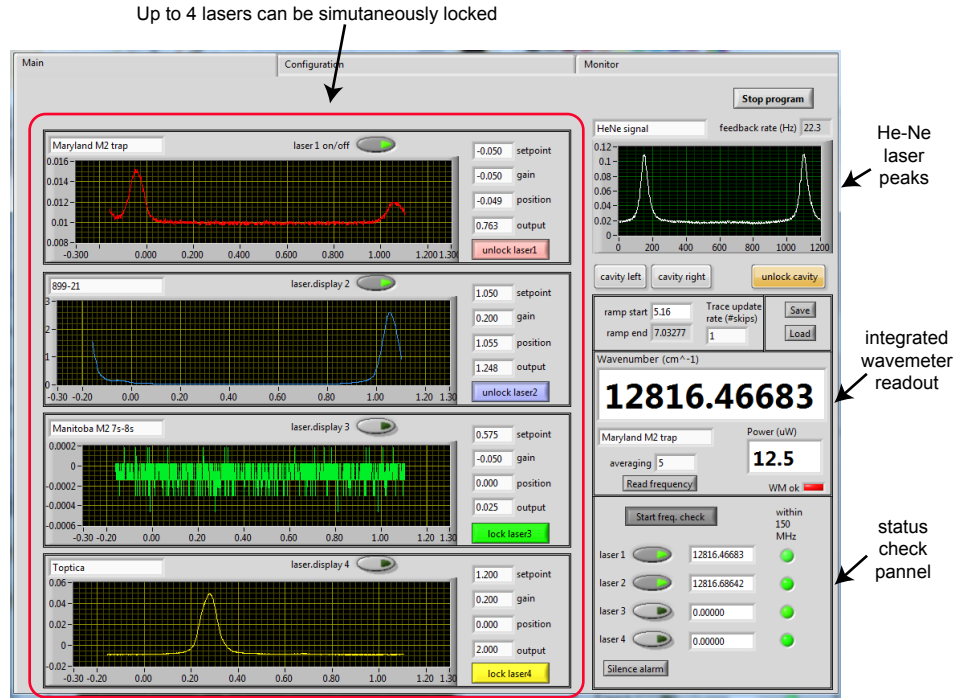


Figure 3.6: Capture display of the scanning cavity laser locking program. The electronic version of this thesis enables zooming in to see the details. See text for explanation of the working principles.

The program in its current status, has a repetition frequency of about 20 Hz, which is relatively slow. For the MHz level stability required for stable MOT operation, we can rely on the intrinsic narrow linewidth of the Ti:sapphire laser used for the trap. Diode lasers might have noise at higher frequency, but are typically

employed for repumping and hence are tolerant on this feedback bandwidth. The long-term stability of the HeNe laser is, in the worse case scenario, 8 MHz over 24 hrs, which would compromise for example the optical PNC experiment (transition linewidth 3 MHz) in data-taking mode. We currently have a Rb saturation spectroscopy based on polarization modulation [60]. This can in the future replace the HeNe, and we could change to modulation transfer spectroscopy [61] when we need an absolute frequency reference to better than 1 MHz.

3.6 Radioactive decays of ^{210}Fr

We choose particular isotope of ^{210}Fr for starting the PNC measurements. One of the main reasons for this decision is that the radioactivity should be reasonable and relatively straight forward to control. Radiation safety is a complex issue, which we do not intend to completely address here. We only discuss briefly the main concerns and more detailed discussions and precautions can be found in TRIUMF safety reports from John Behr.⁸

⁸See for example (internal reference) TRIUMF Elog Francium entry 473, <https://elog.triumf.ca/Francium/General/473>. Log-in required.

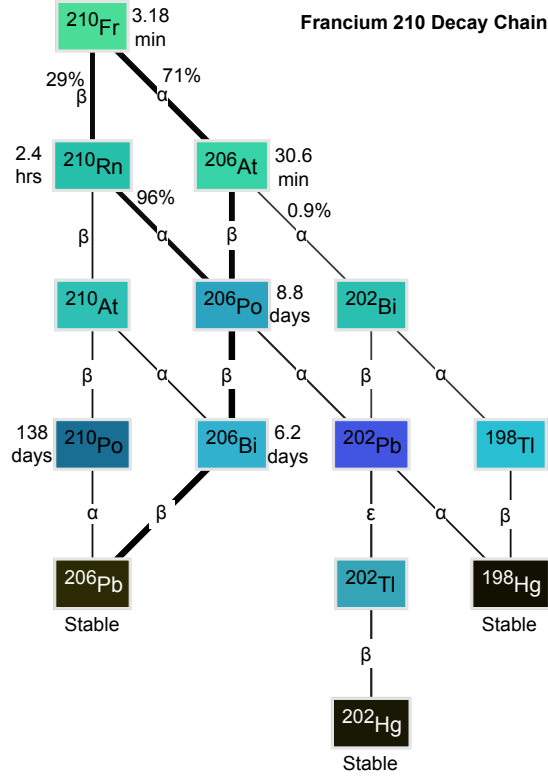


Figure 3.7: ^{210}Fr radioactive decay chain. Darker colored boxes indicates longer decay lifetime. Stable isotopes are in black boxes. The thickness of the lines gives a general guideline to the relative percentage of the decays. Besides the self-explaining α and β radiations, ϵ denotes electron capture, and we have omitted γ radiation which accompanies with most of the decays. The most dangerous ionization radiation, the alpha particles, has short lifetimes in the francium and radon isotopes involved, and will not penetrate the vacuum apparatus in normal operation. The relatively long lived polonium isotopes requires safety attention while opening the UHV system after irradiation.

Among the four types of radiations that TRIUMF has or could have in experimental areas, we have three: The alpha particle is a composite particle with two protons and two neutrons, which is essentially the He nucleus. It can be stopped by a piece of paper, as well as our body tissue, and certainly the vacuum chamber

walls. When there is neither vacuum openings nor leaks, the alphas do not pose any radiation hazard for us. The beta particles, or high-energy electrons, can be stopped by a thin metal plate, and is also blocked by the vacuum chamber barrier. Gamma rays on the other hand, penetrate practically everything we have in the laboratory, and needs shielding with concrete when the amount is too high. Fortunately we are not at that level, and since the gamma rays have 4π solid angle distribution, we just have to reduce our body's cross-section, or in other words stay as far away as possible from the trap during beam-times. The control center, where the computers, time sequencing, and data acquisition systems are, is located on the opposite corner of the RF shielded lab room.

The prime concern when we open the vacuum chamber and change things, typically several months after a beam-time, is the remaining alpha radiation. We have to choose isotopes where not only the Fr, but also all the daughter decay products have reasonably short life-times. A general rule is that any α emitter with 3 months to 3 years life-time is quite bad, because if we ingest or inhale them into our bodies, we practically absorb all the ionizing radiation from this source in our lifetime (or shorter, 10 years for example). ^{209}Fr was the isotope that was chosen for the first commissioning run; it has a longest daughter of ^{209}Po with a half-life of 102 years. We have selected ^{210}Fr for starting the anapole moment experiments. Here we plot in Fig. 3.7 its radioactive decay chain, indicating longer life-times with darker colors. The resulting main radiation hazard, immediately after 5 days of beam-time, assuming full irradiation intensity at 4×10^8 ions/s, is 0.2 annual limit of intakes (ALI) from 138 d half-life ^{210}Po , and 41 ALIs from 8.8 d half-life ^{208}Po , if

we were to ingest everything that exists in the science chamber. If we were to inhale all of them, these two dose numbers would be 1.3 ALIs and 142 ALIs, respectively. The above estimations comes from John Behr’s radiation safety report. Of course these are worst case scenarios, as it is impossible to eat or breath all of the radiation immediately after a beam-time run. We expect volatiles to be pumped by the ion pumps, whereas non-volatiles would stick to chamber walls. In addition, when the vacuum system is vented (or broken) the room air gets sucked in, instead of the contents being blown out. Over the three or four times that we have opened the system and swiped for radiation, we never detected anything left.

3.7 Francium 221

^{221}Fr is a special isotope from a practical experimental point of view. It is the only francium isotope with a suitable “precursor” source, ^{225}Ac , and was actually considered by Wieman as a possibility for an APNC experiment [62]. With the proposed anapole experiment however, this isotope is not quite compatible with the neutron-deficient ones we have chosen (^{207}Fr to ^{213}Fr), mainly because the ground state microwave transition frequency of 18.4 GHz is rather different from the 40 to 50 GHz range, e.g. 43.8 GHz for ^{210}Fr , and requires some re-designing of the microwave cavity and related hardware.

Nevertheless this isotope can be useful in tests, especially if it is conveniently available “off-line”, i.e. after the proton beam stopped irradiating the ISAC targets. The ^{225}Ac remaining in the uranium target can be extracted with the help of the

laser ion-source group of Jens Lassen.⁹ We had thought about incorporating a source fully off-line, for example actinium nitrate liquid solution from Oakridge National Lab, and then process the necessary nuclear chemistry steps to have things compatible with the Fr apparatus. Another route that John Behr had explored early on when I just joined the experiment, was to implant the Ac beam (for example from CERN) into a metal target, and then transport it across the continent under hermetic seal. We were discussing in late 2010 what upgrades to our UHV system this requires. It would involve two layers of all-metal gate-valves and a 20" long linear feedthrough. We decided that all these approaches were too complicated to implement, and resorted to the current simpler solution: a rotation feedthrough with a piece of Ta foil, in front of the Y neutralizer, which can be rotated either facing the ion beam, the neutralizer, or out of the way. See Ref. [43] attached for more details.

⁹Unlike alkali atoms, ^{225}Ac does not diffuse easily out of the target, which is why resonance ionization with pulsed lasers have to be employed for the extraction.

Commissioning of the Francium Trapping Facility at TRIUMF

M. Tandecki,^a J. Zhang,^b R. Collister,^c S. Aubin,^d J.A. Behr,^a E. Gomez,^e
G. Gwinner,^c L.A. Orozco^{b,1} and M.R. Pearson^a

^aTRIUMF,

Vancouver, BC V6T 2A3, Canada

^bJQI, Department of Physics and NIST, University of Maryland,
College Park, MD 20742, U.S.A.

^cDepartment of Physics and Astronomy, University of Manitoba,
Winnipeg, MB R3T 2N2, Canada

^dDepartment of Physics, College of William and Mary,
Williamsburg, VA 2319, U.S.A.

^eInstituto de Física, Universidad Autónoma de San Luis Potosí,
San Luis Potosí 78290, Mexico

E-mail: lorozco@umd.edu

ABSTRACT: We report on the successful commissioning of the Francium Trapping Facility at TRIUMF. Large laser-cooled samples of francium are produced from a francium ion beam delivered by the ISAC radioactive ion beam facility. The ion beam is neutralized on an yttrium foil, which is subsequently heated to transfer the atoms into the magneto-optical trapping region. We have successfully trapped ^{207}Fr , ^{209}Fr and ^{221}Fr , with a maximum of 2.5×10^5 ^{209}Fr atoms. The neutral cold atoms will be used in studies of the weak interaction through measurements of atomic parity non-conservation.

KEYWORDS: Laser cooling; Instrumentation for radioactive beams (fragmentation devices; fragment and isotope, separators incl. ISOL; isobar separators; ion and atom traps; weak-beam diagnostics; radioactive-beam ion sources)

¹Corresponding author.

Contents

1	Introduction	2
2	Weak interaction in atoms	2
3	Requirements of the Francium Trapping Facility	4
3.1	RF shielding and temperature environment	4
3.2	Magnetic field environment	5
3.3	Radiation safety	5
4	Francium production and delivery	6
4.1	Production of francium at TRIUMF	6
4.2	Beamline of the FTF	6
5	Francium Trapping Facility	8
5.1	The capture assembly	8
5.1.1	Neutralizer chamber	8
5.1.2	The MOT for capturing Fr	10
5.1.3	Faraday cup and α detector	10
5.2	Laser systems	11
5.2.1	Frequency determination and stabilization	12
5.3	Experimental control and acquisition	12
5.3.1	Sequencer	12
5.3.2	Data acquisition and camera operation	12
5.3.3	Transfer cavity lock	13
6	Tests with stable Rb	13
6.1	Off-line Rb^+ source	14
7	Commissioning run with Fr	14
7.1	Different isotopes	16
7.2	Trapping results and efficiency	16
8	Outlook and conclusions	17

1 Introduction

Parity non-conservation (PNC) is a unique signature of the weak interaction. Thanks to this property it is possible to study the weak interaction in the presence of other, dominating interactions like the electromagnetic one. Shortly after the discovery of PNC, the possibility of observing it in atomic systems, due to the possible existence of a neutral weak current, was considered [1].

We have initiated a program, at the Francium Trapping Facility (FTF) at ISAC/TRIUMF, to study weak interaction physics at low energy through atomic parity non-conservation (APNC) [2] in neutral francium (Fr) atoms. The scarcity of the unstable atoms can be compensated for by the techniques of laser cooling and trapping applied to radioactive atoms [3] that allow for long-term interrogation of the atoms under well-controlled conditions.

The APNC measurements rely on two aspects; first, an apparatus with a well-defined handedness, and second, the interference between a weak-interaction-induced transition and an electromagnetically allowed transition. The control of the environment and the apparatus require careful planning at all stages, in particular since the measurement takes place in an accelerator hall, where changing magnetic fields and large RF electromagnetic fields can introduce noise and systematic effects. The program requires a reliable laser cooling and trapping apparatus that efficiently uses the radioactive ions. While the accelerator delivers fast ions to our facility, the planned experiments require slow neutral atoms.

Our APNC apparatus consists of two parts, the capture assembly and the science chamber. The first step in the manipulation of francium is to accumulate the francium ions on an yttrium foil. The francium is released in atomic form (because of the lower work function of yttrium with respect to francium [4]) by resistive heating of the foil, and it is trapped in a magneto-optical trap (MOT). All of this happens in the capture assembly. Briefly, a MOT uses a combination of near-resonant laser light (red-detuned from resonance by Δ) with a three-dimensional magnetic field gradient to produce a force that is both velocity-dependent (dissipative) and position-dependent (restorative) to cool and capture neutral atoms that are moving at velocities lower than a capture velocity, v_c (about 15 m/s) [3]. Once trapped, the atoms can be probed in the capture assembly or transported to the science chamber for the actual APNC measurements in a well-controlled environment.

This paper reports the successful commissioning of the FTF at the ISAC facility of TRIUMF; we focus on the capture assembly, as the science chamber was not constructed yet at the time of the commissioning run. Section 2 briefly reviews the physics of APNC, followed by the requirements for the measurements and facility in section 3. The production and delivery of francium into the FTF is presented in section 4, while an overview of the FTF is given in section 5. Brief results from measurements with rubidium are presented in section 6. Section 7 summarizes the results from the on-line commissioning run. Section 8 gives conclusions for the described work and an outlook.

2 Weak interaction in atoms

Atomic parity non-conservation arises from the parity-violating exchange of Z^0 bosons between the atomic constituents, leading to a mixing of atomic levels of opposite parity [2]. As a result, otherwise parity-forbidden electric-dipole transitions can be excited between states of the same parity. Several processes lead to APNC. If the nucleons and electrons are described as as a vector and

an axial vector current respectively this leads to nuclear spin-independent APNC (*nsi*-APNC) [2]. Nuclear spin-dependent APNC (*nsd*-APNC) occurs in three ways [1, 5]; (i) an electron interacting weakly with a single valence nucleon (nucleon axial-vector current and electron vector current), (ii) an electron experiencing an electromagnetic interaction with a nuclear chiral current created by parity-violating weak interactions between nucleons (anapole moment) [5, 6], and (iii) the combined action of the hyperfine interaction and the nuclear spin-independent Z^0 exchange interaction from nucleon vector currents [7–9]. In heavy atoms, process ii) is the dominant source of *nsd*-APNC [6, 7, 10].

The FrPNC collaboration is working towards measurements of both types of PNC effects [11]. The attractiveness of Fr for *nsi*-APNC experiments has been discussed since the early 1990s in the context of searches for new physics beyond the Standard Model (SM) [10, 12–15]. The atomic theory and structure of Fr ($Z = 87$) can be understood at a level similar to that of Cs ($Z = 55$), where the most precise measurement to date has been performed [16, 17], yet the APNC effect has been calculated to be 18 times larger [18, 19].

All recent and on-going experiments in atomic PNC rely on the large enhancement of the effect in heavy nuclei (large Z), first pointed out by the Bouchiats [20–22]. The weak interaction transition amplitudes are exceedingly small, and an interference method is commonly used to measure them. A typical experiment measures a quantity that has the form

$$|A_{\text{PC}} \pm A_{\text{PNC}}|^2 \approx |A_{\text{PC}}|^2 \pm 2\text{Re}(A_{\text{PC}}A_{\text{PNC}}^*), \quad (2.1)$$

where A_{PC} and A_{PNC} represent the parity-conserving (typically much larger) and parity non-conserving amplitudes respectively. The second term on the right side corresponds to the interference term, which can experimentally be isolated because it changes sign under a parity transformation.

Our strategy for APNC in Fr is to measure the excitation rate of a highly forbidden transition inside a handed apparatus (see the review by the Bouchiats [23]). For the case of *nsi*-APNC it will be the electric dipole transition between the $7s$ and $8s$ levels in Fr that becomes allowed through the weak interaction. Interference between this transition and the one induced by the Stark effect due to the presence of a static electric field generates a signal proportional to the weak charge. We follow a strategy similar to the Cs APNC measurement that reached a precision of 0.35% [16, 17] on the *nsi*-APNC. For the case of *nsd*-APNC it will be the electric dipole transition between hyperfine levels in the $7s$ ground state interfering with the allowed magnetic dipole transition to produce a signal proportional to the anapole moment. In refs. [16, 17] they also obtained the first definite measurement of an anapole moment with an accuracy of 14% by comparing signals from different hyperfine levels. The successful extraction of weak interaction physics from the measured atomic quantities requires a detailed quantitative understanding of the atomic wavefunctions [24–26].

An APNC measurement will generally proceed as follows; we trap and cool atoms on-line at the FTF. The cold francium sample is then transferred to a science chamber with precise control of all electric, magnetic, and electromagnetic fields, as well as better vacuum ($< 10^{-10}$ mbar), where the handed experiments to study APNC take place. We require probing of large numbers of atoms in order to obtain a good signal-to-noise ratio. Our preliminary calculations show that 10^5 to 10^6 trapped atoms at a temperature below 1 mK should be sufficient.

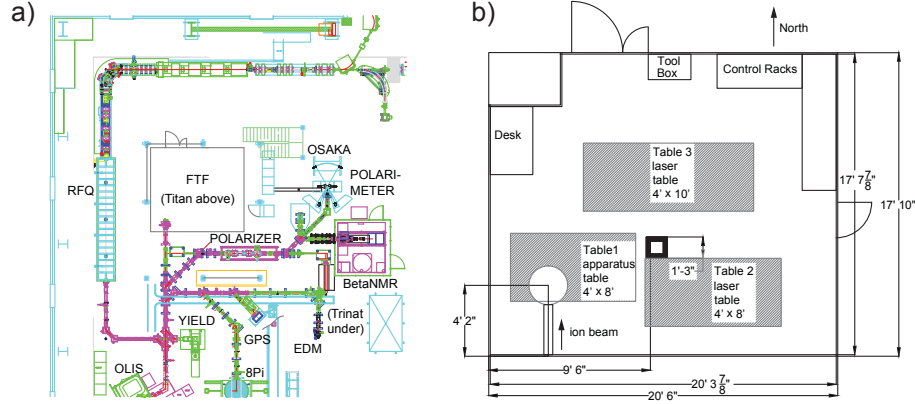


Figure 1. a) FTF in the ISAC I Hall at TRIUMF. b) Layout of the FTF with the francium beamline, optics tables and control equipment in August 2012.

3 Requirements of the Francium Trapping Facility

Reference [27] has a detailed study of all the necessary requirements for the measurement of *nsd*-APNC in Fr. The environmental requirements are similar for the *nsi*-APNC measurement. The ISAC-I Hall at TRIUMF, where our experiment resides, has several linear accelerators, or linacs (see for example the beamline denoted RFQ in figure 1a), that produce ample radio-frequency (RF) electromagnetic fields that can interfere with our measurements. The complete FTF is therefore located inside a Faraday cage.

3.1 RF shielding and temperature environment

The background RF noise at the location of the FTF without the Faraday cage was 21 V/m at 35 MHz and 2.7 V/m at 106 MHz, the most relevant frequencies from the RFQ of the linac on the west side of the FTF (see figure 1a). The dimensions of the Faraday cage are $5.9 \times 6.25 \times 3.66 \text{ m}^3$ under the existing platform that houses the TITAN facility. There is a column that supports the TITAN facility so the shielding of the room has to cover the column appropriately. Universal Shielding Corporation designed and constructed a galvanized steel Faraday cage to be the laboratory of the FTF. The floor, ceiling, and walls are made of metal-covered wood composite, with the appropriate fire retardants. The doors required double sets of grounding strips to ensure no RF leakage into the room. The room has penetrations with RF filters to allow water, air, the beamline, telephone, Ethernet, and other signals and services to enter the room. When the room is properly closed, the Faraday cage attenuates the RF amplitude by more than 100 dB at 35 MHz to levels lower than the noise floor of our measuring instrument.

The requirements on the room temperature are a range of 22–24°C and a stability better than $\pm 1.0^\circ\text{C}$ or better (year round, minute-to-minute). The relative humidity must be stable to $\pm 5\%$. The temperature and relative humidity of the ISAC area of TRIUMF show short-term fluctuations of $\pm 3^\circ\text{C}$ and $\pm 15\%$, respectively, while the long-term ones are season-dependent. Most of the equipment in the FTF requires this level of environmental stability, in particular the lasers and their

locking systems [28]. A few of the systems have extra temperature control as their stability should be better than 0.1°C . The temperature and humidity stabilization is realized by an HVAC system.

3.2 Magnetic field environment

The applied magnetic fields at the center of the science chamber need a fractional control at the 10^{-5} level [27], with applied fields of the order of a few gauss initially. During the summer of 2012, with most of the trapping apparatus (capture assembly) assembled and working, we studied the magnetic field environment of the FTF and measured the spectral density of the magnetic field noise. We measured the magnetic field with a Honeywell HMC1002 Anisotropic Magneto-Resistive (AMR) sensor, which has a precision of $100\text{ }\mu\text{G}$, with a 10 Hz bandwidth and a range of $\pm 2\text{ G}$. The magnetic noise at the experiment is dominated by line noise at 60 Hz and 180 Hz at the mG level that can be controlled with feedback and feedforward.

The magnetic field caused by the TRIUMF cyclotron at the location of the FTF is of the same order as the magnetic field of the Earth, $\sim 0.5\text{ G}$. Above the FTF sits the TITAN facility with superconducting magnets for their Penning traps. Their influence at the MOT is also of the order of the magnetic field of the Earth, and since the magnets operate in steady state, it is possible to correct for the DC fields with appropriate pairs of coils surrounding the apparatus. Measurements before the fall of 2011 at the current location of the FTF indicated that the DC magnetic field varies on the order of 100 mG over the course of several days. While we will not shield the entire room against quasi-static magnetic fields, active control at the science chamber will be necessary to maintain a highly-stable magnetic field environment for precision APNC measurements.

3.3 Radiation safety

The overall design of the FTF incorporates a number of radiation safety features. Radiation safety is an important consideration for experiments at TRIUMF and also a part of standard engineering practices. We briefly describe these standard nuclear physics engineering steps and procedures in the context of francium trapping, since they are not usually encountered in atomic physics experiments.

The FTF is equipped to handle the short-term radiation present during delivery and trapping of francium and also the long-term radiation hazards posed by the francium decay products inside the vacuum system. At present, the radiation levels during francium delivery and trapping are sufficiently low ($< 10\text{ }\mu\text{Sv/hr}$) to permit in situ operation of the FTF by experimenters, though the computer control of the apparatus can be used for future external control of the FTF if higher francium and radiation rates become necessary. The FTF room is designed for connection to ISAC's nuclear exhaust system in case of an accidental vacuum breach during a beamtime or a planned opening of the vacuum system. The turbomolecular pumps on the beamline are connected to this nuclear exhaust as well. Several francium isotopes decay to long-lived isotopes. For example, 8.7% of ^{209}Fr , used during the commissioning run, decays into ^{209}Po , which is an α emitter with a half-life of 102 years. Handling components that are contaminated with these isotopes requires special care as the α radiation is hard to detect and is very damaging to biological tissue when inhaled or ingested (compared to β or γ radiation). The vacuum system components, in particular the neutralizer chamber (see section 5.1.1), have been designed for rapid swap-out in order to minimize exposure to these isotopes.

During the run, spikes in the radiation levels were detected by γ monitors close to the roughing lines of the turbomolecular pumps. The spikes ($> 10 \mu\text{Sv/hr}$) coincided with the heating of the yttrium foil and indicate that significant amounts of activity are pumped out of the vacuum system into the nuclear exhaust. After opening the system, we detected, by γ counting, a relatively large amount of ^{209}Po in the yttrium foil (corresponding to $> 50\%$ of delivered francium) and a small amount in the glass cell (where only upper limits could be set). The reason for the activity in the yttrium foil is that not all francium atoms are released from it during heating, see section 7.2.

4 Francium production and delivery

In this section we briefly describe the production of the francium ions, and their transport to the FTF.

4.1 Production of francium at TRIUMF

A proton beam from the TRIUMF cyclotron with an energy of 500 MeV impinges on a target and produces a number of neutron-rich and neutron-deficient Fr isotopes. The proton current can be as high as $10 \mu\text{A}$ for UC_x targets. These isotopes originate from the interaction of the protons with a hot UC_x target made of many thin wafers of the material; see ref. [29] for information about ISAC. The produced Fr isotopes are surface-ionized in a hot transfer tube, pass through a mass separator that selects a single nuclear mass and are guided through ISAC's low-energy beamline. The production yields of about 1×10^8 Fr/s demonstrated in December 2010 for several francium isotopes have been increased during the two beamtimes in 2012. Although isobaric contaminants may be delivered to the experiment, these unwanted atoms are not trapped, since the MOT employs narrow isomer-specific optical transitions. Figure 2 shows the yield of Fr isotopes available during the commissioning of the UC_x target in December 2010.

4.2 Beamline of the FTF

All the focusing and steering elements of the beamline that deliver Fr^{1+} onto the yttrium neutralizer foil (see section 5.1.1) are electrostatic for mass-independent ion transport. We have the possibility to use the same beamline to feed in stable isotopes such as Rb^+ from a commercial ion source (Kimball Physics ILG-6) to align and test the full system. Four steerer plates and two einzel lenses control the ion beam from ISAC to the neutralizer chamber with the yttrium foil. Furthermore, the 4-sector x-y steerer plates can be independently controlled to add a quadrupole singlet to optimize the final tune after the astigmatic ISAC beam transport design [30]. For a 20 keV beam, the voltages on the einzel lenses are of the order of +12 kV, while the voltages on the steering plates are between ± 300 and ± 400 V.

We ran a test in January 2012 with a stable $^{16}\text{O}^{1+}$ ion beam from ISAC at 20 keV which is similar to the energy used for Fr^{1+} . We delivered 90% of the beam in a location about 20 cm before the neutralizer foil — before the capture assembly was installed — through a 6 mm aperture. The locations of the electrostatic elements and beam diagnostics are indicated in figure 3. Stable $^{238}\text{U}^{1+}$ beam coming out of the target is routinely used at ISAC for tuning the beamline optics prior to Fr delivery.

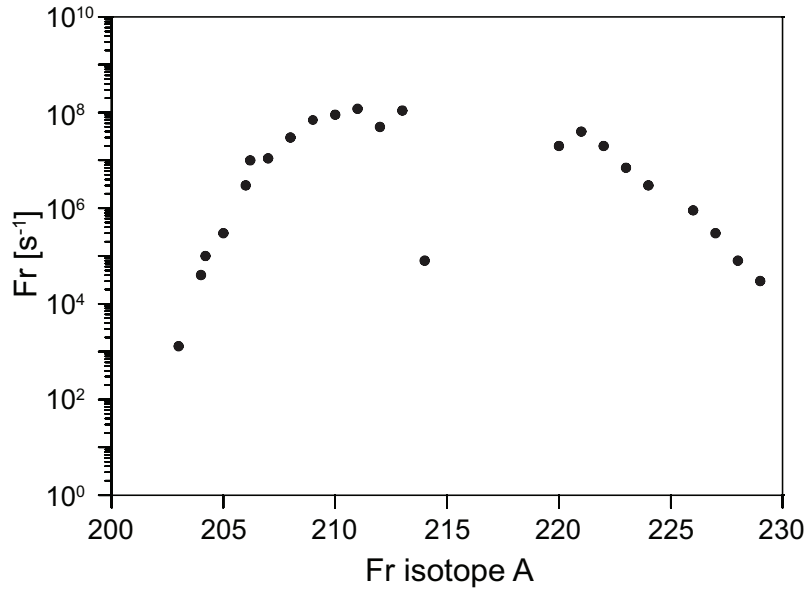


Figure 2. Production yield of Fr isotopes at the ISAC facility at TRIUMF with $2\mu\text{A}$ of protons on a UC_x target in December 2010. Yields have increased an order of magnitude since then.

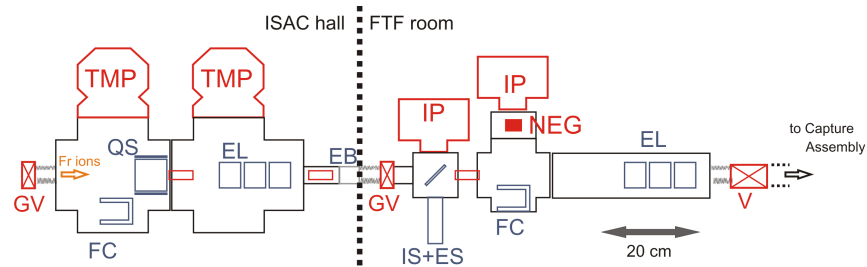


Figure 3. An overview of the beamline delivering the francium ions from the ISAC-I low-energy beamlines to the capture assembly. Part of the beamline is located outside of the room, and part is inside. There is an electric break in the beamline so that the room is not grounded to the outside beamline. The vacuum system is color-coded in red, the beam delivery in blue. The abbreviations used in the figure are the following; EB: electric break, (G)V: (gate) valve, TMP: turbomolecular pump, QS: quadrupole elements + electrostatic steerer, EL: einzel lens, FC: retractable Faraday cup, IP: ion pump, IS+ES: ion source + retractable electrostatic mirror, NEG: non-evaporative getter cartridge. The capture assembly together with the final differential pumping diaphragm (inner diameter of 9.5 mm) are located to the right of the final valve. Bellows (staggered lines in the figure) link different pieces of the beamline.

The vacuum inside ISAC low-energy beamlines is of the order of 10^{-7} mbar, while we require a vacuum in the capture assembly that is three orders of magnitudes lower. The first section of the FTF beamline is pumped by two 550 l/s turbomolecular pumps (Varian Turbo-V 551 Navigator), which are located outside of the Faraday cage. Combined with differential pumping diaphragms (with a diameter of 25.4 mm and a length of 50.8 mm), they bring down the pressure by two orders of magnitude. The second section, inside the Faraday cage, is pumped by two 30 l/s ion pumps

(Duniway DGD-050-5143-M) and a non-evaporable getter (NEG) cartridge (SAES WP 38/950-ST 707, with a 430 l/s pumping speed for H_2) and is separated from the capture assembly by a tube with a diameter of 9.5 mm and a length of 19 mm. The locations of the different components of the vacuum system is shown in figure 3.

5 Francium Trapping Facility

The FTF consists of the Faraday cage (see section 3.1) that contains all the experimental equipment required to carry out the APNC measurements in the future. Some of the most important components of the facility will be described in this section; the capture assembly for trapping the francium ions into a MOT, the associated lasers, and the control and acquisition software.

5.1 The capture assembly

The capture assembly is connected to the beamline and sits about 1.6 m above the floor. It consists of three main parts: the neutralizer, the glass cell for the MOT, and the diagnostics with a Faraday cup and α detector (figure 4). A stainless steel chamber (Kimball Physics) houses the collimator and the dual-position neutralizer. The collimating aperture of 9.5 mm diameter (not shown in figure 4) is held on a groove grabber (Kimball Physics) at the entrance of the chamber and is used for tuning the ISAC ion beam.

The high-efficiency neutralization and capture scheme developed at Stony Brook [31] has been used as a starting point for the design of the Y neutralizer. There are two important improvements on the previous design. All related parts are mounted on one 4.5-inch conflat (CF) flange and attached on one side, as to mitigate possible safety concerns related to the decay products of francium if we have to replace the neutralizer. The current to the yttrium foil is now delivered by fixed contacts instead of the continuous wire used before that was the dominant failure mode (when breaking) in the previous design. The design allows for the atoms to be transferred from the capture MOT to the science chamber below.

5.1.1 Neutralizer chamber

The ion beam is focused on the Y foil (with a thickness of $25\ \mu\text{m}$) in the catching position (see figure 4 and figure 5a). After accumulating the radioactive ions (for about 20 s) the neutralizer holder rotates to its delivery position and a current runs through the thin foil raising its temperature to not more than 700°C by running a current of about 8.9 A. The chamber has a window mounted on one of the mini-CF ports at the top of the chamber that allows observation of the neutralizer holder to measure the temperature using a pyrometer and ensure its proper rotation. Two other mini-CF ports at the bottom have electrical feedthroughs installed for the collimator read-out and for the Rb dispensers (SAES) that provide neutral Rb atoms to align and test the MOT. The neutralizer up position seals the bottom of the MOT glass cell. The figure does not show a rotatable Ta foil, also on a pneumatic feedthrough, that we have used to accumulate ^{225}Ac that decays into ^{221}Fr [32]. The Ta foil and its mount can be removed simply by taking the flange out. A combination of two pumps maintain the vacuum in the chamber: a 20 l/s ion pump (Duniway) and an ion-getter pump (NexTorr by SAES), that has 100 l/s pumping speed for hydrogen.

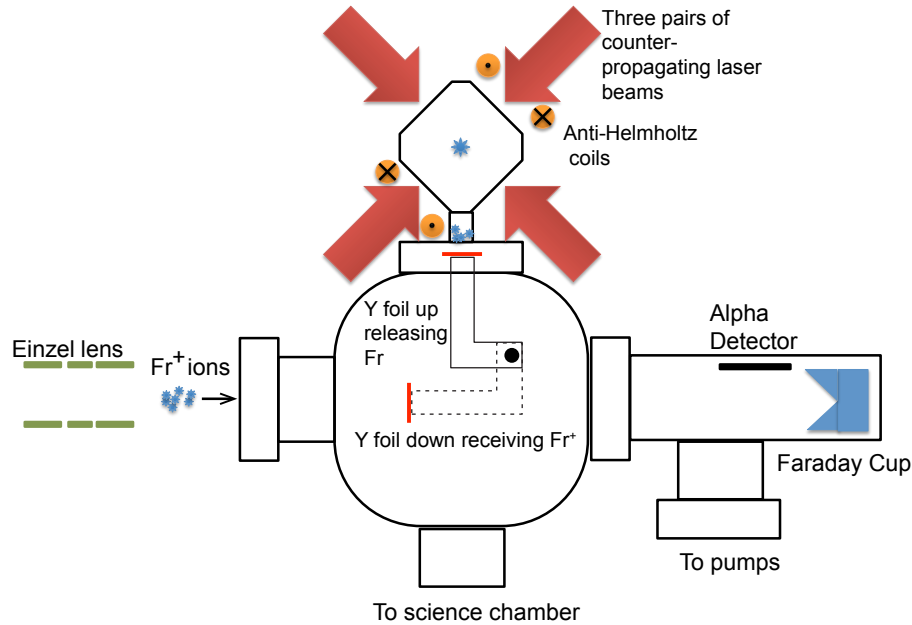


Figure 4. Schematic of the capture assembly. The Fr^{+1} ions impinge on the yttrium neutralizer. After accumulation, the foil is rotated and heated to release the francium atoms into the glass cell where they are trapped in the MOT. When the foil is in the upper position, the francium ions impinge on the beam diagnostics system at the end of the beamline.

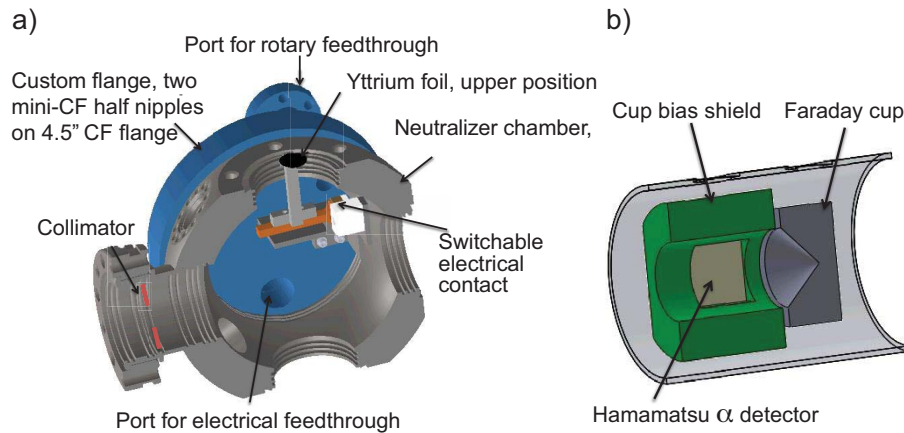


Figure 5. Fr^{+} ion beam accumulation and detection in the capture assembly. a) Cut-away view of the neutralizer chamber. b) Cut-away view of the Faraday cup and α detector assembly.

We are in the process of adding hardware interlocks that will monitor the position of the neutralizer holder and the Ta foil and the intensity and duration of the current pulse applied to the Y foil so as to prevent damage to the foil. The interlocks will not require software control and they will default to a safe state in case of a power or hardware failure.

5.1.2 The MOT for capturing Fr

The atom trap itself is situated in a glass cell with a silane-based dry-film coating to avoid sticking of the Fr atoms to the walls, while providing many atom-wall interactions that re-thermalize the Maxwell-Boltzmann distribution of the atoms at each ‘bounce’. These numerous ‘bounces’ provide multiple opportunities to capture the atoms in the MOT [33]. We follow a procedure based on ref. [34] using the silane-based compound SC-77, with modifications established by trial-and-error over the years.

The pulsed-mode operation of the trap has many benefits; by keeping the trapping cell open most of the time, we ensure a good vacuum resulting in a long trap lifetime. Closing the trap with the neutralizer delivers the neutral atoms into the trapping region and prevents them from escaping before they are trapped. Having the yttrium cold most of the time reduces damage to the dry-film coating. Finally, the francium is accumulated on the yttrium foil rather than in the MOT, thus reducing losses. After collecting a laser-cooled sample, the atoms will then be transferred vertically down to a second chamber for the planned precision experiments. Preliminary tests using stable Rb with an off-line trap show excellent transfer efficiency (50%), see refs. [35–37]; the atom cloud is pushed downwards by a short (2 ms), on-resonance laser pulse of 0.5 mW, while the trap light for the MOT is turned off and the repumping light remains on. A ‘counter push’ is not required to successfully trap the atoms in the second chamber.

A pair of water-cooled coils provide an axial magnetic field gradient of 7 G/cm for regular MOT operation, but are capable of up to 20 G/cm. We use additional Helmholtz coils to compensate for environmental magnetic fields. The ion pump produces a significant field (about 3 G and a gradient of 0.3 G/cm) at the trap despite our use of mu-metal shielding around the magnet of the ion pump.

Figure 6 shows the schematic of the capture trap with the MOT glass cell mounted on top of the neutralizer chamber, surrounded by the optics that deliver the laser beams on each side of the glass cell cube. Three identical sets of optics expand optical-fiber-delivered trapping light into 5 cm diameter beams; large beams are required to maximize the trapping efficiency [31]. The beams are collimated and circularly polarized. A further three sets of optics retro-reflect the laser light as required for a MOT. All the optics are mounted using commercial opto-mechanics (Thorlabs cage system). The opto-mechanical systems are supported by a stainless steel structure (exoskeleton) that ensures alignment of all the optics while protecting the glass cell. The polarization elements at the trap are optimized for 718 nm, resulting in a minor mismatch when operating with Rb. The data acquisition (i.e. cameras and photomultiplier tube (PMT)) and laser systems are described in section 5.3.2 and section 5.2 respectively.

5.1.3 Faraday cup and α detector

Crucial for diagnostics before and during an on-line run is the Faraday cup at the end of the beam-line shown in figure 4 and figure 5b. The Faraday cup allows tuning the ion optics with stable beam. The tuning is done remotely in the ISAC control room; electrostatic elements and beamline diagnostics can be controlled and read back through the TRIUMF EPICS control system [38]. A suppression electrode before the cup can be biased to prevent unwanted escape of backscattered electrons. The francium yields are sufficiently high that the radioactive ion beam intensity can also

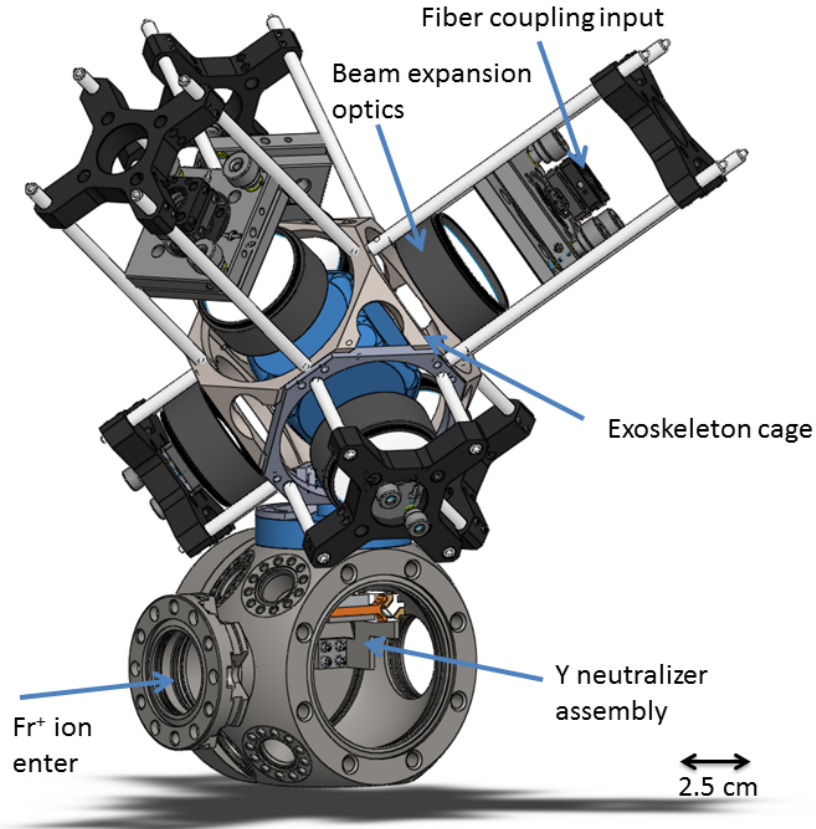


Figure 6. Drawing of neutralizer chamber with the glass cell (highlighted in blue) for the MOT and the required optics. Not shown are the magnetic field coils. The size of the larger CF flanges is 4.5 in.

be measured by the Faraday cup. Care must be taken when doing that, since the radioactive decay will distort the readings of the Faraday cup. Charged particle emission (α and β radiation) will induce a current after a sufficiently strong radioactive source has been accumulated. β^- particles will result in an extra positive current, while α particles will give an additional negative current. Next to it, but not looking into the ion beam, is a silicon photodiode (Hamamatsu S3590-09) for α detection. The detector reading increases every time the Y foil is in the upper position, and we use it as an extra monitor for the francium beam (see figure 7). The solid angle of particles emitted from the center of the Faraday cup onto the α detector is ~ 0.176 sr (1.4%). The information of the α decay allows identification of elements and isotopes.

5.2 Laser systems

The cooling, trapping, and spectroscopy lasers reside on two separate optical tables in the laboratory and are all locked to a scanning Fabry-Perot cavity [28]. There are two titanium-sapphire lasers (Coherent 899-21, 899-01) pumped by one 18 W pump laser (Coherent Verdi V18). Another titanium-sapphire laser (M Squared SolisTiS), pumped by a 10 W laser (Coherent Verdi G10), was not yet fully commissioned at the time of the run. It will, however, serve as an efficient and reli-

able trap laser for future runs in the FTF, delivering about 1.7 W at 718 nm and 2.6 W at 780 nm. Furthermore there are two diode lasers (Toptica DL100 and Sacher) at 780 nm and 817 nm respectively. The relevant frequencies for Rb are 780 nm (D2 line) and 795 nm (D1 line), for francium they are 718 nm (D2 line) and 817 nm (D1 line).

5.2.1 Frequency determination and stabilization

Francium does not have any stable isotopes, and a straightforward frequency reference to lock the lasers is not available. At this point we use a two-step approach. Firstly, a wavemeter (Bristol 621A) provides an approximate frequency determination. It has an accuracy of 60 MHz, while for trapping an absolute accuracy of 5 to 10 MHz is required. Secondly, to lock the lasers during a run we use a scanning Fabry-Perot cavity, once the correct frequencies for trapping have been found [28]. The cavity locking scheme is described in more detail in section 5.3.3 as part of the software controls.

5.3 Experimental control and acquisition

At the time of the commissioning run, three main programs were available to run the experiment: a sequencer to control the experimental cycle (section 5.3.1), a program to acquire data from the various imaging systems (section 5.3.2) and a program to frequency-stabilize the lasers to the transfer cavity (section 5.3.3). The programs for experimental control and acquisition are written in LabVIEW or LabWindows. All control is done from PC computers inside the Faraday cage. They are connected to the outside through optically-isolated connections to prevent RF and ground contamination.

5.3.1 Sequencer

The timing unit of the sequencer is an FPGA (PulseBlaster PB24-100-32k from SpinCore) that is used to send out digital triggers to devices directly or to trigger analog signals (NI-PCI 6713 cards). It was created originally by other research groups for atomic physics studies [39]. This system is capable of complicated sequences of pulses and voltages that will be required in the future. However, during the commissioning run, the timing sequence of the experiment was simple enough to be generated by two digital delay generators (DG535 from Stanford Research Systems).

5.3.2 Data acquisition and camera operation

Given the importance of images in laser trapping, we have several cameras available to acquire images of the atom cloud. Two charge-coupled device (CCD) cameras (Roper Scientific RTE/CCD-1300-Y/HS and Imi-tech IMB-42FT) were used during the commissioning run to image the trap and to measure the number of atoms and the lifetime of the trap. The Imi-tech camera uses a commercial zoom lens (Computar MLH-10x) to give a broad field-of-view to locate the trap more easily. The Roper Scientific camera uses a custom-made double relay 1:1 imaging system with achromatic lenses. The latter camera allows to bin several pixels together to reduce the noise and enhance the detection of small atom clouds.

A third, 1:1, imaging system has been installed since the commissioning run. It was designed with the help of commercial ray-tracing software (OSLO). The system includes a holder to insert

optical filters in the parallel section of the first relay and also a variable aperture between relay sections. A beam splitter at the end of the imaging system sends 30% of the light to a CCD camera (Micropix M-640) to ensure proper alignment of the field aperture while the remaining 70% reaches a photomultiplier tube for sensitive spectroscopic measurements.

We have adapted an available program for images, initially developed at the U. of Toronto [40], to capture and process the optical fluorescence images from trapped atoms. This program can operate the Imi-tech and Micropix cameras; it can handle any FireWire-compatible camera. The Roper Scientific camera uses a program developed in our group based on LabVIEW drivers provided by the manufacturer.

5.3.3 Transfer cavity lock

The absence of readily-available atomic references at the exact frequencies necessary for the francium trapping requires the use of a transfer lock technique. We have implemented, based on previous work in ref. [28] a way to transfer the frequency stability of a HeNe laser (Melles-Griot 05-STP-901) to other lasers using a scanning, confocal Fabry-Perot interferometer. The free spectral range of the cavity is 300 MHz with a finesse of 100 at 718 nm. Analog input and output is controlled by two National Instruments cards (PCI-6221 and PCI-6713).

The program sends a voltage ramp to a voltage amplifier (Exfo RG-91), which is then sent to one (or both) piezo crystal(s) of the cavity assembly. Light from the HeNe and the lasers requiring stabilization will be transmitted through the cavity at specific voltages of the ramp. After the cavity the light from each laser is separated either by frequency using dichroic filters or by polarizing beam splitters, and is detected by photodiodes. The photodiode signals are acquired in synchronization with the voltage ramp and the relative frequency of the lasers with respect to the HeNe peaks is kept constant using a software-based PID feedback algorithm. At the time of the commissioning run everything was set up to stabilize four lasers. The feedback bandwidth is of the order of 20 Hz, dominated by the voltage ramp (~ 25 ms) duration, with only a small computational overhead. The stability of the lock is of the order of ± 5 Mhz over a few days. This is mainly limited by (i) the frequency stability of the HeNe, (ii) non-linearities in the expansion of the piezo crystals with respect to the applied voltage, and (iii) changes of atmospheric conditions, thus influencing the optical length of the cavity by changes of the refractive index of air between the mirrors. The last factor has been corrected recently by operating the transfer cavity under vacuum.

6 Tests with stable Rb

Testing the trapping apparatus with stable Rb has been crucial for understanding its performance. These tests allow us to verify the proper working of the MOT, and to align all the cameras and detectors. The exoskeleton provides good alignment of the MOT beams, but cameras (or probe beams for future measurements) are installed independently of it. An important test is to ensure that the zero of the magnetic field and the location of the trap coincide as much as possible. We have found that the Fr trap can appear slightly off from the Rb trap, but not more than 2 mm.

In the future, as the sequences for the experiment become more complicated, tests with stable Rb will become more and more important. They are useful to verify measurement schemes and to quantify systematic effects without using radioactive beamtime.

Table 1. Operating parameters for the September 2012 commissioning run.

Parameter	Value	Range	Optimized
Magnetic gradient	10 G/cm	± 5 G/cm	yes
Trapping intensity	5 mW/cm ²	± 5 mW/cm ²	no
Repumping intensity	5 mW/cm ²	± 5 mW/cm ²	no
Frequency stability	1 MHz	± 5 MHz/day	partially
Yttrium foil temperature	T < 700 °C	± 50 °C	no
Vacuum	< 10 ⁻⁹ mbar		

6.1 Off-line Rb⁺ source

We installed a Kimball ILG-6 Rb¹⁺ source for delivering an off-line ion beam to test the ion optics and the neutralizer. A removable electrostatic mirror deflects the Rb⁺ beam towards the neutralizer. However, when sending an ion beam across, we found that its contribution to the atoms trapped is indistinguishable from that coming from the neutral gas background introduced by the ion source. The distance between the ion source and the neutralizer is less than 100 cm, while at Stony Brook the distance to the Rb source that produced the ions was closer to 10 meters and included a few stages of differential pumping. There is no plan to remedy this issue, because the beam optics have been tested sufficiently in the meantime and the neutralizer scheme is working reliably.

7 Commissioning run with Fr

We had five twelve-hour shifts between September 2nd and 5th, 2012 for commissioning. The isotope of choice for the test was ²⁰⁹Fr, as the wavelengths of the lasers necessary for trapping that isotope are well known from previous work at Stony Brook [10, 41], it is produced at relatively high rates ($\sim 10^9$ Fr/s), and it minimizes long-lived α -emitting progeny. ISAC delivered 10^6 – $5 \cdot 10^8$ Fr¹⁺ to the neutralizer, depending on attenuators inserted in the early stages of the beam transport. We monitor the activity by looking at the α -decay of the atoms on the Si detector next to the Faraday cup.

Table 1 summarizes the parameters of the trap. Three of them have not been optimized yet: the laser power and stability, and the Y foil temperature. The latter was heated conservatively during commissioning.

We also suspect that the coating of the cell was not optimal, but it worked adequately during the run. We will get a new cell that will be coated and tested following our previous approach [31].

A steady-state beam from ISAC delivers activity into the Y neutralizer in the down position for a fixed time between 10 and 20 s (see figure 4). Pneumatic actuators operated with solenoid valves rotate the position of the neutralizer to the upper position for about 1.5 s. Once the neutralizer is up, a ~ 8.9 A current flows through it and heats it for about 1 s to a temperature of less than 700°C. The neutral francium is released and enters the glass cell for trapping. The new connection scheme for the neutralizer heating current (see figure 5a) worked well and reliably during 7000 repetitions; before the run it was already tested without the final yttrium foil for about 25000 cycles.

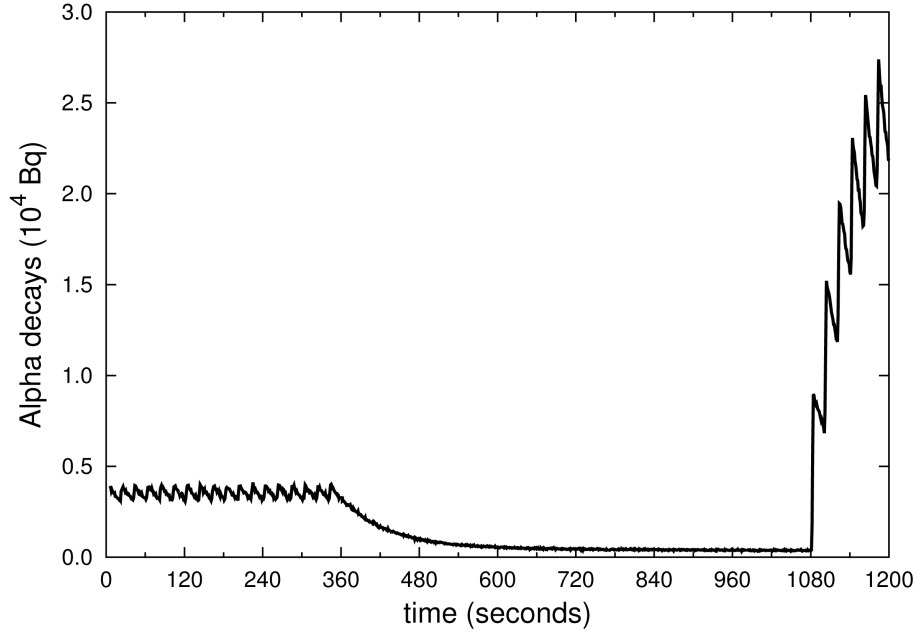


Figure 7. Sample output of the α detector during the commissioning run. At the beginning of the time sequence ^{207}Fr is being trapped. The ‘staggering’ is caused by the yttrium foil blocking the beam most of the time. In the middle there is no radioactive beam. At the end of the time sequence (at 1080 seconds), ^{209}Fr is delivered to the FTF.

The francium beam reaches the Faraday cup when the neutralizer is up. This allows us to monitor the α decays that give a direct measurement of the number of ions delivered. Figure 7 shows such a signal which increases every 20 s. It also shows the change of isotope, from ^{207}Fr to ^{209}Fr , which was realized in about ten minutes. This same detector serves to measure the lifetime of the activity as it decays, which is dominated by the decay products of the corresponding Fr isotope.

Figure 8a) shows a false color image from the Roper Scientific camera that looks at the fluorescence at 718 nm. The size of the trap is about $500\text{ }\mu\text{m}$ in its largest dimension. We do not apply a procedure to accumulate atoms in the capture MOT, as that would require sheltering the cold atoms from the hot burst of new Fr that arrive. Tests off-line with Rb have shown that we can accumulate in a second chamber as long as the vacuum of the second chamber is sufficiently good [37]. Accumulation can be done by having the MOT in the second chamber on — with atoms from the previous cycle still trapped —, while a new batch of atoms is transferred from the capture MOT.

The software that processes the images requires as input the intensity of the trapping beams as well as the laser detuning to determine the number of trapped atoms. This serves to calculate the number of atoms by knowing how many photons are scattered per unit time. Independent tests with Rb using absorption imaging show good quantitative agreement with this way of measuring the number of atoms. While trapping Fr it is difficult to know the exact laser detuning to better than one half linewidth (4 MHz). This is in contrast with Rb (or any element with stable or long-lived isotopes) where the exact detuning is well-known since the laser frequency can be determined by comparison to a stable reference source.

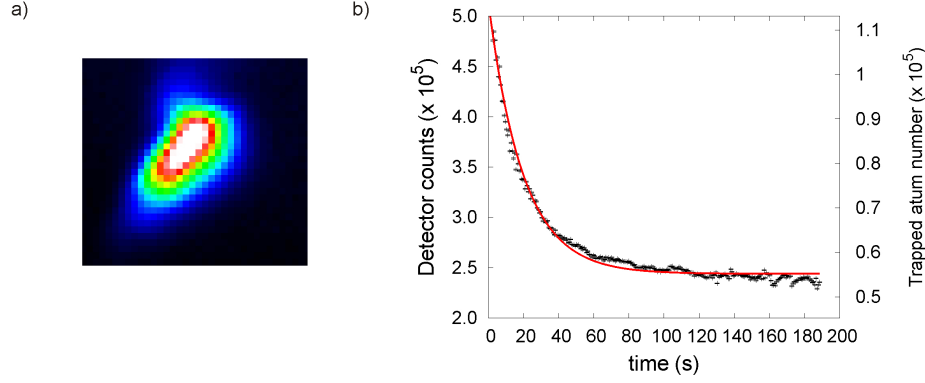


Figure 8. Fr MOT performance. a) False color CCD image of the MOT fluorescence of a cloud of about 10^5 ^{209}Fr trapped at the FTF. The pixel size of the camera is $6.7 \times 6.7 \mu\text{m}^2$; an area of $0.86 \times 0.86 \text{ mm}^2$ is shown. b) Black data points: integrated fluorescence from the trap as a function of time. Red line: an exponential fit results in a lifetime of about 20 s, even though there are deviations from this model in the data. The right y-axis is only approximate for these data as the calculated atom number has an uncertainty of $\sim 40\%$.

Table 2. Frequencies for trapping and repumping of the three working isotopes. The accuracy of $\pm 0.002 \text{ cm}^{-1}$ comes from the wavemeter and the fact that these are not the resonance frequencies.

Isotope	Trap (cm^{-1})	Repumper - D2 (cm^{-1})	Repumper - D1 (cm^{-1})
207	13923.548	13924.945	
209	13923.470	13924.888	12238.380
221	13922.952	13923.560	12237.054

7.1 Different isotopes

We report the successful trapping of ^{207}Fr for the first time, based on the frequencies of the D1 and D2 lines measured at ISOLDE in the 1980's [42–44]. ^{221}Fr was used by the Boulder group [45], and we trapped it on-line to prepare for tests of an off-line Fr source [32].

The frequencies for ^{209}Fr (see table 2) agree with our previous work and with the work of the Legnaro group [46]. The frequencies for ^{221}Fr agree with the trapping done by the Boulder group [45]. The stability of the cavity while switching between isotopes enables us to measure isotope shifts with good accuracy using electro-optical modulator (EOM) sideband optical spectroscopy [47].

7.2 Trapping results and efficiency

We have successfully trapped up to 2.5×10^5 ^{209}Fr atoms at the FTF. This gives an efficiency of about 0.05%, which we calculate by taking the peak number of atoms in the trap and dividing it by the incoming francium beam integrated over the accumulation time. Figure 8b) shows the decay of a ^{209}Fr trap that is not refilled; the lifetime of 20 s is the result of having good vacuum of the order of 10^{-10} mbar. We found, however, that, despite several stages of differential pumping in our beamline, the ISAC low-energy beamlines were still influencing our trap lifetime depending on changes in environmental temperature (and thus water vapor pressure).

The reason for the difference of more than a factor of 20 from the best efficiency achieved at Stony Brook [31] comes from three main factors: limited laser power, imperfect neutralizer heating, and the suspected low performance of the dryfilm coating.

The laser power available for trapping can be trivially increased. Our new laser system (M Squared SolisTis) in combination with a high-power fiber will provide five times more intensity; i.e. from ~ 200 mW going into the fiber to about 1 W. The efficiency from this upgrade is expected to increase by a factor of 15; the laser light can be red-detuned further from resonance while maintaining the same photon scattering rate, and as a result the capture velocity, v_c , is increased [48]. From measurements of the release of francium after the ion beam was turned off, we can deduce that about 10% of francium atoms available in the yttrium foil were released on each heating cycle. This could be improved by a factor of 5 by heating the neutralizer more homogeneously to higher temperature to reach 50% [31]. Taking these two improvements into account, an efficiency of 3–4% becomes possible.

8 Outlook and conclusions

The FTF is operating well. We have trapped up to 2.5×10^5 ^{209}Fr atoms, which corresponds to an efficiency of 0.05%. The vacuum allows to have long trap lifetimes of about 20 s.

We are in the process of designing and constructing the science chamber and have identified the issues that need improving on the capture assembly. They include a new Y foil for neutralization with better electrical contact for more uniform heating, a new laser (M Squared SolisTis) in combination with a high-power fiber that delivers more trapping light.

We expect a transfer efficiency to the science chamber in Fr similar or better to the one reached with Rb (50%) since Fr is heavier and has less transverse expansion. The goal of 10^6 atoms in the science chamber for the weak interaction measurements [27, 35] is within reach for our system.

Acknowledgments

We would like to thank the ISAC staff at TRIUMF for developing the Fr beam. NRC, TRIUMF, and NSERC from Canada, DOE and NSF from the U.S.A., and CONACYT from Mexico support our work.

References

- [1] Y.B. Zel’dovich, *Parity nonconservation in the 1st order in the weak-interaction constant in electron scattering and other effects*, *Sov. Phys. JETP* **9** (1959) 682.
- [2] M. Bouchiat and C. Bouchiat, *Parity violation in atoms*, *Rept. Prog. Phys.* **60** (1997) 1351.
- [3] G.D. Sprouse and L.A. Orozco, *Laser trapping of radioactive atoms*, *Ann. Rev. Nucl. Part. Sci.* **47** (1997) 429.
- [4] T. Dinneen, A. Ghiorso and H. Gould, *An orthotropic source of thermal atoms*, *Rev. Sci. Instrum.* **67** (1996) 752.
- [5] V.V. Flambaum, I.B. Khriplovich and O.P. Sushkov, *Nuclear anapole moments*, *Phys. Lett. B* **146** (1984) 367.

- [6] V. Flambaum and D. Murray, *The Anapole moment and nucleon weak interactions*, *Phys. Rev. C* **56** (1997) 1641 [[nucl-th/9703050](#)].
- [7] W. Haxton and C.E. Wieman, *Atomic parity nonconservation and nuclear anapole moments*, *Ann. Rev. Nucl. Part. Sci.* **51** (2001) 261 [[nucl-th/0104026](#)].
- [8] W. Johnson, M. Safronova and U. Safronova, *Combined effect of coherent Z exchange and the hyperfine interaction in atomic PNC*, *Phys. Rev. A* **67** (2003) 062106 [[hep-ph/0302029](#)].
- [9] J. Ginges and V. Flambaum, *Violations of fundamental symmetries in atoms and tests of unification theories of elementary particles*, *Phys. Rept.* **397** (2004) 63 [[physics/0309054](#)].
- [10] E. Gomez, L.A. Orozco and G.D. Sprouse, *Spectroscopy with trapped francium: advances and perspectives for weak interaction studies*, *Rep. Prog. Phys.* **66** (2006) 79.
- [11] G. Gwinner et al., *Fundamental symmetries studies with cold trapped francium atoms at ISAC*, *Hyp. Int.* **172** (2006) 45.
- [12] W.J. Marciano and J.L. Rosner, *Atomic parity violation as a probe of new physics*, *Phys. Rev. Lett.* **65** (1990) 2963 [Erratum *ibid.* **68** (1992) 898].
- [13] J. Behr and G. Gwinner, *Standard Model tests with trapped radioactive atoms*, *J. Phys. G* **36** (2009) 033101 [[arXiv:0810.3942](#)].
- [14] H. Davoudiasl, H.-S. Lee and W.J. Marciano, *Muon Anomaly and Dark Parity Violation*, *Phys. Rev. Lett.* **109** (2012) 031802 [[arXiv:1205.2709](#)].
- [15] M.J. Ramsey-Musolf and S.A. Page, *Hadronic parity violation: a new view through the looking glass*, *Annu. Rev. Nucl. Part. Sci.* **56** (2006) 1.
- [16] C.S. Wood, S.C. Bennett, D. Cho, B.P. Masterson, J.L. Roberts, C.E. Tanner and C.E. Wieman, *Measurement of parity nonconservation and an anapole moment in cesium*, *Science* **275** (1997) 1759.
- [17] C.S. Wood, S.C. Bennett, J.L. Roberts, D. Cho and C.E. Wieman, *Precision measurement of parity nonconservation in cesium*, *Can. J. Phys.* **77** (1999) 7.
- [18] V. Dzuba, V. Flambaum and O. Sushkov, *Calculation of energy levels, E1 transition amplitudes and parity violation in francium*, *Phys. Rev. A* **51** (1995) 3454.
- [19] M.S. Safronova and W.R. Johnson, *High-precision calculation of the parity-nonconserving amplitude in francium*, *Phys. Rev. A* **62** 022112 (2000).
- [20] M.A. Bouchiat and C. Bouchiat, *Parity violation induced by weak neutral currents in atomic physics I*, *J. Phys. (Paris)* **35** (1974) 899.
- [21] M. Bouchiat and C. Bouchiat, *Weak Neutral Currents in Atomic Physics*, *Phys. Lett. B* **48** (1974) 111.
- [22] M.A. Bouchiat and C. Bouchiat, *Parity violation induced by weak neutral currents in atomic physics 2*, *J. Phys. (Paris)* **36** (1975) 493.
- [23] M.A. Bouchiat and C. Bouchiat, *An atomic linear Stark shift violating P but not T arising from the electroweak nuclear anapole moment*, *Eur. Phys. J. D* **15** (2001) 5.
- [24] S. Porsev, K. Beloy and A. Derevianko, *Precision determination of electroweak coupling from atomic parity violation and implications for particle physics*, *Phys. Rev. Lett.* **102** (2009) 181601 [[arXiv:0902.0335](#)].
- [25] S. Porsev, K. Beloy and A. Derevianko, *Precision determination of weak charge of ^{133}Cs from atomic parity violation*, *Phys. Rev. D* **82** (2010) 036008 [[arXiv:1006.4193](#)].

- [26] V. Dzuba, J. Berengut, V. Flambaum and B. Roberts, *Revisiting parity non-conservation in cesium*, *Phys. Rev. Lett.* **109** (2012) 203003 [[arXiv:1207.5864](#)].
- [27] E. Gomez, S. Aubin, G.D. Sprouse, L.A. Orozco and D.P. DeMille, *Measurement method for the nuclear anapole moment of laser-trapped alkali-metal atoms*, *Phys. Rev. A* **75** (2007) 033418.
- [28] W.Z. Zhao, J.E. Simsarian, L.A. Orozco and G.D. Sprouse, *A computer-based digital feedback control of frequency drift of multiple lasers*, *Rev. Sci. Instrum.* **69** (1998) 3737.
- [29] M. Dombsky et al., *Commissioning and initial operation of a radioactive beam ion source at ISAC*, *Rev. Sci. Instrum.* **71** (2000) 978.
- [30] R. Baartman, *Low energy beam transport design optimization for RIBs*, *Nucl. Instrum. Meth. B* **204** (2003) 392.
- [31] S. Aubin, E. Gomez, L.A. Orozco and G.D. Sprouse, *High efficiency magneto-optical trap for unstable isotopes*, *Rev. Sci. Instrum.* **74** (2003) 4342.
- [32] FRPNC collaboration, *Off-line source for Fr*, in preparation (2014).
- [33] C. Monroe, W. Swann, H. Robinson and C. Wieman, *Very cold trapped atoms in a vapor cell*, *Phys. Rev. Lett.* **65** (1990) 1571.
- [34] J.A. Fedchak, P. Cabaay, W.J. Cummings, C.E. Jones and R. S. Kowalczyk, *Silane coatings for laser-driven polarized hydrogen sources and targets*, *Nucl. Instrum. Meth. A* **391** (1997) 405.
- [35] D. Sheng, L.A. Orozco and E. Gomez, *Preliminary studies for anapole moment measurements in rubidium and francium*, *J. Phys. B* **43** (2010) 074004 [[arXiv:1001.0817](#)].
- [36] D. Sheng, J. Zhang and L. A. Orozco, *Sensitivity test of a blue-detuned dipole trap designed for parity non-conservation measurements in Fr*, *Rev. Sci. Instrum.* **83** (2012) 043106 [[arXiv:1204.5223](#)].
- [37] A. Pérez Galván, *Studies of atomic properties of francium and rubidium*, Ph.D. Thesis, University of Maryland, College Park, MD (2009) [<http://drum.lib.umd.edu/handle/1903/9273>].
- [38] R. Keitel et al., *Design and commissioning of the ISAC control system at TRIUMF*, in proceedings of *International Conference on Accelerator and Large and Large Experimental Physics Control (ICALPCS99)*, Trieste, Italy (1999), pg. 674 [cds.cern.ch/record/532717/files/tc1p64.pdf].
- [39] J.V. Porto and I.B. Spielman, private communication (2013).
- [40] S. Aubin et al., *Trapping fermionic 40K and bosonic 87Rb on a chip*, *J. Low Temp. Phys.* **140** (2005) 377.
- [41] J.S. Grossman, L.A. Orozco, M.R. Pearson, J.E. Simsarian, G.D. Sprouse and W.Z. Zhao, *Hyperfine anomaly measurements in francium isotopes and the radial distribution of neutrons*, *Phys. Rev. Lett.* **83**, 935 (1999).
- [42] ISOLDE collaboration, J. Bauche et al., *Accurate wavenumbers of the first resonance doublet of francium atoms and relativistic contribution to isotope shifts in the resonance doublets of francium and cesium atoms*, *J. Phys. B* **19** (1986) L593.
- [43] ISOLDE collaboration, A. Coc et al., *Hyperfine structures and isotope shifts of $^{207-213,220-228}\text{Fr}$; possible evidence of octupolar deformation*, *Phys. Lett. B* **163** (1985) 66.
- [44] ISOLDE collaboration, A. Coc et al., *Isotope Shifts, Spins and Hyperfine Structures of ^{118}Cs , ^{146}Cs and of Some Francium Isotopes*, *Nucl. Phys. A* **468** (1987) 1.
- [45] Z.-T. Lu, K.L. Corwin, K.R. Vogel, C.E. Wieman, T.P. Dinneen, J. Maddi and H. Gould, *Efficient collection of Fr into a vapor cell magneto-optical trap*, *Phys. Rev. Lett.* **79** (1997) 994.

- [46] S. Sanguinetti et al., *Accurate measurements of transition frequencies and isotope shifts of laser-trapped francium*, *Opt. Lett.* **34** (2009) 893.
- [47] FrPNC collaboration, *Isotope shifts in neutron-deficient isotopes between ^{206}Fr and ^{213}Fr* , in preparation (2014).
- [48] K. Lindquist, M. Stephens and C. Wieman, *Experimental and theoretical study of the vapor-cell Zeeman optical trap*, *Phys. Rev. A* **46** (1992) 4082.

RECEIVED: June 23, 2014

REVISED: August 22, 2014

ACCEPTED: September 19, 2014

PUBLISHED: October 21, 2014

Offline trapping of ^{221}Fr in a magneto-optical trap from implantation of an ^{225}Ac ion beam

M. Tandecki,^a J. Zhang,^b S. Aubin,^c J.A. Behr,^{a,1} R. Collister,^d E. Gomez,^e
G. Gwinner,^d H. Heggen,^a J. Lassen,^a L.A. Orozco,^b M.R. Pearson,^a S. Raeder^{a,2}
and A. Teigelhöfer^{a,d}

^aTRIUMF,

Vancouver, BC V6T 2A3, Canada

^bJQI, Department of Physics and NIST, University of Maryland,
College Park, MD 20742, U.S.A.

^cDepartment of Physics, College of William and Mary,
Williamsburg VA 2319, U.S.A.

^dDept. of Physics and Astronomy, University of Manitoba,
Winnipeg, MB R3T 2N2, Canada

^eInstituto de Física, Universidad Autónoma de San Luis Potosí,
San Luis Potosí 78290, Mexico

E-mail: behr@triumf.ca

ABSTRACT: We demonstrate a new technique to prepare an offline source of francium for trapping in a magneto-optical trap. Implanting a radioactive beam of ^{225}Ac , $t_{1/2} = 9.920(3)$ days, in a foil, allows use of the decay products, i.e. ^{221}Fr , $t_{1/2} = 288.0(4)$ s. ^{221}Fr is ejected from the foil by the α decay of ^{225}Ac . This technique is compatible with the online accumulation of a laser-cooled atomic francium sample for a series of planned parity non-conservation measurements at TRIUMF. We obtain a 34 % release efficiency for ^{221}Fr from the recoil source based on particle detector measurements. We find that laser cooling operation with the source is 8^{+10}_{-5} times less efficient than from a mass-separated ion beam of ^{221}Fr in the current geometry. While the flux of this source is two to three orders of magnitude lower than typical francium beams from ISOL facilities, the source provides a longer-term supply of francium for offline studies.

KEYWORDS: Laser cooling; Instrumentation for radioactive beams (fragmentation devices; fragment and isotope, separators incl. ISOL; isobar separators; ion and atom traps; weak-beam diagnostics; radioactive-beam ion sources)

¹Corresponding author.

²Present address: IKS, KULeuven, 3000 Leuven, Belgium.

Contents

1	Introduction	1
2	Method	2
2.1	Experimental setup	4
2.2	Calculations of collection efficiencies	5
2.3	Other isotopes	7
3	Experiment	7
3.1	Particle detector measurement	7
3.2	Magneto-optical trap measurements	9
4	Discussion	10
5	Conclusion	11

1 Introduction

Trapped radioactive isotopes provide unique experimental systems for low-energy tests of the Standard Model [1, 2]. Recent and planned experiments include correlation measurements in nuclear β decay [3–6], investigations of weak neutral currents [7, 8] and electric dipole moment (EDM) measurements [9]. The precision for these experiments requires high statistics, along with a detailed investigation of systematic effects. Radioactive ion beam (RIB) facilities or long-lived radioactive sources can provide the radioactive samples for these experiments.

RIB facilities can deliver a wide range of different isotopes; however, available beamtime is shared by many different experiments. Long-lived radioactive sources complement — or provide an alternative to — radioactive ion beams. They can be created in a short time (< 1 day) during an online beamtime with a low chance of failure, while being able to deliver experimenters with a source that will last for weeks. Such a source can provide radioactive atoms for a longer duration which is crucial for experiments where systematic effects need to be investigated in detail. The drawbacks of using a radioactive source are its restriction to certain isotopes and additional radiological hazards.

Radioactive sources have been or are used in a number of experiments for testing fundamental symmetries, such as the EDM search in ^{225}Ra [9], trapping of ^{221}Fr [10], and correlation measurements in β decay [11], as well for nuclear structure studies using a ^{252}Cf source [12]. In order to work with short-lived isotopes ($t_{1/2} < 1$ day), the source must include a long-lived precursor isotope. For example, the ^{221}Fr source of ref. [10] consists of an oven that releases the ^{221}Fr atoms into a magneto-optical trap (MOT), while retaining the long-lived ^{225}Ac precursor. In the case of the ^{82}Rb source of [11], the source consists of a ^{82}Sr precursor which releases Rb ions, while the Sr

remains bound in a molecule in the source; the ^{82}Rb ions are subsequently mass separated to avoid ^{85}Rb contamination. More recently, the CARIBU facility [12] has implemented a ^{252}Cf precursor source, which uses an RF gas catcher to efficiently extract spontaneous fission decay products for use in experiments.

In this paper, we present the design, construction, and testing of a radioactive ^{221}Fr source based on a ^{225}Ac precursor sample implanted in a tantalum foil. The ^{221}Fr source was developed to support the program of weak interaction studies through parity non-conservation measurements in francium at the ISAC RIB facility at TRIUMF. The offline francium source is integrated into the trapping apparatus and can be used for testing the laser cooling system and investigating systematic effects in experiments, while the much higher yield francium beam produced directly by ISAC is essential to acquire statistics for precision measurements. Alternating between the two modes of operation is possible without opening the system to atmospheric pressure. The techniques mentioned in the previous paragraph do not allow this easily in our geometry, or they require a substantial modification of the infrastructure of ISAC. Two parity non-conservation experiments are planned; one to study the electric-dipole parity-forbidden $7S \rightarrow 8S$ transition and one to study the anapole moment using the microwave ground state hyperfine transition. For the $7S \rightarrow 8S$ experiment, ^{221}Fr can be used to optimize the system for the reduction of systematic effects [14]. For the anapole experiment, ^{221}Fr will be hard to use for the final experiments, since its ground state splitting is significantly different from the neutron-deficient francium isotopes (i.e. 15.5 GHz versus ~ 45 GHz [15]). Two examples of what can be done with this source for the latter project are the optimization of the dipole trap and measurement of differential AC Stark shifts [16], or the study of the N dependence of the signal from the atoms in a cavity (optical or microwave) to avoid effects associated with the weak coupling regime of cavity QED that may mix atomic levels in unwanted ways [17].

The paper is organized as follows: the method is described, along with simulations, in section 2. We have performed several measurements to quantify the efficiency of the technique in section 3, which are discussed in section 4.

2 Method

The ^{221}Fr source consists of a precursor isotope, such as ^{225}Ac , implanted in a tantalum foil at a beam energy of 20 keV. When a ^{225}Ac nucleus undergoes alpha decay to ^{221}Fr , this daughter nucleus has a recoil energy of about 105 keV, which is sufficient to escape from the foil. We use another foil made of yttrium, placed 3 mm away from the tantalum foil, to catch the recoiling ^{221}Fr ions and neutralize them; when the yttrium foil is heated it emits neutral ^{221}Fr atoms. The tantalum and yttrium foils are on independent mechanical stages so that they can be appropriately positioned for each of three operations: implantation, recoil catching, and neutralized emission into the MOT vapor cell.

As an alternative to implanting the source with the ^{225}Ac precursor, we can also use either ^{225}Ra or ^{225}Fr . Both of these alternate precursor isotopes have a β decay path to ^{225}Ac . Figure 1 shows all the relevant decay paths to ^{221}Fr , and its subsequent α decay to ^{217}At . The half-life of ^{221}Fr is $t_{1/2} = 288.0(4)$ s, based on a weighted average of values found in [18–20].

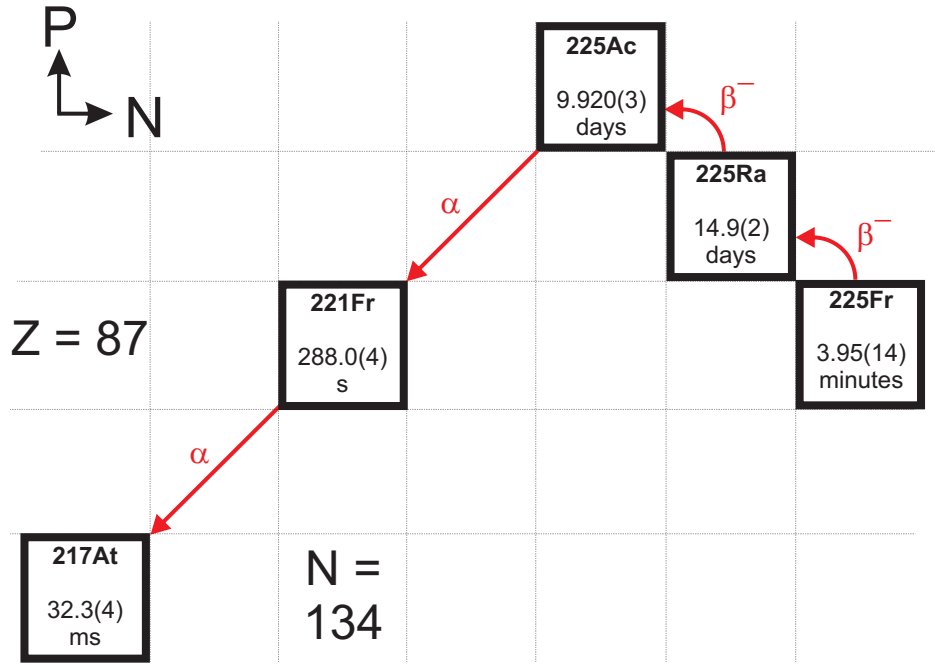


Figure 1. Decay chains for ^{225}Ac , ^{225}Ra and ^{225}Fr ; the proton number (P) is shown on the vertical axis and the neutron number (N) on the horizontal axis. The different boxes show the isotope on top and the corresponding half-life below. Branching ratios below 0.1 % are not listed here. This chain eventually ends with stable ^{209}Bi .

An ^{225}Ac source has a half-life of 9.920(3) days [21], and a ^{221}Fr rate which is initially $8.0 \cdot 10^{-7}$ of the implanted ^{225}Ac amount. A source consisting of ^{225}Ra has a half-life of 14.9(2) days, requiring a build-up time for the ^{225}Ra to decay to ^{225}Ac to reach a maximum ^{221}Fr rate of $2.4 \cdot 10^{-7}$ of the implanted ^{225}Ra after 17.5 days. A ^{225}Fr source is equivalent to one of ^{225}Ra for all intents and purposes, with its half-life of about 4 minutes. A ^{225}Ra or ^{225}Fr source results in a lower yield of ^{221}Fr , but the life of such a source is longer than an ^{225}Ac source. The isotope to choose depends on the experimental requirements and on the source isotope rate that can be delivered.

The ^{221}Fr rates from such a source should be compared to online francium yields which are of the order of 10^6 – 10^9 Fr/s for the neutron-deficient francium nuclei 206 – ^{213}Fr at ISOL facilities [22, 23]. An implantation of ^{225}Fr at maximum ISOLDE rates [23] can produce a source in little over 1 hour which releases ^{221}Fr at rates of $1 \cdot 10^6$ Fr/s; similarly, a 1-day implantation results in a ^{221}Fr rate of $2 \cdot 10^7$ Fr/s. This is at the lower end of the range of online yields from UC_x targets at ISOL facilities. However, the useful life of this source is longer than a month, whereas a francium source accumulated online is limited by the radioactive francium half-lives.

The production of a source of ^{225}Ac at ISAC has one additional advantage compared to ^{225}Ra or ^{225}Fr ; after a long-term exposure to proton irradiation of a UC_x target, ^{225}Ac continues to be released from the target if it remains hot ($\sim 2200^\circ\text{C}$), whereas ^{225}Ra diffuses out of the target within

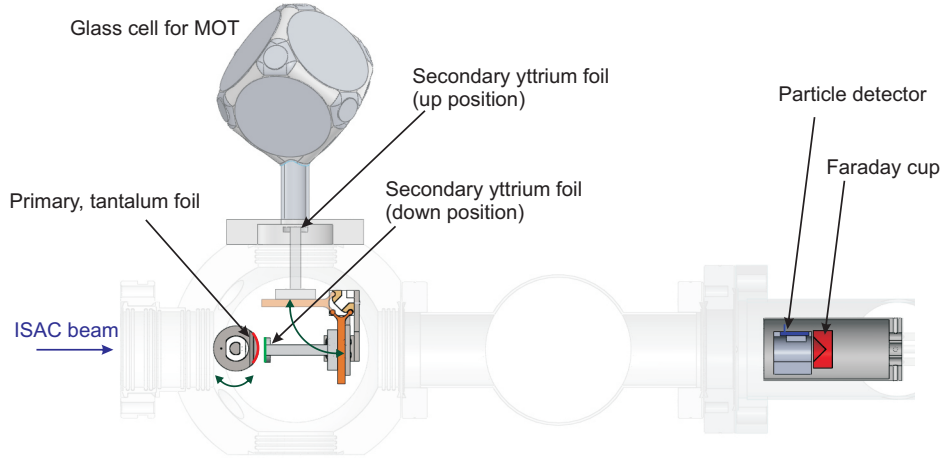


Figure 2. Schematic figure of the apparatus, highlighting parts relevant for this paper: shown on the left, the yttrium (secondary) foil — which rotates upwards to release francium in the glass cell — and the tantalum (primary) foil, and shown on the right, the particle detector in blue and the Faraday cup in red.

hours. The amount of ^{225}Ac that stays in the target will be higher for thick sources (i.e. at ISOLDE), whereas at ISAC recent UC_x targets consist of thin wafers to enhance the diffusion of short-lived species like francium. After an online running period, targets are typically not removed immediately to let them ‘cool down’ for some period. It is possible to create the required source without interfering with online beamtimes and minimal interference with target maintenance operations. This is how the ^{225}Ac source was created for the experiment described in this paper.

The integration of the ^{221}Fr source into the francium trapping apparatus is explained in section 2.1, while efficiencies and limitations of the technique for our geometry, isotope and implantation energy are explored through simulations in section 2.2. Other possibilities using the same technique are briefly noted in section 2.3.

2.1 Experimental setup

Ref. [13] explains in detail the online operation of the francium trapping apparatus. Briefly, among many other elements, francium is created at the ISAC facility at TRIUMF (see [24]) by bombarding a UC_x target with 500 MeV protons with an intensity up to $10\,\mu\text{A}$ for this type of target. The francium atoms are surface-ionized, pass through a mass separator, and are delivered to the experiment with a beam energy of typically 20–30 keV. In our experiment the ion beam is focussed onto an yttrium foil that accumulates and neutralizes the francium ions. We will refer to this yttrium catcher foil as the secondary foil in this paper. After the accumulation, typically 20 s, the foil rotates 90° upwards out of the path of the ion beam and faces a glass cell. Then it is heated by running a current through it to release neutral francium. The francium atoms are released into the glass cell and collected in a MOT, which is a combination of three perpendicular pairs of counter-propagating laser beams and a quadrupole magnetic field.

To add the functionality of the offline ^{221}Fr source a tantalum foil is added to the system upstream of the yttrium foil, as shown in figure 2. Tantalum was chosen because it is an inert material.

We will refer to this foil as the primary foil. The tantalum foil itself is mounted on a cylindrical holder on a rotational feedthrough, which allows it to face the ion beam, to face the yttrium foil and to be outside of the path of the ion beam for normal online operation. When they are facing each other, the gap between the primary and secondary foils is ~ 3 mm. For this measurement the yttrium foil was circular with a 1 cm diameter, while the tantalum foil is somewhat larger than this. An ^{225}Ac beam from ISAC impinging on the primary foil generates the ^{225}Ac source. After adequate accumulation, we can rotate the primary foil to face the secondary foil so that ^{221}Fr can be implanted in the latter. Each of these two assemblies is mounted independently on its own CF4.5" flange to enable the possibility of easy removal or exchange to limit radiation exposure.

2.2 Calculations of collection efficiencies

The goal of the simulations is to estimate the efficiency of the technique; this was done with the SRIM simulation code [25]. The ^{225}Ac implantation energy is 20 keV, the primary foil material is tantalum and the geometry is as described above (with a distance of 3 mm between the two foils being the most important parameter). The simulations are performed as realistically as possible within the SRIM simulation environment. We start with a 20 keV ^{225}Ac beam implanted into a tantalum foil; the resulting implantation profile, which has an average implantation depth of 55 Å with a straggle of 22 Å, is used as input for a second simulation to characterize the transport of recoiling francium from the first foil into the second one. The online beam is modelled as coming from one point with zero emittance; realistic beam profiles can be obtained by convolution. The curvature of the primary foil (over the beam spot) is small enough to introduce only small corrections. Figure 3 shows implantation profiles into yttrium of a 20 keV ^{221}Fr beam and of ^{221}Fr emitted from a tantalum and silicon foil. The implantation depth from the online beam is 129 Å with a straggle of 46 Å. The depth from the offline sources is on average more (270 Å for Ta), owing to the higher energy of ~ 105 keV minus 20 keV, but a fraction is also implanted close to the surface; the ^{221}Fr decay products emanate from a localized source and recoil at random angles, whereas the online source comes from a parallel beam. Different primary foil materials result in slightly different emission efficiencies. Tantalum ($Z = 73$, $A = 181$), a relatively heavy nucleus, causes a lot of energy straggling of the implanted beam. Silicon ($Z = 14$, $A = 28\text{--}30$) on the other hand, despite causing less straggling, does not result in a higher efficiency, 31 %, compared with 34 % for tantalum. Figure 4 shows the emission rate as a function of the emission angle out of the foil. Surprisingly, at small angles, the rate is higher than expected; atoms emitted at larger angles, and initially backscattered atoms as well, contribute to this higher rate at small angles, while reducing the rate at larger angles.

A side effect of this point-like source is that the lateral distribution on the yttrium foil will be larger than from an online beam; an ^{225}Ac beam having a Gaussian lateral profile with a 1σ radius of 1.5 mm, or 90 % within a 3.2 mm radius, with a distance of 3 mm (5 mm) between the two foils, results in a ^{221}Fr distribution with a Gaussian profile with a 1σ radius of 3 mm (4.5 mm). Therefore, 75 % (46 %) ends up on the 1 cm-diameter foil and 45 % (22 %) in the same 3.2 mm radius as the mass-separated beam.

These two effects, a larger average implantation depth and a larger spot size, have an important effect for our experiments. In order to load the MOT, we dispense the ^{221}Fr embedded in the yttrium foil by heating it. The heating is done by sending a current through the foil (typically ~ 10 A

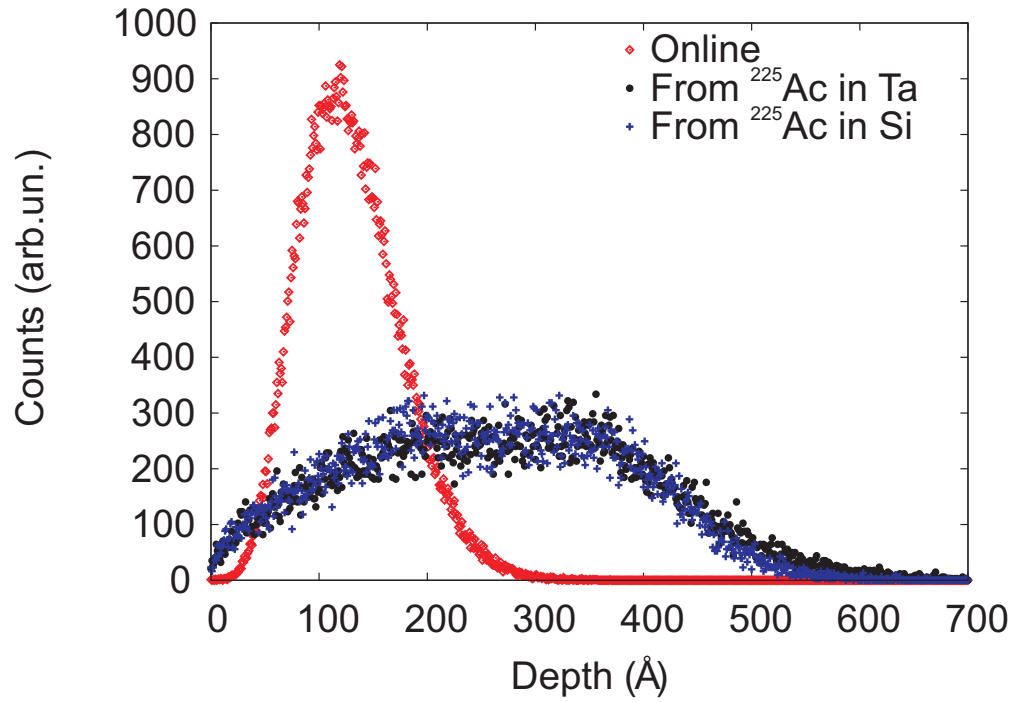


Figure 3. Implantation profiles for ^{221}Fr into Y from different sources. In (red) diamonds ^{221}Fr online from ISAC, in (blue) crosses ^{221}Fr from ^{225}Ac in a Ta foil and in (black) dots ^{221}Fr from ^{225}Ac in a Si foil. The data are normalized such that the integrated count rate is one million for each curve.

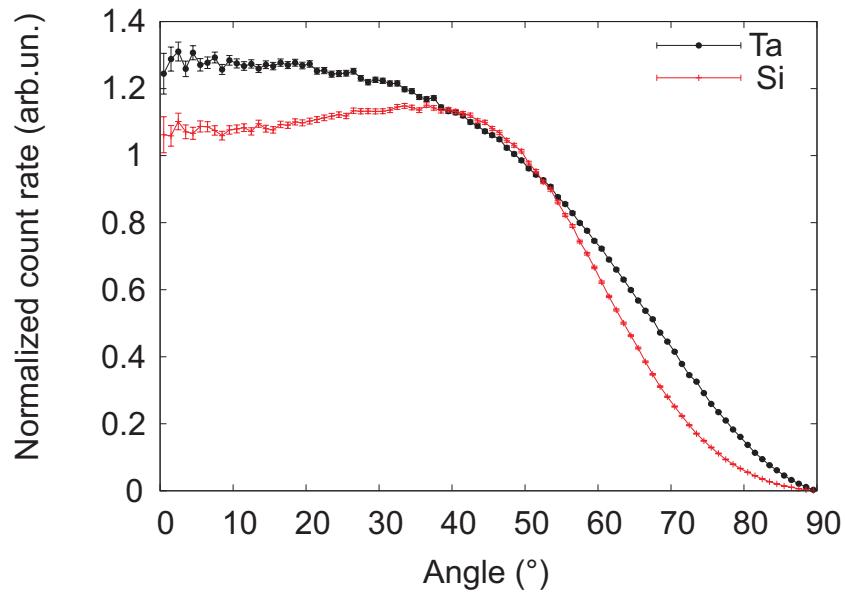


Figure 4. Histogram (with bins of 1°) showing the total emission rate of ^{221}Fr out of tantalum (black line with dots) and silicon (red line without dots), as a function of the emission angle with respect to the surface normal. Data are normalized to the angular emission rate for isotropic emission over 4π .

for ~ 1 s). The deeper average implantation of the ^{221}Fr in the yttrium reduces the dispensed amount roughly by a factor of two. This is estimated by using the diffusion coefficient of francium in yttrium, $1.6(9) \cdot 10^{-14} \text{ cm}^2/\text{s}$ [26], and equation (3) in reference [27] for the time-dependent released fraction. This loss can be minimized by increasing the amount or duration of the heating, which was not done at this time to avoid possible damage to the foil. Visual inspection shows that the heating profile is a stripe with a larger temperature in the center and a lower temperature towards the legs, where the heat sinks. The area that is effectively heated is about $1/3$ of the total foil size. Since the spot size from ^{221}Fr escaping the tantalum foil is much larger than the online beam spot size, one expects — for the same heating conditions — a decrease in efficiency. Also, the 1 cm-diameter neck of the glass cell for the MOT limits the amount of ^{221}Fr that can be trapped in the MOT (see figure 2).

2.3 Other isotopes

Extensions to other isotopes and elements are straightforward. The only requirement for the source is that the mother isotope of the isotope of interest should undergo α decay (giving the daughter nucleus a sufficiently high recoil energy), and the initial source should be reasonably long-lived, longer than a week. We are interested in ^{221}Fr , but ^{217}At is released as well into the yttrium foil with an efficiency of 12 %.

Finally, a different isotope of francium, ^{223}Fr , could be used in our geometry by forming an ^{227}Ac source. However, the α branching ratio of ^{227}Ac is low (1.4 %) so that a sizeable source would be required to generate useable quantities of ^{223}Fr , presenting a significant radiological hazard. This decay has been used in the past to study the structure of ^{223}Fr by α and γ spectroscopy [28].

3 Experiment

A 20 keV $^{225}\text{Ac}^+$ beam impinges on the primary foil for 18.5(5) hours of at an average rate of 6.0(6) pA (or $3.7(4) \cdot 10^7 \text{ Ac/s}$) from the ISAC target without active proton irradiation — but after an online running period. In-source resonant laser ionization using a two-step laser excitation scheme into an auto-ionizing state in ^{225}Ac [29, 30] enhances the extraction efficiency by two orders of magnitude over pure surface ionization. Earlier tests on a UC_x target showed that during proton irradiation one third of produced isotopes at mass 225 is ^{225}Ac , while the rest is mainly ^{225}Ra . Thanks to the in-source resonant laser ionization any contribution from contaminants is negligible. A total of $2.5(3) \cdot 10^{12}$ ^{225}Ac atoms are implanted in the foil. Using the ^{225}Ac half-life of 9.920 days yields a total decay rate of ^{225}Ac into ^{221}Fr of $1.9(2) \cdot 10^6/\text{s}$, immediately after the end of the implantation.

3.1 Particle detector measurement

The ^{225}Ac source rotates towards the Faraday cup and α detector assembly (see figure 2) and the yttrium foil rotates out of the way to measure the ^{221}Fr release rate for comparison with simulations. The solid angle of the Faraday cup seen from the ^{225}Ac source is 0.045(2) %, and the solid angle of the particle detector as seen from the center of the Faraday cup is 1.4(1) %. As the ^{225}Ac source faces the Faraday cup a source of ^{221}Fr builds up on the Faraday cup. The particle detector is a

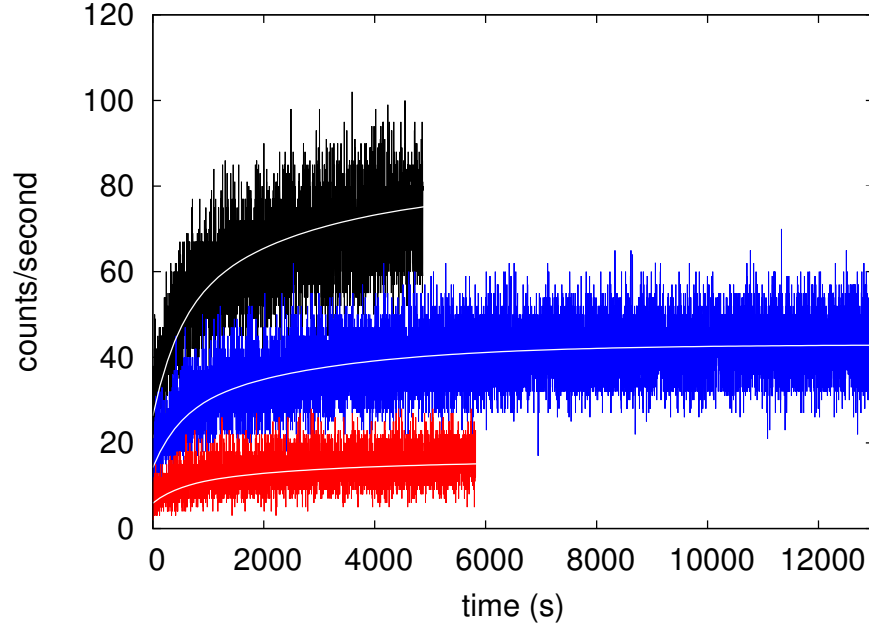


Figure 5. Buildup of a ^{221}Fr source on the Faraday cup as detected by the particle detector, with $t = 0$ s being the start of the ^{221}Fr implantation: 2 hours (black), 9 days (blue) and 23 days (red) after the ^{225}Ac implantation. The white lines overlaid on the data are the best fits for the data sets.

silicon photodiode (Hamamatsu S3590-09). The signal processing consists of a shaping amplifier, a discriminator and a multichannel scaler. Therefore, no energy discrimination of the detected particles is done.

The decay chain starting at ^{221}Fr contains many α and/or β decaying isotopes (see e.g. [20] including half-lives): ^{221}Fr , ^{217}At , ^{213}Bi , ^{213}Po , ^{209}Tl , and ^{209}Pb . Isotopes with a short half-life (< 1 s) will be detected with the same effective half-life as the mother isotope: ^{217}At together with ^{221}Fr and ^{213}Po , ^{209}Tl together with ^{213}Bi . Isotopes with a half-life longer than the time interval used for the analysis (i.e. 1000 s) will not influence the analysis: ^{209}Pb . The remaining relevant quantities are therefore the half-lives of ^{221}Fr and ^{213}Bi , 288.0(4) s and 2737(4) s respectively.

We have made measurements with the particle detector of the ^{221}Fr produced by the ^{225}Ac source at three different times: two hours after the end of the ^{225}Ac implantation and then 9 and 23 days later. The data are shown in figure 5. A simple model of the growth of the ^{221}Fr population deposited in the Faraday cup at a constant rate, where the activity decays into one daughter (^{213}Bi) that in turn decays as well, explains the data reasonably well, as shown in table 1. The count rate on the particle detector as a function of time, $R_{\text{total}}(t)$, is then:

$$R_{\text{total}}(t) = B + R_{\text{Fr}} \cdot \left[1 - \exp(-t/\tau_{\text{Fr}}) \right] + \frac{R_{\text{Fr}}}{\tau_{\text{Fr}} - \tau_{\text{Bi}}} \cdot \left[\tau_{\text{Fr}} \cdot (1 - \exp(-t/\tau_{\text{Fr}})) - \tau_{\text{Bi}} \cdot (1 - \exp(-t/\tau_{\text{Bi}})) \right], \quad (3.1)$$

with τ_{Fr} and τ_{Bi} the ^{221}Fr and ^{213}Bi lifetimes, respectively, B the background count rate and R_{Fr} the ^{221}Fr implantation rate. The background count rate comes from activity present before starting the

Table 1. Fit results for the data from the particle detector measurements. χ^2/NDF is the reduced chi-squared.

Days after implantation	^{221}Fr rate (s^{-1})	χ^2/NDF
0.083	29.6(3)	1031 / 947
9	15.2(2)	1080 / 999
23	4.83(14)	1028 / 999

^{221}Fr implantation, while the ^{221}Fr and ^{213}Bi half-lives are well-known quantities. We validate the model by leaving the ^{221}Fr and ^{213}Bi lifetimes free, but once validated, the model only has the ^{221}Fr implantation rate as free parameter.

For the final analysis we used the first 1000 s of each data set, since we are interested in the ^{221}Fr rate and we want to avoid sensitivity to activity migrating in the system. Fitting an exponential decay through the three ^{221}Fr rates gives 30.0(6) Fr/s, right after the ^{225}Ac implantation. The fitted lifetime is consistent with that of ^{225}Ac decay, indicating the ^{221}Fr source in the tantalum foil has not decayed by other means, e.g. by diffusion out of the primary foil or by having another element present in the system associated with the trapping facility (e.g. Rb, see ref. [13]).

Starting from the estimated ^{221}Fr rate escaping the foil, $1.9(2) \cdot 10^6$ $^{221}\text{Fr}/\text{s}$ (from measured ^{225}Ac rates during the implantation), and taking into account solid angles of 0.045(2) % (^{221}Fr source to Faraday cup) and 1.4(1) % (Faraday cup to particle detector), an increased ^{221}Fr emission rate for these angles by a factor of 1.28(3) (see figure 4), double counting because of ^{217}At decay, leads to an expected rate on the particle detector of 31(4) counts/s. This number is in good agreement with the rates of 30.0(6) counts/s deduced from particle detector measurements.

3.2 Magneto-optical trap measurements

The final test of our offline ^{221}Fr source is to verify that we can use it to load ^{221}Fr into a MOT. We operate the MOT with 120 mW (total over 6 beams) of trapping light on the D2 cycling transition (718 nm) and 8 mW of repumper light on the D1 transition (817 nm). The trapping beams each have an area of about $\sim 20 \text{ cm}^2$. The magnetic gradient of the MOT is 7 G/cm along the strong axis. The correct trapping and repumping laser frequencies were approximatively maintained from the online run one week before through the transfer cavity lock [31]. ^{221}Fr was implanted into the yttrium foil for 10 minutes, about one week (177 hours) after the implantation of the ^{225}Ac . Starting from a ^{221}Fr rate of $1.9(2) \cdot 10^6/\text{s}$, this yields $1.78(19) \cdot 10^8$ ^{221}Fr implanted in the yttrium foil and available for trapping. From these a fraction of $1.3(6) \cdot 10^{-5}$ was trapped in the MOT, with a total trapped amount of 2300(900). This was measured by the fluorescence of the atoms and the total uncertainty is dominated by the uncertainty in total laser power at the atom cloud position and the amount of detuning from resonance. The efficiency of the online run of $5(2) \cdot 10^{-4}$ comes from trapping ^{209}Fr . For ^{221}Fr the efficiency was measured to be a factor of 5 lower during the online run; this can be understood qualitatively from their different atomic structures. The ^{221}Fr atom has a relatively narrow hyperfine splitting, 58 MHz between the cycling trapping transition ($7S_{1/2}F=3 \rightarrow 7P_{3/2}F=4$) and a transition that can decay to the lower hyperfine ground state level

Table 2. Summary of losses from ^{221}Fr escaping the tantalum towards trapping in a MOT. The losses are divided between losses that are inherent to our apparatus (‘overall’), and losses which are only applicable to the technique described in this paper (‘source’).

Loss factor overall	source	^{221}Fr amount	Explanation of loss factor
		$5.20 \cdot 10^8$	^{221}Fr amount in the primary foil
	3	$1.78 \cdot 10^8$	Francium entering the secondary foil
2000		$8.9 \cdot 10^4$	Online trapping efficiency of ^{209}Fr
5		$1.78 \cdot 10^4$	^{221}Fr trapping efficiency as compared to ^{209}Fr
	2–5		Implantation depth
	2–5		Larger ^{221}Fr spot size
	1–10		Possible damage to yttrium foil
		$2.3 \cdot 10^3$	Trapped francium

($7S_{1/2}F = 3 \rightarrow 7P_{3/2}F = 3$), as compared to 518 MHz for ^{209}Fr . A simple 6-level rate equation calculation suggests that for our repumper parameters only 10–15 % is in the $7P_{3/2}$ level at any given time, which reduces the fluorescence per trapped atom proportionally and also reduces the collection efficiency of atoms into the MOT. The process of trapping francium from the online ion beam as compared to ^{221}Fr from the offline ^{225}Ac source is 8_{-5}^{+10} times more efficient, normalized to the amount of ^{221}Fr implanted in the secondary foil. Due to the long implantation times required to accumulate a sufficient amount of ^{221}Fr into the yttrium foil, no systematic studies using the ^{225}Ac source were performed, because at the time e.g. the long-term laser stability was not sufficiently good.

In the optimistic, 1σ -lower-limit case the efficiency of the offline scheme is only 3 times less efficient than the online mode of operation in our measurement. This can be explained by (i) having a non-optimised MOT, or factors inherent to our geometry such as (ii) the more diffuse source of ^{221}Fr on the yttrium foil and (iii) the deeper implantation profile. In the pessimistic, 1σ -upper-limit case one can add that there were some mechanical problems in the system, before this test, causing the yttrium foil to be slightly damaged. This resulted in an irregular heating profile. From our measurement, we are unable to differentiate between losses from each of those separate effects; they are listed in table 2 with an estimate of their effect.

4 Discussion

The α detection measurements suggest no fundamental limitation to this technique; 34 % of implanted ^{225}Ac will escape the foil as ^{221}Fr for our experimental conditions. Our geometry is optimised for online implantation of francium isotopes for this first measurement of trapping ^{221}Fr from an ^{225}Ac source. In the future a better geometry could be found; the addition of a translational feedthrough, for instance, would minimize the distance between the two foils avoiding losses from having a larger francium implantation spot size. The larger implantation depth could be compen-

sated for by an improved operation of the yttrium foil, e.g. more intense heating. The efficiency achieved can now be used to investigate systematic effects (such as those in section 1).

The overall efficiency of our technique is comparable to the experiments mentioned in the introduction. The ^{225}Ac source of [10] had an efficiency of 2 % for ^{221}Fr leaving the oven, the ^{82}Sr source of [11] obtained 35 %, and the CARIBU facility in [12] achieves 35 % for incidence rates of the order of 10^6 atoms/s. The latter two experiments have the advantage of extracting an ion beam, allowing for more favorable implantation properties on the catcher foil. The required infrastructure, however, is much more complex than the one used in our method. While the first method of generating ^{221}Fr in an oven can be implemented in a relatively small space, it does not allow both online and offline francium trapping in our geometry.

A key component of our technique is that it permits the use of the ^{225}Ac source in combination with online beamtime, without modifying the setup and without requiring a modification of the ISAC beamlines further upstream. This can extend the available development time with ^{221}Fr , while allowing high-statistics measurements with online beamtime. Eventually this dual use could be superseded by longer beamtimes becoming available, as promised by the ARIEL facility [32], under construction at TRIUMF, or the planned ISOL@MYRRHA facility [33].

5 Conclusion

We have demonstrated magneto-optical trapping of ^{221}Fr ejected by α decays from a ^{225}Ac source made by implanting a mass-separated ion beam. The use of ejected ^{221}Fr provides one solution to technical difficulties encountered by other methods when trapping decay products released by heating generator material (see ref. [10] and [11]). Such an ^{225}Ac source foil made by implantation could in principle be transportable to remote locations where the primary beam is not available, as can be done at ISOL facilities.

Acknowledgments

This work is supported by NSERC and NRC from Canada, NSF and DOE from U.S.A., CONACYT from Mexico. We acknowledge helpful discussions with H. Gould, K. Johnston, M. Kowalska, P. Kunz and M. Lindroos.

References

- [1] J.A. Behr and G. Gwinner, *Standard model tests with trapped radioactive atoms*, *J. Phys. G* **36** (2009) 033101 [[arXiv:0810.3942](#)].
- [2] N. Severijns, M. Beck, and O. Naviliat-Cuncic, *Tests of the standard electroweak model in nuclear beta decay*, *Rev. Mod. Phys.* **78** (2006) 991 [[nuc1-ex/0605029](#)].
- [3] A. Gorelov et al., *Scalar interaction limits from the $\beta - \nu$ correlation of trapped radioactive atoms*, *Phys. Rev. Lett.* **94** (2005) 142501 [[nuc1-ex/0412032](#)].
- [4] N.D. Scielzo, S.J. Freedman, B.K. Fujikawa, and P.A. Vetter, *Measurement of the $\beta - \nu$ correlation using magneto-optically trapped ^{21}Na* , *Phys. Rev. Lett.* **93** (2004) 102501.

- [5] X. Fléhard et al., *Measurement of the β - ν correlation coefficient $a_{\beta\nu}$ in the β decay of trapped ${}^6\text{He}^+$ ions*, *J. Phys. G* **38** (2011) 055101.
- [6] G. Li et al., *Tensor interaction limit derived from the α - β - ν -correlation in trapped ${}^8\text{Li}$ ions*, *Phys. Rev. Lett.* **110** (2013) 092502.
- [7] E. Gomez, S. Aubin, G.D. Sprouse, L. A. Orozco, and D.P. DeMille, *Measurement method for the nuclear anapole moment of laser-trapped alkali-metal atoms*, *Phys. Rev. A* **75** (2007) 033418 [[physics/0412124](#)].
- [8] E. Gomez, L.A. Orozco and G.D. Sprouse, *Spectroscopy with trapped francium: advances and perspectives for weak interaction studies*, *Rep. Prog. Phys.* **66** (2006) 79.
- [9] R.H. Parker et al., *Efficient, tightly-confined trapping of ${}^{226}\text{Ra}$* , *Phys. Rev. C* **86** (2012) 065503 [[arXiv:1305.7131](#)].
- [10] Z.-T. Lu et al., *Efficient collection of ${}^{221}\text{Fr}$ into a vapor cell magneto-optical trap*, *Phys. Rev. Lett.*, **79** (1997) 994.
- [11] R. Gucker et al., *Magneto-optical trapping of radioactive ${}^{82}\text{Rb}$ atoms*, *Phys. Rev. A* **58** (1998) 1637.
- [12] G. Savard et al., *Radioactive beams from gas catchers: The CARIBU facility*, *Nucl. Instrum. Meth. B* **266** (2008) 4086.
- [13] M. Tandecki et al., *Commissioning of the Francium trapping facility at TRIUMF*, *2013 JINST* **8** P12006 [[arXiv:1312.3562](#)].
- [14] C.S. Wood, S.C. Bennett, J.L. Roberts, D. Cho, and C.E. Wieman, *Precision measurement of parity nonconservation in cesium*, *Can. J. Phys.* **77** (1999) 7.
- [15] ISOLDE collaboration, H. T. Duong et al., *First observation of the blue optical lines of francium*, *Europhys. Lett.* **3** (1987) 175.
- [16] D. Sheng, J. Zhang and L.A. Orozco, *Rb atoms in a blue-detuned dipole trap: Coherence and ground-state differential AC Stark shift*, *Phys. Rev. A* **87** (2013) 063412.
- [17] M.L. Terraciano et al., *Enhanced spontaneous emission into the mode of a cavity QED system*, *Opt. Lett.* **32** (2007) 982 [[quant-ph/0702168](#)].
- [18] H.B. Jeppesen et al., *Alpha-decay half-life of ${}^{221}\text{Fr}$ in different environments*, *Eur. Phys. J. A* **32** (2007) 31.
- [19] F. Wauters et al., *Half-life of ${}^{221}\text{Fr}$ in Si and Au at 4 K and at millikelvin temperatures*, *Phys. Rev. C* **82** (2010) 064317 [[arXiv:1010.6250](#)].
- [20] G. Suliman et al., *Half-lives of ${}^{221}\text{Fr}$, ${}^{217}\text{At}$, ${}^{213}\text{Bi}$, ${}^{213}\text{Po}$ and ${}^{209}\text{Pb}$ from the ${}^{225}\text{Ac}$ decay series*, *Appl. Rad. Isot.* **77** (2013) 32.
- [21] S. Pommé et al., *Measurement of the ${}^{225}\text{Ac}$ half-life*, *Appl. Rad. Isot.* **70** (2012) 2608.
- [22] ISAC yield database, <http://mis.triumf.ca/science/planning/yield/beam>.
- [23] ISOLDE yield database, https://oraweb.cern.ch/pls/isolde/query_tgt.
- [24] M. Domsbysky et al., *Commissioning and initial operation of a radioactive beam ion source at ISAC*, *Rev. Sci. Instrum.* **71** (2000) 978.
- [25] J.F. Ziegler, M.D. Ziegler and J.P. Biersack, *SRIM — The stopping and range of ions in matter*, *Nucl. Instrum. Meth. B* **268** (2010) 1818.
- [26] C. de Mauro et al., *Measurement of diffusion coefficients of francium and rubidium in yttrium based on laser spectroscopy*, *Phys. Rev. A* **78** (2008) 063415.

- [27] D. Melconian et al., *Release of ^{37}K from catcher foils*, *Nucl. Instrum. Meth. A* **538** (2005) 93.
- [28] R.K. Sheline et al., *Experimental and theoretical study of the nuclear structure of ^{223}Fr* , *Phys. Rev. C* **51** (1995) 1708.
- [29] J. Lassen et al., *Resonant ionization laser ion source project at TRIUMF*, in the proceedings of the 6th *International Workshop on Application of Lasers in Atomic Nuclei Research (LASER 2004)*, May 24–27, Poznań, Poland (2004).
- [30] S. Raeder et al., *In-source laser spectroscopy developments at TRILIS — Towards spectroscopy on actinium and scandium*, *Hyperfine Interact.* **216** (2013) 33.
- [31] W.Z. Zhao, J.E. Simsarian, L.A. Orozco, and G.D. Sprouse, *A computer-based digital feedback control of frequency drift of multiple lasers*, *Rev. Sci. Instrum.* **69** (1998) 3737.
- [32] J. Dilling, R. Krücken and L. Merminga, *ARIEL overview*, *Hyperfine Interact.* **225** (2014) 253.
- [33] T. Nilsson, *European RIB facilities — Status and future*, *Nucl. Instrum. Meth. B* **317** (2013) 194.

Chapter 4: Precision PNC apparatus: the science chamber.

The capture trap with the glass cell, is ideal for high efficient collection of the scarce francium atoms. This trap however has limitations for our planned precision experiments. We need the following:

1. Possibility to place inside, position, and control equipments such as electrodes and microwave cavity mirrors.
2. Ample optical access for laser beams that include: trapping, preparation, excitation and detection, together with PNC excitation laser/microwave and imaging.
3. Control of the electric and magnetic environment in the interaction region: center of the chamber.

We also have to address concerns over possible nuclear contamination and its effects. The new science chamber provides accessibility with a compact overall size. It also features a non-magnetic construction for control of the stray B field and its gradient. We describe in this chapter the science chamber for precision PNC measurements, and the atom transfer from the capture MOT. We first summarize the requirements determined by the physics goals, and then go into the design specifics of the science chamber, its construction and commissioning. Appendix A

contains the engineering drawings.

4.1 Science chamber requirements

Both the microwave and the optical PNC experiments have stringent requirements. Incorporating two different proposed measurement methods, one involving electrodes that must guarantee static electric field uniformity and reversal symmetry, the other involving a precision microwave Fabry-Perot cavity, is particularly challenging. Chapter 2 laid out the general ideas and requirements of the two planned experiments. Here we summarize and illustrate the needs that the science chamber must fulfill. The overall choice of metal material over a glass chamber, comes from a combination of flexibility: easier to open and close flanges; and nuclear safety: it is much harder to knock and shatter a metal chamber. Some further requirements are related to the potential systematic effects, which we will discuss briefly here. More thorough details about the systematic effects can be found in Ref. [8] for the optical experiment, and Ref. [30] for the microwave experiment. We start with the microwave/anapole experiment.

4.1.1 Microwave experiment

The microwave experiment aims at a measurement of the anapole moment, and involves the transition between the hyperfine levels of the electronic ground state. Chapter 2 section 2.2 established the measurement plans, i.e. positioning the atoms in the center of a microwave cavity with an optical dipole-trap.

Geometric constraints

We have physical size constraints from the microwave cavity, which contains a pair of 3 inch diameter mirrors. We choose this size because it is large enough for a good Fresnel number, while being the largest for commercial availability and ease of handling. In order for the orthogonal MOT beams (1 inch optics) to clear the microwave mirrors, these mirrors should be separated by at least 15 cm. This sets the minimum internal volume. We want the microwave wavelength to be much shorter than the 15 cm mirror separation to minimize the mode distortion. This is the reason why we choose the neutron deficient Fr isotopes, which has hyperfine splittings around 40 50 GHz.

DC Magnetic field

We want to operate at the first order (linear) insensitive set-point, which corresponds to bias magnetic fields at 1500 G level ¹the anapole moment experiment requires m_F changing transitions, e.g. $m_F = 0$ to $m_F = 1$ for ^{209}Fr . See Ref. [30]. for the Bosonic isotopes [30], or at the 3 G level for the Fermionic isotopes [31], respectively. At these quadratic bottoms, the second order Zeeman effect remains, with a coefficient of 84 Hz/G², which would shift the line center by 0.3 Hz with 60 mG of magnetic field offset. This corresponds to 40 ppm level control on the 1500 G field. The fermionic isotopes with small bias field relaxes this requirement significantly. The large bias field also requires putting coils as close to the atoms as possible, and we choose the re-entrant viewport pocket design, common in groups such as those in the JQI.

¹T

Ultrahigh Vacuum

The hyperfine transition essentially has an infinite lifetime compared to our experimental timescale. We then have infinite time to probe, as long as we can keep the atoms trapped. An optical dipole trap lifetime is largely influenced by the vacuum background gas collisions, and we need the UHV pressure to be below 10^{-10} Torr for the long interrogation.

The requirements for the science chamber from the anapole experiment are then mainly as follows:

1. Enough volume and clearance for a pair of Fabry-Perot cavity mirrors, separated by about 6 inches, with size of at least 3 inches diameter to avoid clipping of the (wavelength 7 mm) microwave field.
2. Magnetic field control, to avoid introducing (time-varying) fringe fields and gradients at the tens of mG level, even with the switching of bias at the 1.5 kG level.
3. Ultra-high vacuum at sub 10^{-10} Torr level, for long storage times of atoms in the optical dipole trap.
4. Room for placing the magnetic field coils close to the center of the chamber as much as possible, for easily generating magnetic field gradients or large bias fields.
5. Enough ports for UHV electrical feedthroughs, e.g. for piezo-actuator drivers to position the cavity mirrors.

4.1.2 Optical experiment

Geometric concerns

The DC electric field, used for amplifying the PNC signal, should be uniform over the region of the atomic cloud. We have set an lower bound of 10^{-4} , which seems easy to satisfy due to the sub-mm size of the atom cloud in a MOT. We have however chosen to start with trapping laser beams expanded to the limit of 1 inch optics, and with this spacing between the two electrodes the needed field uniformity requires their physical size to be at least 4 inches. The optical power buildup cavity does not occupy much space, with the only concern being that the dielectric surfaces should be far from the atoms to prevent charge buildup.

Here we take a brief detour and discuss about the spurious patch electric field and its relation to the systematic error. This discussion can be generalized to provide guidelines also about the microwave PNC systematics. We recall that the interference technique amplifies the signal by an amount proportional to: $A_{\text{Stark}}/A_{\text{E1-PNC}}$. This however, also means that the parity non-conserving asymmetry signal, is smaller by the same ratio, compared to the parity conserving signal, which is proportional to $|A_{\text{Stark}}|^2$. Suppose we want to amplify the PNC by a factor of 10^3 , and we desire a measurement precision of 1%, the Stark field reversal precision has to be better than $10^{-3} \cdot 10^{-2} = 10^{-5}$. This not only applies to the electric field reversal, but also the M1 interference microwave field in the anapole experiment. The Cs experiment actually had even better control [8]. Note that however, anything else not directly entering linearly into the interference signal, does NOT

require such a precise reversal.

Patch electric fields can be passively reduced by locating dielectric surfaces far enough from the trap.² These are compatible with the metal chamber construction with decent internal volume right now.

Magnetic field

The bias magnetic field during the optical PNC excitation is an example where the exact value and reversal precision is not as important as the misalignment control. We expect a very similar level of control as in the Cs experiment [8], which is around hundreds of μG . The few Gauss level bias field we need to apply, or the quadrupole magnetic field of the MOT which is turned on and off, are all much lower than the 1500 G bias field for the microwave experiment. In fractional precision the sub-mG requirement is compatible with that of the microwave PNC experiment.

Summarizing for the optical PNC experiment: fortunately the two very different experiments require similar internal volume, accessibility, and magnetic field control.

4.2 Design and Construction

Accessibility and magnetism are the two major concerns. Based on the geometrical constraints and ease of handling, we have chosen 8 inch CF as the largest major size of flanges, which satisfies both the experiments. For the magnetism, we

²The presence of stray patch fields is a commonly encountered challenge, for example in experiments with Rydberg atoms [63], optical atomic clocks [64], or ion trapping [65]. The exact origins and solutions are not well established in the AMO community, so we might eventually resort back to the segmented electrodes and measure along different directions, similar again to the Boulder Cs experiment.

explored many material possibilities and considered various companies or actually having it constructed by TRIUMF's own machine shop, while eventually resorting to Pfeiffer Vacuum in Germany. All the flanges are made out of 316LN-ESR stainless steel, with vacuum firing to remove the residual magnetism, as well as improving the UHV by pre-releasing the hydrogen trapped in the bulk material.

4.2.1 Accessibility

Figure 4.1 shows the science chamber design as built. For convenience we define the up/down, left/right (as one would see entering the lab) and front/back as the z , y , and x directions, respectively. The chamber body is symmetric under parity flip except for the z direction, where the atoms will arrive from above. The top is then designed to have a 2.75 inch CF flange in the center, to connect to the transfer/middle vacuum system. The other major faces, i.e. the front/back, left/right, and the bottom side, all have 8 inch CF flanges in the center. The MOT laser beams enter through the x direction as well as the 2.75 inch CF ports in the perpendicular yz plane, and are 45° angled from the z direction. There are 8 additional 2.75 inch CF flanges, 4 on top and 4 on the bottom respectively, arranged with the same 45° angle with respect to the z axis, and rotated 30° along the y axis, such that optical access is available as long as the rotationally symmetric microwave cavity (along the y axis) clears the MOT trapping beams. Four more 2.75 inch CF flanges are added on the top at 22.5° angle with the z axis, for auxiliary purposes (e.g. the current plan for pumping laser beams in the optical PNC experiment).

These flanges all directly face the center, where the atom trap is. Eight 4.5 inch CF flanges, modified according to Kimball physics flange OD of 4.13 inches, located at the corners of the front and back faces, do not have direct line of sight to the center, and are designed to accommodate vacuum pumps, high voltage electrical feedthroughs or in-vacuum magnetic field sensors.

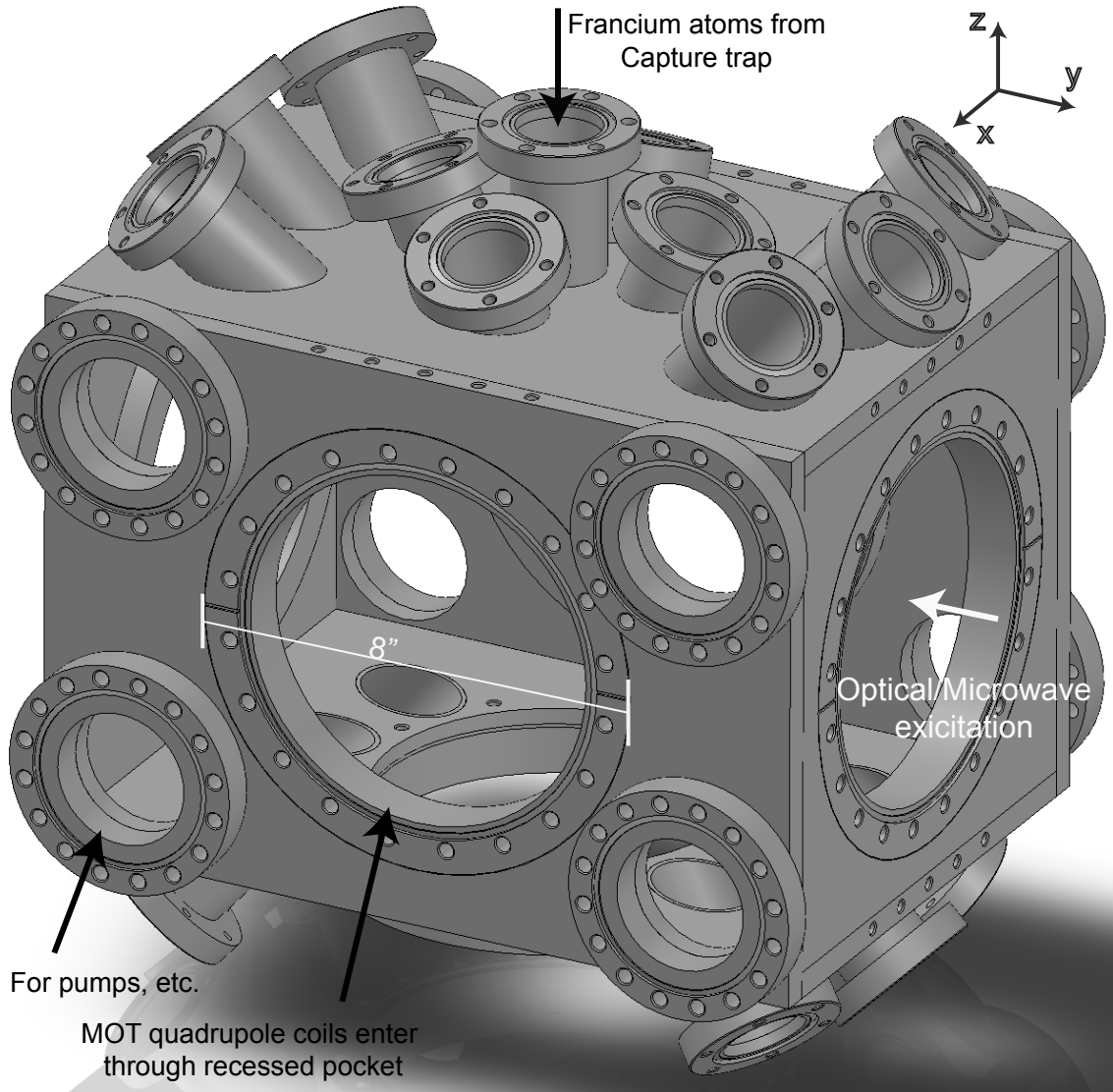


Figure 4.1: The science chamber: Isometric view of the 3D CAD model.

Fig 4.2 shows the schematic for how the chamber incorporates the microwave

and optical experiments.

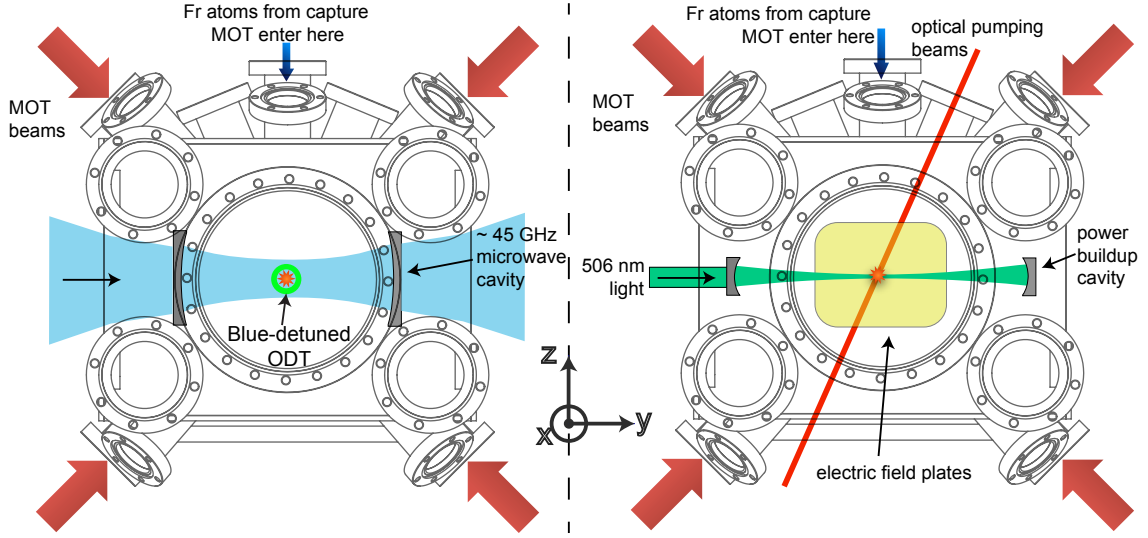


Figure 4.2: PNC experimental setups with the science chamber. Left: microwave; right: optical.

4.2.2 Magnetism and ultrahigh vacuum solutions

The 10^{-5} level magnetic field control requirement is at the verge of necessity for μ metal shielding. We choose to not passively shield to retain the accessibility, and add active compensation when needed. The science chamber materials, i.e. the walls and flanges, are all reasonably far away (at least 5 inches distance) from the active measurement region, and we have set the design goal of relative permeability of ≤ 1.05 , instead of over-engineering with completely non-magnetic materials such as titanium or aluminum. This requirement is satisfied by carefully treated (e.g. quenched) 316L Stainless Steel raw material, however is compromised after the cold working (milling, lathing, etc.) or welding. Grade 300 series SS in general share this property, with the best example being 304 SS. Its magnetism shares

the common feature with 316 L, while being more prone to non-magnetic to ferromagnetic phase transitions after machining. In practice, after measuring a great range of actual UHV parts as well as half-finished machine shop pieces, we found that they could all have relative permeabilities at the 1.3 level, and sometimes even depend on the raw material batch or the grain direction. The ideal material should possess the following properties: crystal structure (which determines the magnetic phase) robust against metal-working, reasonable machinability and weldability, low outgassing, and preferably low conductivity for reducing the eddy-currents during magnetic field switching. Leveraging these and the cost concerns, we resorted to a construction with 316 LN flanges, built by Pfeiffer Vacuum (or Trinos, the company that Pfeiffer acquired) in Germany.

A critical processing of the chamber after machining and welding was the “vacuum firing”. This process is basically high temperature baking at up to 1050 °C, with a relatively short duration of less than 3 hours. The ferromagnetism caused by the cold-working and welding, i.e. the crystal structure that was changed from the austenitic stainless phase, on the edges and interfaces of the bulk material, would “desolve” back into the original crystal phase. The additional benefit is that the outgassing, especially of hydrogen, is greatly reduced³. Not all grades of stainless are suitable for this process though, as it will actually soften the conflat flange knife-edge. Our 316 LN flange material has well above the hardness required for a reasonable UHV sealing lifetime (about 50 times of opening and closing), and is

³See for example presentations from CERN vacuum group, e.g. <https://cas.web.cern.ch/cas/Spain-2006/PDFs/Chiggiato-2.pdf>.

still hard enough after the vacuum-firing. The 304 SS and 316 L SS grades on the other hand, have the risk of becoming too soft. This makes the mixture material construction (316 L walls and tubes with 316 LN flanges) an excellent solution.

We note a detail about the surface finishing: Kimball Physics have all their chambers and parts electro-polished, for reducing the surface area and the out-gassing. European chamber manufacturers typically use glass-bead blasting for the surface-finishing. We have no problems with this treatment, tested by the excellent vacuum pressure (15 nA on a 45 L/s ion pump, or 1×10^{-11} , with only mild baking of the UHV system (1 week, below 150 °C).

4.3 The entire UHV system and peripherals

The science chamber resides 70 cm vertically down from the capture glass cell. The entire UHV includes the transfer section between the two chambers, with direct line-of-sight clearance for the atom transfer, mechanical separation for uncoupling vibrations, good differential pumping, and the option for entirely separating the two systems with all-metal-valves. The top and bottom systems are also connected in the roughing section, where the combined pumping with a Turbo pump is then directed outside of the FTF, dumping into the ISAC nuclear exhaust. We have constructed the UHV system with selected low magnetic permeability components near the science chamber.

The carefully designed UHV system provides the environment, and we have to bring in the lasers and magnetic fields for the trapping and manipulations, plus

the imaging system for detections.

4.3.1 UHV system

Transfer section

The glass cell of the capture trap is on top of the neutralizer chamber, as described in Chapter 3. On the bottom of the neutralizer chamber, an all metal valve, a close-coupler, a 2.75 inch CF cubical chamber from Kimball physics, a mechanical shutter and a welded bellows are connected sequentially. The separation of the two MOT centers is about 70 cm. We use the shutter to close the path between the upper and lower vacuum systems, and only open it when we are transferring atoms. This design is beneficial for two purposes: maintaining the excellent vacuum pressure we have in the science chamber, and reducing the amount of radioactive contamination. It has an oval/rectangle shaped metal piece attached to the shaft of a rotation feedthrough. We have included the 2.75 inch CF cubical chamber, for letting the mechanical shutter “flag” have enough clearance, as well as for laser access for a 2D MOT/molasses to re-focus when the atoms travel through the middle of the transfer path if needed.

Pumps on the science chamber

The science chamber is pumped by a 45 l/s ion pump from Gamma Vacuum (model 45S), and a 200 l/s NEG getter pump from SAES (model Capacitor D 200). We use the current and pressure reading on the ion pump as the main vacuum gauge. The MOT lifetime is of course the eventual vacuum performance benchmark. Now

the science chamber vacuum is routinely 30 nA on the ion pump current, which correspond to about 3×10^{-11} mbar pressure.

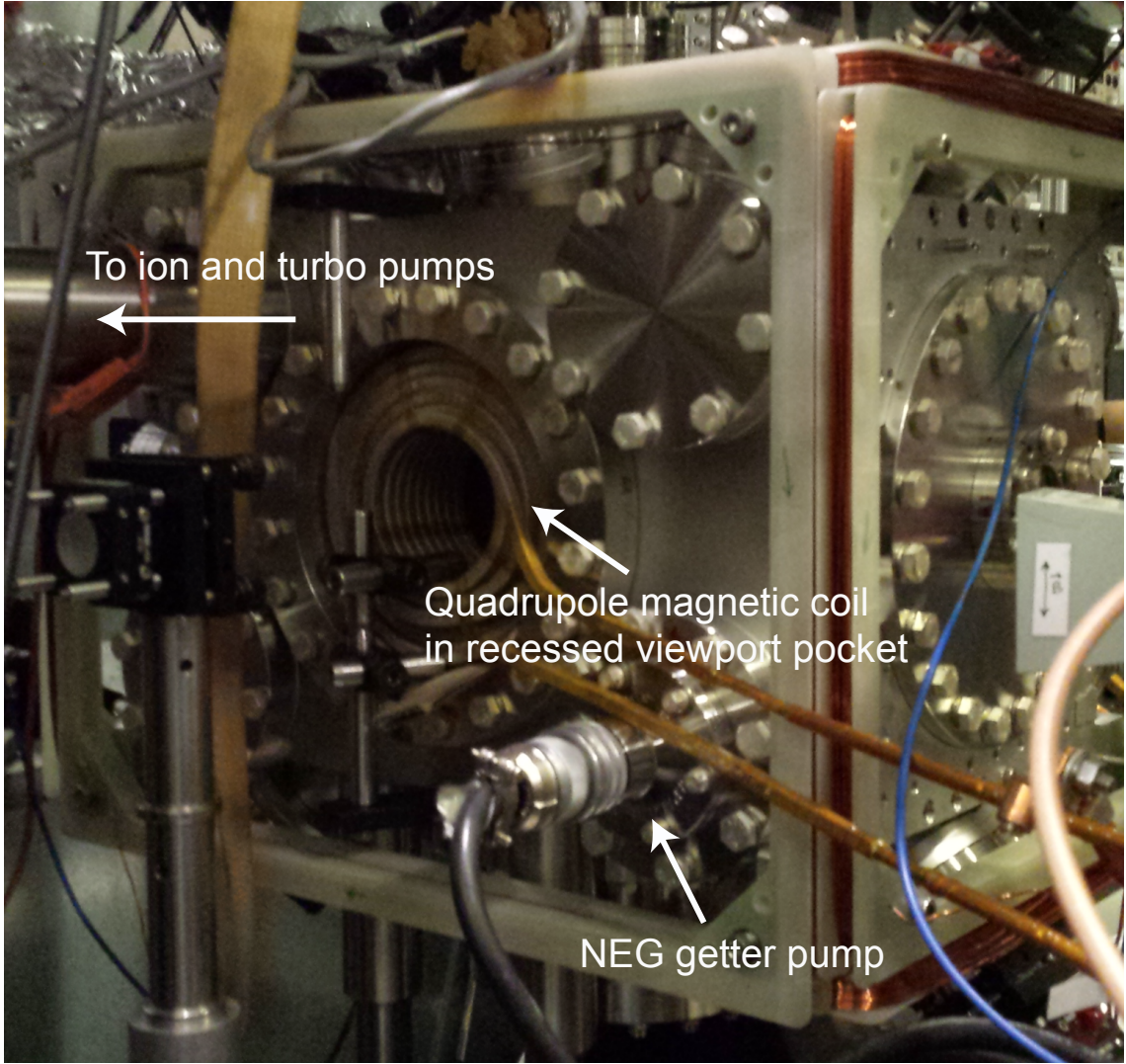


Figure 4.3: Picture of the science chamber.

The position of the ion pump is moved as far away from the science chamber as is permitted by other physical constraints, mainly the beamline stand. Adding a standard 4.5 inch CF nipple, the trap location is about 70 cm away from the exit of the ion pump flange. We can look up the magnetic field plot from the manufacturer, and the stray field created by the ion pump at the trap is about 70

mG with 1 mG/cm gradient.

Also worth noting is the roughing system, which involves a turbo pump (Pfeiffer Vacuum HiPace 80) inside of the room, backed up by a scroll pump outside of the laser room in ISAC hall. Since we have already employed the science chamber for the last beamtime, the entire system has been exposed to radioactivity, and must only pump through this turbo assembly.

Viewports

Standard off-the-shelf UHV viewports usually possess magnetism from the glass-to-metal seal, in addition to that from the 304 SS flange material. A commonly used material for the “sleeve” joining to the glass is Kovar, which has a thermal expansion coefficient matching well with that of 7056 glass. We cannot afford this, given the careful choices for the chamber itself. The laser viewports we purchased are constructed from 316 LN flanges with 316 L sleeves, sealed to optical quality (20/10 scratch/dig) fused quartz glass. Anti-reflection coating covering 500 nm to 1100 nm is applied to all the surfaces. MPFPI have manufactured all the 2.75 inch CF viewports, total quantity 22, 16 of which are attached to the science chamber and 4 attached to the middle Kimball cube. We also have two 8 inch CF re-entrant viewports from the same company⁴. These viewports, especially the glass to metal seal parts, are closest to the atoms, and can be replaced by more non-magnetic versions later on if it is experimentally established to be necessary. The 2.75 inch

⁴Several groups in the ultracold atom community uses re-entrant viewports from another company UKAEA special techniques group, who has a special technique of diffusion bonding that can be applied to a wide range of materials, and can potentially have better non-magnetic constructions. The price is however steep, and we have obtained quotes for a stainless steel construction for the 8 inch re-entrant viewports (with inconel tube and 316 LN flanges) at more than two times the price of that from MPFPI.

CF viewports on the other hand, are sufficiently far away. We measured 10 mG stray field at less than 1 inch away from these viewports, and estimate less than 10 μ G at the trap center.

4.3.2 Peripherals

Quadrupole magnetic field coils

The quadrupole magnetic field for the MOT, are produced by a pair of water-cooled coils recessing into the chamber body. The wire has a 0.23 inch square cross-section and hollow core in the center, where cooling water from a standard laser chiller (ThermoTek T225P) runs through. The material come from old stock from TRIUMF magnetic wires, and already glass-fiber cover to provide the insulation. We find the winding process to be a bit more challenging than the 0.16 inch cross-section wires commonly used for e.g. Zeeman-slowers in the JQI. The stiffness requires higher torques during the winding and better clamping while the epoxy holding the coil together is curing.

Bias magnetic field coils

The bias magnetic field coils are winded on forms machined out of G10. A cross-section of 0.375 inch square allows about 100 turns for every form, which given the separation of 12 inch between the opposite ones forming a pair, yields about 10 Gauss of magnetic field generated with 6 A of current. Due to the G10 material hardness and temperature tolerance, these coil assembly can withstand baking of up to 180 °C without the need of removing them from the science chamber (see Fig. 4.4

for details of the assembly). We rely on the machining precision of the science chamber and the coil holder, for the orthogonality of the bias field directions.

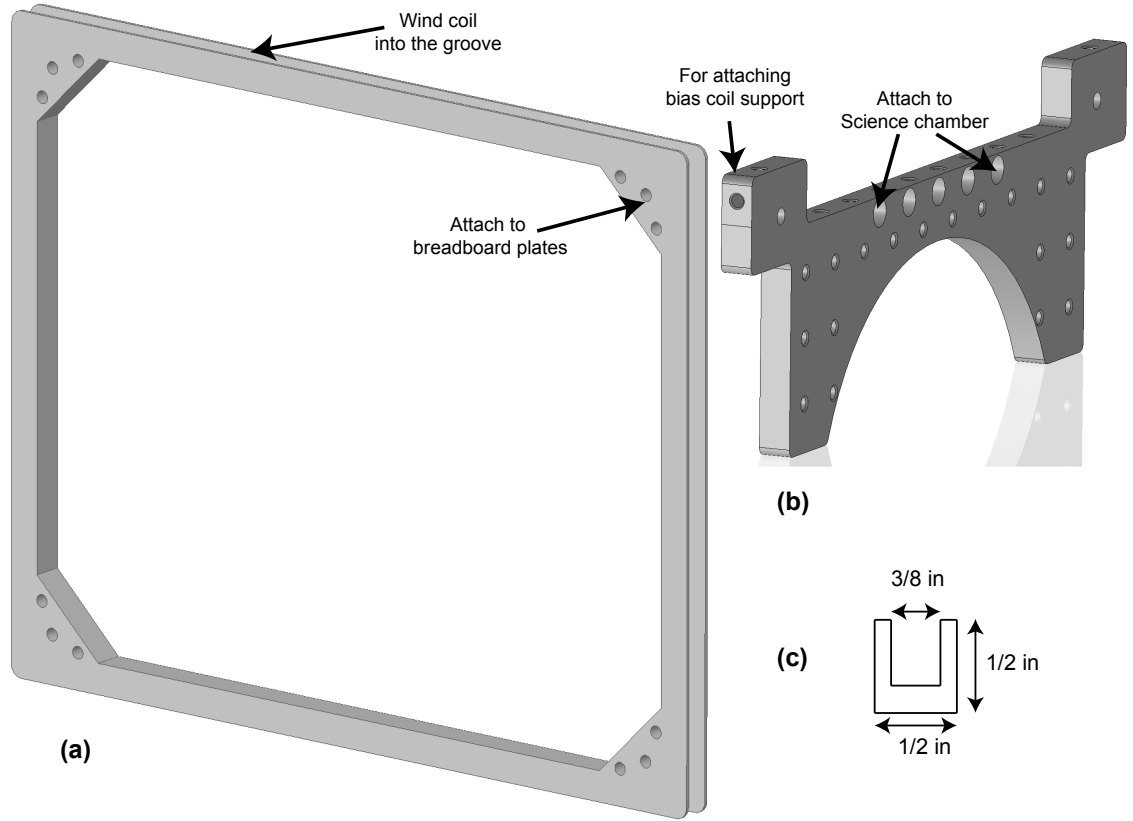


Figure 4.4: Peripheral for the science chamber: Bias coil support. (a) coil winding support made out of G10. (b) Aluminum plate used for attaching the coil forms to the science chamber, as well as providing flexible mounting solutions for optics.

Support system

The designed optics platform is a large (36 inch square) piece of stone-epoxy mixture molded board manufactured by a company named Castinite⁵. A non-metal construction with only brass screw-inserts for mounting optical components, has the advantage that it introduces zero magnetism or eddy current. Standard 12 inches by 18 inches breadboards can fit to either of the four sides in the horizontal plane,

⁵www.castinite.com

which also makes a convenient height for posts, since the castinite surface is designed to be flush with the bottom of the four major 8 inch CF flanges.

We encountered an issue trying to install this breadboard with the science chamber: the Gamma ion pump HV cable is protruding below and interferes with the platform. We have inquired to Gamma Vacuum and they do not carry an angled T for the particular HV connector used. We resorted to machining a 1.5 inches diameter hole into the platform. It is currently sitting in ISAC hall waiting to be installed during the next vacuum opening, as topologically it is a bit non-trivial to maneuver during the installation (see Fig. 4.5 for the conceptual assembly of the sice chamber with the Castinite).

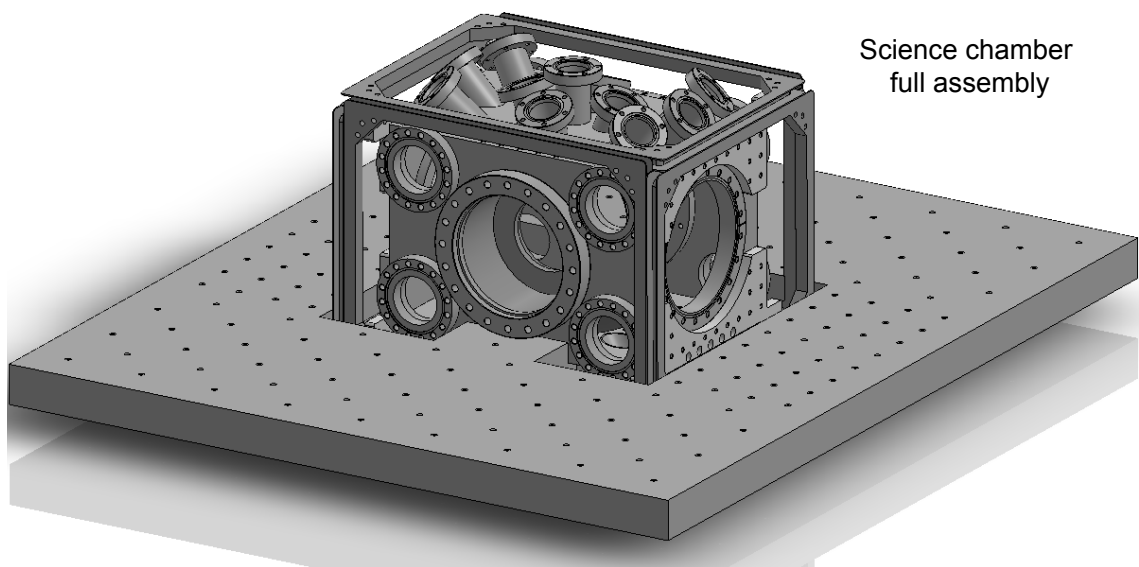


Figure 4.5: Science chamber full assembly with peripherals.

Main imaging system

The imaging system is currently along the vertical direction, entering into the volume of the science chamber though another re-entrant viewport from the bottom.

This design ensures the highest numerical aperture that is conveniently achievable, for high efficiency photon collection. Figure 4.6 shows a schematic of the imaging system, which is a double relay system with front-end collection optics consisting of 2 inch diameter $f = 10$ cm achromatic lenses. An $f - 2f - f$ system refocuses the fluorescent light from the atom cloud, which is to a good approximation a point source, to a focal plane where we place a graduated aperture. The science chamber design is excellent for reducing light-scattering, due to the tube portion for the 2.75 inch ports and the recess for the horizontal axis. However the background light from the trap laser beams is still visible in the imaging system. Closing the aperture greatly reduces this background. The light is then collimated again, where we have chosen a 1 inch diameter achromatic doublet lens with 3 cm focal length, for reducing the overall length of the system. We split the collimated light with a polarizing beam splitter, before re-focusing into the CCD camera (model FL3-GE-03S1M-C) and the Photo-multiplier tube (Hamamatsu H7422-50), on the two branches respectively. A PBS is used instead of a non-polarizing beam splitter, for extinguishing the (also polarized) push beam from the top on the PMT branch. A tiny portion of this push beam can already trip the PMT, i.e. produce too much photo-current such that the protection circuit shuts the PMT off.

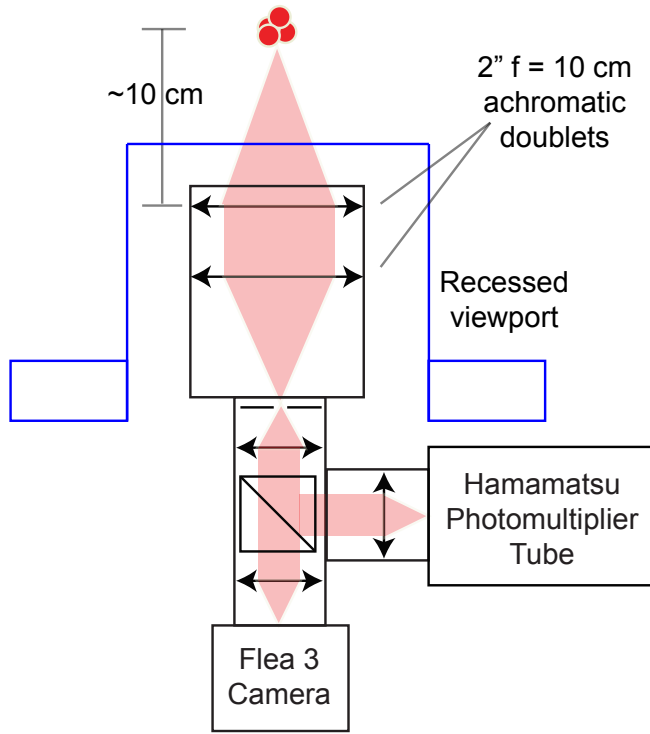


Figure 4.6: Schematic for the main imaging system.

Auxiliary imaging system

The auxiliary imaging system serves diagnostic purposes, especially for measuring the atom transfer efficiency. Figure 4.7 shows the system on the science chamber. We have two identical systems, cameras (Point Grey Flea 3) and imaging systems, built just with one Thorlabs 7.5 cm achromatic doublet each for simplicity, housed in lens tubes. We adopt standard designs from the JQI, and have the opto-mechanics assembled from 30 mm cage system from Thorlabs for mounting directly onto the 2.75 inch CF flanges of the science chamber.

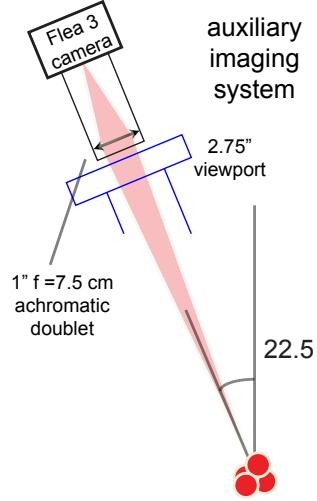


Figure 4.7: Auxiliary imaging system.

4.4 Laser optics layout

Incorporating ^{87}Rb and several francium isotopes including ^{210}Fr in the same experimental setup, also presents a design challenge. Optical fibers deliver all the laser lights to the traps. The laser arrangement then must have the right frequency detunings and intensities prior to launching into the fibers. Figure 4.8 shows the level diagram addressed by various branches of the trapping laser.

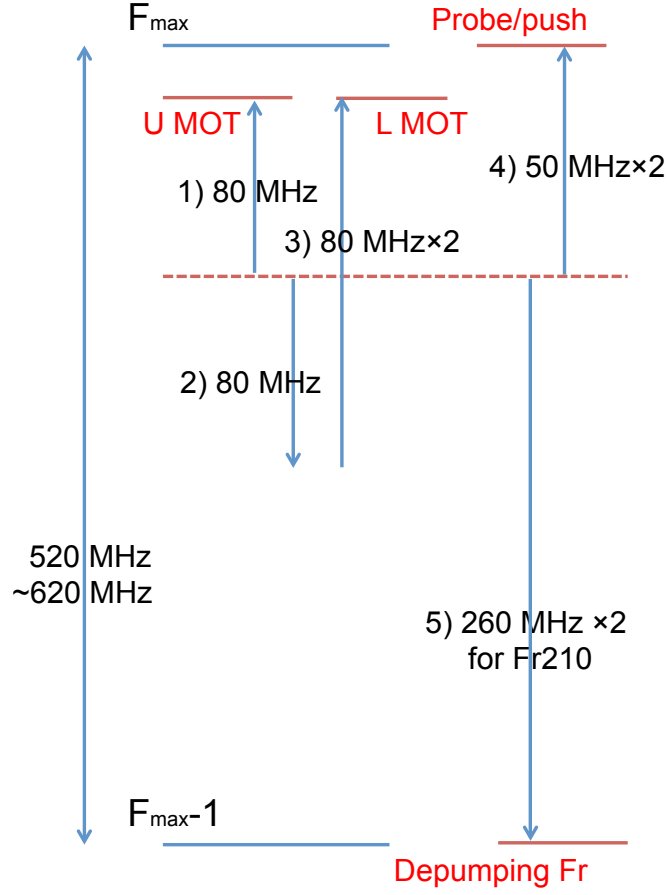


Figure 4.8: Trap laser branches addressing different purposes for the two MOTs.

The trap laser optics design allows partial independent control of laser delivery to the two traps: power is essentially re-distributed between them, for enabling either one to have maximum intensity possible. The maximum optical power deliverable for the two traps, are about 1.5 W and 400 mW respectively, the science chamber trap being lower because the laser beam goes through many more optical components. Their intensities are roughly the same, because of the 1 inch optics used as compared to the 2 inch optics design for the capture trap. Figure 4.9 shows the final optical arrangement that distributes the trap laser optics to the two chambers.

Trap laser optics layout

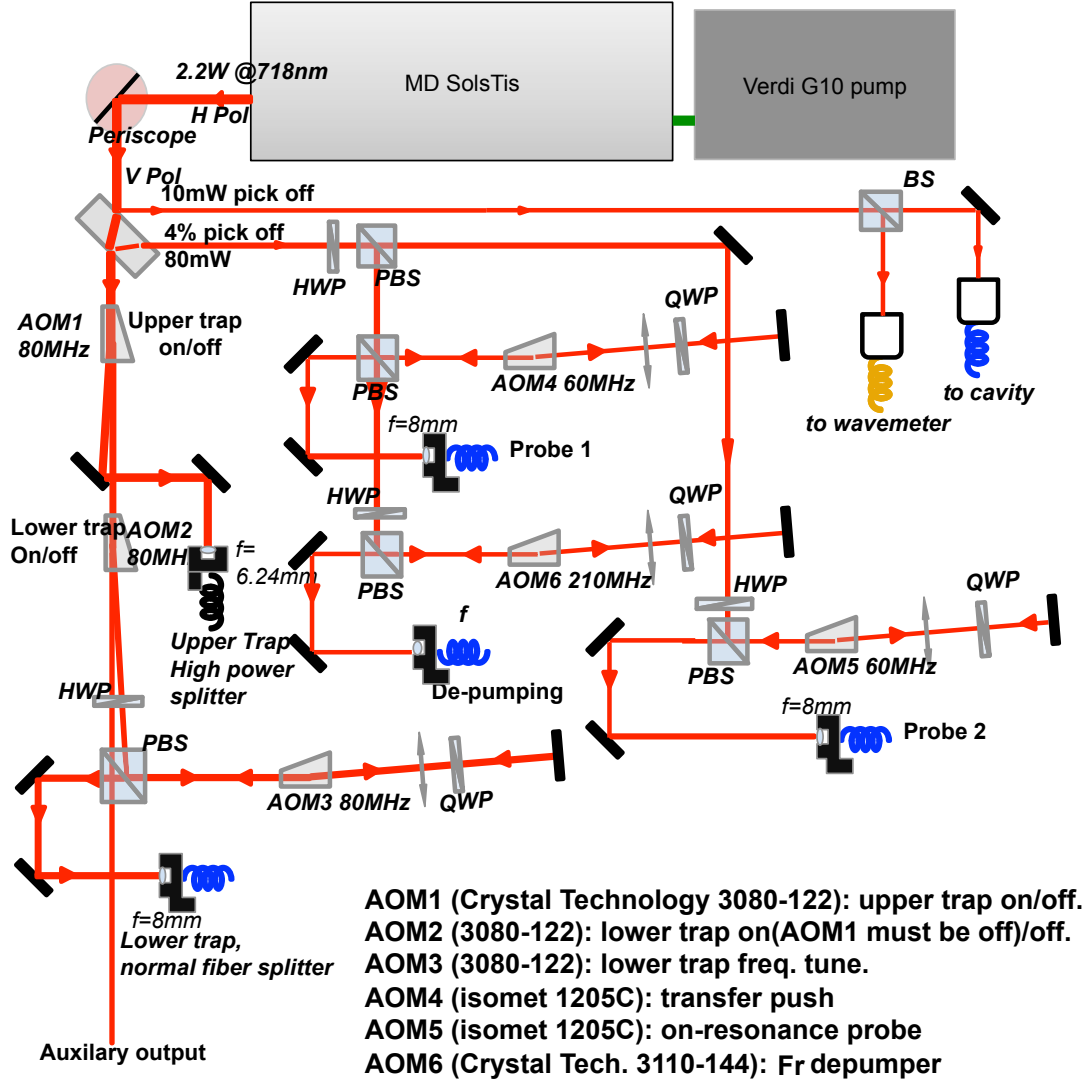


Figure 4.9: Schematic trap laser layout on the optics table.

4.5 Experimental control hardware and software.

Figure 4.10 shows a simplified schematic for the experimental control and data-acquisition system. The time-sequencing system (left side in Fig. 4.10) follows the architecture and utilizes the software developed in Trey Porto and Ian Spielman

groups at the JQI. We have however completely upgraded our hardware to a PXI based system, which does not require that the control computer have multiple PCI slots. We use either a pulse-blaster card or a National Instrument FPGA (PXI-7815R) to provide precise timing triggers and all digital signals. We have a 64 channel analog output card (Marvin Test GX1649) to provide all analog signals needed for AOMs, magnetic field control, etc. The control software uses exactly the same interface as the JQI versions, though the hardware interfaces codes have been heavily modified, thanks to the hard work by Michael Tandecki. We also added a “loop scan” function, which allows us to sweep a parameter, e.g. microwave frequency, well suited for spectroscopy experiments.

The data-acquisition system (right side in Fig. 4.10) either obtains images from cameras, or count photons from PMTs into multichannel scalers. Figure 4.10 shows both the control software interface (upper left), and the MCS software interface (upper right).

4.6 Atom transfer.

Atom transfer is a commonly encountered issue in ultracold atom research, with experimental solutions ranging from magnetic transfer [66], moving optical dipole traps or lattices [67, 68], or by direct pushing with an on-resonance laser light [69, 70], etc. We have followed the third approach because of the simplicity, and transfer the atoms vertically downwards with a push laser pulse close to the $D2$ resonance.

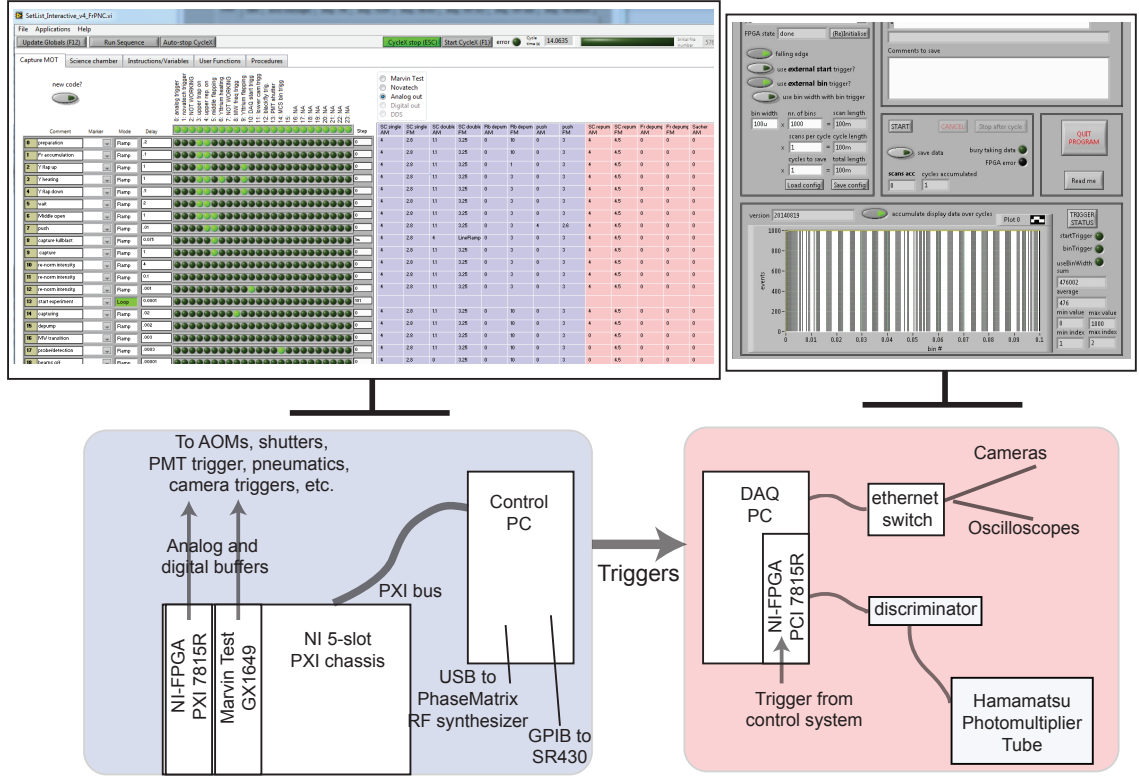


Figure 4.10: Experimental control and data-acquisition system. The screenshots can be seen when zooming in with the electronic version of this file. The sequencing system (left) sends digital triggers to various devices such as analog output cards, photomultiplier tubes, and cameras. The data acquisition system consists of cameras.

The science chamber has Rb dispensers for laser-trapping tests independent of the transfer. This allows us to optimize the optics and the magnetic fields, and ready to receive the atoms from the capture trap. Our starting point is an on-resonance probe beam with 2 mW of laser power and 2 ms pulse duration, quadrupole field of the capture trap is left on. Figure 4.11 illustrates a typical overall sequence, starting from the capture and transfer stages, which takes about 1.5 seconds each. The top and bottom vacuum systems have direct line of sight connection for less

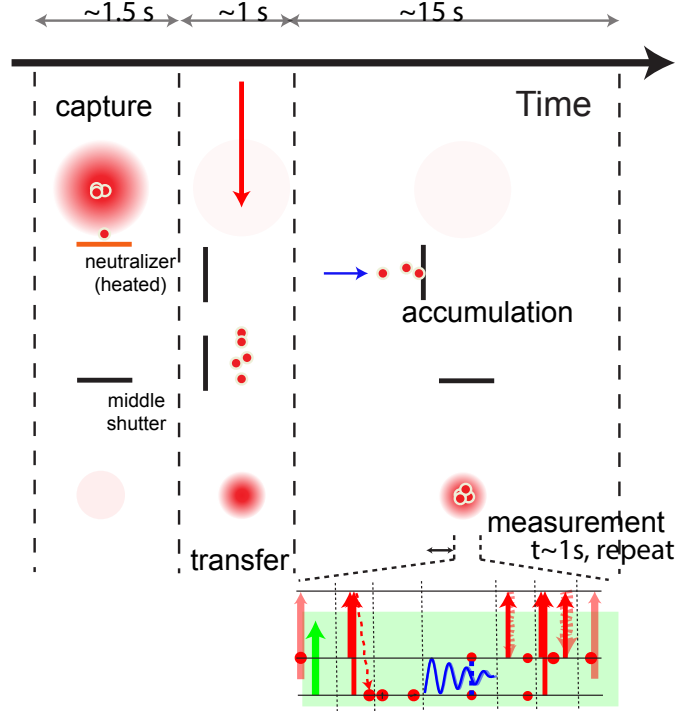


Figure 4.11: Timing sequence for atom capture and transfer into the science chamber. The physical travel of the two mechanical parts, i.e. the neutralizer holder and the (middle) mechanical shutter, sets the timescale of the heating/releasing and transferring steps at the 1.5 s level.

than 10% of the time during when the middle shutter is opened. The laser push pulse duration is at the sub 10 ms timescale, and repetitive measurement can start immediately after the atoms are transferred to the second MOT. The actual laser interaction time, e.g. the trapping of released Fr atoms, or the push/transfer beam, have timescales of the order of 10 ms or less. While PNC experiments are being performed (repetitively with the same atomic sample) in the science chamber, the atomic ions from the accelerator keep implanting and accumulating in the neutralizer foil. Typical duration for this (overall) measurement step can be up to 15 s or the limit of trap lifetime due to either radioactive decay or vacuum background gas

collisions.

The cameras and imaging systems are identical, however the fluorescence intensities do not directly reflect the relative atom numbers, mainly because the trapping beams have different intensities, which is taken into account for the estimation of the 10% efficiency. Figure 4.10 shows the picture on the capture trap (top) and the picture of the transferred Fr atoms on the science trap (bottom). The diagonal size of the sensor is 1/4 inch, as is indicated in the left picture, serves as a reference lengthscale. The false color can be very deceptive as well, as these pictures are taken independently, normally with automatic color scales, which might not be the same for the two.

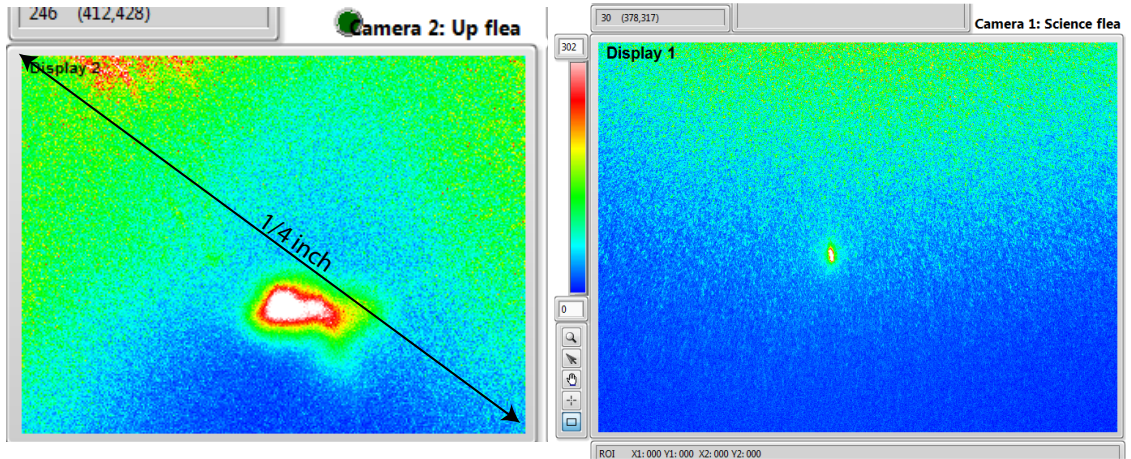


Figure 4.12: Picture of francium atoms in the capture trap (left) and transferred into the science chamber (right).

We have demonstrated transfer of Rb atoms with about the same efficiency as was achieved at UMD, i.e. around 50%. The Fr transfer efficiency however has not reached the same level so far. Figure 4.12 shows the Fr atoms in the capture

and the science chamber MOT. During the beamtime in December 2014, we tried the francium transfer as soon as both the accelerator side and our laser trap side were ready⁶, and immediately observed a small but bright transferred francium atom cloud in the science chamber MOT. We made some measurements of the laser intensities, and estimate 10% transfer efficiency for the francium. Because of the failure of the neutralizer foil shortly after this quick success, there was no time to optimize anything. One example is the push laser intensity, which only had 600 μW power before fiber coupling due to the optics chain not being broadband for covering Rb at 780 nm and Fr at 718 nm without touching, and they were not tuned to best condition. We believe this transfer efficiency could be increased by at least a factor of 5.

⁶Which took about 8 hours of tuning, as is typical for past beam times.

Chapter 5: Precision spectroscopy of the francium $D1$ line.

Immediately after our successful demonstration of the high-efficiency francium capture trap, we started physics measurements from November of 2012. We had two experimental runs each lasting about 4 days (10 shifts), and finished the measurements in late 2013. We perform precision spectroscopy on the 817 nm $D1$ line along a chain of francium isotopes. We have developed an efficient spectroscopy technique based on rapid scanning of RF modulated laser sidebands, ideally suited for our francium atom trap in pulsed-mode operation. This method has enabled data-acquisition with good signal-to-noise ratio after only a few seconds. These measurements are precise enough to reveal two finite nuclear size correction effects, namely the hyperfine anomaly and the isotope shift, respectively. Our results serve as nice benchmarks for state-of-the-art atomic theory, as well as future many-body nuclear structure calculations, which are prerequisites for interpreting future PNC experiments in Fr. We present detailed descriptions of the experimental techniques, an empirical theoretical treatment with emphasis on the nuclear structure, and discuss further implications to our proposed PNC experiments. At the end of the chapter is a copy of the paper under review based on hyperfine measurements and the published one on isotope shifts. I have lead the analysis of the hyperfine mea-

surements and will focus my discussion on that. The isotope shift analysis was lead by Robert Collister, and the article is included for completeness. Again we recommend the reader to look at the papers first and then proceed to read the chapter as complementary information. We start by an overview of the physical origin of these two effects, arising from the finite nuclear size corrections.

5.1 Physics case: finite nuclear size corrections.

Let us first consider the hyperfine interaction for electronic states with $J = 1/2$. The lowest order hyperfine splitting Hamiltonian can be written in a simple form:

$$H_{\text{hfs}} = A_{\text{hfs}} \mathbf{I} \cdot \mathbf{J}, \quad (5.1)$$

where A_{hfs} is the magnetic dipole constant, \mathbf{I} and \mathbf{J} are the nuclear and electronic spins. For the $7S_{1/2}$ and $7P_{1/2}$ states concerned in this chapter, the hyperfine Hamiltonian can be regarded as the interaction between the magnetic dipole moment of the nucleus and the (inhomogeneous) magnetic field created by the electron orbiting around it. A point-like magnetic dipole is in most cases a fairly good approximation, however precise measurements reveal the effect from the finite spatial extent of the nuclear wavefunction. The effect arising from the finite magnetization distribution, referred to as the hyperfine anomaly (HFA) or the Bohr-Weisskopf (BW) effect [71], is the dominating term when we compare between different isotopes. We measure the $D1$ line hyperfine splittings to extract information about this contact field effect, i.e. happening when the electronic wavefunction penetrates into the nucleus.

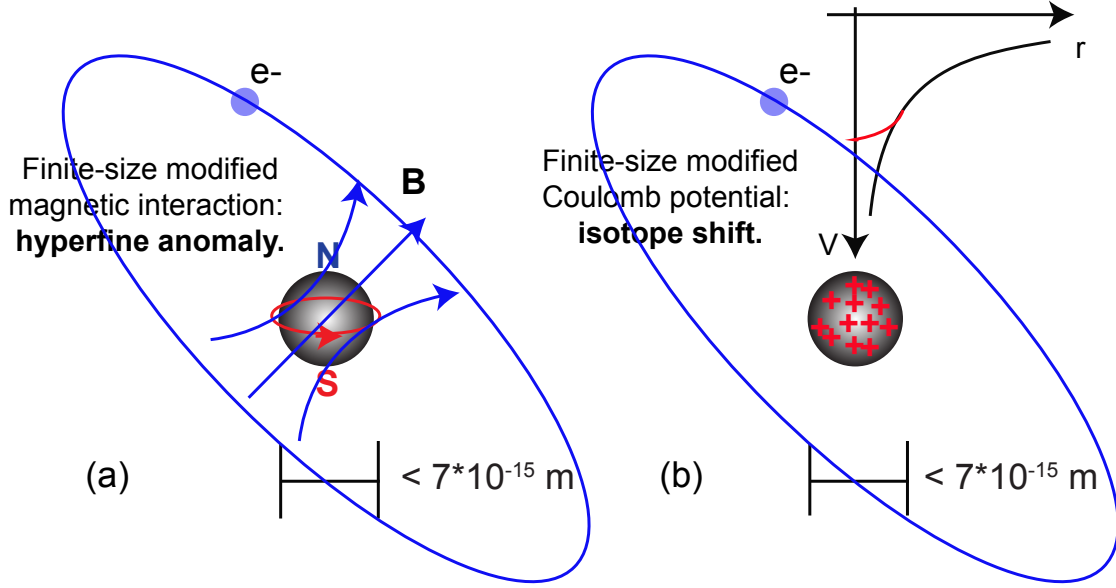


Figure 5.1: Physical origins of hyperfine anomaly and isotope shift. Both effects arise due to a finite nuclear size correction. The hyperfine anomaly is dominated by the spatial extent of proton and neutron wavefunctions, whereas the isotope shift originates from the collective nuclear charge distribution.

Fig. 5.1 (a) illustrates the HFA, dominated by the valence nucleons since the rest of the nucleons are paired up and does not contribute to the magnetism.

The isotope shift (IS) arises from a different finite size effect: the spatial extent nuclear charge distribution¹. Figure 5.1 (b) illustrates this correction, which is a collective effect, where all the protons contribute. Note that in both the HFA and IS we can only compare between isotopes, i.e. the changes in these finite size corrections.

¹There is also contribution from the mass shift.

5.2 Measurement techniques and systematic effects

We probe these physical effects by laser spectroscopy of the $D1$ in the MOT. We use a rapid-scanning spectroscopy method which probes and recaptures the same atom ensemble from a single heating pulse for many times. This method, first proposed by Eduardo Gomez, has lots of advantages such as recycling the limited supply of radioactive atom source, and circumventing systematic drifts of the atom number and laser frequency. We focus on the measurement techniques and systematic effects in this section, especially on the hyperfine anomaly experiment. The isotope shift measurement method is a nice extension with lower measurement precision, which we will integrate into the discussion. Variations of this rapid-scanning technique could potentially be applied in our planned optical APNC experiment, where long atomic coherence time is not necessary.

5.2.1 Rapid-scanning spectroscopy.

The scarcity of available francium atoms, and the pulsed nature of our capture trap, means that we only have one sample of million atoms every 20 s or so. Scanning rapidly enables efficient use of this sample by recycling the atoms after a spectroscopy cycle. We also eliminate effects from the time varying (exponentially decaying) atom number. We perform a single scan in 10 ms, on the RF signals applied to fiber electro-optical modulator (EOM), with the sidebands covering a frequency range of 140 MHz.

Figure 5.2 shows the experimental setup schematics, in particular the RF

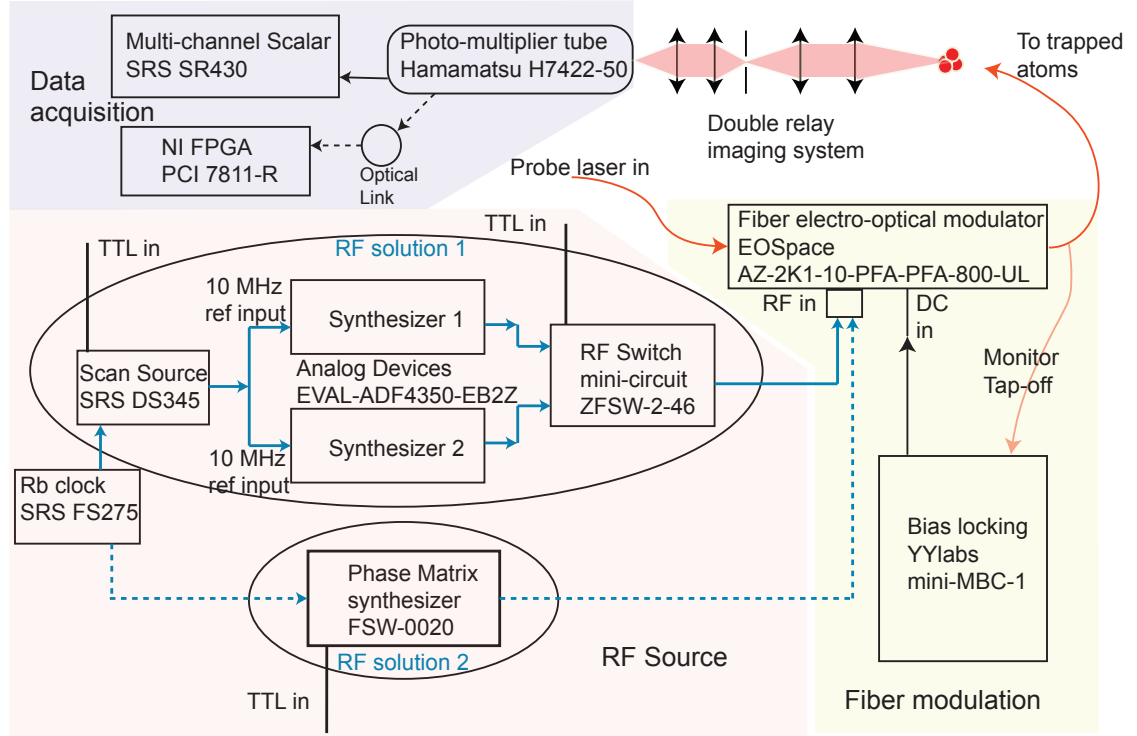


Figure 5.2: Schematic of experimental setup, divided into three sections besides the atom trap: RF synthesis system, fiber modulation, and data acquisition. Blue lines represent RF signals, typically of the order of 3 GHz, i.e. about half of the $7P_{1/2}$ splittings. Red curvy lines indicate fiber coupled probe laser light. Black lines are digital and analog signals used for controlling the instruments and acquiring data. Dashed lines represent alternative (later) solutions that we only implemented in the runs in the fall of 2013.

synthesis highlighted on the left bottom. We have used two RF frequency synthesis methods, the first one is based on Analog Devices (AD) ADF4350 evaluation boards (EVAL-ADF4350-EB2Z), and the second one relies on a commercial frequency synthesizer (PhaseMatrix FSW0020). The AD scanning relies on feeding the Phase Locked Loop (PLL) inputs of two AD cards with scanning signal from a Stanford Research Systems DS345 synthesizer sweeping over 5% of the range around 10 MHz. For example in ^{207}Fr we scan the DS345 from 9.76 MHz to 10.24 MHz in 10 ms. The DS345 synthesizer is in turn referenced to a Rb clock (Stanford Research Systems FS275). We used two AD cards at different frequencies (higher or lower than 10 MHz input) in switching mode, because of the limited scanning range of a single card (70 MHz). This synthesis chain was our only solution before we acquired the commercial synthesizer from PhaseMatrix in 2013. This synthesizer could only do 100 μs steps, so we have to scan about 1MHz per step to achieve the same speed. Some data from this shows step-like shape.

We collect the light into a double relay imaging system, and count the fluorescence photons with a photomultiplier tube module (PMT, Hamamatsu H7422-50) optimized for infrared sensitivity. The data is acquired by a multichannel scaler (MCS), which gives the number of counts per timing-bin (typically 640 ns). The MCS also had two different versions. In the November of 2012 we borrowed a Stanford Research Systems SR430 from JQI. Later we returned it to Maryland and developed our own MCS solution with a National Instrument FPGA card (NI PCI-7811R). The SR430 has a built-in discriminator, which we can set the level just with front panel operation. The FPGA chain employs a photon counting unit (Hama-

matsu C9744), which converts the millivolts PMT output into TTL signal. This is in turn sent to the FPGA via an optical link, which separates the grounds between the PMT side and computer side.

Figure 5.3 shows the experimental sequence and the data-accumulation. We use a “trap chop” method to eliminate the ac Stark shift from the trap laser itself. This also serves as a reference for evaluating this shift from other lasers, which we will detail in the next section. We typically accumulate 600 scans (6 seconds) to achieve good signal to noise ratio, ranging from above 20 for more abundant isotopes such as ^{209}Fr or ^{213}Fr , to about 5 in more scarce isotopes such as ^{206g}Fr and $^{206m1}\text{Fr}$, the ground and isomeric states that we are able to trap for this isotope. One clear distinction between our fast RF scanning method with the method used in Ref. [72,73], is that the laser frequency drift becomes a common mode effect. We eliminate the need for scanning the laser carrier frequency and repeating the scan at different RF sideband frequency as reported in Ref. [72]. The previous Fr HFA measurement also suffered from background scattered light from the laser central carrier, which for a glass cell without AR coating can be quite prominent. Cascaded free-space electro-optical amplitude modulators were used for turning the probe laser off [73]. Our fiber electro-optical modulator provides intensity modulation with a Mach-Zender interferometer configuration, with one arm phase-modulated and one arm unaffected. The offset point is controlled by a DC bias voltage and is sensitive to temperature and other environmental changes. This poses a serious disadvantage that the scattering background will not only be present, but also slowly-varying with time. We solve this with a bias controller (YYlabs mini-MBC-1). A small tap-off is

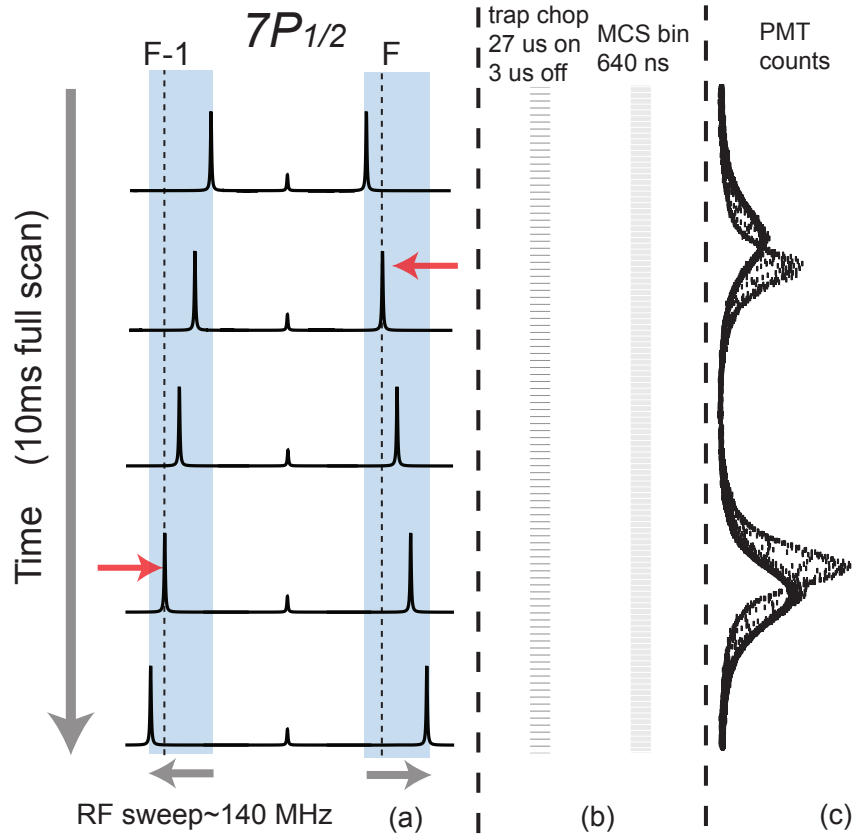


Figure 5.3: Scanning the RF over 140MHz is addresses the upper/lower hyperfine level with the \pm sideband from the fiber EOM. Data is collected regardless of whether the trapping laser is on or off, while the “trap chopping” is repeated every 30 μ s with 10% duty cycle. Each entire scan takes only 10 ms, and a typical data of 600 scans accumulated is shown under the “PMT counts” column. With the MCS bin width of 640 ns, the histogram has superb smoothness. Red arrows indicate when resonance fluorescence occur, which manifests as two peaks with overlay. They are with trap laser and off respectively, visualizing the ac Stark effect. And the opposite displacement comparing the two hyperfine peaks, is a direct result from the opposite directions of the RF sideband scans, reflecting the ac Stark shift being a common mode effect.

sent to a monitoring photodiode on the bias controller board, which in turn provides a DC signal with kHz dithering and PID feedback, locking the fiber modulator at the null point of the amplitude modulation.

The isotope shift measurement is a nice extension of the above described experimental technique. Fortuitously the IS values lie close by the 3 GHz value of our RF sidebands. We change the RF frequency range to near the expected location, keep the laser locked with the He-Ne referenced cavity, and wait for the ISAC operators to switch the isotopes for us. This switching usually takes 30 minutes. Reference [74] contains more experimental details.

5.2.2 Systematic errors

We now discuss the various systematic effects and evaluation of their uncertainties.

Magnetic field: the dominating systematic effect

The linear Zeeman shift is our main source of systematic uncertainty. We leave the quadrupole magnetic field on during the scans, and the atoms trapped in the MOT are (unevenly) distributed among all Zeeman sub-levels, which we can not resolve in our laser spectroscopy. If the atom cloud is positioned well at the null of the quadrupole field, and the atoms have equal populations contributing positive and negative shifts, the Zeeman effect should vanish when we probe with a linearly polarized laser. Real-life situation is complicated by the imperfect alignment and the messy optical pumping processes in the MOT. We put an upper bound on the

Zeeman systematic uncertainty by measuring the hyperfine separations after changing various parameters, such as the polarization of the probe beam, the magnetic field gradient, or displacing the position of the atoms either by changing the power of the probe, by removing the retro-reflected probe beam or by inserting a thick piece of glass in one of the trap arms to imbalance it. We have combinations of different tests in both Fr and Rb.

We apply a current to the quadrupole field ranging from 40 A to 70 A, corresponding to magnetic field gradient on the strong axis of 10 G/cm to 17.5 G/cm. For Fr the location of a single peak can shift as much as 1.2 MHz, however the HFS varies within a 400 kHz range with no clear dependency with the applied current.

The probe laser can push the atom cloud position through the photon recoil force, into a slightly different magnetic field environment. During the data-acquisition we have the probe laser retro-reflected. The characterizations with Rb exaggerate this effect by increasing the probe laser power (kept lower than 200 μ W during actual scans) by at least a factor of two, which introduced a trap displacement between 0.6 mm to 0.8 mm. Such displacements would maximally introduce 1.1 MHz shift at 10 G/cm gradient for a fully stretched state, and we see no clear variations at the 500 kHz level.

We measure the HFS changes by altering the probe laser polarization with a 780 nm zero-order quarter-wave plate. We observe a 800 kHz change switching from π (linear) to σ^+ , while the change is less than 200 kHz between π and σ^- .

probe beams². Similar effects in Fr show up with the upper limit between the 370 kHz to 500 kHz, depending on the isotope. We conservatively estimate the final Zeeman uncertainty for Fr, by using the 800 kHz limit, multiplied by the largest uncertainty in the laser probe polarization. This determined (unfortunately) by the lost of record of the exact wave-plate mounting orientation during the first Fr run. The rotation mount could be $\pm 10^\circ$ away from the desired angle, and we obtain 540 kHz maximum uncertainty due to the linear-Zeeman effect.

Differential ac Stark shift

The trap laser connects to the upper hyperfine level of the ground state, which is also where the probe laser excites the atoms from. This introduces an ac Stark shift for $D1$ line frequency, as well as line-broadening. Figure 5.4 illustrates these effects. The observed shift is 5 MHz, and we calculate 3.6 MHz from the scalar lightshift for our typical trap laser intensities. The line is broadened from 10 MHz with the trap laser off, to 14 MHz with the trap laser on. The scalar shifts for two hyperfine levels cancel out, however we observe a residual $250 \text{ kHz} \pm 100 \text{ kHz}$ differential shift. This can be explained by considering the two $7P_{1/2}$ hyperfine levels have different Zeeman manifolds, which experiences different vector lightshifts. Note that both the scalar and vector lightshifts from the trap laser vanish since we only analyze our data from when it is turned off³. We in turn use these numbers to estimate the ac Stark shift from other light sources, i.e. the repumper laser and

²The atoms in a MOT do not have a well defined magnetization axis, and we refer the polarization to the probe laser propagation direction.

³We obtain a “chopping filter” by recording the trap laser scattering from the glass cell when no Fr MOT is present. This provides the criteria for our data-filtering. The on/off extinction ratio is better than 0.5%.

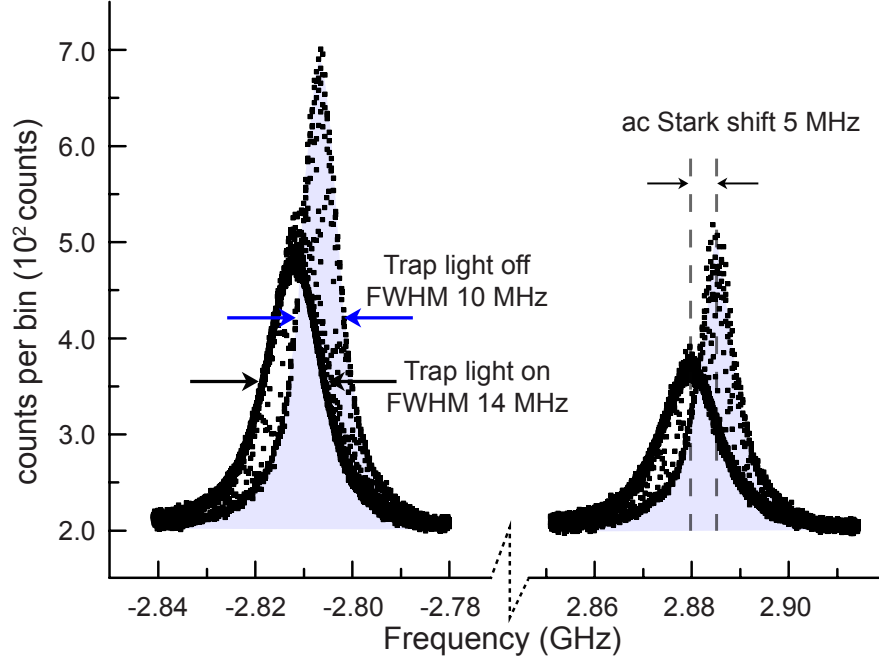


Figure 5.4: Sample data showing the AC Stark shifts while we chop the trapping laser light. The thicker and broader lines to the left (~ 14 MHz full width half maximum (FWHM)) are when the trap light is on, and the ones to the right (10 MHz FWHM) are when the trap light is off.

the probe laser. The Fr repumper on the $D2$ line is 45 GHz away from the upper hyperfine level, and adds an negligible effect. The probe laser carrier is about 3 GHz from either of the two $7P_{1/2}$ levels, and will introduce < 50 kHz shift when not suppressed. The fiber-modulator lock suppression renders this negligible.

One non-negligible source of ac Stark shift, is from the presence of the other laser sideband. We lock the laser carrier at about 30 MHz to 40 MHz away from the center, so that the split of the two peaks is about 70 MHz. When one sideband is on resonance with one $7P_{1/2}$ hyperfine level, the other sideband is always affecting the ground $7S_{1/2}$ state, due to its tens of MHz proximity to the other hyperfine $D1$ line. This is the main contribution to our final ac Stark effect, and we obtain a

correction of 90 kHz and an uncertainty of ± 60 kHz.

Background and line-shape distortions.

We observed some backgrounds on the MCS photon counts, that exist even when there are no trapped atoms. We only found during the September 2013 beam time that it is because the AC cards output power is not flat. This translates directly into the laser power in the two sidebands, and appears in the PMT counts due to residual light scatterings from the glass cell. In addition to this, when the fiber-modulator carrier suppression performance is drifting over time, we have a time-varying background that changes at the 30 min time-scale⁴. We record the background without trapped atoms immediately after we take the data, and analyze the effect from it. Figure 5.5 shows a scan with an uneven slope (top) and the background itself (bottom). We fit the data with either a Lorentzian profile, or with a polynomial profile addition. We fit the background with a polynomial function and compare to the fit parameters from the data with the peak. The shift of the line center is 100 kHz, with variations at our statistical uncertainty level.

Besides the background which has no correlation with the peak locations, we also have line-shape distortions that shows up as a residual structure, barely visible in Fig. 2 of the attached hyperfine anomaly article Ref. [75]. The asymmetric residual is much more evident if we add multiple data sets together, while each data set contains 600 scans accumulated over 6 seconds. We tried multiple data-fitting models that adds asymmetric parameters to the Lorentzian function, including a

⁴These effects were removed later in 2013, by an improved fiber-modulator locking and scanning with the PhaseMatrix synthesizer.

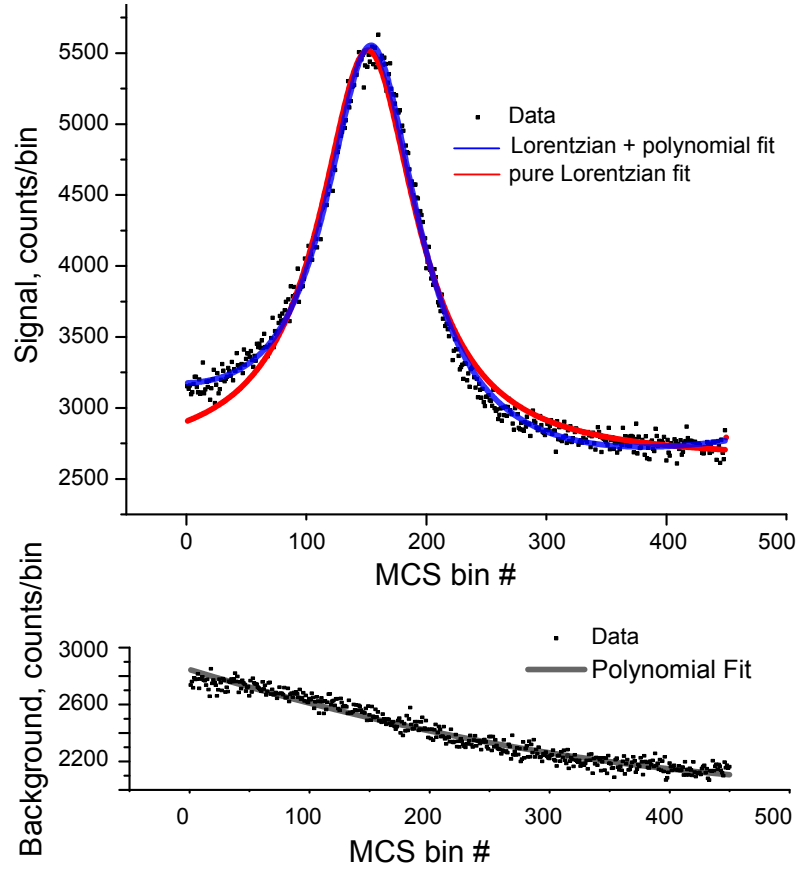


Figure 5.5: Lorentzian fits with and without subtraction of background, and a polynomial model of the background, which originates from residual scattered laser light and RF scan power variations.

Fano-type model [76], and a sigmoidal asymmetric model [77]. They do not remove the residual structure that is seen in Fig. 2 of Ref. [75]. The possible sources of the line-skewing includes laser frequency drifts during data-accumulation, and the previously mentioned time-varying ac Stark shift. We evaluate the total uncertainty from the line-shape deviations, including the backgrounds, to be 100 kHz.

Scan linearities, Doppler effect, etc.

We also take into account several other systematic effects that are much smaller. The RF scanning linearity is significantly better compared to a laser scanning (e.g. in Ref. [72]). We checked this by beating down the frequency with a fixed frequency RF synthesizer and looking at the time-varied signal with an oscilloscope. Fitting the sinusoidal signal at multiple time points in a scan yields a result of negligible (<100 Hz) error on the RF frequency calibration. We also compared the RF frequencies from the AD cards with that from the PhaseMatrix synthesizer operating in list trigger mode. We evaluate the Doppler effect by pushing the atom cloud with single-pass probe laser, and record the atom velocity with the CCD camera. The effect on the HFS is below 10 kHz.

Adding all the above uncertainties in quadrature, our total systematic shift uncertainty is **552 kHz**. See attached Ref. [75] for the HFS measurement results for our chain of Fr isotopes.

5.3 Hyperfine anomaly: empirical calculation and the shell model.

We use the ratios of the $7P_{1/2}$ HFS, including isotopes measured at TRIUMF [75] and those in Stony Brook [72], in conjunction with the $7S_{1/2}$ measurements primarily from ISOLDE at CERN (see Ref. [75] and therein), to extract information about the hyperfine anomaly. As outlined in Section 5.1.1, the anomaly variations between different isotopes, is dominated by the Bohr-Weisskopf effect of magnetic nature. It lies in a unique interface between atomic and nuclear physics, since the calculation of this effect involves both the wave-function of the atomic electron, and that of the proton and neutron in the nucleus. Here we employ an empirical treatment based on the calculations in Refs. [78, 79]. We are able to make reasonable predictions for the anomaly contribution from the single valence neutrons along our Fr isotopic chain. We can also qualitatively explain the behavior at the edge of our isotopic chain with a nuclear shell model picture with Nilsson deformed nucleus [80]. The calculations in the references that we use are reasonably old and the problem deserves attention and re-examination from modern state-of-the-art atomic and nuclear theories. We present our result as a sensitive probe for subtle effects arising from these contact interactions, and an open invitation for theorists to explain the hyperfine anomaly with modern tools. This section details our “theoretical” explanation, primarily intended for an atomic physics experimentalist to understand the HFA.

5.3.1 Hyperfine interaction: electronic wavefunction integrals

For the $S_{1/2}$ and $P_{1/2}$ electronic states that we are concerned with, the quadrupole moment is zero. We first write the magnetic hyperfine interaction hamiltonian:

$$H_{\text{hfs}} = -\frac{1}{c} \int \mathbf{j}_N(\mathbf{r}) \cdot \mathbf{A}(\mathbf{r}) d^3\mathbf{r}, \quad (5.2)$$

where $\mathbf{j}_N(\mathbf{r})$ denotes the nuclear current density at point \mathbf{r} in the nucleus, and $\mathbf{A}(\mathbf{r})$ is the vector potential produce by the electron at position \mathbf{r} of the nucleus:

$$\mathbf{A}(\mathbf{r}) = \frac{1}{c} \int \frac{\mathbf{j}_e(\mathbf{r}_e)}{|\mathbf{r} - \mathbf{r}_e|} d^3\mathbf{r}_e. \quad (5.3)$$

Evaluating this hamiltonian over a hyperfine state and comparing to that of a point-like magnetic distribution, we have the “fractional anomaly”, which is the parameter used to quantify the Bohr-Weisskopf effect [79]:

$$\epsilon_{\text{BW}} = \frac{\langle nJIF | H_{\text{hfs}} | nJIF \rangle}{\langle nJIF | H_{\text{hfs}}^{\text{p.d.}} | nJIF \rangle} - 1,$$

where $H_{\text{hfs}}^{\text{p.d.}}$ denotes the hyperfine hamiltonian with a point-like magnetic dipole approximation. Integrating out the spin and angular coordinates of the electron, we have

$$\epsilon_{\text{BW}} = \frac{\langle II | \int d^3\mathbf{r} (\mathbf{r} \times \mathbf{j}_N) \cdot [\int_0^r (\frac{r_e}{r})^3 (F^{nJ} \cdot G^{nJ} / r_e^2) dr_e + \int_r^\infty (F^{nJ} \cdot G^{nJ} / r_e^2) dr_e] | II \rangle}{\langle II | \int d^3\mathbf{r} (\mathbf{r} \times \mathbf{j}_N) \cdot [\int_0^\infty (F^{nJ} \cdot G^{nJ} / r_e^2) dr_e] | II \rangle} - 1 \quad (5.4)$$

where the F^{nJ} and G^{nJ} are the large and small part of the electronic Dirac wavefunction, r_e is the radial coordinate of the electron, and $|II\rangle$ is the nucleon eigenwavefunction.

Explicitly separating the electronic and nuclear operators, following the approach in Ref. [79], we have the electronic part:

$$\begin{aligned}
N(R_i) &= \frac{\int_0^{R_i} (F^{nJ} \cdot G^{nJ} / r_e^2) dr_e}{\int_0^\infty (F^{nJ} \cdot G^{nJ} / r_e^2) dr_e} \\
K(R_i) &= \frac{\int_0^{R_i} (F^{nJ} \cdot G^{nJ} / r_e^2) (r_e / R_i)^3 dr_e}{\int_0^\infty (F^{nJ} \cdot G^{nJ} / r_e^2) dr_e}, \tag{5.5}
\end{aligned}$$

where R_i is the radial coordinate of an individual nucleon; and the nuclear magnetic dipole moment defined as:

$$\mu_I = \langle II | \frac{1}{2c} \int (\mathbf{r} \times \mathbf{j}_N) d^3\mathbf{r} | II \rangle / \mu_N, \tag{5.6}$$

where μ_N denotes the nuclear magneton. Further separating the spin and angular contributions to the nucleon current, we arrive at this simplified expression derived by Bohr and Weisskopf [71]:

$$\epsilon_{\text{BW}} = -\langle N(R) \rangle \alpha_S + \langle K(R) \rangle \eta - \langle N(R) - K(R) \rangle \alpha_L, \tag{5.7}$$

where the α_S and α_L are the fractional spin and orbital contributions to the nuclear magnetic dipole moment, and η is the spin-dipole term allowing for non-spherical

contributions. As noted in Ref. [81], these three parts are analogous to the contact, orbital, and spin-dipole parameters often used to analyze the electronic part of the hyperfine structure.

The calculations of the electronic integrals in Eq. 5.5 require knowledge of the radial part of the Dirac wavefunction modified by the finite size of the nucleus, and is usually evaluated by an expansion in powers of r/R_N , where R_N can be regarded as an “overall” size of the nucleus. This requires a particular model of the actual nuclear charge distribution. Bohr and Weisskopf evaluated the electronic integrals considering the nuclear charge distribution as in between uniform in the volume and uniform on the surface of a sphere [71]. Stroke in Ref. [78] calculated with three different distributions, those of Ref. [71] plus a trapezoidal one⁵, and obtained different results. Of these, the most accurate is the one calculated with a trapezoidal charge distribution, which was the best approximation based on electron scattering experiment data available at the time. Contrary to the conclusion in Ref. [78] that different distributions change the result by a considerable amount, Ref. [82], which is a more modern calculation, use 3 different distributions and less than 5% variations, when keeping the magnetization radius fixed. Recent atomic theories taking into nuclear size effects typically use two parameter Fermi-distributions [83].

⁵Or rather, a polynomial “Hofstadter” type distribution fitting to match parameters of the trapezoid, see Ref. [78].

Table 5.1: electronic wavefunction integrals, interpolated from calculations in Ref. [78]

Electronic state	b_{2s}	b_{4s}
$7S_{1/2}$	6.13	-1.91
$7P_{1/2}$	1.59	-0.49

The expansion in powers of nuclear moments leads to the following expressions:

$$\begin{aligned}
N(R) &= b_2 \cdot \langle r^2/R_N \rangle + b_4 \cdot \langle r^4/R_N \rangle. \\
K(R) &= \frac{2}{5}b_2 \cdot \langle r^2/R_N^2 \rangle + \frac{4}{7}b_4 \cdot \langle r^4/R_N^2 \rangle.
\end{aligned} \tag{5.8}$$

We use the numerical values in Ref. [78] and interpolate for Fr. The results are tabulated in Table 5.1.

The anomaly then reduces to:

$$\begin{aligned}
\epsilon &= -(\alpha_S [b_2(1 + (2/5)\eta)G_1 + b_4(1 + (4/7)\eta)G_2] \\
&+ \alpha_L [(3/5)b_2G_1 + (3/7)b_4G_2])
\end{aligned} \tag{5.9}$$

where $G_1 = \langle r^2/R_N^2 \rangle$ and $G_2 = \langle r^4/R_N^4 \rangle$ are evaluated over the nuclear wavefunctions⁶. We now switch gears and examine the nuclear wavefunctions in the framework of the spherical shell model.

⁶Note that in some calculations Martensson-Pendrill's group performed, the $\langle r^6 \rangle$ term is found to amount to several percent of the anomaly, which is below our precision but matters, for example, in stable isotopes ^{203}Tl and ^{205}Tl [83].

5.3.2 Spherical shell model nuclei: ^{207}Fr to ^{213}Fr .

The nuclear shell model is analogous to the Aufbau principle in atomic physics, which describes the electronic structure as they gradually fill up the “shells”, which contains orbitals⁷. The closed-shell nuclei are analogs of noble gasses. However since the nucleons interact with each other via the strong force instead of the Coulomb force for atomic electrons, the potential inside of the nucleus is much better described by a simple harmonic oscillator (SHO) potential. The SHO potential is in fact an amazingly good approximation for many applications, especially phenomenological ones. One step beyond that sometimes a Fermi-like potential called the “Woods-Saxton” potential [84] is used. Including the spin-coupling interaction, the resulting “magic numbers” are 2, 8, 20, 28, 50, 82, and 126⁸. Both protons and neutrons have these magic numbers, or in other words the nucleon interactions to good extent do not depend on the electrical charge. Near the heavy mass region where Fr lies, ^{208}Pb is the “doubly-magic” nucleus, with proton number $Z = 82$ and neutron number $N = 126$. It is the starting point, the black-box “core” for modern theoretical calculations. Figure 5.6 shows a diagram illustrating the nuclear shell model, highlighting our example isotope ^{210}Fr . Five protons are added to the $h_{9/2}$ orbital above $Z = 82$ shell, and three neutrons are removed from the $p_{1/2}$ and $f_{5/2}$ orbitals below the $N = 126$ shell.

These orbital wavefunctions provide the basis for evaluating the nuclear in-

⁷The shell model was developed by Maria Goeppert-Mayer and J. Hans D. Jensen, who shared half of the Nobel Prize in Physics in 1963. Goeppert-Mayer was the second and last female Physics Nobel laureate, after Madam Curie.

⁸The numbers are instead 2, 10, 18, 36, 54, and 86 for atomic electrons.

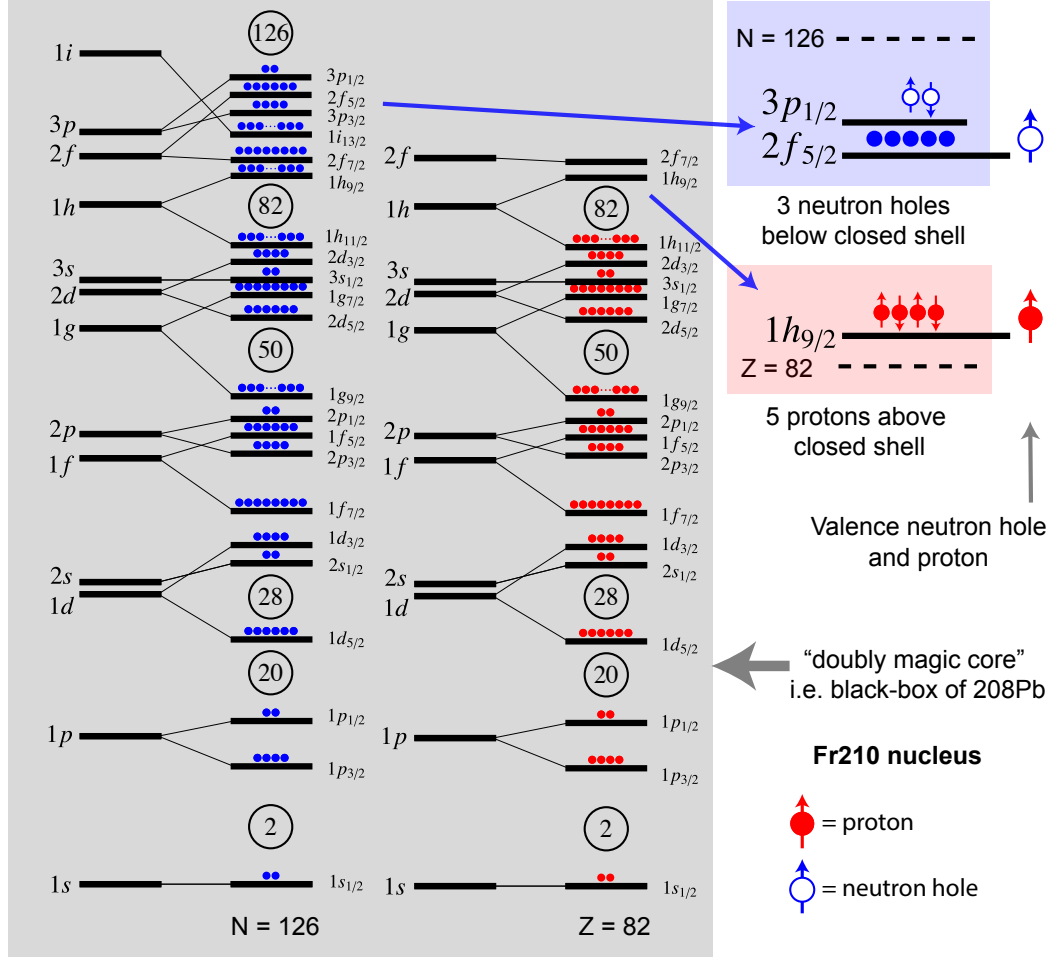


Figure 5.6: Shell model nucleus of ^{210}Fr . The nucleons gradually fill up wavefunction orbitals. For certain numbers of nucleons there are big energy gaps, and form the so called “closed shells”, similar to the electronic structure in noble gases. These numbers are different from atomic magic numbers because of the differences in the potential shape and spin-orbit coupling. Near francium the “doubly magic” nucleus is ^{208}Pb , with 82 protons and 126 neutrons. ^{210}Fr has five proton holes above and three neutron holes below the respective closed shells. The unpaired valence nucleons dominate the magnetic dipole hyperfine interaction.

Table 5.2: Nuclear integrals, angular momentum parameters, and calculated anomalies for valence nucleons in respective orbitals.

Orbital	$\nu p_{3/2}$	$\nu i_{13/2}$	$\nu f_{5/2}$	$\nu p_{1/2}$	$\pi h_{9/2}$
ϵ this work	-1.99	-2.47	-2.75	-3.13	-0.57
ϵ [72]			-1.96	-2.32	-0.50
α_S	1	1	1	1	-0.518
η	0.2	0.4	0.8	2	-0.667
G_2 [78]	0.58	0.61	0.70	0.58	0.52
G_4 [78]	0.53	0.43	0.70	0.53	0.31

Table 5.3: Nuclear moments obtained from nuclear wavefunction based on the Skyrme model [85] in the Pb region.

orbitals	$\nu f_{5/2}$	$\nu p_{1/2}$	$\pi h_{9/2}$
$\langle r^2 \rangle$ /fm ²	27.81	27.80	28.34
$\langle r^4 \rangle$ /fm ⁴	1351.55	1553.29	1135.16

integrals G_1 and G_2 . We use the calculations in Ref. [78] for orbitals nearby the Fr region, and list these numbers in Table 5.2. This table also includes the angular momentum coupling factors, which we will investigate in the next sub-section.

Of course the main interest lies in the sensitivity to the neutron magnetization extent. In Ref. [72], generic nuclear wavefunctions in the Pb region obtained from the Skyrme model were used. The calculated nuclear moments for $f_{5/2}$ and $p_{1/2}$ orbitals are summarized in Table ??.⁹ However, these moments combined with $R_N = 1.07A^{1/3} + 1.5$ fm = 7.89 fm give typically G_1 and G_2 of 0.45 to 0.3, which are a fair amount smaller than those from Ref. [78]. This will reduce the anomaly

⁹Table 5.3 is for book keeping purposes only. The numbers are obtained from an excel file from Stony Brook used to analyze the data in Ref. [72].

of the odd-even isotopes by as much as 40%.

5.3.3 Nuclear g factors and spin alignment.

There are two layers of nuclear g factor couplings involved: 1. the angular momentum addition from the proton and the neutron; 2. the orbital and spin angular momentum addition in a single nucleon. Figure 5.7 illustrates the spin alignments. We first examine the proton and neutron addition.

The total anomaly combining the proton and the neutron is given by [79].

$$\epsilon_{A,S} - \epsilon_{A,P} = \epsilon_{\pi}\beta_{\pi} + \epsilon_{\nu}\beta_{\nu}, \quad (5.10)$$

where β_i is the fractional contributions from the proton and neutron to the magnetic moment. The angular momentum coupling of the proton and neutron g factors gives the respective β factors. We use empirical g factors derived from francium magnetic moments, and tabulate the values along our isotopic chain in Table 5.4. This approach for Fr is used in the recent literature, e.g. in Ref. [86].

The sum over individual nucleons then reduces to the $\pi h_{9/2}$ for isotopes with paired neutrons (odd-even isotopes), and angular momentum coupling between the $\pi h_{9/2}$ and respective neutron orbitals, for example $\nu f_{5/2}$ for ^{210}Fr , for isotopes with an un-paired valence neutron (odd-odd isotopes). The β factors are:

$$\beta_{\pi} = g_{j,p} \frac{g_I - g_{j,n}}{g_I(g_{j,p} - g_{j,n})} \quad (5.11)$$

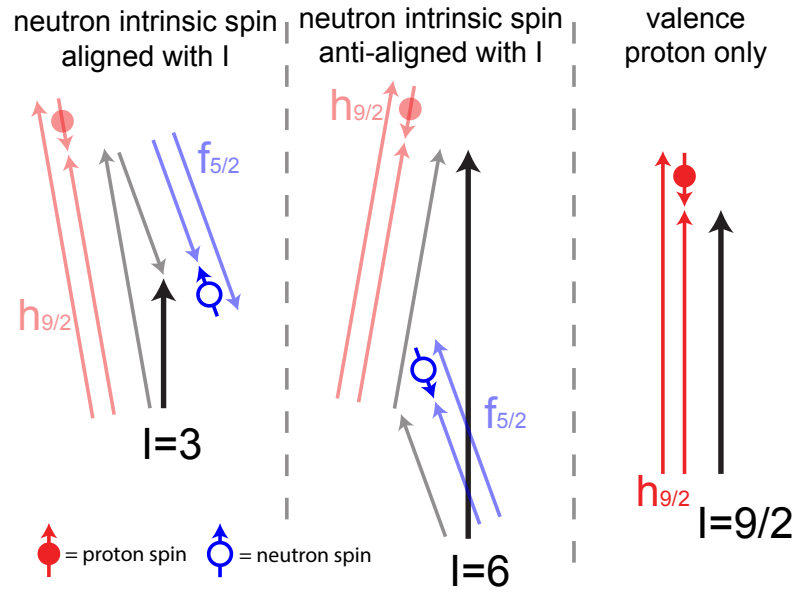


Figure 5.7: Neutron spin alignment with the total nuclear spin. Odd-even isotopes ($^{207,209,211,213}\text{Fr}$) have spins determined by only the single valence proton, and is $I = 9/2$. The odd-odd isotopes have the proton and neutron angular momenta coupled together, to produce either high nuclear spin (e.g. ^{210}Fr $I = 6$ and neutron $f_{5/2}$ pure orbital); or low spin (^{206g}Fr $I = 3$, again assuming a pure orbital). The neutron spin is anti-aligned and aligned with the total nuclear spin, respectively.

Table 5.4: g factors, empirical and experimental magnetic moments, and proton β factors.

Isotope	206m1	206g	207	208	209	210	211	212	213
$g_{j,p}$	0.860	0.860	0.860	0.873	0.873	0.885	0.885	0.893	0.893
$g_{j,n}$	0.351	-0.627	0	0.351	0	0.351	0	1.226	0
μ_{emp}	4.478	4.253	3.870	4.807	3.929	4.319	3.983	4.632	4.019
μ_{exp}	4.69	3.97(6)	3.89(8)	4.75(10)	3.95(8)	4.38(5)	4.00(8)	4.62(9)	4.02(8)
β_π	0.815	0.834	1.0	0.817	1.0	0.849	1.0	0.868	1.0

Where the total nuclear g factor is given by:

$$g_I = \left(\frac{g_{j,p} + g_{j,n}}{2} \right) + (g_{j,p} - g_{j,n}) \frac{I_p(I_p + 1) - I_n(I_n + 1)}{2I(I + 1)}. \quad (5.12)$$

And $\beta_\mu = 1 - \beta_\pi$. Table 5.4 contains the numbers.

We now look at the proton g factors used. For any single valance nucleon, to get $g_{J,p}$ from $g_{L,p}$ and $g_{S,p}$, i.e. the coupling of spin and angular momenta, the formula has the same form as Eq. 5.12:

$$g_J = \left(\frac{g_L + g_S}{2} \right) + (g_L - g_S) \frac{L(L + 1) - s(s + 1)}{2j(j + 1)}. \quad (5.13)$$

These factors determine the α parameters, as listed in table 5.2 in the previous subsection. For the neutron since the orbital angular momentum does not contribute to the magnetic moment, $g_{l,n} = 0$. However for the proton, different “quenching” of g factors could change the size of the proton anomaly. In the main result we have kept the convention of Ref. [72], with g_s quenching factor 0.85, giving $g_j = 0.834$. If we instead use a quenching factor of 0.6, $g_s = 3.35\mu_N$, yielding $g_j = 0.961$. This would change α_S from -0.57 to -0.34, giving a proton anomaly of $\epsilon_{\pi,S-P} = -0.825\%$.

This would reduce the total anomaly of isotopes with $\nu f_{5/2}$ and $\nu p_{1/2}$ orbitals by about 15% and 10% respectively.

We can make use of the above spin couplings to explain some features of the HFA, especially for the case of ^{206}Fr ground and isomeric states. Figure 5.8 highlights the different predictions for ^{206}Fr . The sign reversal of $f_{5/2}$ orbital for ^{206g}Fr ¹⁰ compared to other isotopes with neutrons at this orbital, can be understood by noticing the neutron spin alignment to the total angular momentum of the nucleus. See Fig. 5.7. For neutron $p_{1/2}$, $f_{5/2}$ and proton $h_{9/2}$ states, the nucleon spins are all anti-aligned with the orbital angular momenta. To obtain total nuclear spin of higher than 9/2, which is the case for $^{206m1}\text{Fr}$, ^{208}Fr , ^{210}Fr and ^{212}Fr , the neutron and proton angular momenta are aligned. Therefore the neutron spin I_n , which generates the neutron part of the magnetization, is then anti-aligned with the total nuclear spin I . This however is the opposite for ^{206g}Fr with low spin, and thus the $f_{5/2}$ orbital has I_n and I aligned, whereas $p_{3/2}$ and $i_{13/2}$ have them anti-aligned.

This concludes the discussion of the BW effect for a spherical shell model nucleus. Before we proceed into nuclear structure effects beyond this simple picture, we include the finite charge distribution effect.

5.3.4 The Breit-Rosenthal effect

The hyperfine splitting changes due to the finite nuclear charge distribution, is called the Breit-Rosenthal effect [87]. There are mainly three models of the charge

¹⁰We follow recent literature and refer the nuclear spin $I = 7$ as the ground state. The exact energy level ordering with the low spin state has not been established at the time of this writing. The two nuclear states both decay through alpha emission, and have almost the same lifetimes of about 16 seconds.

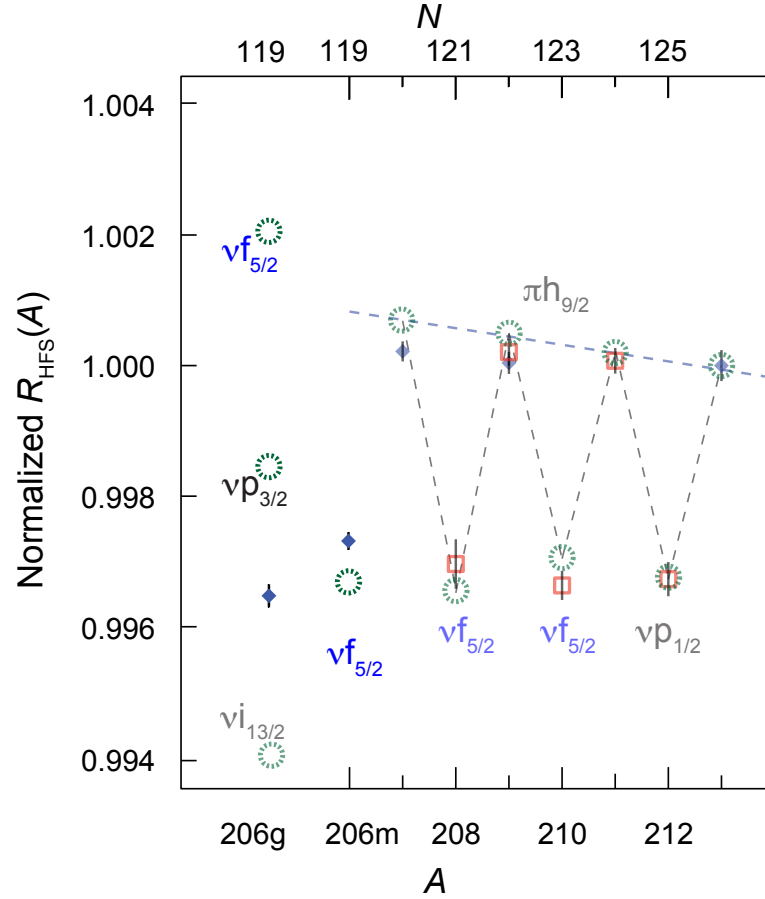


Figure 5.8: Hyperfine anomalies of ^{206}Fr nuclear ground and isomeric states. This is one detailed version of Fig. 4 in Ref. [75]. The green dashed circles are calculations based on pure wavefunction orbitals, however in the case of ^{206g}Fr is not in agreement with either one considered. This suggests a possible mixture of orbitals, and HFA is more sensitive to this effect than the magnetic moment itself. See text for discussions. The dashed lines are to guide the eye, illustrating the even-odd staggering and the proton anomaly trend.

distributions in the literature used to calculate this effect: when first examining the isotopic variation of hyperfine constant, Breit and Rosenthal [87] used a spherical shell charge distribution [87]. Later Crawford and Schawlow used uniform distribution [88]. Rosenberg and Stroke used a trapezoidal distribution [89] and compared results from different models, and found that the BR effect differs. For example for Fr ($Z = 87$) a uniform charge distribution could give 18.5% to the hyperfine splitting, where as a Hofstadter distribution would give 15%. The Hofstadter distribution gives an effect for the $P_{1/2}$ state of 5%. Since the charge radius variation is relatively small, the relatively large BR effect still gives 10^{-4} level variations between adjacent isotopes. However, when comparing the two ends of the isotopic chain, ^{206}Fr and ^{213}Fr , the BR effect could show up at δr_c^2 which is about 30% of the odd-even isotope anomaly. On the other hand, in Ref. [83] a different parameterization is used: $A(\rho_c, \rho_m) \approx A_0(1 - f\lambda_c)$. Where the parameter f is found with Dirac-Fock calculations for several charge distributions to be $f(7S) = 15.8 \times 10^{-4}/\text{fm}^2$, $f(6P_{1/2}) = 4.14 \times 10^{-4}/\text{fm}^2$. And $\lambda_c = 0.94 \times \langle \delta r_c^2 \rangle$, where the factor of 0.94 is for taking into account higher moments. It was also observed that the BR effect can be compared to the BW effect, and the ratio $f/b_{2S} \approx 2.0$. We have used this method and the parameters used for the BR corrections, again taking ^{213}Fr as the reference. The charge radii changes are taken from Ref. [90] and [74]. Results are tabulated in Table 5.5. These numbers are less than half of what is estimated using Ref. [89], and modern atomic theory at an accuracy of 1% or better should be able to resolve this discrepancy.

Table 5.5: Charge radii changes with respect to ^{213}Fr and the Breit-Rosenthal effect. See text for method used.

Isotope	206	207	208	209	210	211	212
$\langle \delta r_c^2 \rangle / \text{fm}^2$	-0.3851	-0.3719	-0.2918	-0.2710	-0.1876	-0.1169	-0.0793
BR effect /%	-0.052	-0.050	-0.040	-0.037	-0.025	-0.016	-0.011

5.4 The Nilsson deformed nucleus, ^{209g}Fr and ^{221}Fr .

The study of nuclear shape coexistence and evolution is one of the central topics of contemporary nuclear physics [91]. Certain transitions from spherical to quadrupole and higher-order deformed shapes are explained as quantum phase-transitions [92]. The Nilsson model [80] is an elegant solution for deviations from a spherical nucleus. Its ingenuity originates from simplifying the complicated many-body nuclear interactions into a tangible framework based on a single particle in a deformed nuclear potential.

In this section we use the Nilsson picture to describe the HFA beyond the spherical shell nucleus. We can qualitatively explain the two isotopes at the edges of our isotopic chain: ^{209g}Fr and ^{221}Fr . These two isotopes mark a clear boundary of the single particle shell model, on both the neutron-deficient and neutron-rich sides of the isotopic chain. We end this chapter by discussing possible implications for the neutron skin and the relationship with the HFA and APNC.

Table 5.6: μ and HFA of ^{206g}Fr calculated with different pure orbitals. The experimental magnetic moment is $3.99 \mu_N$ [86].

orbital	μ_{emp} / μ_N	$\epsilon / \%$
$\nu f_{5/2}$	2.834	0.13
$\nu p_{3/2}$	4.253	-0.64
$\nu i_{13/2}$	-1.982	-0.20

5.4.1 ^{206g}Fr nuclear ground state.

The ground state ^{206g}Fr already shows magnetic moment deviations from the $f_{5/2}$ orbital [86, 93, 94]. We list in Table 5.6 the values of the magnetic moment and the hyperfine anomaly considering three neutron orbitals: $f_{5/2}$, $p_{3/2}$, and $i_{13/2}$. Figure 5.9 plots these calculations and the experiment. The $i_{13/2}$ orbital has an opposite parity and a higher energy, which we do not expect to mix into the neutron orbital. Its calculation is only included for completeness.

Figure 5.9 shows the Nilsson diagram for neutrons below the $N = 126$ shell closure. Six neutron holes gradually occupy the sub-levels $p_{1/2}$ and $f_{5/2}$ orbitals, while the seventh one is the valence neutron contributing to the HFA. The quadrupole moment of ^{206g}Fr [93, 94] indicates a tiny oblate deformation [95]. This however can already introduce level mixings between the highest energy $f_{5/2}$ orbital with the nearby levels of the $p_{3/2}$ orbital. This mixture could produce the larger anomaly in ^{206g}Fr , even though a single particle model in $f_{5/2}$ orbital yield opposite sign of the anomaly.

Nilsson diagram for neutrons, $114 \leq N \leq 126$

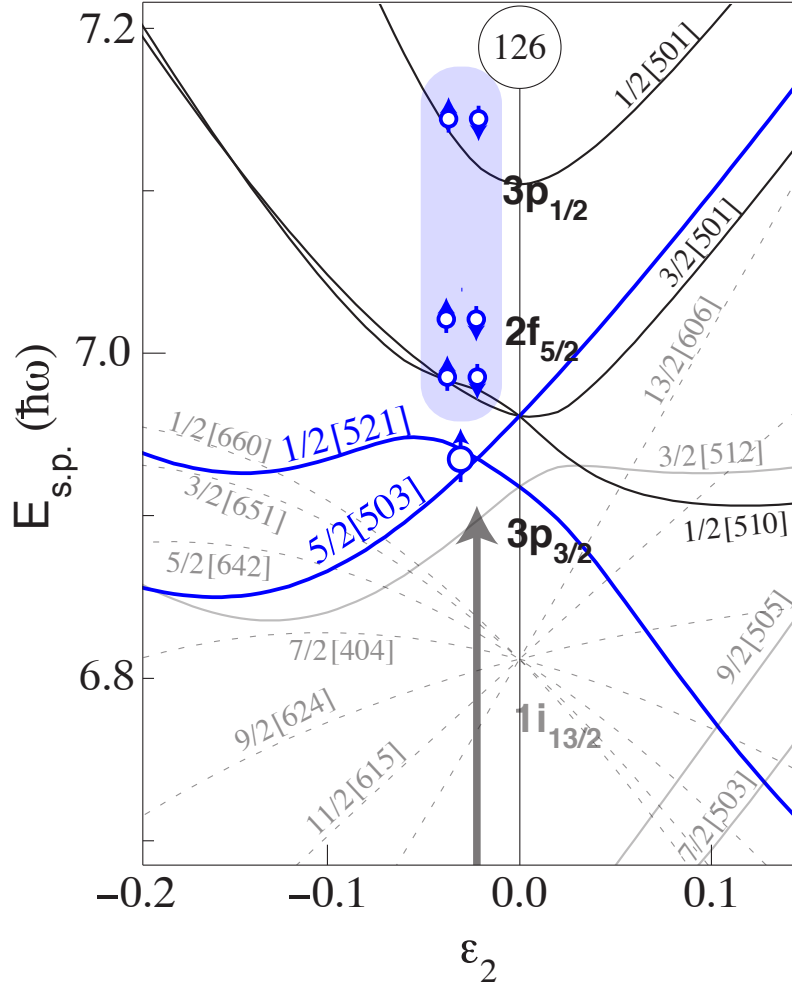


Figure 5.9: Neutron holes of ^{206}Fr in a deformed nucleus. The quadrupole moment [93] indicates a small oblate deformation [95]. The 6 neutrons pair up and occupy lower levels of $p_{1/2}$ and $f_{5/2}$ orbitals. The close lying energy levels of $f_{5/2}5/2$ (denoted as “[503 5/2]” in the Nilsson picture) and $p_{3/2}1/2$ (“[521 1/2]”) renders the valence neutron in a mixture state of two orbitals. Nilsson diagram originally from Ref. [96]. Grey arrow indicate level crossing of $f_{5/2}$ [503 3/2] and $p_{3/2}$ [521 1/2] orbitals. All the numbers indicate various angular momentum and spin quantum numbers. Nilsson diagrams can be lengthy to explain, and I suggest the readers refer to text books such as Ref. [97].

5.4.2 Neutron rich ^{221}Fr .

We then turn into the case of ^{221}Fr , an isotope with 4 pairs of neutrons above the $N = 126$ closed shell. The valence proton still dominates the magnetic moment, and its wavefunction is modified by the Nilsson deformation. Figure 5.10 shows the HFA result highlighting ^{221}Fr . The valence proton resides in the $h_{9/2}$ orbital, however the HFA does not follow the trend of the other odd-even isotopes. This isotope even has nuclear spin $I = 5/2$ instead of $9/2$. We were much puzzled by these strange behaviors and the model used in Ref. [98], until Prof. Alfredo Poves¹¹ pointed out a simple possibility: the fifth valence proton has nuclear angular momentum projecting onto the deformation axis, rendering the nuclear spin as $I = 5/2$.

Figure 5.11 shows a Nilsson diagram for protons near $Z = 82$. The quadrupole moment of ^{221}Fr suggests a prolate deformation [98]. Lower spin states of the $\pi h_{9/2}$ orbital is energetically favored, and the five protons gradually fill up from the $Z = 82$ closed shell. The last valence proton can reside in the $[523\ 5/2]$ orbital, before the $f_{7/2}$ level ($[530\ 1/2]$ highlighted in green in Fig. 5.11) have low enough energy to mix in. The Nilsson model calculations are parameter dependent, and several different sources that we have looked up all predict this level crossing at medium deformations $0.15 < \epsilon_2 < 0.2$ [96,97,99]. Reference [98] however, calculates a much earlier crossing. The authors of Ref. [98] consider much more complicated orbital mixing effects and excitations, and tweak some parameters to obtain agreements between theory and experimental nuclear moments. Our treatment here is considerably simpler: the

¹¹Then visiting TRIUMF from Spain.

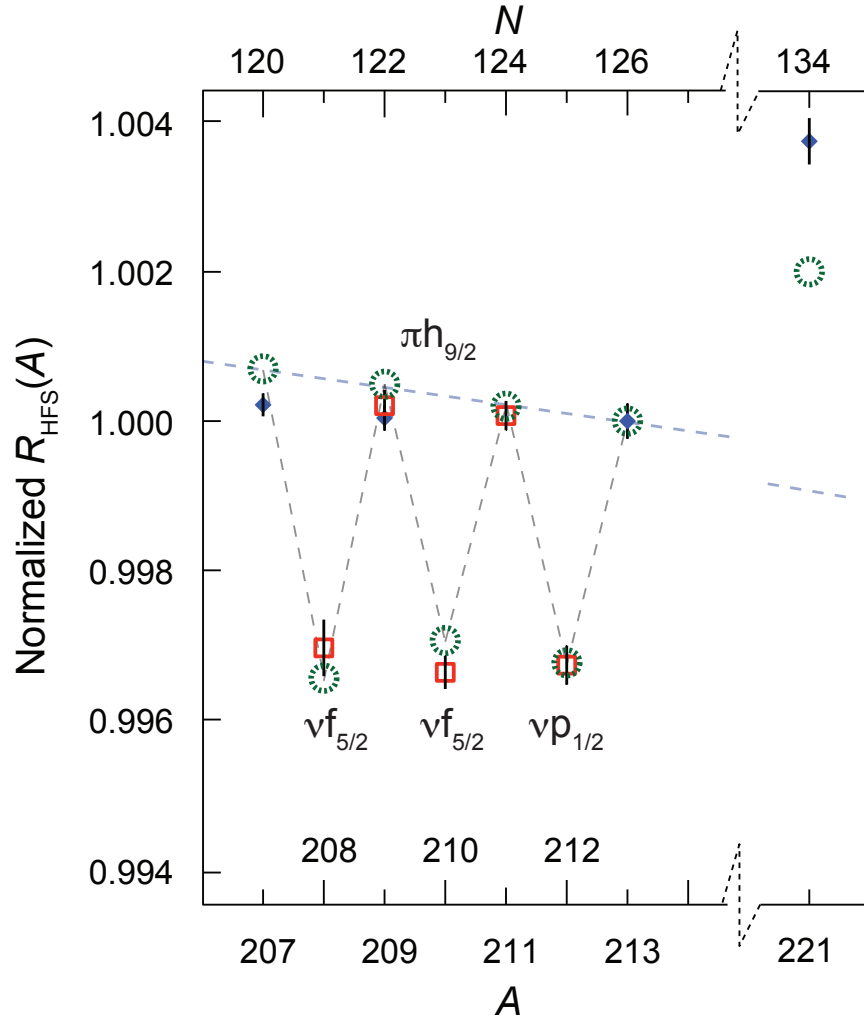


Figure 5.10: Hyperfine anomalies in a chain of francium isotopes, ^{207}Fr to ^{221}Fr . This is another detailed version of Fig. 4 in Ref. [75]. See text for explanations emphasizing the neutron rich ^{221}Fr .

tabulated orbital mixtures in Ref. [99] give less than 5% contributions from other orbitals. We also obtain a reasonable magnetic moment¹², taking into account the Clebsh-Gordan coupling coefficients and the proton spin-asymmetry contributions.

5.5 Possible implications of the hyperfine anomaly.

5.5.1 Magnetic moment relationship with the anapole moment.

As is discussed in Chapter 1, understanding the nuclear structure, in particular the electromagnetic currents inside of the nucleus within the finite size (7 fm max radius for Fr), is crucial for the interpretation for an anapole moment experiment. The hope is that with a next-order quantity such as the BW effect, could shine light on to the nuclear structure models used for calculating the nuclear anapole, and provide an important benchmark on the theoretical accuracy. This might require the magnetic moment itself being calculated to reasonable precision, as compared to our empirical approach of deriving it from experimental values.

The nuclear magnetic moment has both direct and indirect relationships with the anapole. In fact, as pointed out both in the context of extreme single particle model (see e.g. Ref. [100]) and a much more sophisticated shell model calculation (Ref. [14]), the anapole moment acts like the magnetic moment. Ref. [100] has given an analytical expression for the anapole coupling constant

$$\kappa_a = 1.15 \times 10^{-3} A^{2/3} \mu_{p,n} \zeta_{p,n} \quad (5.14)$$

¹²See Ref. [75] text, courtesy of John Behr.

Nilsson diagram for protons, $Z \geq 82$ ($\epsilon_4 = \epsilon_2^2/6$).

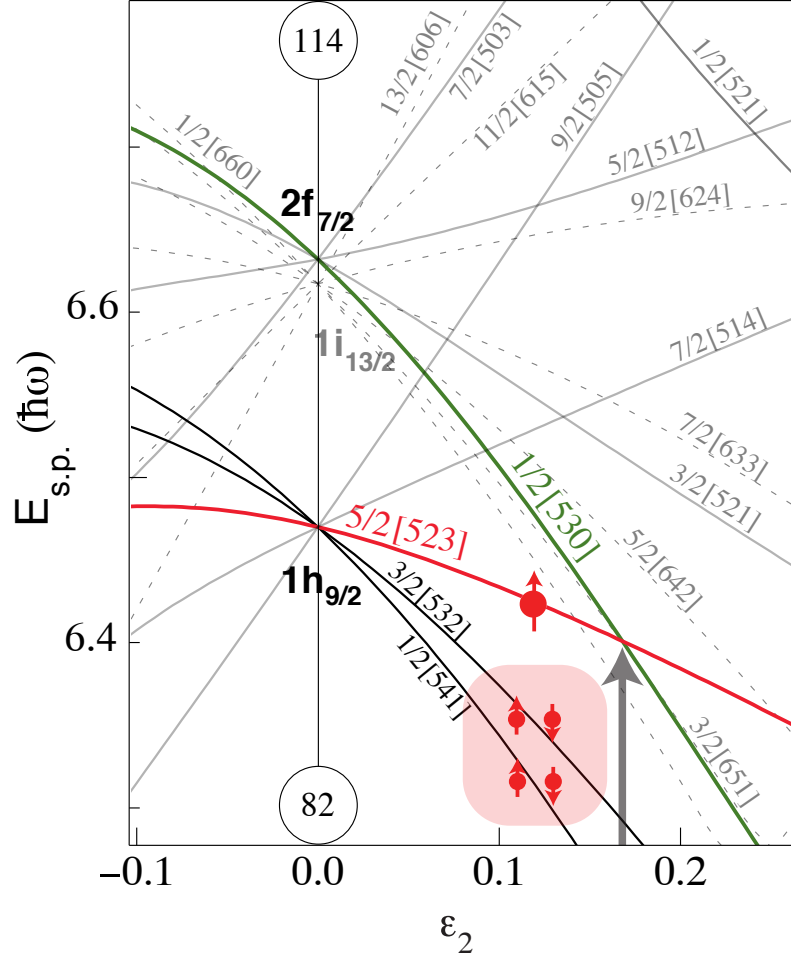


Figure 5.11: Protons of ^{221}Fr in a deformed nucleus. The quadrupole moment suggests prolate deformation [98], where lower spin states of $h_{9/2}$ become energetically favored. Four protons pair up and occupy the lower levels of the $h_{9/2}$ orbital, leaving the valence proton predominantly in the $h_{9/2}5/2$ state (denoted as “[523 5/2]”). The Nilsson diagram is originally from Ref. [96]. It shows the crossings of $h_{9/2}$ [523 5/2] and $f_{7/2}$ [530 1/2] orbitals, see text.

where $\mu_{p,n}$ is the magnetic moment of the valence nucleon, $\zeta_{p,n}$ is the dimensionless effective weak coupling for the valence nucleon. The factor $A^{2/3}$ accounts for the valence nucleon interacting with the core, and is the source of the heavy atom enhancement. By contrast the most extensive many-body nuclear structure theory studies [14], inspired by the Cs work, calculate the anapole to be about half the size of the spherical shell model calculation [100], the latter being in good agreement with experiment. The authors of Ref. [14] use the magnetic moment to benchmark the accuracy for both the Cs and Tl nuclei. In addition, the single particle magnetic dipole is used to understand the radiative correction terms that also contribute to the nuclear spin-dependent (NSD) parity violation, which in turn matters for the dominance of the anapole in all the NSD-PNC interactions [101].

5.5.2 Neutron density and neutron skin.

The neutron skin, a measure of how much the spatial extent of the neutrons exceed that of the protons (i.e. the charge distribution), has attracted great interest in recent years (see for example [102–105] and references therein). A measurement of this (bulk) property would provide important information for nuclear structure models, in particular theories on isospin symmetry breaking, as well as shining light on neutron star physics. The most recent experimental efforts being carried out are best represented by the ^{208}Pb Radius Experiment (PREX) at Jefferson lab, where parity-violating electron scattering is used to probe the neutron radius [103]; and also the (more precise) experiment carried out in Mainz by measuring coherent pion

photo production [105].

In the early paper from Fortson, where the “chain of isotopes” method of measuring APNC was proposed [26], the neutron skin effect was considered to be the dominant uncertainty, when the atomic theory uncertainties are removed by comparing different isotopes. This can either be viewed as a curse for (nuclear spin-independent) APNC measurements, or be turned around as a tool for probing the nuclear structure, if the Standard Model is believed. The neutron skin thickness defined by the neutron and proton radii difference, Δr_{np} , is of the order of 3% of the charge radius, and its uncertainties (before PREX and Mainz measurements) is estimated in Ref. [106] to add to APNC uncertainty at the 0.2% level. This situation has not changed much given the new results unfortunately, because of the relatively large error bars and disagreement of the central values, let along the interpretations (see e.g. [107]). However, as both Refs. [106, 108] argued, the neutron skin effects in APNC are correlated along the isotopic chain, and the slope has little model dependence, unlike the value itself. Everything converges to the 0.2% level, for a test of the Standard Model to be competitive with the Cs experiment.

The relationship between HFA and the neutron skin is indirect and elusive. If there were no higher order terms present and only the $\langle r^2 \rangle$ term is present, this is directly the nucleon radius. This is a crude truncation, however it could still hypothetically produce the neutron single orbital radius. When the atomic theory is trusted to 0.5% or better precision, by observing certain relationships between different moments, the (single valence) neutron radii can be extracted. This however, is hindered by the magnetic moment coupling and the absolute size of the HFA

contribution from the proton. Remember from the previous sections, the proton angular momentum coupling factors for odd-odd isotopes are determined empirically from their odd-even neighbors, with neutron core (all the paired ones) assumed to not contribute to the magnetic moment, which is not true at the 1% level of precision. Also, as is emphasized in many places in this chapter, an important distinction is that the single particle wavefunction extent is a completely different quantity than the neutron radius of the ensemble. Their relationship is that the former roughly can be viewed as residing on the outer surface, and will modify the parameters of the Fermi distribution [109]. The interaction of single particle with the core is by itself an interesting subject, however here we do not deem the HFA as an observable with enough predictive power for neutron skin related APNC physics.

Hyperfine anomalies in Fr: boundaries of the spherical single particle model

J. Zhang (张颀颀)¹, M. Tandecki², R. Collister³, S. Aubin⁴, J. A. Behr², E. Gomez⁵, G. Gwinner³, L. A. Orozco¹, M. R. Pearson², and G. D. Sprouse⁶

¹*Joint Quantum Institute, Department of Physics, University of Maryland, and National Institute of Standards and Technology, College Park, MD 20742, U.S.A.* ²*TRIUMF, Vancouver, BC V6T 2A3, Canada.* ³*Dept. of Physics and Astronomy, University of Manitoba, Winnipeg, MB R3T 2N2, Canada* ⁴*Department of Physics, College of William and Mary, Williamsburg VA 2319, U.S.A.* ⁵*Instituto de Física, Universidad Autónoma de San Luis Potosí, San Luis Potosí 78290, México.* ⁶*Department of Physics and Astronomy, Stony Brook University, Stony Brook, New York 11794-3800, U.S.A.*

(Dated: June 30, 2015)

We have measured the hyperfine splitting of the $7P_{1/2}$ state at the 100 ppm level in Fr isotopes ($^{206g,206m,207,209,213,221}\text{Fr}$) near the closed neutron shell ($N = 126$ in ^{213}Fr). The measurements in five isotopes and a nuclear isomeric state of francium, combined with previous determinations of the $7S_{1/2}$ splittings, reveal the spatial distribution of the nuclear magnetization, i.e. the Bohr-Weisskopf effect. We compare our results with a simple shell model consisting of unpaired single valence nucleons orbiting a spherical nucleus, and find good agreement over a range of neutron-deficient isotopes ($^{207-213}\text{Fr}$). Also, we find near-constant proton anomalies for several even- N isotopes. This identifies a set of Fr isotopes whose nuclear structure can be understood well enough for the extraction of weak interaction parameters from parity non-conservation studies.

PACS numbers: 21.10.Gv, 27.80.+w, 32.10.Fn

Weak interaction studies in heavy atoms require for their interpretation precise knowledge of the atomic and nuclear wavefunctions. To extract nucleon-nucleon weak interaction couplings from the weak interaction induced parity-violating anapole moment [1], nuclei with simple and regular magnetic properties are desirable [2–4]. The nuclear magnetic moment is used to benchmark nuclear structure theories for calculating the anapole moment [3], which is a contact field effect produced inside the finite extent of the nucleus. Here we explore the regularity of the magnetic properties of a chain of Fr isotopes and find that $^{207-213}\text{Fr}$ in the vicinity of the neutron shell closure mark a range where the nuclear structure is sufficiently tractable for standard model tests and constraints on new physics [5].

To lowest order, the atomic hyperfine interaction can be described using a point-like nucleus characterized by the magnetic dipole moment. Deviations from the point-like approximation of the nucleus, referred to as hyperfine anomalies, come from considering how finite magnetic and charge distributions affect the interaction between the magnetization of the nucleus and the magnetic field created by the electrons. The magnetic contribution is known as the Bohr-Weisskopf (BW) effect [6, 7]. The difference in the nuclear charge distribution (Breit-Rosenthal (BR) effect [23–25]) produces very small variations between isotopes, leaving the BW effect dominant [26, 27]. As a new generation of proposed parity violation experiments in atoms (including Fr) and molecules starts [8–14], it is important to understand the limiting factors due to the nuclear structure, e.g. the nuclear magnetization, for the interpretation

of parity-violating anapole moments [2–4].

Here we present a systematic study of the variations of the hyperfine splittings (HFS) in a chain of Fr isotopes. Our measurements include ^{213}Fr with the closed neutron shell (magic number $N = 126$), $^{206g,m}\text{Fr}$, ^{207}Fr , and ^{209}Fr on the neutron-deficient side, and the neutron-rich ^{221}Fr . In the region of $^{207-213}\text{Fr}$ with up to 6 neutron holes, we find near-constant magnetic hyperfine anomalies for the odd- Z , even- N isotopes [15]. The neutron rich odd-even isotope ^{221}Fr shows a different behavior due to the deformation of the nucleus. The odd- Z , odd- N isotopes have anomaly contributions from both the proton and the valence neutron.

BW effect measurements usually require precise knowledge of both, hyperfine structure constants and magnetic moments. Measurements of the nuclear magnetic dipole moment in Fr are limited to ^{211}Fr [16] and ^{210}Fr [17]. Empirical values for other isotopes are usually obtained by scaling with the isotopic ratios of the hyperfine constants based on these two experiments, both of which have uncertainties larger than 1% and cannot be used to extract the hyperfine anomaly. A different approach to study the BW effect which circumvents the limited precision in the magnetic moments comes from the suggestion by Persson [18] that was implemented in Fr [15], Tl [19] and Eu [20]. This method relies on looking at the ratio between hyperfine splittings of two levels where the electron wavefunctions are overlapping differently with the nuclear wavefunction, and consequently is sensitive to the differences in their hyperfine anomalies. We can normalize the change in this ratio to a specific isotope (^{213}Fr) for purpose of directly

revealing the contribution from the neutron wavefunction. See Ref. [7] for a review and Ref. [21] for a recent compilation of all available hyperfine anomaly data.

The magnetic hyperfine interaction W can be written as [18, 22]

$$W_{\text{extended}}^l = W_{\text{point}}^l(1 + \epsilon_l), \quad (1)$$

where ϵ_l is a small quantity that depends on the particular isotope, and on the atomic state ($l = S$ or P). The $7P_{1/2}$ electron overlaps with the nuclear wavefunctions more uniformly than the $7S_{1/2}$ electron. The ratio R of the hyperfine splittings for an isotope with mass number A is sensitive to the nuclear magnetization distribution [15]

$$R_{\text{HFS}}(A) = \frac{W_{\text{extended}}^S}{W_{\text{extended}}^P} \approx R_0(1 + \epsilon_S(A) - \epsilon_P(A)), \quad (2)$$

with R_0 the ratio of hyperfine structure constants for a point nucleus. Since both states have $J = \frac{1}{2}$, the extraction of precise magnetic hyperfine structure constants from the measurements is not hampered by the presence of higher order nuclear moments. The relative size of ϵ_P grows with nuclear charge number Z , and is about 1/3 of ϵ_S in Fr [22].

We measure the $7P_{1/2}$ hyperfine splitting of Fr at the 100 ppm level in a number of isotopes. We use these measurements in combination with the $7S_{1/2}$ hyperfine splittings [34–37] to determine $R_{\text{HFS}}(A)$ to study changes in the hyperfine anomaly. These measurements are carried out at the Francium Trapping Facility (FTF) at TRIUMF [8]. We briefly summarize the operation of the FTF: A 500 MeV proton beam irradiates a target that consists of uranium carbide foils to produce between 10^7 to 10^9 Fr⁺/sec of the selected isotope [28]. We produce an ultracold sample of neutral Fr atoms for Doppler-free spectroscopy by capturing typically a few 10^5 atoms in a magneto-optical trap (MOT). Two Ti:Sapphire lasers (trap and repumper) form the MOT on the D_2 line (718 nm) and leave the D_1 line (817 nm) background free for the measurement (Fig. 1(a)). A computer-controlled Fabry-Perot cavity monitors and stabilizes [29] the long-term frequency variation of all of the lasers to better than ± 5 MHz.

A third Ti:Sapphire laser excites the transition from the upper ground state hyperfine level to each of the two $7P_{1/2}$ hyperfine levels at 817 nm (Fig. 1(a)). We amplitude-modulate the probe laser with a fiber electro-optic modulator (EOM, EOSpace AZ-2K1-10-FPA-FPA-800-UL) that suppresses the carrier and produces sidebands at about half the hyperfine splitting, such that the two sidebands are separated by the size of the splitting [30]. With this method we produce rapid scans of the sidebands [31] that minimize many systematic effects compared to scanning the carrier frequency [15]. For instance, we are less sensitive to atom number fluctuations or laser frequency drifts, and the frequency axis of the scan can be precisely characterized since it lies in the microwave regime. We produce the microwaves with phase-locked-loop synthesizers referenced to a Rb clock (SRS FS275). The frequency sweep

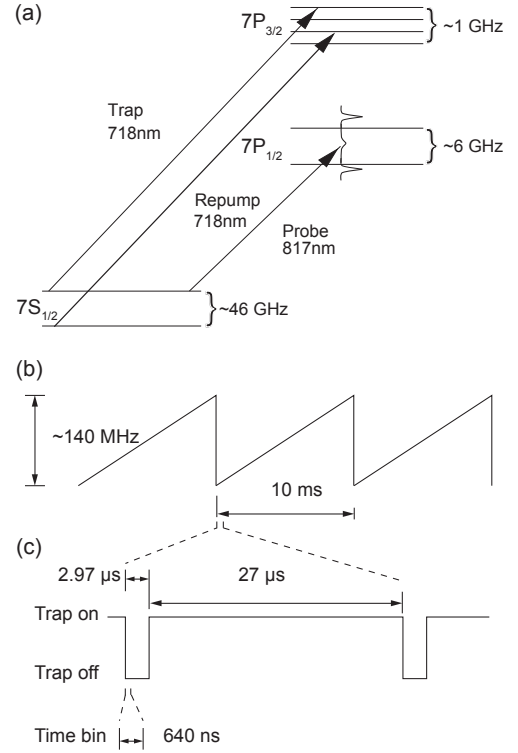


FIG. 1. Measurement scheme. (a) Atomic energy levels relevant for trapping and measuring. (b) Sideband frequency scan around 2.9 GHz (isotope-dependent). (c) Time sequence for trapping and data collection.

covers 140 MHz in 10 ms (Fig. 1(b)). The probe beam has a 3 mm diameter with 100 μ W power in each sideband and is retro-reflected to minimize trap displacement from radiation pressure imbalance.

We collect the fluorescence light with a double relay imaging system (numerical aperture of 0.12) with an interference filter at 817 nm and an edge filter at 795 nm to suppress background light, in particular the trapping laser at 718 nm. A photomultiplier tube (Hamamatsu H7422-50) operating in photon counting mode detects the fluorescence, and we record the photon events as a function of time with a multichannel scaler (SRS SR430). We use a typical bin width of 640 ns with count rates below 250 kilocounts/s. We avoid the ac Stark shift from the MOT trapping light with an experimental cycle of 27 μ s of trapping followed by 2.97 μ s of probing with the trap laser off (Fig. 1(c)). Data with signal-to-noise ratios of $\gtrsim 20$ are obtained within a few seconds. Fig. 2 shows a typical spectrum, which yields a HFS splitting with statistical uncertainty at the 30 kHz level. The two peaks indicate the modulation frequency where the +1 (-1) sideband is resonant with the upper (lower) hyperfine peak.

The linear Zeeman effect is the dominant systematic uncertainty, because the quadrupole magnetic field of the MOT stays on during the measurement, and the atoms pop-

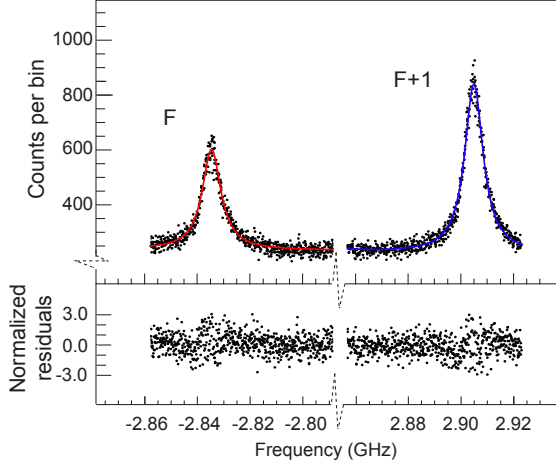


FIG. 2. Sample of experimental data. Top: Fluorescence counts as a function of sideband frequency for ^{213}Fr with separate Lorentzian fits to each of the resonances. The hyperfine splitting is the difference of the frequency position of the two peaks and it gives 5739.60 ± 0.030 MHz. Bottom: Normalized residuals of the fits.

ulate all Zeeman sub-levels. We characterized this effect by changing the magnetic field gradient (7 to 15 G/cm), probe laser polarization (linear as used in the measurement, to circular), and the position of the atom cloud (1 mm dislocation). We put an upper bound of 540 kHz systematic uncertainty from the Zeeman shift. This agrees well with auxiliary tests in Rb. The sideband laser power changes during the scan due to RF power variations, which contributes to a background structure in the data. We take scans without the trapped atoms to record this background. These variations, in addition to line-asymmetries caused by laser drifts during the data accumulation, create small line-shape deviations from a Lorentzian function, as can be seen in the residual structures of the fit in Fig 2. We evaluate a systematic uncertainty of 100 kHz from the line-shape distortions. The differential ac Stark shift from the trap laser is mitigated by the fast chopping technique, and the shift from the repump laser is 90 kHz with an uncertainty of 60 kHz [32]. Other potential systematic effects include Doppler shifts, probe laser power, frequency calibration and linearity of the scan, which we all evaluated to be at a negligible level. The total systematical uncertainty is 552 kHz.

Table I shows the hyperfine splittings of the $7P_{1/2}$ state for the five isotopes from this work, together with those reported in Ref. [15]. The uncertainty includes both the statistical and systematic error contributions stated above. For ^{209}Fr and ^{221}Fr we find good agreement with Ref. [15] and Ref. [33], respectively, with smaller error bars. The table also lists the ratio $R_{\text{HFS}}(A)$ introduced in Eq. 2, based on the literature values for the $7S_{1/2}$ splittings [34–37]. The normalized ratio of the hyperfine anomalies

TABLE I. Isotope, spin (I), $7P_{1/2}$ hyperfine splittings (HFS) and ratio $R_{\text{HFS}}(A)$ of $7S_{1/2}$ and $7P_{1/2}$ splittings for $^{206-213,221}\text{Fr}$. We illustrate the neutron orbital configuration (ν orbital) and its spin alignment with respect to the total nuclear spin (ν spin).

Isotope	I	HFS($7P_{1/2}$)	$R_{\text{HFS}}(A)$	ν orbital	ν spin
^{206g}Fr	3	6009.14(55)	7.6022(14) ^b	$ap_{3/2} + bf_{5/2}$	$\downarrow\nu\uparrow I$
^{206m}Fr	7	6521.56(57)	7.6086(10) ^c	$f_{5/2}$	$\uparrow\nu\uparrow I$
207	4.5	5559.04(55)	7.6308(12) ^d		
208	7	6561.0(2.3) ^a	7.6053(30) ^{c,d}	$f_{5/2}$	$\uparrow\nu\uparrow I$
209	4.5	5639.5(1.0) ^a	7.6307(16) ^d		
209	4.5	5638.36(56)	7.6323(13) ^d		
210	6	6150.9(1.3) ^a	7.6035(17) ^d	$f_{5/2}$	$\uparrow\nu\uparrow I$
211	4.5	5710.5(1.0) ^a	7.6297(15) ^d		
212	5	6556.0(1.0) ^a	7.6042(17) ^d	$p_{1/2}$	$\uparrow\nu\uparrow I$
213	4.5	5739.43(55)	7.6292(18) ^e		
221	2.5	2431.0(55)	7.6581(26) ^d		
221	2.5	2433.0(3.9) ^f	7.652(12) ^d		

^a Ref. [15]. The $7S_{1/2}$ values come from ^b Ref. [34], ^c Ref. [35], ^d Ref. [36], ^e Ref. [37]. For ^{208}Fr , the HFS($7S_{1/2}$) is the weighted average and scaled uncertainty of the two measurements following Ref. [38]. ^f Ref. [33].

$R_{\text{HFS}}(A)/R_{\text{HFS}}(213)$ (with ^{213}Fr taken as the reference isotope for convenience), in a chain of isotopes $A = 206-213$ and 221 is shown in Fig. 3. The isotopes span neutron numbers between $N = 119$ to 134 . The red squares correspond to measurements from Ref. [15], and the blue diamonds are the new results. For $A = 206$ we measured both the low spin ($I = 3$) nuclear ground state ^{206g}Fr , and the first high-spin ($I = 7$), long-lived isomeric state ^{206m}Fr (lifetime > 10 s, deduced from MOT lifetime). We clearly distinguish ^{206m}Fr from ^{206g}Fr in the MOT due to their different trapping and repumping laser frequencies.

The shell model explains reasonably well the magnetic moments of the light Fr isotopes near $N = 126$ [39]. We consider only the dominant orbitals of single nucleons in the shell model to calculate hyperfine anomaly differences for the $7S_{1/2}$ and $7P_{1/2}$ electronic states [7, 22]. The total anomaly combining the proton and the neutron is given by [7]

$$\epsilon_S - \epsilon_P = \epsilon_\pi \beta_\pi + \epsilon_\nu \beta_\nu, \quad (3)$$

where $\beta_{\pi,\nu}$ are the fractional contributions to the magnetic moment from the proton and the neutron, respectively. The calculated anomalies (in %) for a valence proton (ϵ_π) or neutron (ϵ_ν) for $\pi h_{9/2}$, $\nu p_{1/2}$, $\nu f_{5/2}$, and $\nu p_{3/2}$ orbitals are -0.57 , -3.13 , -2.75 , and -1.75 respectively. The total anomaly is represented by the green circles in Fig. 3. Even though the single particle neutron anomalies are a few times larger than that of the proton, the neutron fractional contribution β_ν is typically only 15%, depending on the orbitals, yielding a contribution from the valence neutron of about the same size as the calculated proton anomaly.

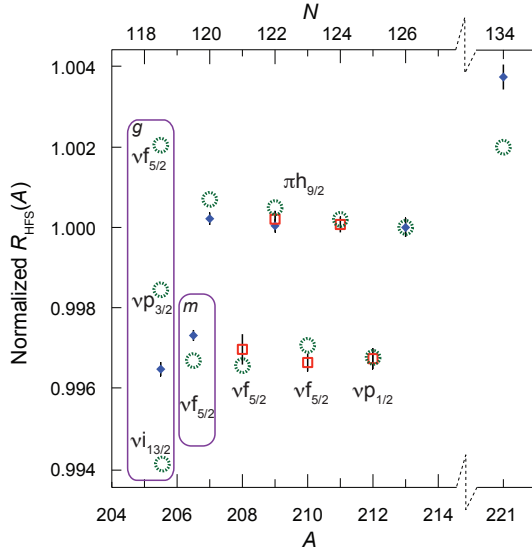


FIG. 3. (color online) $R_{\text{HFS}}(A)$ as defined in Eq. 2, for several Fr isotopes normalized to the value for ^{213}Fr (closed neutron shell $N=126$). Blue diamonds are current measurements. Red squares are from Ref. [15]. The green circles are predictions based on Ref. [22]. The ground state ^{206g}Fr is shown to the left of the isomer ^{206m}Fr . Both are enclosed in rectangles with the respective calculations. The proton resides on the indicated $\pi h_{9/2}$ orbital.

Our data shows that the even-odd staggering trend is preserved from ^{213}Fr with a closed neutron shell, down to ^{206}Fr . The neutron-deficient odd-even isotopes $^{207,209,211,213}\text{Fr}$ all have near-constant anomalies, differing by a small amount consistent with variations due to the changes in the charge distribution (BR effect) [23–27]. This confirms the previous assumption that the anomaly in these isotopes is due primarily to the single valence proton in the $\pi h_{9/2}$ orbital of the spherical shell [15]. ^{221}Fr is also odd-even, with the valence proton in the same $\pi h_{9/2}$ orbital. However the 8 neutrons above closed shell create deformation, leading to a rather different anomaly, which we explain in more detail later. For odd-odd isotopes ($^{208,210,212}\text{Fr}$), the calculations for the respective neutron orbitals are in good agreement with the experimental data.

For ^{206g}Fr , there are some differences compared to a pure $\nu p_{3/2}$ orbital, which also holds for the magnetic moment [34, 35, 40]. However other nearby orbitals ($\nu f_{5/2}$ or $\nu i_{13/2}$) give very different values, or even opposite signs with respect to the normalization. The calculations using

different orbitals for ^{206g}Fr are shown in Fig. 3. We note that the odd-odd isotopes have the same sign and roughly the same value of the neutron anomaly contribution. This is a coincidence resulting from the angular momentum coupling, even though their neutron orbitals and nuclear spins are different. This is illustrated by the fact the calculation for lower nuclear spin ($I = 3$) $\nu f_{5/2}$ (^{206g}Fr) produces an opposite sign compared to the higher spin isotopes ($^{206m,208,210}\text{Fr}$), as $I = 3$ demands the neutron spin to be anti-aligned with the total nuclear spin (see the last column of Table I).

Deviating from the spherical shell model, the Nilsson picture [41] considers the nuclear energy level changes due to a deformation. Calculations [43] have shown that the $f_{5/2}$ and $p_{3/2}$ neutron orbitals have a level-crossing of the $[521\ 1/2]$ and $[503\ 5/2]$ sub-states at a very small (negative) deformation parameter $|\epsilon_2| \leq 0.05$, a range consistent with the measured quadrupole moment [35]. The valence neutron of ^{206}Fr can have a mixture of these two orbitals, which shows effects in the magnetic moment [35]. The anomaly is more sensitive to this orbital mixture, and could have a value outside of the range delimited by the two pure orbital predictions. This is because operator evaluations such as $\langle f_{5/2} | r^2 | p_{3/2} \rangle$ break the orthogonality of the two eigenfunctions, resulting a linear dependence of the anomaly to such mixtures, compared to the quadratic dependence of the magnetic moment.

The neutron-rich odd-even isotope ^{221}Fr has only the proton anomaly contribution. Its Nilsson deformation parameter lies in a positive small to intermediate range, $0.1 \leq \epsilon_2 \leq 0.2$ [16], and the valence proton still occupies the $h_{9/2}$ orbital. However, its angular momentum projects on to the nuclear symmetry axis, such that the nuclear spin becomes $I = 5/2$ [43]. Calculations in [43] yield more than 95% of the wavefunction in the $\pi h_{9/2}[523\ 5/2]$ state. Treating ^{221}Fr with this predominant contribution we obtain a correct sign of the anomaly with respect to ^{213}Fr , as shown in Fig. 3, and a magnetic moment of $+1.85\ \mu_N$, in reasonable agreement with the value $+1.58(3)\ \mu_N$ empirically scaled from the hyperfine splitting [16]. We note that this is a considerably simpler picture than the nuclear model used in Ref. [16]. The Nilsson calculations are parameter-dependent, and the states with lower angular momentum projections used in Ref. [16] would involve more contributions from configuration mixing effects.

In conclusion we present precise measurements of the $7P_{1/2}$ hyperfine splitting in several francium isotopes. The results allow us to study the hyperfine anomaly starting from a closed neutron shell (^{213}Fr $N = 126$) with a simple nuclear distribution, to the boundaries of the single-particle spherical shell model. We demonstrate high-quality spectroscopic measurements, both with ground state nuclei as well as with an isomer. The present results provide the basis for testing the validity and accuracy of future nuclear structure calculations, which will be necessary to extract weak interaction physics from parity non-conservation

measurements in francium.

We thank A. Poves for helpful discussions. We acknowledge support from DOE and NSF from the USA, NRC through TRIUMF and NSERC from Canada, and CONACYT from Mexico. R.C. acknowledges financial support from a University of Manitoba Graduate Fellowship.

-
- [1] C. S. Wood, S. C. Bennett, D. Cho, B. P. Masterson, J. L. Roberts, C. E. Tanner, and C. E. Wieman, *Science* **275**, 1759 (1997).
 - [2] V. V. Flambaum and D. W. Murray, *Phys. Rev. C* **56**, 1641 (1997).
 - [3] W. C. Haxton, C. P. Liu, and M. J. Ramsey-Musolf, *Phys. Rev. C* **65**, 045502 (2002).
 - [4] W. Wilburn and J. Bowman, *Phys. Rev. C* **57**, 3425 (1998).
 - [5] B. M. Roberts, Y. V. Stadnik, V. A. Dzuba, V. V. Flambaum, N. Leefer, and D. Budker, *Phys. Rev. D* **90**, 096005 (2014).
 - [6] A. Bohr and V. F. Weisskopf, *Phys. Rev.* **77**, 94 (1950).
 - [7] S. Büttgenbach, *Hyperfine Interactions* **20**, 1 (1984).
 - [8] M. Tandecki, J. Zhang, R. Collister, S. Aubin, J. A. Behr, E. Gomez, G. Gwinner, L. A. Orozco, and M. R. Pearson, *Journal of Instrumentation* **8**, P12006 (2013).
 - [9] E. Gomez, S. Aubin, G. D. Sprouse, L. A. Orozco, and D. P. DeMille, *Phys. Rev. A* **75**, 033418 (2007).
 - [10] N. Leefer, L. Bougas, D. Antypas, and D. Budker, arXiv: 1412.1245 (2014).
 - [11] M. Nuñez Portela, J. van den Berg, H. Bekker, O. Böll, E. Dijck, G. Giri, S. Hoekstra, K. Jungmann, A. Mohanty, C. Onderwater, B. Santra, S. Schlessler, R. Timmermans, O. Versolato, L. Wansbeek, L. Willmann, and H. Wilschut, *Hyperfine Interactions* **214**, 157 (2013).
 - [12] L. Bougas, G. E. Katsoprinakis, W. von Klitzing, J. Sapirstein, and T. P. Rakitzis, *Phys. Rev. Lett.* **108**, 210801 (2012).
 - [13] S. B. Cahn, J. Ammon, E. Kirilov, Y. V. Gurevich, D. Murphree, R. Paolino, D. A. Rahmlow, M. G. Kozlov, and D. DeMille, *Phys. Rev. Lett.* **112**, 163002 (2014).
 - [14] B. M. Roberts, V. A. Dzuba, and V. V. Flambaum, arXiv: 1412.6644v1, to appear in *Annual Review of Nuclear and Particle Science*, vol. **65** (2015).
 - [15] J. S. Grossman, L. A. Orozco, M. R. Pearson, J. E. Simsarian, G. D. Sprouse, and W. Z. Zhao, *Phys. Rev. Lett.* **83**, 935 (1999).
 - [16] C. Ekström, L. Robertsson, and A. Rosén, *Physica Scripta* **34**, 624 (1986).
 - [17] E. Gomez, S. Aubin, L. A. Orozco, G. D. Sprouse, E. Iskrenova-Tchoukova, and M. Safronova, *Phys. Rev. Lett.* **100**, 172502 (2008).
 - [18] J. R. Persson, *Eur. Phys. J. A* **2**, 3 (1998).
 - [19] A. E. Barzakh, L. K. Batist, D. V. Fedorov, V. S. Ivanov, K. A. Mezilev, P. L. Molkanov, F. V. Moroz, S. Y. Orlov, V. N. Panteleev, and Y. M. Volkov, *Phys. Rev. C* **86**, 014311 (2012) and *Phys. Rev. C* **88**, 024315 (2013).
 - [20] S. Zemlyanoi, D. Karaivanov, Y. Gangrsky, K. Marinova, B. Markov, and J. Badamsambuu, *Hyperfine Interactions* **196**, 107 (2010).
 - [21] J. Persson, *Atomic Data and Nuclear Data Tables* **99**, 62 (2013).
 - [22] H. H. Stroke, R. J. Blin-Stoyle, and V. Jaccarino, *Phys. Rev.* **123**, 1326 (1961).
 - [23] J. E. Rosenthal and G. Breit, *Phys. Rev.* **41**, 459 (1932).
 - [24] M. F. Crawford and A. L. Schawlow, *Phys. Rev.* **76**, 1310 (1949).
 - [25] H. J. Rosenberg and H. H. Stroke, *Phys. Rev. A* **5**, 1992 (1972).
 - [26] Ann-Marie Martensson-Pendrill, *Phys. Rev. A* **74**, 2184 (1995).
 - [27] The BR effect in the Fr region is at the 10% level of the BW effect, and is model dependent. Our inclusion of this effect is based on the calculation in Ref. [26].
 - [28] P. Bricault, F. Ames, M. Dombisky, P. Kunz, and J. Lassen, *Hyperfine Interactions* **225**, 25 (2014).
 - [29] W. Z. Zhao, J. E. Simsarian, L. A. Orozco, and G. D. Sprouse, *Rev. Sci. Instrum.* **69**, 3737 (1998).
 - [30] The fiber EOM is a Mach-Zehnder interferometer with the offset point locked by a bias controller (YYlabs Micro-MBC-1) to a null point for suppressing the carrier, which contributes to the background signal. We keep the laser locked near the midpoint of the two hyperfine transitions and scan the modulation frequency.
 - [31] R. Collister, G. Gwinner, M. Tandecki, J. A. Behr, M. R. Pearson, J. Zhang, L. A. Orozco, S. Aubin, and E. Gomez (FrPNC Collaboration), *Phys. Rev. A* **90** (2014).
 - [32] By comparing data with the trapping beam on and off we measure a 5 MHz common shift of the two hyperfine transitions, a 250 ± 100 kHz differential shift, and a line width increase from 10 to 14 MHz. We scale this with the repump laser power, taking into account the trap laser detuning, and obtain less than 60 kHz differential Stark shift.
 - [33] Z. -T. Lu, K. L. Corwin, K. R. Vogel, C. E. Wieman, T. P. Dinneen, J. Maddi, and Harvey Gould, *Phys. Rev. Lett.* **79**, 994 (1997).
 - [34] A. Voss, M. R. Pearson, J. Billowes, F. Buchinger, B. Cheal, J. E. Crawford, A. A. Kwiatkowski, C. D. P. Levy, and O. Shelbaya, *Phys. Rev. Lett.* **111**, 122501 (2013).
 - [35] A. Voss, F. Buchinger, B. Cheal, J. E. Crawford, J. Dilling, M. Kortelainen, A. A. Kwiatkowski, A. Leary, C. D. P. Levy, F. Mooshammer, M. L. Ojeda, M. R. Pearson, T. J. Procter, and W. Al Tamimi, *Phys. Rev. C* **91**, 044307 (2015).
 - [36] A. Coc, C. Thibault, F. Touchard, H. T. Duong, P. Juncar, S. Liberman, J. Pinard, J. Lermé, J. L. Vialle, S. Büttgenbach, A. C. Mueller, A. Pesnelle, and the ISOLDE Collaboration, *Phys. Lett. B* **163B**, 66 (1985), and *Nuc. Phys. A* **468**, 1 (1987).
 - [37] H. T. Duong, P. Juncar, S. Liberman, A. C. Mueller, R. Neugart, E. W. Otten, B. Peuse, J. Pinard, H. H. Stroke, C. Thibault, F. Touchard, J. L. Vialle, K. Wendt, and the ISOLDE Collaboration, *Europhys. Lett.* **3**, 175 (1987).
 - [38] K.A. Olive et al. (Particle Data Group), *Chin. Phys. C*, **38**, 090001 (2014), Section 5.5.2, p. 14.
 - [39] C. Ekström, in *Advances in Quantum Chemistry*, Vol. 30, edited by P.-O. Löwdin (Academic Press, San Diego, CA, USA, 1998) pp. 361–378.
 - [40] K. M. Lynch, J. Billowes, M. L. Bissell, I. Budinčević, T. E. Cocolios, R. P. De Groote, S. De Schepper, V. N. Fedosseev, K. T. Flanagan, S. Franchoo, R. F. Garcia Ruiz, H. Heylen, B. A. Marsh, G. Neyens, T. J. Procter, R. E. Rossel, S. Rothe, I. Strashnov, H. H. Stroke, and K. D. A.

Wendt, Phys. Rev. X **4**, 011055 (2014).

[41] B. R. Mottelson, and S. G. Nilsson, Phys. Rev. **99**, 1615 (1955).

[42] We included the calculation for the $\nu i_{13/2}$ orbital because

excited-state nuclei near this region could have this orbital.

However this does not show up in the Nilsson diagrams [43].

[43] J. P. Davidson, *Collective Models of the Nucleus* (Academic Press, New York, 1968).

Isotope shifts in francium isotopes $^{206-213}\text{Fr}$ and ^{221}Fr

R. Collister and G. Gwinner

Department of Physics and Astronomy, University of Manitoba, Winnipeg, Canada MB R3T 2N2

M. Tandecki, J. A. Behr, and M. R. Pearson

TRIUMF, Vancouver, Canada BC V6T 2A3

J. Zhang and L. A. Orozco

JQI, Department of Physics and NIST, University of Maryland, College Park, Maryland 20742, USA

S. Aubin

Department of Physics, College of William and Mary, Williamsburg, Virginia 23186, USA

E. Gomez

Instituto de Física, Universidad Autónoma de San Luis Potosí, San Luis Potosí 78290, Mexico

(FrPNC Collaboration)

(Received 4 June 2014; published 7 November 2014)

We present the isotope shifts of the $7s_{1/2}$ to $7p_{1/2}$ transition for francium isotopes $^{206-213}\text{Fr}$ with reference to ^{221}Fr collected from two experimental periods. The shifts are measured on a sample of atoms prepared within a magneto-optical trap by a fast sweep of radio-frequency sidebands applied to a carrier laser. King plot analysis, which includes literature values for $7s_{1/2}$ to $7p_{3/2}$ isotope shifts, provides a field shift constant ratio of 1.0520(10) and a difference between the specific mass shift constants of 170(100) GHz amu between the D_1 and D_2 transitions, of sufficient precision to differentiate between *ab initio* calculations.

DOI: [10.1103/PhysRevA.90.052502](https://doi.org/10.1103/PhysRevA.90.052502)

PACS number(s): 32.10.Fn, 31.30.Gs, 37.10.Jk, 42.62.Fi

I. INTRODUCTION

The variation in the atomic transition energy between isotopes of the same element is known as the isotope shift. It arises due to a combination of nuclear and atomic effects, requiring detailed knowledge of both for accurate predictions. Isotope shifts provide information about the nuclear charge distribution (for examples, see [1,2]) and are sensitive to electron correlations. They have been employed in the search for space and time variation of the fine-structure constant (α) [3] and play a role where accurate spectroscopic information is required, for example when calculating stellar element abundances [4].

Francium, with its high nuclear charge ($Z = 87$) and relatively simple, alkali electronic configuration, has attracted a lot of attention as a candidate for fundamental symmetry tests [5–7]. These investigations require a thorough knowledge of both the atomic and nuclear structure, in particular the overlap of the electronic wave functions with the nucleus, to which optical isotope shifts are sensitive. The interpretation of atomic parity nonconservation measurements also relies on accurate many-body theory [8], for which isotope shifts provide benchmarks.

In the present work, we measure the optical isotope shift between laser-trapped, cold francium isotopes (see Fig. 1). The isotope shift can be separated into two distinct parts: the field shift, caused by variation in the charge distribution in the nucleus, and the mass shift, caused by the different kinetic energy of the finite-mass nucleus. For a complete treatment of the optical isotope shift, see Refs. [9,10].

The mass shift comes directly from the changing mass of the nucleus. In the center-of-mass frame,

$$\Delta E = \mathbf{P}^2/2M = \left(\sum_i \mathbf{p}_i \right)^2 / 2M, \quad (1)$$

where M is the nuclear mass, \mathbf{P} is the nuclear momentum, and \mathbf{p}_i is the momentum of the i th electron. In all but the lightest of elements, the mass shift can be separated into two parts:

$$\Delta E = \frac{1}{2M} \sum_i \mathbf{p}_i^2 + \frac{1}{M} \sum_{i>j} \mathbf{p}_i \cdot \mathbf{p}_j, \quad (2)$$

where the first term, i.e., the normal mass shift or Bohr reduced mass effect, can be determined exactly and the second term, i.e., the specific mass shift arising from the change in momentum correlations between electrons, is much more difficult to calculate.

Isotope shifts are measured with respect to a reference isotope. The contribution of the normal mass shift to the frequency shift of an optical transition is

$$\delta\nu_{NMS}^{AA'} = \nu(A') \frac{m_e(M_A - M_{A'})}{M_{A'}(M_A + m_e)}, \quad (3)$$

where $\nu(A')$ is the transition frequency of the reference isotope with mass number A' , $M_A(M_{A'})$ is the nuclear mass of the measured (reference) isotope, and m_e is the mass of the electron, which can be neglected in the denominator. The electron correlations for the specific mass shift must be very well known in order to check the theoretical models used to extract, e.g., the time variation of α [3]. Francium, as the heaviest alkali, is more tractable than multivalence electron systems such as lead, making it very suitable for testing calculations. Together, the total mass shift $\delta\nu_{MS}$ between isotopes of mass numbers A and A' , and following the form of Eq. (3), can be written as

$$\delta\nu_{MS}^{AA'} = (N + S) \frac{M_A - M_{A'}}{M_A M_{A'}}, \quad (4)$$

where N, S are the normal and specific mass shift constants.

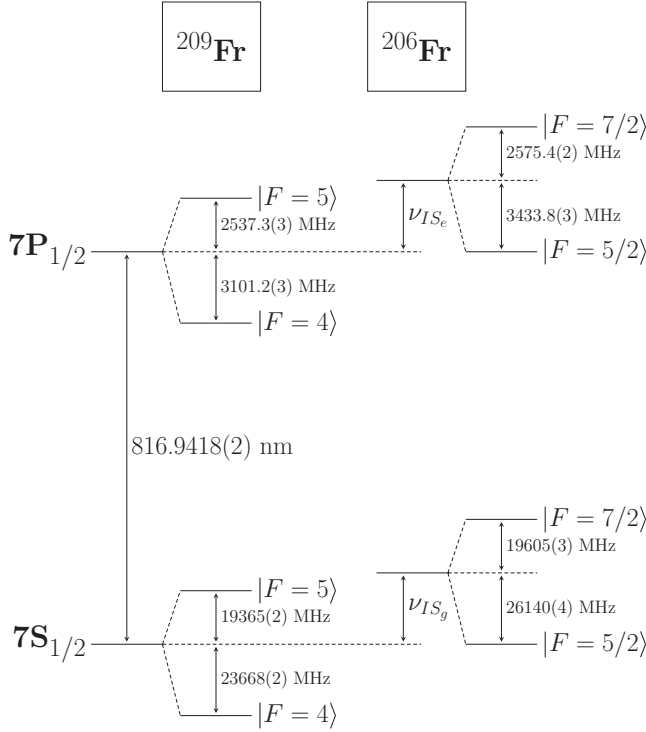


FIG. 1. Energy-level diagram of ^{209}Fr and ^{206}Fr showing the $7s_{1/2}$ and $7p_{1/2}$ levels. The isotope shift of the D_1 line is measured between the centers of gravity of the ground and excited states comprising the transition, i.e., the difference between the isotope shifts of those two states ($\nu_{IS_e} - \nu_{IS_g}$).

The field shift is due to the modification of the point-charge Coulomb potential by a finite-size nucleus. This results in a contraction of the spacings between electronic bound-state energies of an atom. The contraction is isotope dependent so that there is a difference in the transition frequency between isotopes,

$$\delta\nu_{FS}^{AA'} = F\delta\langle r^2 \rangle^{AA'}, \quad (5)$$

where $\delta\langle r^2 \rangle^{AA'}$ is the difference in the mean nuclear charge radii squared of the two isotopes. The field shift constant F is

$$F = -\frac{\pi a_0^3}{Z} \Delta|\psi(0)|^2 f(Z), \quad (6)$$

where $\Delta|\psi(0)|^2$ is the change of the electron charge density at the nucleus between the states involved in the transition and $f(Z)$ is an increasing function of Z that accounts for relativistic and nuclear shape corrections.

The sum of mass and field shifts gives the total isotope shift,

$$\delta\nu_{IS}^{AA'} = (N + S) \frac{M_A - M_{A'}}{M_A M_{A'}} + F\delta\langle r^2 \rangle^{AA'}, \quad (7)$$

which we measure in our experiment and compare to theoretical predictions.

II. EXPERIMENTAL SETUP

We trap neutral francium atoms in a magneto-optical trap (MOT) at the Francium Trapping Facility at TRIUMF in Vancouver, Canada [11]. Francium has no stable isotopes; the TRIUMF Isotope Separator and Accelerator (ISAC) facility delivers up to 10^9 Fr ions s^{-1} , which are high rates for radioactive beam standards, and we trap them to achieve the large densities conducive to high-precision measurements. A 500 MeV, 10 μA proton beam impinges upon a uranium carbide (UCx) target to produce a large range of isotopes. The products are surface ionized on a hot ($\sim 2200^\circ\text{C}$) rhenium-coated tantalum tube, accelerated to ~ 20 keV, and then mass selected by passing through a pair of magnetic dipoles. The francium ions are delivered to the experiment where they accumulate in an yttrium neutralizer foil that is rotated and heated for 1 s, causing the now neutral atoms to emerge from the foil and enter the trapping volume on a 20 s cycle. Roughly 2.5×10^5 atoms with trap lifetime > 10 s for ^{209}Fr are initially trapped before trap losses and radioactive decays reduce that number in the time between yttrium heating pulses. A schematic of the experimental apparatus is available in Fig. 4 of Ref. [11].

The isotope shift measurements we have performed involve the fast radio-frequency (rf) scan of sidebands on a carrier (probe) laser to locate specific transitions in a particular isotope with respect to a reference one. Figure 2 depicts the measurement scheme. First, we collect one isotope in the MOT, such as ^{206}Fr in Fig. 2, tune the probe laser frequency to lie in the hyperfine multiplet of the D_1 line originating from the upper hyperfine ground state, and sweep the sideband frequency in 10 ms to find the transition. Next, we change the isotope in the trap, to, e.g., ^{209}Fr , and sweep the rf sidebands again to find the desired transition while the carrier remains locked. The measured difference in rf frequencies is used to calculate the isotope shift. Data collection occurred during two experimental periods using two different rf generation schemes (details below). In the first period, we measured the isotope shifts of $^{206,207,213}\text{Fr}$ with respect to ^{209}Fr , while the second yielded $^{206,208-212,221}\text{Fr}$ with a fixed laser position and no need to return to a reference for each new isotope.

Our rf sideband method finds the transitions to both excited hyperfine levels. Thus we also obtain the hyperfine splittings to 100 ppm precision, which is sufficient to study changes in the hyperfine anomaly [12]. The hyperfine splittings and nuclear spin are required to calculate the hyperfine shifts of the ground and excited states, which are different for each isotope. These are necessary to extract the isotope shift since we need to locate the center of gravity of the transition. We determine the isotope shift from

$$\delta\nu_{IS} = (\nu_1 - \nu_2) + (\nu_{HF_g} - \nu_{HF_e}) - (\nu_{HF_g} - \nu_{HF_e})_{\text{ref}}, \quad (8)$$

where $\nu_{1,2}$ are the rf frequencies where the hyperfine transitions are observed (see Fig. 2), and $\nu_{HF_{g(e)}}$ are the hyperfine shifts of the ground (excited) states for the measured isotope and the reference. The common probe laser frequency is not included, as it cancels out. The hyperfine shifts are given by

$$\nu_{HF} = \frac{\nu_{HFS}}{2I + 1} [F(F + 1) - I(I + 1) - J(J + 1)], \quad (9)$$

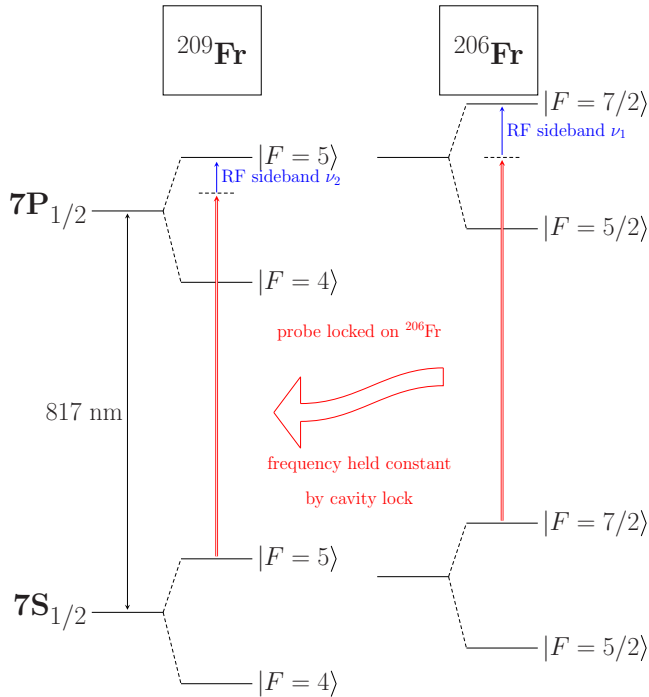


FIG. 2. (Color online) Isotope shift measurement scheme; splittings not to scale. The transition to the upper hyperfine excited state $F = 7/2$ is located in ^{206}Fr and the probe laser frequency is locked using the external Fabry-Perot cavity. Then ^{209}Fr is trapped and the transition to $F = 5$ is located by changing the rf frequency only, leaving the carrier laser frequency unchanged. This difference in rf frequencies gives the D_1 transition isotope shift once we know the hyperfine shifts (see Fig. 1).

where ν_{HFS} is the hyperfine splitting, and I , J , and F are the nuclear spin, electronic, and total angular momentum quantum numbers, respectively.

Our method of setting the carrier laser frequency between the hyperfine levels allows a clean extraction of the total $7p_{1/2}$ splitting independent of the exact carrier laser frequency. The difference of the observed transition centroids in a single scan is the hyperfine splitting; any shift in one centroid position caused by laser offset is canceled by a corresponding shift in the other centroid, assuming there is no laser drift during a single rf sweep.

The probe laser frequency is locked to this position via a scanning Fabry-Perot cavity and a stabilized Melles-Griot 05-STP-901 HeNe laser, transferring the long-term stability of the HeNe to the other laser (for details, see [11,13]). We keep the probe laser locked during the isotope change in the MOT. The probe laser is a Ti:sapphire laser operating at 817 nm; we send linearly polarized light into an EOSpace AZ-2K1-10-PFA-PFA-800-UL amplitude modulator for sideband generation. A fiber carries the probe light to the atoms, and the light is retroreflected to minimize any pushing of the atoms as they scatter photons. The 10 mW/cm^2 in each sideband is enough to saturate the transition, and the fluorescence collects in our detection system (details below) when a sideband frequency is resonant with a hyperfine level.

The laser light for the MOT [14] is produced by a pair of commercial Ti:sapphire ring lasers operating at 718 nm. They are coupled into a fiber splitter to generate the three spatial beams at two frequencies that are retroreflected to trap on each axis. Laser powers delivered to the trap are limited by the coupling fibers, resulting in approximately 20 mW/cm^2 in the trapping beams and 5 mW/cm^2 in the repumping beams; all beams have $1/e^2$ power diameters of 5 cm. Quadrupole magnetic field coils provide a field gradient of 7 G/cm (strong axis). The typical detuning of the trap laser is about 15 MHz, roughly two and a half linewidths detuned to the red. Once the transitions are found, the lasers are locked to the stabilized HeNe via the scanning Fabry-Perot cavity. The stability of the laser-lock system is important and will be discussed below.

Sidebands are generated by an rf signal applied to the fiber modulator, consisting of a lithium niobate electro-optic modulator in one arm of a Mach-Zehnder interferometer. A YYLabs Mini-MBC-1 modulation bias controller card gives a bias voltage to the modulator to keep the carrier suppressed. This increases the power to the sidebands and reduces the scattered light from the carrier.

Two different rf synthesizer setups have been used to measure the isotope shifts. One, employed during the first experimental data collection period, involves Analog Devices (AD) AD4350 synthesizers mounted on a pair of UG-110 evaluation boards to generate the rf frequencies desired. The boards operate using a phase-locked loop (PLL) stabilized voltage controlled oscillator (VCO) referenced to a 10 MHz clock. A continuous output frequency sweep is performed by manipulating the input clock frequency using a Stanford Research Systems DS345 function generator. The scanning range (70 MHz) of one frequency synthesizer is limited to how far the clock can be moved off the nominal set point before the PLL is lost and the VCO becomes unlocked, resulting in output instability and unresponsiveness to further clock manipulation. This frequency-dependent range, along with the 4.4 GHz maximum frequency, limits the isotopes we could measure with these boards using ^{209}Fr as a reference. Two of the boards are employed along with an rf switch synchronized with the clock sweep to pass the correct synthesizer output allowing for $\sim 140 \text{ MHz}$ of continuous frequency scanning.

The second rf setup, used for the second data collection period, uses a Phase Matrix QuickSyn FSW-0020, a direct digital synthesizer using a fundamental VCO and PLL to generate frequencies from 0.5–20 GHz. This synthesizer allows us to tune the probe laser sidebands to any of the D_1 transitions in the isotopes we trap. The output sweep is digitally controlled stepwise at a maximum 7 kHz rate, giving us 70 frequency steps in the 10 ms allocated for each measurement. The probe lockpoint is maintained for all isotopes and the sideband frequency is tuned to locate both D_1 transitions for each isotope once it is trapped. Thus this setup has the additional advantage of not requiring a return to a reference isotope for each subsequent measurement.

On-resonance scattered light is collected by a double-relay optical system and detected by a Hamamatsu H7422 photomultiplier tube (PMT). An interference filter centered at 820 nm and an edge filter with 795 nm cut-on wavelength are in place to block light other than the D_1 line scattered photons in order to reduce background counts. A Stanford Research

Systems SR430 multichannel scaler (MCS) collects the signal from the PMT as a function of time. The MOT operates with trap and repumper lasers on the D_2 line at 718 nm and thus they do not contribute appreciably to the background.

In order to minimize ac Stark shifts of the $7s$ ground state, the trap laser light is extinguished periodically during the 10 ms rf sweep on a $32\ \mu\text{s}$ cycle of 50 MCS bins that are each 640 ns long. The chopping cycle is $21.76\ \mu\text{s}$ (34 bins) with the light on, followed by $7.04\ \mu\text{s}$ (11 bins) with the light extinguished by an acousto-optic modulator with a greater-than- 10^4 extinction factor, and ended by the remaining $3.2\ \mu\text{s}$ (5 bins) with the light back on.

III. RESULTS

We measure the D_1 isotope shifts for isotopes $^{206}\text{--}^{213}\text{Fr}$ with respect to ^{221}Fr . Analysis of the data yields the frequency difference between isotopes of the hyperfine transitions, which we use to calculate the isotope shift [see Fig. 1 and Eq. (8)]. The splittings of the $p_{1/2}$ level are obtained by taking the difference of the sideband frequencies of the two transitions from a single scan [see Fig. 3(a)]. Our reported isotope shifts are ultimately calculated with reference to ^{221}Fr and we recalculate the literature D_2 isotope shifts from reference ^{212}Fr to ^{221}Fr for the King plot analysis which follows.

To obtain the transition frequency difference, we calibrate the frequency of each MCS bin by measuring the output of our frequency generators. The outputs of the latter are mixed down to allow the wave forms to be observed directly on an oscilloscope, where they are captured to be fit to sinusoids at fixed times during the 10 ms scan. The fitted frequencies show that both the AD cards and Phase Matrix synthesizer behave as expected as long as the AD cards remain phase locked to their input clocks. All measured frequencies are as predicted with uncertainties of less than 10 kHz, enabling us to construct a linear frequency-time correspondence of the rf, which we use to calibrate the MCS.

The peaks in the data are fit with Lorentzians on a quadratic background using the ROOT analysis package to determine the centroid of each transition. We do not consider the effect of trap losses or nuclear decays on the fit, as the 10 ms scan length is

TABLE I. Overview of our measurements and literature values that are relevant for calculating isotope shifts to be used for a King plot. Literature D_2 isotope shifts ($\delta\nu_{IS}$) are reported with ^{212}Fr as the reference, with the exception of the ^{206}Fr D_2 value, which is measured with respect to ^{208}Fr . They have been recalculated using the ^{212}Fr to ^{221}Fr isotope shift from [16] to be common with our D_1 isotope shifts. Nuclear spins and $A(S_{1/2})$ values are from the literature and $A(P_{1/2})$ are from our measurements [12]. The final isotope shift uncertainty reported in parentheses is a combination of our measurement uncertainty and the A coefficient uncertainties needed to calculate the centers of gravity.

Isotope	This work		Spin	Literature values		Source
	$A(P_{1/2})$ (MHz)	$D_1\delta\nu_{IS}$ (MHz)		$A(S_{1/2})$ (MHz)	$D_2\delta\nu_{IS}$ (MHz)	
206	1716.9(2)	29175(5)	3	13052.2(20)	30684(5)	[17]
207	1111.9(1)	27432(6)	9/2	8484.(1)	28809(5)	[16]
208	874.68(8)	27210(4)	7	6650.7(8)	28573(4)	[16]
209	1127.7(1)	25432(3)	9/2	8606.7(9)	26698(4)	[16,18]
210	946.33(9)	24927(3)	6	7195.1(4)	26178(4)	[16,18]
211	1142.1(1)	23300(5)	9/2	8713.9(8)	24465(4)	[16,18]
212	1192.2(1)	22437(4)	5	9064.4(15)	23570(2)	[16,19]
213	1147.9(1)	20869(7)	9/2	8757.4(19)	21929(3)	[16,19]
221	811.5(2)	0	5/2	6209.9(10)	0	[16,19]

much shorter than the 20 s lifetime of the trap or the 15 second to 20 minute half lives of the isotopes. Statistical uncertainties from these fits are less than 100 kHz and in some cases less than 15 kHz. The peaks typically have Lorentzian widths of 8 MHz for data collected with the trap light off; this is partly due to saturation broadening of the 5.4 MHz natural linewidth, calculated from the measured lifetime of the $7p_{1/2}$ state [15].

An example scan is provided in Fig. 3 for the ^{206}Fr to ^{209}Fr D_1 isotope shift. Table I summarizes the results; the reported errors for the D_1 isotope shifts are the quadratic sums of the measurement error, and hyperfine shift errors, calculated from $A(s_{1/2})$ and $A(p_{1/2})$ errors and nuclear spins, for both the measured isotopes and the reference ^{221}Fr . Additionally, we measured the $7p_{1/2}$ hyperfine splitting of $^{206}\text{Fr}^m$ ($t_{1/2} \approx 16$ s) to be 6524.3(6) MHz and the shifts with respect to ^{221}Fr for the

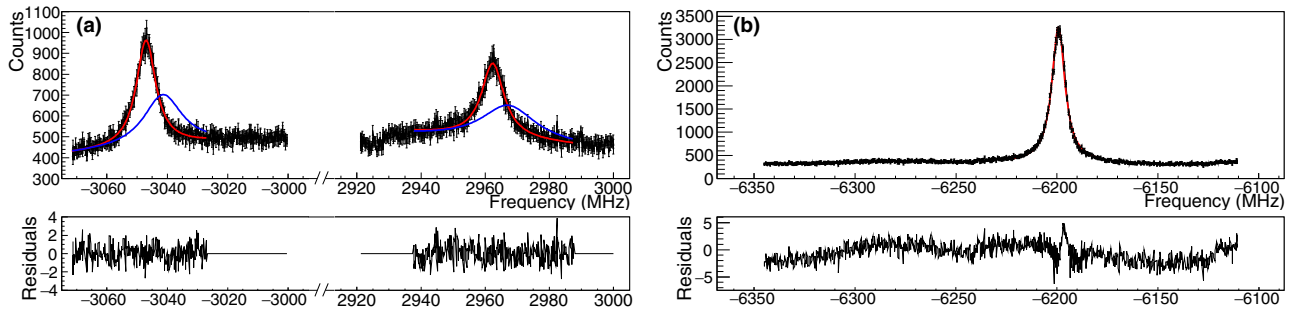


FIG. 3. (Color online) Data of (a) the $7p_{1/2}$ splitting of ^{206}Fr and (b) the reachable transition in ^{209}Fr using the AD4350 rf generator along with the normalized residuals of their fits. The Lorentzian fits on a quadratic background are shown (red line). The hyperfine splitting of the excited state is obtained from scans such as (a), where it is the difference of the centroids of both peaks. The blue lines show the ac Stark shifted peaks in the presence of the trapping laser light (data points not shown). The reference isotope measurement for the isotope shift shows a single transition peak; the other is roughly 6 GHz away, well outside the range of our scan. Transitions are identified by knowing the directions of both the probe laser detuning from the midpoint and rf sweep.

D_1 transition (i.e., rf frequencies $\nu_1 - \nu_2$) to be 11774(2) MHz for the transitions involving the lower $7p_{1/2}$ states and 15864(2) MHz for the upper $7p_{1/2}$ states. Without knowing the nuclear spin or the $A(s_{1/2})$, we cannot extract an isotope shift or $A(p_{1/2})$ value from those measurements.

The dominant systematic effect in our isotope shift measurement is given by the laser-lock drift; all other contributions are well below this one. Other sources of systematic error are ac Stark shifts, Zeeman shifts, and background contributions. These are more important for the hyperfine splitting measurement as laser drift in this case causes a broadening but no shift in the observed transition energy.

Our laser-locking system exhibits slow drifts over the time between measurements as the isotope in the trap was changed. This involves changes in the mass separator of the ISAC facility as well as changing the laser frequencies, and took between 30 to 60 minutes before the next isotope was measured. Long-term observations of the Fabry-Perot cavity and helium-neon laser exhibited drifts below 3 MHz over periods of one hour for the system in use during the first experiment. The drift was determined by feeding into the cavity a laser stabilized via saturated absorption spectroscopy in rubidium. We discovered the drift was largely due to uncontrolled feedback by back reflection from optical surfaces into the HeNe laser, temperature drift-induced expansion of the cavity tube, and nonlinearity of the piezo scanning the cavity length. Thus, for our first isotope shift measurements, we conservatively place the sum of systematic errors at ± 3 MHz, dominated by the laser-lock drift. Many of these laser stability issues were improved for the second set of measurements; we introduced an optical isolator to prevent feedback into the HeNe, the cavity is held under vacuum and is temperature locked via proportional-integral-derivative control, and we lock the probe laser to a frequency such that its locking peak in the cavity nearly coincides with that of the HeNe, suppressing piezo nonlinearity effects on the measurement. These improvements reduce the systematic error of the laser drifts to below ± 2 MHz.

The ac Stark shift of the ground state by the D_2 line excitation is eliminated by chopping the trapping laser light while the rf sideband sweep is occurring. For the splitting measurements, any shift present is canceled to first order by having the probe frequency set between the two transition frequencies; any change in the ground state shifts the measured transition frequencies the same amount, which cancels when taking the difference. The repumper frequency is set an isotope-dependent approximate 43 GHz away, making its contribution to the Stark shift negligible. The ac Stark shift of the ground state from the off-resonance probe laser sideband is estimated at less than 180 kHz based on measured intensity and detunings.

Zeeman shift is due to nonzero magnetic fields across the atom cloud in the trap and must be accounted for as the quadrupole magnetic field of the MOT remained on when taking a measurement. The effect of the magnetic field is estimated by two methods: varying the current in the quadrupole coils generating the field and changing the polarization of the light exciting the D_1 transition. The change in polarization will induce transitions between different magnetic sublevels or m_F states by the usual selection rules, each of which has a

m_F -dependent Zeeman shift. Furthermore, even with perfectly linear light, we would still induce $\Delta m_F = 0, \pm 1$ due to the changing direction of the quadrupole field around the zero point. We performed these tests both online with francium and offline with rubidium; both alkalis have very similar behavior in magnetic fields. Altogether, the measurements place an upper bound on the contribution to the systematic error by the magnetic field of 540 kHz.

Background counts are minimized by the spatial filtering of the imaging system: a double relay with an aperture at the image plane. An interference filter centered around 820 nm in front of the PMT and chopping the trap laser during measurement also reduce background counts. Additionally, proper control of the fiber modulator voltage bias greatly suppresses the intensity of the carrier output, reducing its contribution to background. We did observe fluctuations in the shape of the background. These are likely caused by drifts in the phase between paths through the amplitude fiber modulator, due to small changes in temperature or bias voltage, resulting in more background light at the carrier frequency. Investigating this effect over many scans by fitting with different-order polynomials changes the fit centroid less than 100 kHz and we add this to the systematic uncertainty.

Additionally, there is a systematic uncertainty introduced from the literature $A(s_{1/2})$ values that we use to calculate the ground-state hyperfine shift [16–19] required to find the center of gravity and hence the isotope shift. Measurement of this quantity constitutes an entirely different experimental technique, and we do not currently have the means to measure these 40–50 GHz splittings ourselves. Therefore, we add the 1–4 MHz uncertainties calculated from the published ground-state values to our isotope shift measurement uncertainty.

IV. KING PLOT ANALYSIS

In all but the lightest nuclei, a King plot [10] separates the mass and field shift components of the isotope shift and allows comparison between different atomic transitions. The plot requires isotope shifts for two atomic transitions as well as the masses [20] of the isotopes measured. Our measurements on the D_1 line along with existing data for the D_2 line [16–18] provide shifts in eight francium isotopes with respect to ^{221}Fr . Taking Eq. (7) for two transitions and combining them to eliminate $\langle r^2 \rangle^{AA'}$ gives

$$\left(\frac{M_A M_{A'}}{M_A - M_{A'}} \right) \delta \nu_{IS, D2} = (N_{D2} + S_{D2}) - (N_{D1} + S_{D1}) \frac{F_{D2}}{F_{D1}} + \frac{F_{D2}}{F_{D1}} \left(\frac{M_A M_{A'}}{M_A - M_{A'}} \right) \delta \nu_{IS, D1}, \quad (10)$$

a linear equation in isotope shifts weighted by isotopic masses, which we shall call the modified isotope shifts (MIS), with a slope given by the ratio of the field shift constants and intercept dependent on the differences in the mass shift constants. The normal mass shift can be calculated exactly; thus the intercept can be used to determine the difference in specific mass shift constants. A deviation from unity of the slope tells the ratio of the electronic overlap with the nucleus of the $7p_{1/2}$ and $7p_{3/2}$ states.

The King plot in Fig. 4 uses isotopes $^{207-213}\text{Fr}$, with ^{221}Fr as a reference; ^{206}Fr is excluded from the fit for reasons discussed below. We find that $F_{D2}/F_{D1} = 1.0520(10)$ and $(N_{D2} + S_{D2}) - (N_{D1} + S_{D1}) \frac{F_{D2}}{F_{D1}} = 190(100)$ GHz amu with $\chi^2/ndf = 4.996/5$. The normal mass shift constants are $N_{D1} = 201$ and $N_{D2} = 229$ GHz amu from Eq. (3) with negligible errors given by the uncertainty in atomic masses. This leaves the specific mass shift constant difference (δS) between the two transitions $\delta S = S_{D2} - S_{D1} \frac{F_{D2}}{F_{D1}} = 170(100)$ GHz amu.

The outlier of ^{206}Fr (labeled in red in Fig. 4) requires a comment. This isotope was measured in our two data collections with results in agreement with each other from the different methods, suggesting it is not a measurement error. There is a 10σ deviation from the straight-line fit that we are unable to explain. Including this isotope in the fit produces a $\chi^2/ndf = 38.6/6$, again with the point falling 6σ away from the fit line; thus it is likely that there is some physical reason for the discrepancy. Evaluation of the complicated considerations in a more complete field shift theory [21] proves insufficient to explain this discrepancy; we are not at a sensitivity to observe those higher-order effects, which come in at the few MHz level and are within our error bars. It is possible some nuclear effect is responsible for this deviation; the unusual nuclear magnetic dipole and spectroscopic electric quadrupole likewise suggest the ^{206}Fr nucleus deviates from the behavior exhibited by the heavier $A \leq 213$ isotopes [17].

There is a known correction to the field shift from the electronic density changing over the nuclear volume, which depends on the nuclear charge distribution [21]. The corrections in $\delta\langle r^4 \rangle$ and $\delta\langle r^6 \rangle$ can be related in various basic nuclear charge distributions to the change in charge radii $d\langle r^2 \rangle/dA$ [22]. This quantity then shows odd-even staggering. However, such a phenomenological correction would be within the errors of our measurements, and an inspection of the residuals in Fig. 4 show no significant difference between the odd-odd and even-even isotopes. This effect is unable to account for our discrepancy.

Furthermore, these higher-order corrections make the field shift coefficients F isotope dependent. Thus, since we are mainly concerned with the atomic calculations behind the isotope shift N, S, F values as predicted from theory, we will exclude ^{206}Fr from the linear fit used to evaluate those coefficients.

Using ^{212}Fr as the reference isotope minimally shifts the fit results. The χ^2/ndf is slightly poorer at 5.047/5 and the slope has moved 0.5 σ to 1.0526(7). The change in the fit is due to the systematic errors in the measurement of the reference isotope; that common error is now with respect to ^{212}Fr instead of ^{221}Fr . Furthermore, using ^{212}Fr as the reference puts the ^{221}Fr King plot point in a location that dominates the fit. Therefore, we will continue to use ^{221}Fr as the reference isotope.

Calculations for the field shift and specific mass shift constants have been performed using several methods: many-body perturbation theory and closed-cluster approaches [8], as well as many-body perturbation theory calculation [23]. Our results and their predictions are summarized in Table II for the field shifts and Table III for the specific mass shifts. In Table III, the finite field result uses the average of three different methods

TABLE II. Field shift constants (MHz/fm²) obtained from three theoretical methods along with the experimental ratio (uncertainty) obtained from the King plot analysis shown in Fig. 4.

Method	$7S_{1/2}$	$7P_{1/2}$	$7P_{3/2}$	F_{D2}/F_{D1}
$BO(\Sigma^\infty)^a$	-20463	-693	303	1.0504
$SD + E3^a$	-20188	-640	361	1.0512
M-P ^b	-20782	-696	245	1.0468
Expt. (this work)				1.0520(10)

^aDzuba, Johnson and Safronova [8].

^bMårtensson-Pendrill (M-P) [23]

which vary in their consideration of higher-order effects and the fourth column uses the $(SD + E3)$ value from Table II for F_{D2}/F_{D1} for the results from [8]. Using the $[BO(\Sigma^\infty)]$ value instead would cause no change at this sensitivity. The fit of the King plot agrees with the field shift constants predicted by the closed-cluster method $(SD + E3)$ at the 1σ level and with the perturbation theory $[BO(\Sigma^\infty)]$ method at the 2σ level, and does not agree with the prediction from [23]. The specific mass shift constants extracted from this King plot intercept agree with the finite field and Mårtensson-Pendrill (M-P) results at the 1σ level and the perturbation theory at the 2σ level.

We can also fix the F_{D2}/F_{D1} ratio to theory and see what specific mass shift constants fit our data. The slope of the King plot is set in turn to the theory values and the resulting δS are displayed in Table III. These δS exhibit a linear trend as a function of field shift ratio. Fitting this line results in

$$\delta S = (102 \pm 2) \times 10^3 \left(\frac{F_{D2}}{F_{D1}} - 1.0520 \right) + 170 \pm 7, \quad (11)$$

allowing a δS value (in GHz amu) to be calculated from our measurements for any future field shift theory predictions.

The deviation from unity in the experimental King plot slope of 0.0520(10) corresponds to a 2% measurement. The total ratio has been measured to 0.1%, well below the stated 1% accuracy of the theory [8]. This analysis is limited by our reliance on previous D_2 line measurements and the ground-state hyperfine A coefficients extracted from those measurements. Our D_1 isotope shift uncertainties are inflated

TABLE III. Specific mass shift constants (GHz amu) obtained from three theoretical methods along with the experimental value (uncertainty) obtained from the King plot analysis shown in Fig. 4. The results from fixing the King plot slope to the different theory values are also shown.

Method	$7S_{1/2}$	$7P_{1/2}$	$7P_{3/2}$	δS
PT ^a	-786.1	-53	7.9	24
FF ^a	-237	-62	77	130
M-P ^b	-570	-154	-18	117
Expt. (this work)				170(100)
Fixed slope $BO(\Sigma^\infty)$				90(9)
Fixed slope $SD + E3$				8(9)
Fixed slope M-P				-359(9)

^aPerturbation theory (PT) and finite field (FF) approaches [8].

^bMårtensson-Pendrill (M-P) [23]

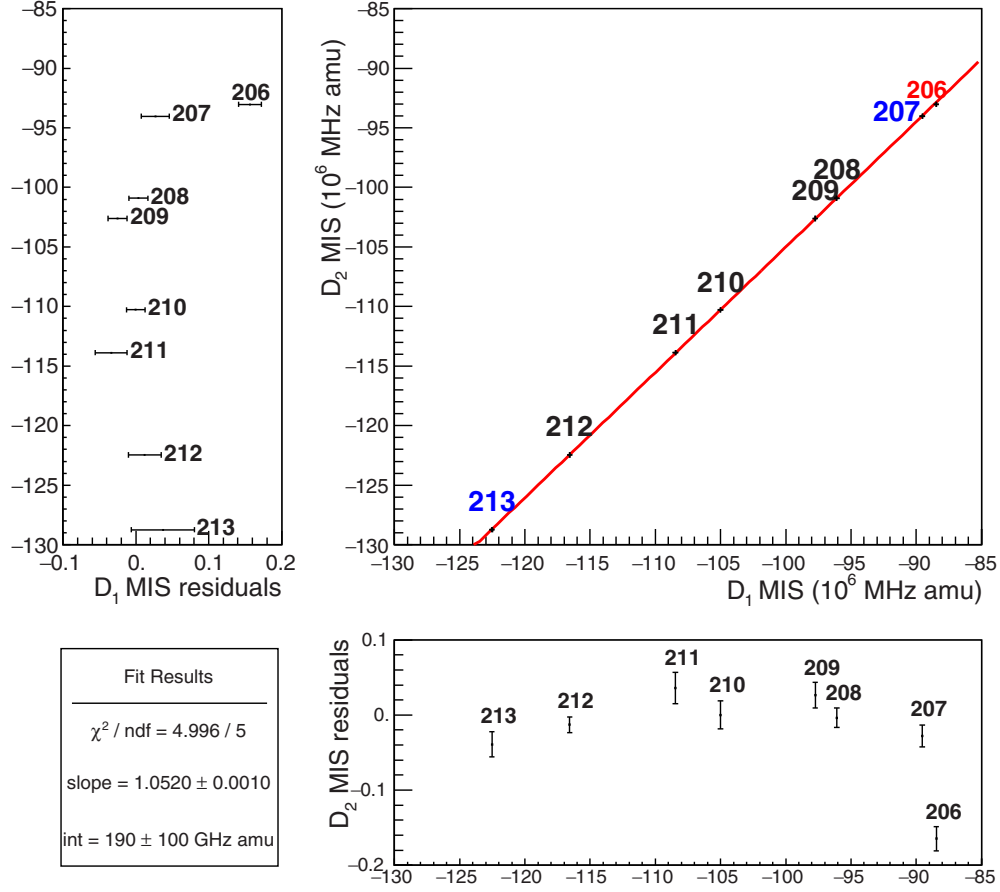


FIG. 4. (Color online) King plot of the modified isotope shifts (MIS) on the D_2 and D_1 lines for francium. Existing D_2 line isotope shifts are recalculated using ^{221}Fr as the reference isotope. We provide results for $^{206-213}\text{Fr}$ D_1 isotope shifts. The slope of the fitted line gives the ratio of the field shift constants for the two transitions. The intercept provides the corresponding difference in the mass shift constants. Plots of the D_1 and D_2 residuals are shown. The blue $^{207,213}\text{Fr}$ are from the first experimental run data and the black $^{208-212}\text{Fr}$ are from the second run data. The red ^{206}Fr point is not used in the fit for reasons explored in the text.

by typically a factor of two due to the uncertainties of the ground-state A coefficients alone. Improving the experimental result would require more precisely measuring both of these quantities.

V. SUMMARY

We have measured isotope shifts on the D_1 line in $^{206-213}\text{Fr}$ with respect to ^{221}Fr using a fast rf sweep of laser sidebands. A King plot allows us to separate the field shifts ratio, $F_{D2}/F_{D1} = 1.0520(10)$, and mass shifts in these isotopes and

we deduced the specific mass shifts relation, $S_{D2} - S_{D1} \frac{F_{D2}}{F_{D1}} = 170(100) \text{ GHz amu}$, in good agreement with the theory predictions.

ACKNOWLEDGMENTS

The authors would like to thank the ISAC staff at TRIUMF for developing the Fr beam. This work is supported by NRC, TRIUMF, and NSERC from Canada, U.S. Department of Energy and U.S. NSF, and CONACYT from Mexico. R.C. acknowledges financial support from a University of Manitoba Graduate Fellowship.

-
- [1] W. Nörtershäuser, R. Sánchez, G. Ewald, A. Dax, J. Behr, P. Bricault, B. A. Bushaw, J. Dilling, M. Döbbsky, G. W. F. Drake, S. Götte, H.-J. Kluge, T. Kühl, J. Lassen, C. D. P. Levy, K. Pachucki, M. Pearson, M. Puchalski, A. Wojtaszek, Z.-C. Yan, and C. Zimmermann, *Phys. Rev. A* **83**, 012516 (2011).
 - [2] A. Nieminen, P. Campbell, J. Billowes, D. H. Forest, J. A. R. Griffith, J. Huikari, A. Jokinen, I. D. Moore, R. Moore, G. Tungate, and J. Äystö, *Phys. Rev. Lett.* **88**, 094801 (2002).
 - [3] M. G. Kozlov, V. A. Korol, J. C. Berengut, V. A. Dzuba, and V. V. Flambaum, *Phys. Rev. A* **70**, 062108 (2004).
 - [4] W. Aoki, S. G. Ryan, J. E. Norris, T. C. Beers, H. Ando, N. Iwamoto, T. Kajino, G. J. Mathews, and M. Y. Fujimoto, *Astrophys. J.* **561**, 346 (2001).
 - [5] J. Ginges and V. Flambaum, *Phys. Rep.* **397**, 63 (2004).
 - [6] M. J. Ramsey-Musolf and S. A. Page, *Ann. Rev. Nucl. Part. Sci.* **56**, 1 (2006).

- [7] G. Gwinner, E. Gomez, L. Orozco, A. Perez Galvan, D. Sheng, Y. Zhao, G. Sprouse, J. Behr, K. Jackson, M. Pearson, S. Aubin, and V. Flambaum, [Hyperfine Interact.](#) **172**, 45 (2006).
- [8] V. A. Dzuba, W. R. Johnson, and M. S. Safronova, [Phys. Rev. A](#) **72**, 022503 (2005).
- [9] K. Heilig and A. Steudel, [At. Data Nucl. Data Tables](#) **14**, 613 (1974).
- [10] W. H. King, *Isotope Shifts in Atomic Spectra*, Physics of Atoms and Molecules (Plenum, New York, 1984).
- [11] M. Tandecki, J. Zhang, R. Collister, S. Aubin, J. A. Behr, E. Gomez, G. Gwinner, L. A. Orozco, and M. R. Pearson, [J. Instrum.](#) **8**, P12006 (2013).
- [12] J. Zhang *et al.* (unpublished).
- [13] W. Z. Zhao, J. E. Simsarian, L. A. Orozco, and G. D. Sprouse, [Rev. Sci. Instrum.](#) **69**, 3737 (1998).
- [14] See, e.g., C. J. Foot, [Contemp. Phys.](#) **32**, 369 (1991).
- [15] J. E. Simsarian, L. A. Orozco, G. D. Sprouse, and W. Z. Zhao, [Phys. Rev. A](#) **57**, 2448 (1998).
- [16] A. Coc, C. Thibault, F. Touchard, H. Duong, P. Juncar, S. Liberman, J. Pinard, J. Lermé, J. Vialle, S. Büttgenbach, A. Mueller, and A. Pesnelle, [Phys. Lett. B](#) **163**, 66 (1985).
- [17] A. Voss, M. R. Pearson, J. Billowes, F. Buchinger, B. Cheal, J. E. Crawford, A. A. Kwiatkowski, C. D. Philip Levy, and O. Shelbaya, [Phys. Rev. Lett.](#) **111**, 122501 (2013).
- [18] S. Sanguinetti, R. Calabrese, L. Corradi, A. Dainelli, A. Khanbekyan, E. Mariotti, C. de Mauro, P. Minguzzi, L. Moi, G. Stancari, L. Tomassetti, and S. Veronesi, [Opt. Lett.](#) **34**, 893 (2009).
- [19] H. T. Duong, P. Juncar, S. Liberman, A. C. Mueller, R. Neugart, E. W. Otten, B. Peuse, J. Pinard, H. H. Stroke, C. Thibault, F. Touchard, J. L. Vialle, K. Wendt (ISOLDE Collaboration), [Europhys. Lett.](#) **3**, 175 (1987).
- [20] G. Audi, O. Bersillon, J. Blachot, and A. Wapstra, [Nucl. Phys. A](#) **729**, 3 (2003).
- [21] S. A. Blundell, P. E. G. Baird, C. W. P. Palmer, D. N. Stacey, and G. K. Woodgate, [J. Phys. B](#) **20**, 3663 (1987).
- [22] I. Angeli, [Acta Phys. Hungarica A](#) **17**, 3 (2003).
- [23] A.-M. Mårtensson-Pendrill, [Mol. Phys.](#) **98**, 1201 (2000).

Chapter 6: Preparation work with the microwave cavity and the Optical Dipole Trap.

This chapter summarizes other advances in the program, related to the microwave system and the optical dipole trap for the anapole moment measurement.

6.1 Microwave cavity.

The microwave system for generating and delivering the ≈ 45 GHz radiation is elaborate and deserves explanation. Figure 6.1 shows an schematic of the main elements of the the microwave synthesis and delivery chain. We use the PhaseMatrix FSW 0020 synthesizer, which is an excellent low phase noise source with output frequency up to 20 GHz. We set its output frequency to about 11.5 GHz, and use two frequency doublers in cascade to produce the desired frequency. The first one (Marki Microwave ADA 2050) has coax connections and doubles to 23 GHz, and the second one (Narda DB01-0552) has coax input and WG-19 waveguide output, delivering 46 GHz. Both are amplified doublers. The rest of the delivery chain is only partially assembled at the time of this writing. All units after the Narda doubler before the horns are WG-19 waveguide components. A high power amplifier can delivery of up to 4 W of power (Millitech 19-130479A) for amplification of 23

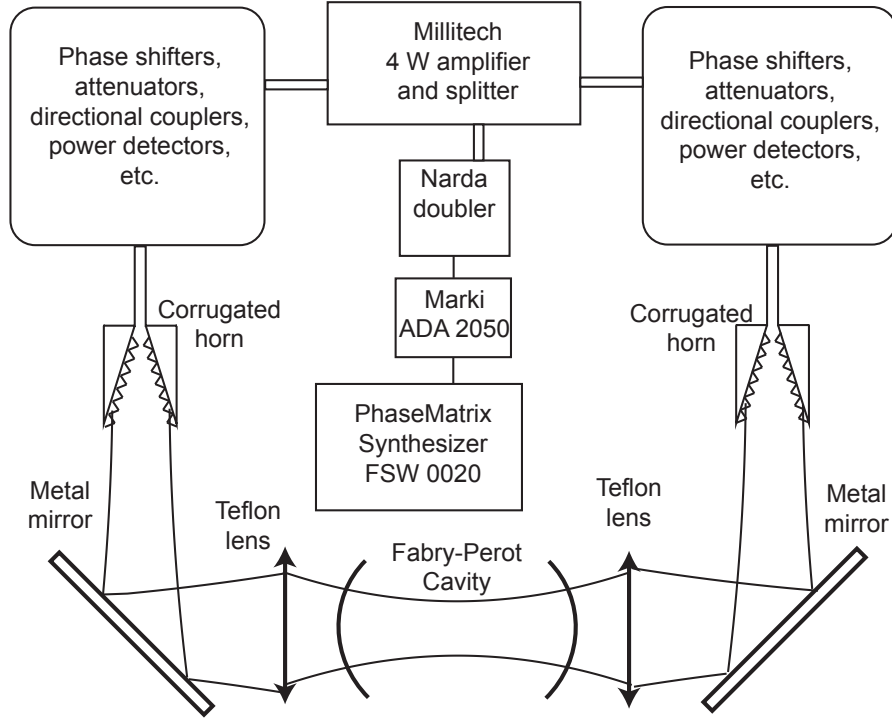


Figure 6.1: Schematic of the 46 GHz microwave synthesis and delivery system. We have assembled partially in test setups. The counter propagating beams injecting from both sides of the cavity is needed because of the beam balancing requirement. We have circulators and isolators to avoid damage to the amplifier. We avoid using coaxial cables because they are lossy compared to waveguides and free space transmission. See text for detailed explanations.

dB from 43 to 47 GHz), and split into two branches, each with identical components such as phase shifters, attenuators, and couple to free-space with corrugated horns before impinging into mode matching teflon lenses (Thorlabs LAT100 and LAT300).

The requirements in Ref [110] on the microwave field are stringent in terms of mode quality, standing wave condition, and polarization. We have chosen to work in the “quasi-optical” regime, which means thinking about the microwaves as Gaussian beams propagating in free-space, deflecting with metal mirrors and focusing

with lenses. Our microwave Fabry-Perot cavity has mirrors with sub-wavelength patterned metal surface reflectors. The mirror substrates are 3" diameter plano-concave optical blanks made out of BK7 glass, with 0.15 m radii of curvature on the concave surface. We coat the concave surface with high conductivity metal such as Cu, Ag, or Al. Aluminum is used for the current version for convenience due to its corrosion resistancy. In order to have several skin-depths for 46 GHz microwave to prevent excess losses, we chose the metal coating to be at least $2\text{ }\mu\text{m}$ thick. We use photo-lithography to imprint patterns on the metal, which allows microwave transmission without severe perturbation of the Gaussian mode distribution. We have tried various patterns including a 2D periodic hole array, and now we resort to a polarization selective 1D grid, which has an additional advantage due to the polarization selectivity. The curved surface presents a challenge for the lithography, and Michael Kossin has explored solutions based on 3D printing. Figure 6.2 shows (a) the pattern, (b) a photo-mask made from a 3D printer, and (c) an example fabricated mirror. The tests we present next are based on these mirrors.

Figure 6.3 shows our test setup of the microwave cavity. The mirror separation is close to 12.5 cm, which gives a free spectral range (FSR) of 1.2 GHz (close to confocal cavity). Scanning the input frequency over two free-spectral-ranges allows easy optimization of the alignment via the tip and tilt of the input mirror (to the left in Fig. 6.3). Just before the emitting horn (Millitech SFH-19-R0010), a directional coupler (Millitech CGC-19-RL300) and then a detector (Militech DET-19-RPFW0) followed by a low noise current amplifier (Stanford Research SR570) whose output goes into an oscilloscope allows the characterization the reflected power. A

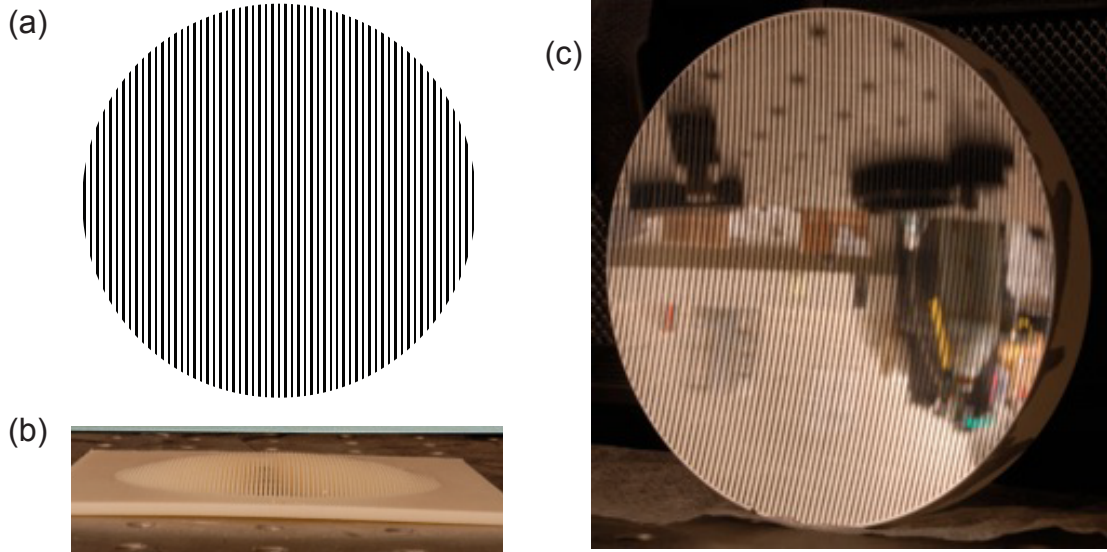


Figure 6.2: Photomask for producing the microwave cavity mirror with lithographic technique. (a) example pattern: lines provide polarization selectivity, (b) 3D printed photo-mask, and (c) a fabricated mirror.

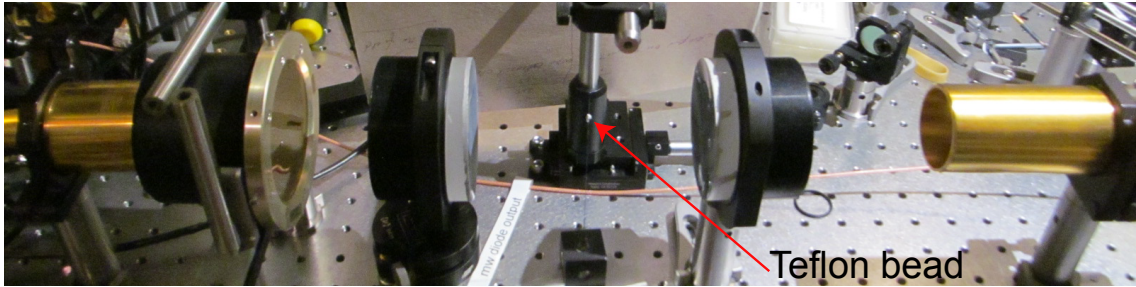


Figure 6.3: Photograph of the microwave Fabry-Perot cavity test setup.

grid polarizer (Millitech GFS-00-K200S03) ensures linear polarization entering the Fabry-Perot resonator to better than 10^{-4} intensity, consistent with the specifications.

Figure 6.4 shows the transmission resonance around 47 GHz together with a Lorentzian fit (red). The full width at half maximum (FWHM) is 0.92 (5) MHz, which gives us a good measure of the total losses of the system from mirror transmission and mirror absorption.

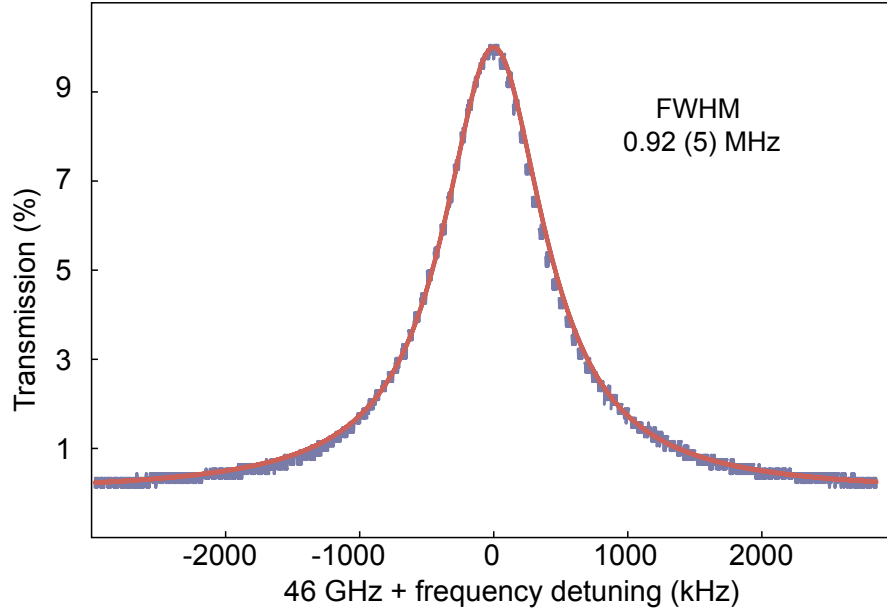


Figure 6.4: Transmission measurement on resonance after the microwave passes through the cavity (blue lines) and fit to a Lorentzian in red.

The calculation of the mode waist ($1/e^2$ intensity radius) of the cavity predicted that the waist is only 1.9 wavelengths or 1.2 cm. A preliminary measured profile is in Fig. 6.5 where we have used the “teflon bead” method. We scan the microwave over the transmission peak as the one seen in Fig. 6.4 and then look at the change in the frequency of resonance with respect to the no bead position as we scan the a small teflon bead (less than 1 mm in size) attached to a cotton string, placed inside of the cavity at the center of the mode in both the transverse and longitudinal directions. The bead changes the phase inside the cavity depending on where it sits and we can directly see the shape of the field. The extracted field waist of 12.0 ± 0.2 mm agrees with the expected value of 12.3 mm. The random errors of the data points are smaller than the size of the points. The continuous red line shows a Gaussian fit that gives the intensity as a function of position. Using the

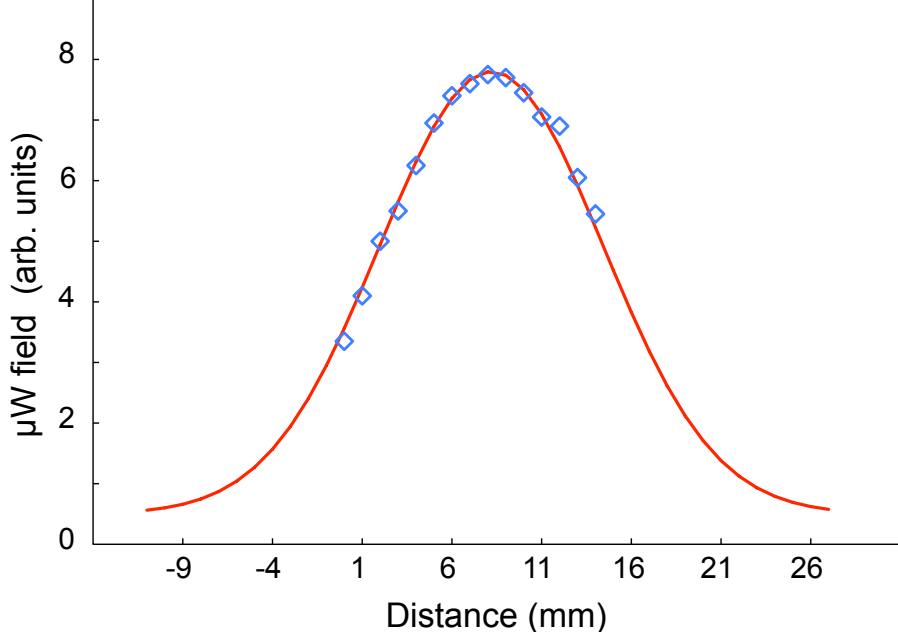


Figure 6.5: Measured transverse mode of the microwave cavity (blue points) and the Gaussian fit (red).

same method we were able to see the standing wave structure of the mode with the appropriate $\lambda/2$ periodicity.

Table 6.1 presents a summary of the measured properties of the cavity. The tests were done using an input power of about 7 dBm (5 mW) impinging on the mirror, corresponding to about 33 dBm (2W) power circulating inside the cavity. We see no problems so far regarding to excess heating of the cavity mirrors. The power dissipation when we place the cavity under vacuum and inject a full 4 W of RF power available from the amplifier, remains an open question. Reference [110] assumes that we could have a field of 479 V/m with 58 mW input power. The current enhancement factor of 416 is a factor of 4 smaller than the one in that reference, however our amplifier can give 60 times more power. We are currently preparing an article with these preliminary results.

Table 6.1: Microwave cavity parameters.

Property	Value	Units
Working frequency	47	GHz
Working wavelength	6.4	mm
Separation	0.125	m
FSR (calculated)	1190	MHz
Radius of Curvature	0.15	m
FWHM (measured)	0.92 ± 0.05	MHz
Q (measured)	51300	
Finesse (measured)	1309	
Power enhancement	417	
Transmission for one mirror (power)	8.3×10^{-4}	
Absorption for one mirror (power)	15.7×10^{-4}	
Cavity transmission (power)	0.12	
Polarization extinction	2.5×10^{-4}	

6.2 Sensitivity test of Rb atoms trapped in an optical dipole trap.

At the beginning of my graduate studies before the apparatus moved to Vancouver we were able to perform tests in Rb with a blue-detuned optical dipole trap, as required for the anapole measurement where we want to minimize lightshifts. These resulted in two papers [111,112]. The first paper was a sensitivity test to see if we could measure the influence of a second field on a Rabi oscillation, the success of this test was key to our moving to TRIUMF. The abstract of the paper D. Sheng, J. Zhang, and L. A. Orozco, *Sensitivity test of a blue-detuned dipole trap designed for parity non-conservation measurements in Fr*, Rev. Sci. Inst. **83**, 043106 (2012) is as follows:

“A dynamic blue-detuned optical dipole trap with stable ^{87}Rb atoms produces a differential ac Stark shift of 18 Hz in the ground state hyperfine transition, and it preserves the ground state hyperfine superpositions for a long coherence time of

180 ms. The trapped atoms undergoing microwave Rabi oscillations are sensitive to a small signal, artificially generated with a second microwave source, phase locked to the first, to look like a parity-non conserving quantity. They effectively resolve the interference between the two amplitudes, providing a method to calibrate the signal-to-noise ratio in similar experiments, such as the ongoing efforts in Fr.”

The second paper was a measurement of the differential AC stark shift due to the presence of the dipole trap appeared in Rb. The paper looks at the scalar shift, its dependence on geometry, power and frequency detunings. It has been published as D. Sheng, J. Zhang, and L. A. Orozco, *Rb atoms in a blue-detuned dipole trap: Coherence and ground-state differential ac Stark shift*, Phys. Rev. A. **87**, 063412 (2013) is as follows:

“Blue-detuned dipole traps and their ability to preserve atomic coherences are interesting for precision measurement applications. In this paper, we present experimental studies on the differential ac Stark shift of the ground state hyperfine splitting in ^{87}Rb atoms confined in a dynamic blue-detuned dipole trap. We systematically study the power and detuning effects on the Rabi resonance frequency (differential ac Stark shift) and its linewidth (coherence) and find that their performance is compatible with future parity violation experiments in Fr.”

Chapter 7: Conclusion.

We have constructed the Francium Trapping Facility at TRIUMF and trapped up to one million radioactive atoms. The yield in the rare-isotope beam source at TRIUMF combined our high-efficiency trapping enables atomic parity non-conservation experiments with highly promising signal to noise ratio. We take great care with controlling potential radiation hazards, as well as the higher demand for the reliability of the apparatus compared to traps with stable atoms that are available on a everyday basis.

We have demonstrated high precision spectroscopy with the excited state hyperfine splitting and isotope shift measurements, for a better understanding of the nuclear structure and benchmarking the atomic theory. These tests are beneficial for the interpretations of the parity-violating anapole moment in the nucleus, and extracting the weak charge of the nucleus for standard model tests, respectively.

We have designed a new generation of the science chamber, and demonstrated atom transfer from the capture chamber. The science chamber offers excellent vacuum background, as well as enabling much better control of the electro-magnetic field environment. Precision state experiments will soon commence, with the intended near future stages being the observation of the DC Stark-induced transition

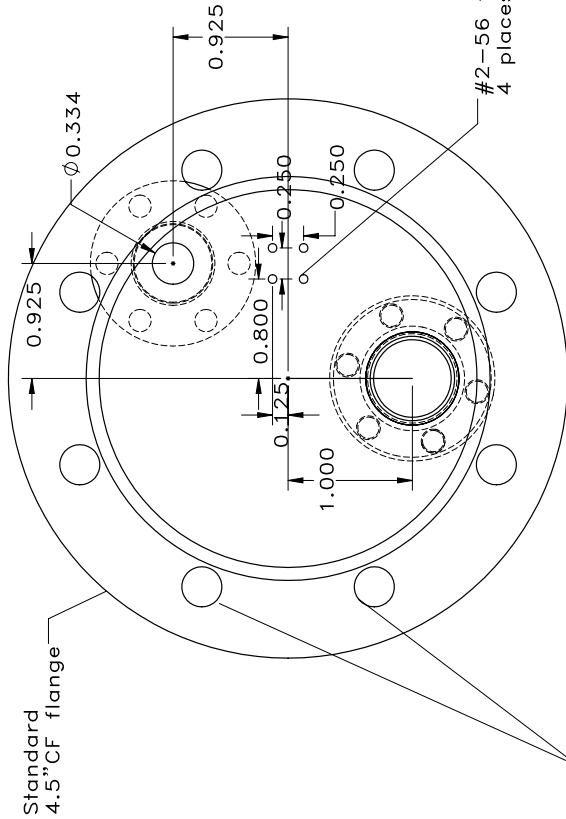
and a precision microwave frequency measurement of the ground state hyperfine splitting.

We are also progressing on better understandings of the systematic effects and other limitations for the proposed PNC experiments. Along with the exciting advances in other fronts of AMO physics, in particular quantum control and metrology, one could envision great future possibilities for measuring atomic parity non-conservation in Fr, for example squeezing to beat the quantum projection noise limit.

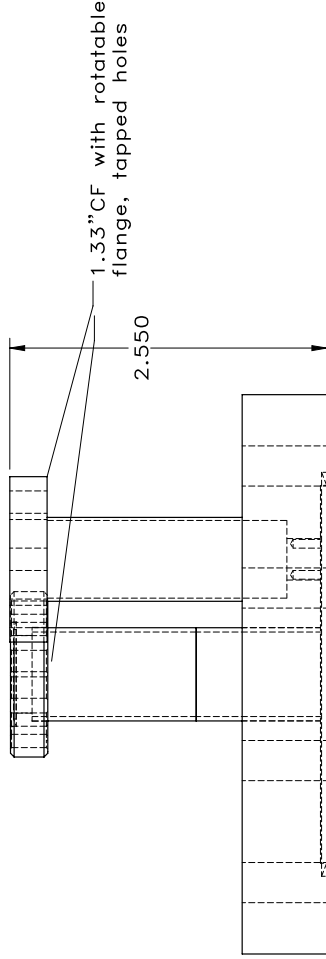
With these, I conclude this thesis, with great hope and love for the future of APNC experiments.

Appendix A: Mechanical drawings

Material: 304SS
tolerances 0.002 on welding
Quantity: 2
Drawing Scale: 1:1



Please note
orientation of holes
defines the 1.33"CF locations



1. two 1.33"CF half nipples
welded onto a 4.5"CF flange.
2. four tapped holes on inner side
of 4.5"CF flange.

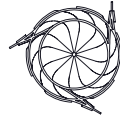
Please note
orientation of holes
defines the 1.33"CF locations

TOLERANCES UNLESS OTHERWISE SPECIFIED		REV	DATE	REVISION DESCRIPTION	BY	APPD
DECIMALS	.X ± 0.1 .XX ± 0.01 .XXX ± 0.005					
ANGULAR	± 1.0°					
SURFACE FINISH	125 µ inch					
ALL DIMS IN INCHES						
DESIGNED	J. Zhang	SUB-ASSY				
DRAWN	J. Zhang	ASSEMBLY				
CHECKED						
REA/WPN #						
TRACKING #						

REMOVE ALL BURRS AND SHARP EDGES

DO NOT COPY THIS DOCUMENT
CONTAINS PROPRIETARY INFORMATION

THIS DRAWING, SUBJECT MATTER AND INFORMATION
CONTAINED THEREIN, IS THE SOLE, EXCLUSIVE AND
PROPERTY OF TRIUMF LABORATORY, AND SHALL NOT BE
REPRODUCED OR USED IN WHOLE OR IN PART,
WITHOUT EXPRESSED WRITTEN PERMISSION OF THE
TRIUMF LABORATORY OR ITS REPRESENTATIVES.

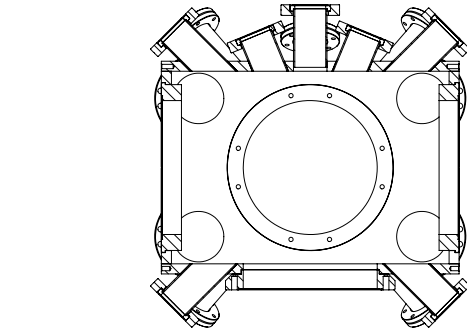
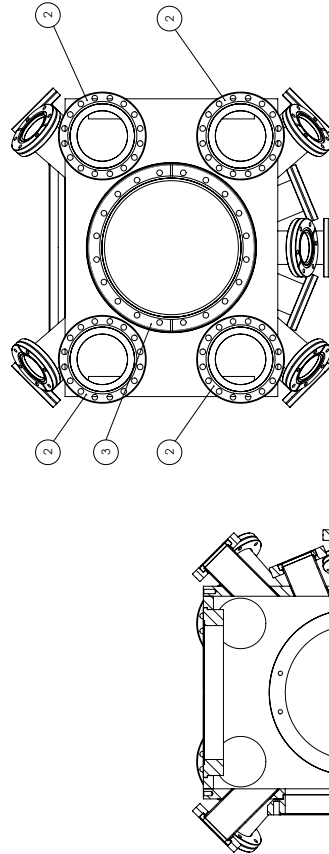
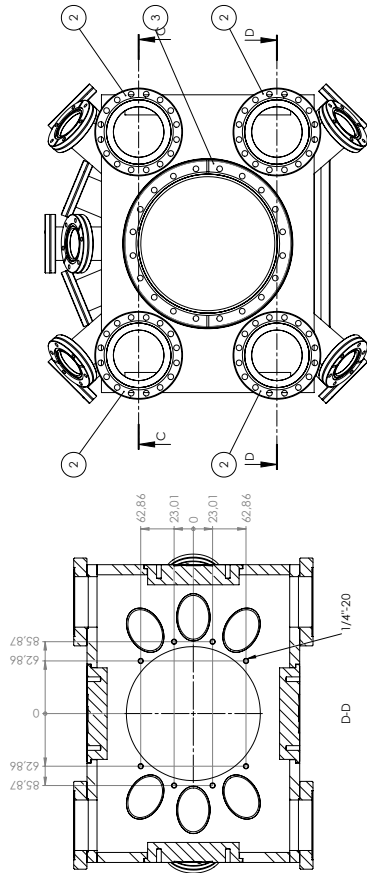


TRIUMF
4004 WESBROOK MALL
VANCOUVER, BRITISH COLUMBIA
CANADA V6T 1Z4

CANADA'S NATIONAL LABORATORY FOR
PARTICLE AND NUCLEAR PHYSICS

Custom Flange

SCALE	1:1	DWG NO.		SIZE	B	SHEET	1	REV
DATE						OF	1	



weld advice
welding tolerances in
accordance to DIN EN ISO 13920
all joints TiG - welded
all fillet welds completed
with an appropriate additional

POS.-NR.	BENENNUNG	Beschreibung	Material	MENGE
1	972021-148-10-00	Chamber Body	1.4435	
2	972021-148-00-08	Unlimited Flange	ANSI 16EN	8
3	972021-148-00-10	Weld on flange	ANSI 16EN	4
4	972021-148-00-11	Weld on flange	ANSI 16EN	4
5	972021-148-00-30	customized DN160	ANSI 16EN	1
6	480 FAD 040-40x1.5	flange rotatable thru	ANSI 16EN	
7	PR-40X1.5E1-1-H-1.6	flange rotatable,	ANSI 16EN	16
8	PR-40X1.5E1-1-H-1.6	flange, 16 in. x 70	1.4404	
9	PR-40X1.5E1-1-H-1.6	Rotr Ø 40 x 1.5 x 60	1.4404	4
10	PR-40X1.5E1-1-H-1.6	Rotr Ø 40 x 1.3 x 95	1.4404	12

PFEIFFER VACUUM CHAMBER MODEL 1000		TOLERANCES GOSS ISO 278-8K	SCALE 1:3 DIM A11	DATE 12/01/2000 SHEET 1 OF 1
DRAWING TO APPROVAL CHAMBER ASSY		MATERIAL 316L	DATE 12/01/2000 SHEET 1 OF 1	DATE 12/01/2000 SHEET 1 OF 1

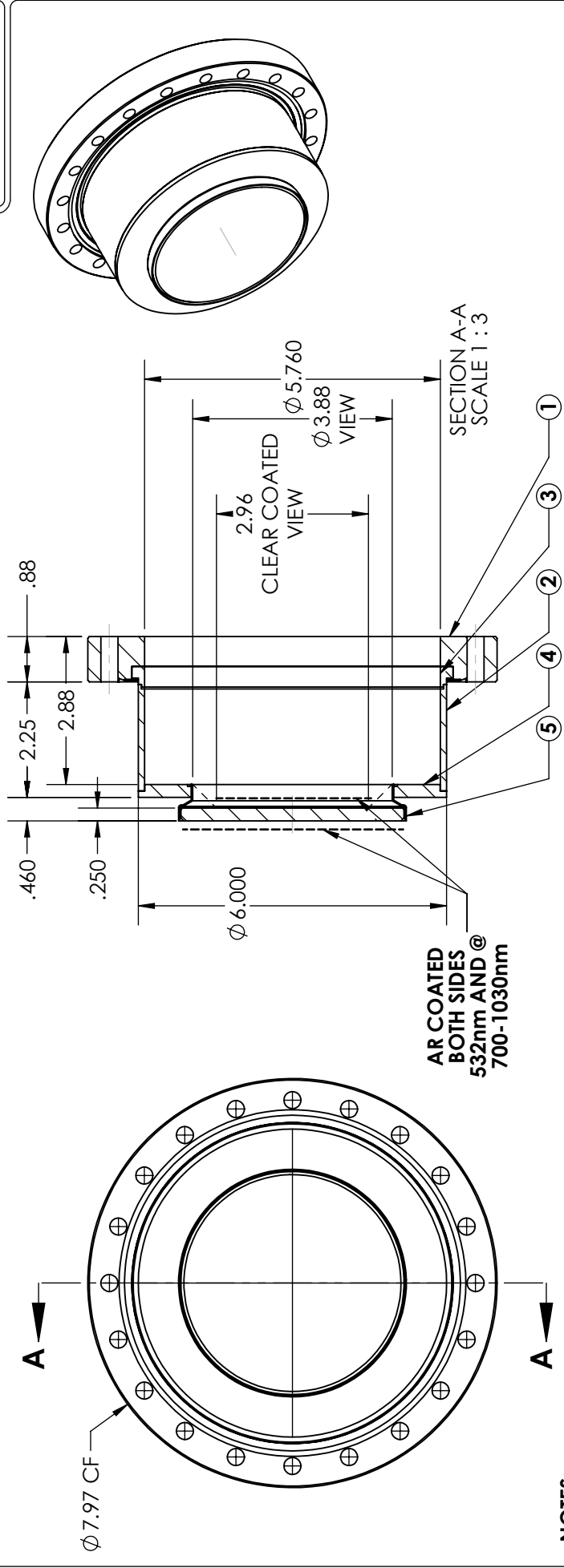
REVISIONS			
REV.	DESCRIPTION	DATE	APPROVED
A	CHANGED RE-ENTRANT TUBE LENGTH FROM 2.75" TO 2.25"	8/19/2014	RD

Q6590-1

REV 8/19/2014

A

Q6590-1



- NOTES:
1. MATERIAL: CORNING HPFS 7980 FUSED SILICA OR EQUIVALENT
 2. HOMOGENEITY GRADE: A
 3. INCLUSION CLASS: 0
 4. FLATNESS: $\lambda/4$ @ 632nm
 5. SURFACE FINISH: 20/10 SCRATCH-DIG
 6. PARALLELISM: < 10 ARC SECONDS
 7. AR COATED BOTH SIDES 532nm AND @ 700-1030nm
 8. LEAK RATE < 1×10^{-9} ATM CC/SEC HE

ITEM NO.	DESCRIPTION	QTY
1	FLANGE 316LN STN STL	1
2	TUBE 316 L STN STL	1
3	ADPT 316L STN STL	1
4	ADPT 316L STN STL	1
5	COATED SUB ASSEMBLY 532nm AND AT 700-1030nm	1

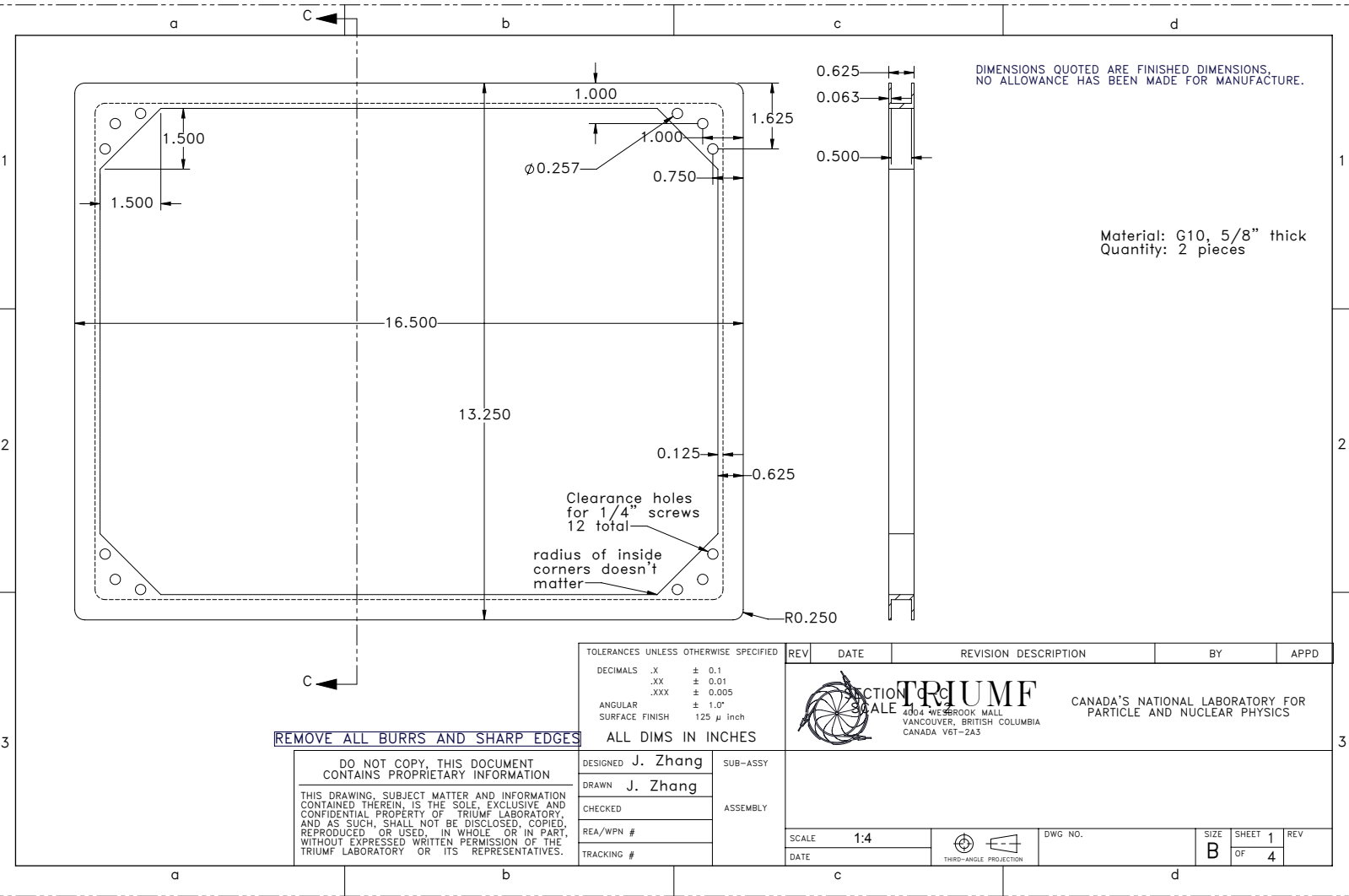
QUOTATION

TITLE: FUSED SILICA VIEWPORT AR COATED 532nm AND @ 700-1030nm		SIZE	DWG. NO.	REV
		A	Q6590-1	A
LAST SAVED DATE		8/19/2014		
TUESDAY, AUGUST 19, 2014 11:39:14 AM				

DATE		JB	DRAWN BY	DO NOT SCALE DRAWING
6/20/2014			CHECKED	
6/20/2014			ENG APPR.	
6/20/2014				

UNLESS OTHERWISE SPECIFIED:		MPF PRODUCTS INC.	
DIMENSIONS ARE IN INCHES		CONFLAT	
TOLERANCES:			
ANGULAR: MACH $\pm 1/2^\circ$			
TWO PLACE DECIMAL			
THREE PLACE DECIMAL			

PROPRIETARY AND CONFIDENTIAL		ANY REPRODUCTION IN PART OR AS A WHOLE WITHOUT THE WRITTEN PERMISSION OF MPF PRODUCTS INC. IS PROHIBITED.	
USED ON:			



DIMENSIONS QUOTED ARE FINISHED DIMENSIONS.
NO ALLOWANCE HAS BEEN MADE FOR MANUFACTURE.

Material: G10, 5/8" thick
Quantity: 2 pieces

TOLERANCES UNLESS OTHERWISE SPECIFIED		
DECIMALS	.X	± 0.1
	.XX	± 0.01
	.XXX	± 0.005
ANGULAR		± 1.0°
SURFACE FINISH		125 µ inch

REV	DATE	REVISION DESCRIPTION	BY	APPD
-----	------	----------------------	----	------



SECTION 3 TRIUMF
SCALE 1:4
4004 WESBROOK MALL
VANCOUVER, BRITISH COLUMBIA
CANADA V6T-2A3

CANADA'S NATIONAL LABORATORY FOR
PARTICLE AND NUCLEAR PHYSICS

REMOVE ALL BURRS AND SHARP EDGES

ALL DIMS IN INCHES

DO NOT COPY, THIS DOCUMENT
CONTAINS PROPRIETARY INFORMATION

THIS DRAWING, SUBJECT MATTER AND INFORMATION
CONTAINED THEREIN, IS THE SOLE, EXCLUSIVE AND
CONFIDENTIAL PROPERTY OF TRIUMF LABORATORY,
AND AS SUCH, SHALL NOT BE DISCLOSED, COPIED,
REPRODUCED OR USED, IN WHOLE OR IN PART,
WITHOUT EXPRESSED WRITTEN PERMISSION OF THE
TRIUMF LABORATORY OR ITS REPRESENTATIVES.

DESIGNED	J. Zhang
DRAWN	J. Zhang
CHECKED	
REA/WPN #	
TRACKING #	

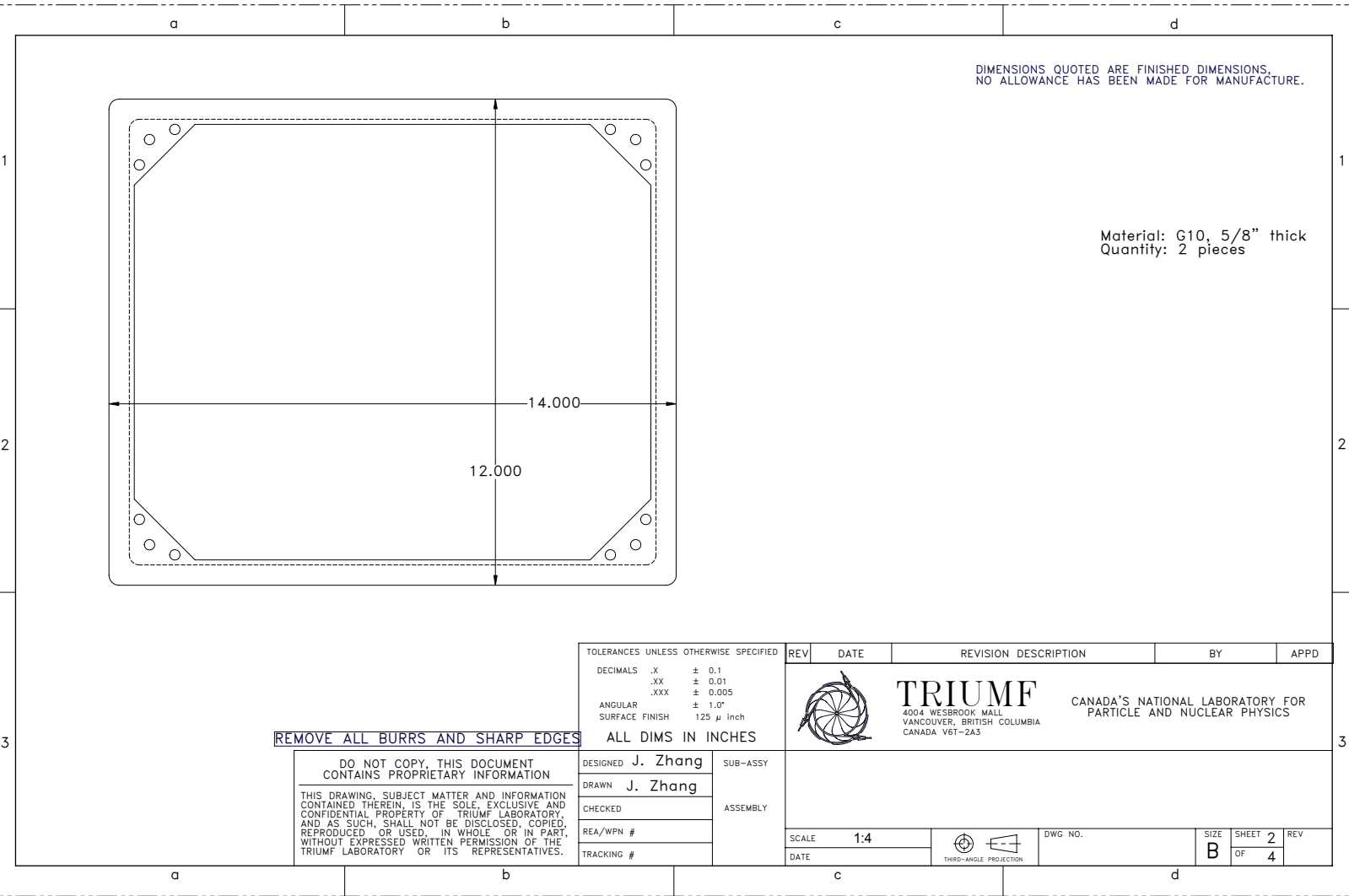
SUB-ASSY
ASSEMBLY

SCALE	1:4
DATE	



DWG NO.



SIZE	SHEET	1	REV
B	OF	4	

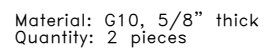


DIMENSIONS QUOTED ARE FINISHED DIMENSIONS.
NO ALLOWANCE HAS BEEN MADE FOR MANUFACTURE.

Material: G10, 5/8" thick
Quantity: 2 pieces

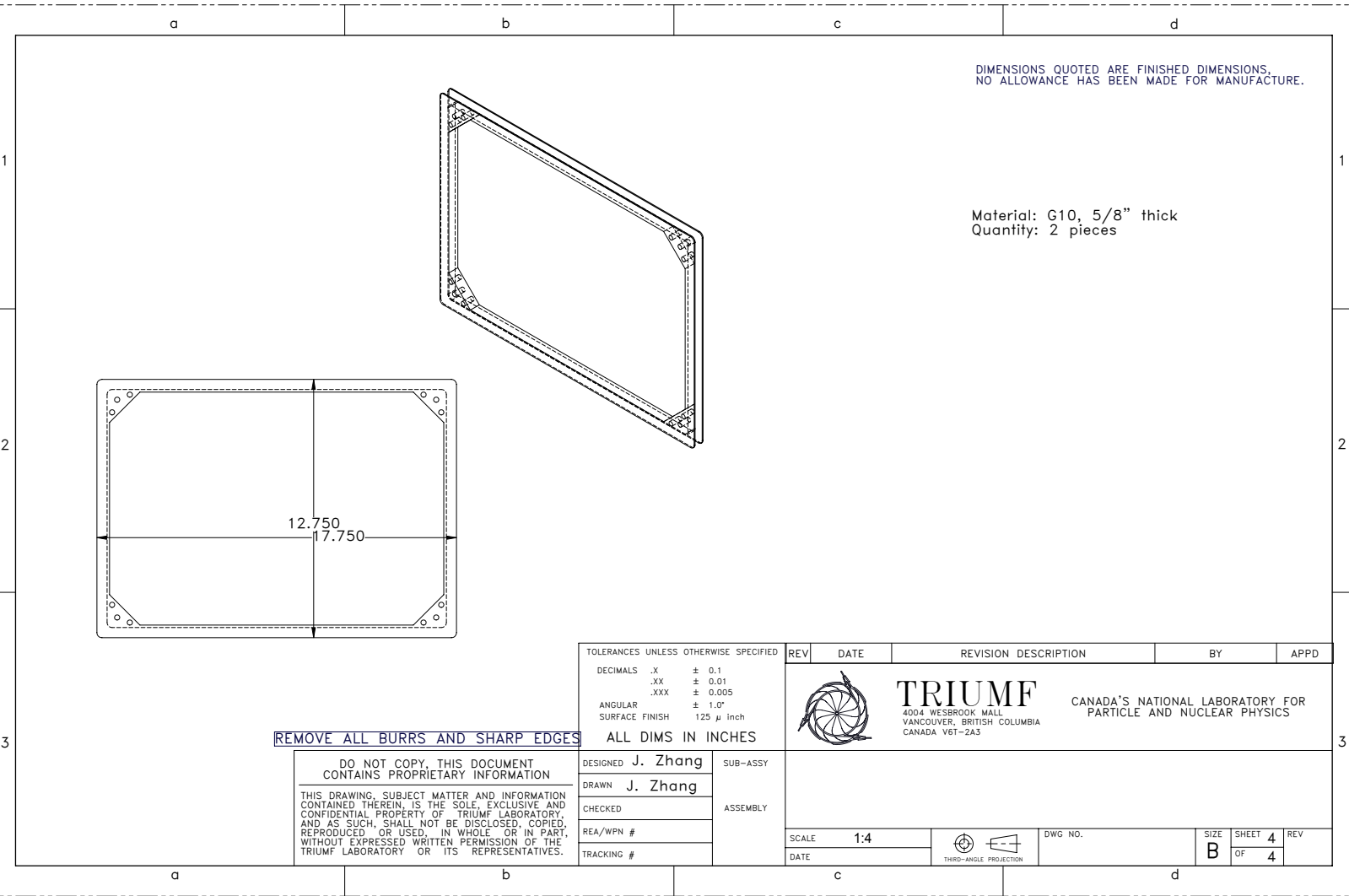
REMOVE ALL BURRS AND SHARP EDGES

TOLERANCES UNLESS OTHERWISE SPECIFIED		REV	DATE	REVISION DESCRIPTION	BY	APPD				
DECIMALS	.X ± 0.1 .XX ± 0.01 .XXX ± 0.005	<div><div>TRIUMF 4004 WESBROOK MALL VANCOUVER, BRITISH COLUMBIA CANADA V6T-2A3</div><div>CANADA'S NATIONAL LABORATORY FOR PARTICLE AND NUCLEAR PHYSICS</div></div>								
ANGULAR	± 1.0°									
SURFACE FINISH	125 µ inch									
ALL DIMS IN INCHES										
DESIGNED J. Zhang	SUB-ASSY ASSEMBLY	<div><div>DO NOT COPY, THIS DOCUMENT CONTAINS PROPRIETARY INFORMATION</div><div>THIS DRAWING, SUBJECT MATTER AND INFORMATION CONTAINED THEREIN, IS THE SOLE, EXCLUSIVE AND CONFIDENTIAL PROPERTY OF TRIUMF LABORATORY, AND AS SUCH, SHALL NOT BE DISCLOSED, COPIED, REPRODUCED OR USED, IN WHOLE OR IN PART, WITHOUT EXPRESSED WRITTEN PERMISSION OF THE TRIUMF LABORATORY OR ITS REPRESENTATIVES.</div></div>								
DRAWN J. Zhang										
CHECKED										
REA/WPN #										
TRACKING #										
		SCALE 1:4		<div><div>THIRD-ANGLE PROJECTION</div></div>		DWG NO.		SIZE	SHEET 2	REV
		DATE				B	OF 4			



DO NOT COPY, THIS DOCUMENT
CONTAINS PROPRIETARY INFORMATION


THIS DRAWING, SUBJECT MATTER AND INFORMATION
CONTAINED THEREIN, IS THE SOLE, EXCLUSIVE AND
CONFIDENTIAL PROPERTY OF TRIUMF LABORATORY,
AND AS SUCH, SHALL NOT BE DISCLOSED, COPIED,
REPRODUCED OR USED, IN WHOLE OR IN PART
WITHOUT EXPRESSED WRITTEN PERMISSION OF
THE TRIUMF LABORATORY OR ITS REPRESENTATIVES.



DIMENSIONS QUOTED ARE FINISHED DIMENSIONS,
NO ALLOWANCE HAS BEEN MADE FOR MANUFACTURE.

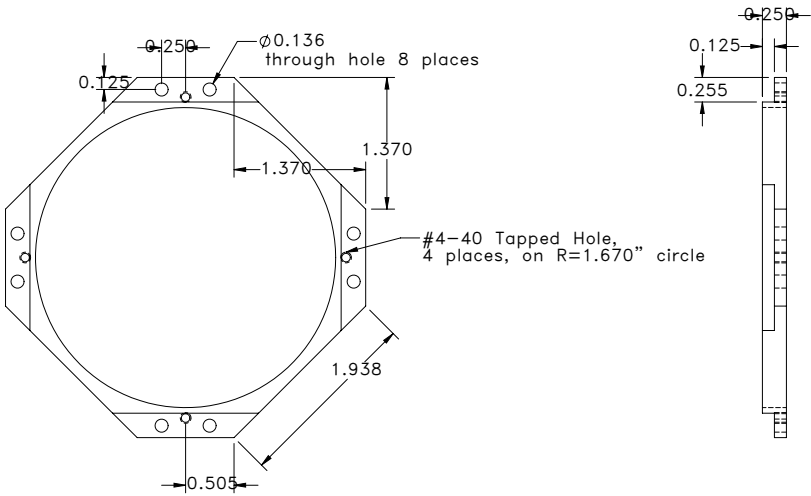
Material: G10, 5/8" thick
Quantity: 2 pieces

REMOVE ALL BURRS AND SHARP EDGES

TOLERANCES UNLESS OTHERWISE SPECIFIED		REV	DATE	REVISION DESCRIPTION	BY	APPD
DECIMALS .X ± 0.1 .XX ± 0.01 .XXX ± 0.005 ANGULAR SURFACE FINISH 125 µ inch		<div><div>TRIUMF 4004 WESBROOK MALL VANCOUVER, BRITISH COLUMBIA CANADA V6T-2A3</div><div>CANADA'S NATIONAL LABORATORY FOR PARTICLE AND NUCLEAR PHYSICS</div></div>				
ALL DIMS IN INCHES						
DESIGNED	J. Zhang	SUB-ASSY <				

Material: 316L SS
Use default tolerances

DIMENSIONS QUOTED ARE FINISHED DIMENSIONS, NO ALLOWANCE HAS BEEN MADE FOR MANUFACTURE.



REMOVE ALL BURRS AND SHARP EDGES

TOLERANCES UNLESS OTHERWISE SPECIFIED		REV	DATE	REVISION DESCRIPTION	BY	APPD
DECIMALS	.X ± 0.1 .XX ± 0.01 .XXX ± 0.005	<div><div>TRIUMF 4004 WESBROOK MALL VANCOUVER, BRITISH COLUMBIA CANADA V6T-2A3</div><div>CANADA'S NATIONAL LABORATORY FOR PARTICLE AND NUCLEAR PHYSICS</div></div>				
ANGULAR	± 1.0°					
SURFACE FINISH	125 µ inch					
ALL DIMS IN INCHES						
DESIGNED	J. Zhang	<div>Cover Lid</div> <div>Model available in: trwin\\scratch\\jzhang</div>				
DRAWN	J. Zhang					
CHECKED	Y. Shin					
REA/WPN #		<div>SCALE 1:1</div> <div>DATE</div> <div><div>THIRD-ANGLE PROJECTION</div></div> <div>DWG NO.</div> <div>SIZE B</div> <div>SHEET 1 OF 1</div> <div>REV</div>				
TRACKING #						

REMOVE ALL BURRS AND SHARP EDGES

DIMENSIONS QUOTED ARE FINISHED DIMENSIONS.
NO ALLOWANCE HAS BEEN MADE FOR MANUFACTURE.

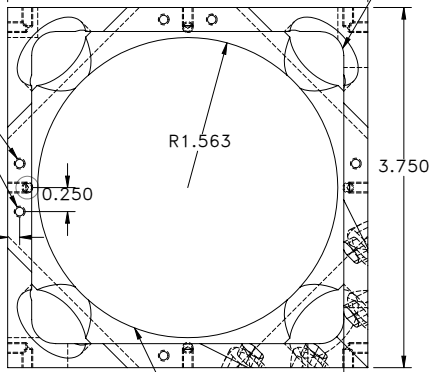
Material: 316L SS
Use default tolerances

#4-40 tapped holes,
.2" deep, 6 places,
2 each on non-angled sides,
1 each on angled sides

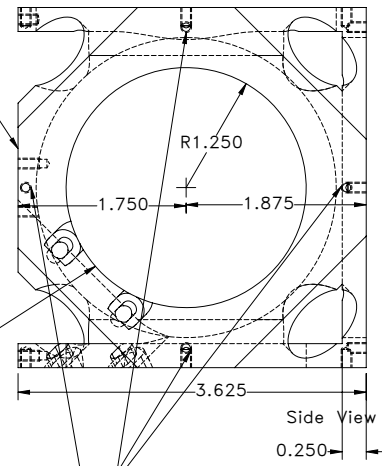
Inside cuts can have .25" radius

shaving 1/8" off to enable
the lid to be mounted.
Note that this shouldn't affect the angle cuts.
If possible please do this recess at the very last,
to avoid positioning errors

Remove the cube corners and create
flat surfaces. Then dia=0.875" holes through.
8 corners in total. From corner, go 0.791" down,
and that will give the 1.938" triangles, 4 of them.
The other 4 has 1.761" triangles because of the
0.125" shave off. See note on the top right of this
sheet.



Front View



Side View

Two faces with mounting slots have
R=1.250(1 1/4") bore,
All other faces have R=1.563(1 9/16") bore.

TOLERANCES UNLESS OTHERWISE SPECIFIED		
DECIMALS	.X	± 0.1
	.XX	± 0.01
	.XXX	± 0.005
ANGULAR		± 1.0°
SURFACE FINISH		125 µ inch
ALL DIMS IN INCHES		

REV	DATE	REVISION DESCRIPTION	BY	APPD
 TRIUMF 4004 WESBROOK MALL VANCOUVER, BRITISH COLUMBIA CANADA V6T-2A5				
CANADA'S NATIONAL LABORATORY FOR PARTICLE AND NUCLEAR PHYSICS				

Isometric View


DO NOT COPY, THIS DOCUMENT
CONTAINS PROPRIETARY INFORMATION

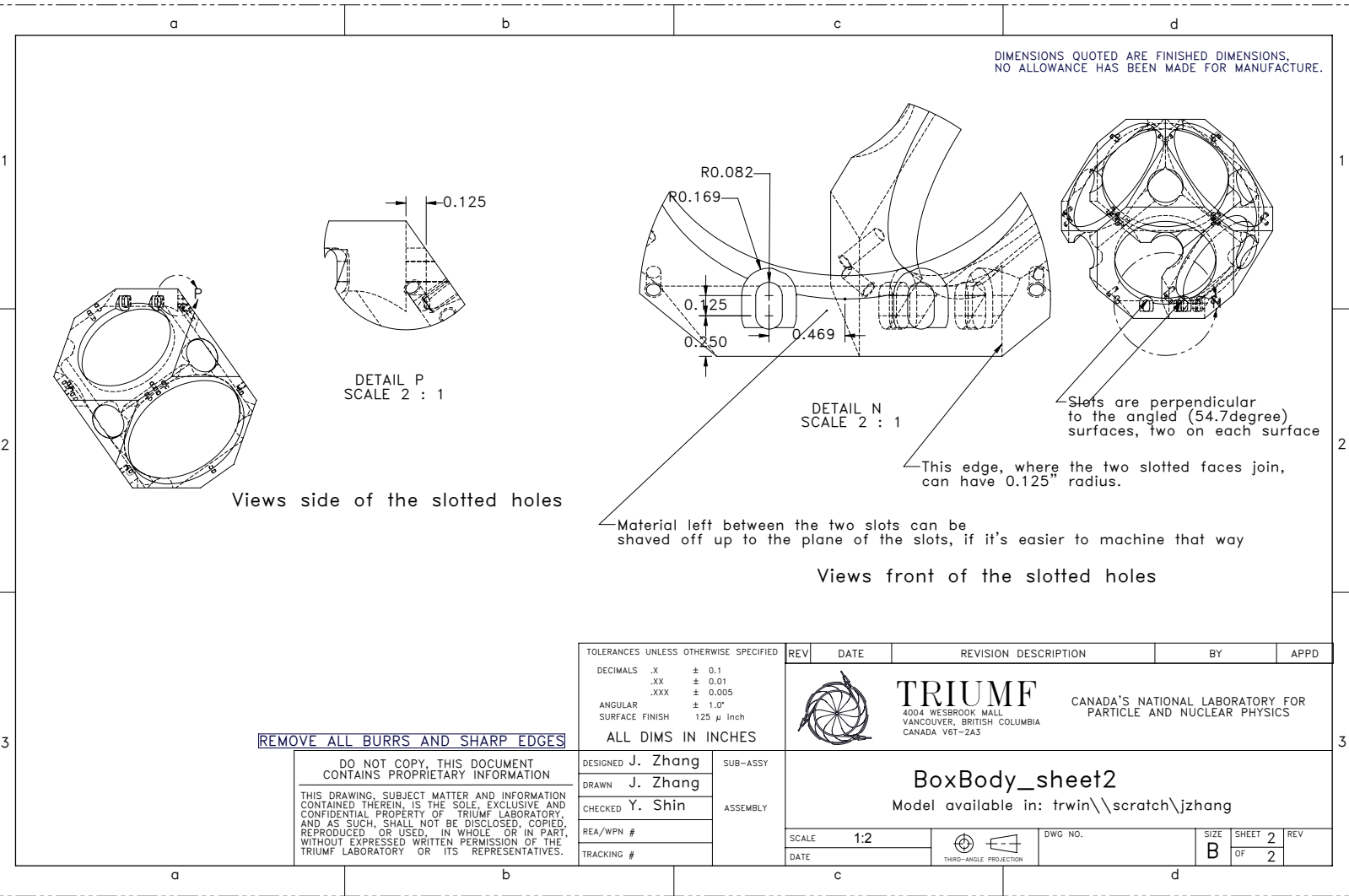
THIS DRAWING, SUBJECT MATTER AND INFORMATION
CONTAINED THEREIN, IS THE SOLE, EXCLUSIVE AND
CONFIDENTIAL PROPERTY OF TRIUMF LABORATORY,
AND AS SUCH, SHALL NOT BE DISCLOSED, COPIED,
REPRODUCED OR USED, IN WHOLE OR IN PART,
WITHOUT EXPRESSED WRITTEN PERMISSION OF THE
TRIUMF LABORATORY OR ITS REPRESENTATIVES.

DESIGNED	J. Zhang	SUB-ASSY
DRAWN	J. Zhang	ASSEMBLY
CHECKED	Y. Shin	
REA/WPN #		
TRACKING #		

BoxBody_sheet1

Model available in: trwin\\scratch\\jzhang

SCALE	1:2		DWG NO.	SIZE	SHEET	REV
DATE				B	OF 2	1



Bibliography

- [1] C. S. Wood, S. C. Bennett, D. Cho, B. P. Masterson, J. L. Roberts, C. E. Tanner, and C. E. Wieman. Measurement of parity nonconservation and an anapole moment in cesium. *Science*, 275:1759, 1997.
- [2] I. B. Khriplovich. *Parity Nonconservation in Atomic Phenomena*. Gordon and Breach, New York, 1991.
- [3] J Mitroy, M S Safronova, and Charles W Clark. Theory and applications of atomic and ionic polarizabilities. *Journal of Physics B: Atomic, Molecular and Optical Physics*, 43(20):202001, 2010.
- [4] J. Bernabéu and F. Mart´-Vidal. *Colloquium* : Time-reversal violation with quantum-entangled b mesons. *Rev. Mod. Phys.*, 87:165–182, Feb 2015.
- [5] P. A. Vetter, D. M. Meekhof, P. K. Majumder, S. K. Lamoreaux, and E. N. Fortson. Precise test of electroweak theory from a new measurement of parity nonconservation in atomic thallium. *Phys. Rev. Lett.*, 74:2658, 1995.
- [6] M. J. D. Macpherson, K. P. Zetie, R. B. Warrington, D. N. Stacey, and J. P. Hoare. Precise measurement of parity nonconserving optical rotation at 876 nm in atomic bismuth. *Phys. Rev. Lett.*, 67:2784, 1991.
- [7] D. M. Meekhof, P. Vetter, P. K. Majumder, S. K. Lamoreaux, and E. N. Fortson. High-precision measurement of parity nonconserving optical rotation in atomic lead. *Phys. Rev. Lett.*, 71:3442, 1993.
- [8] C S Wood, S C Bennett, J L Roberts, D Cho, and C E Wieman. Precision measurement of parity nonconservation in cesium. *Can. J. Phys.*, 77:7, 1999.
- [9] M. A. Bouchiat and C. Bouchiat. Parity violation induced by weak neutral currents in atomic physics 1. *J. Phys. (Paris)*, 35:899, 1974.
- [10] V. A. Dzuba, V. V. Flambaum, and O. P. Sushkov. Calculation of energy levels, $e1$ transition amplitudes, and parity violation in francium. *Phys. Rev. A*, 51:3454, 1995.

- [11] M. S. Safronova and W. R. Johnson. High-precision calculation of the parity-nonconserving amplitude in francium. *Phys. Rev. A*, 62:022112, 2000.
- [12] S. G. Porsev, K. Beloy, and A. Derevianko. Precision determination of electroweak coupling from atomic parity violation and implications for particle physics. *Phys. Rev. Lett.*, 102:181601, May 2009.
- [13] V. A. Dzuba and J. C. Berengut, V. V. Flambaum, and B. Roberts. Revisiting parity non-conservation in cesium. *Phys. Rev. Lett.*, 109:203003, Nov 2012.
- [14] W. C. Haxton, C P Liu, and M J Ramsey-Musolf. Nuclear anapole moments. *Phys. Rev. C*, 65:045502, 2002.
- [15] W. C. Haxton and C. E. Wieman. Atomic parity nonconservation and nuclear anapole moments. *Annu. Rev. Nucl. Part. Sci.*, 51:261, 2001.
- [16] B. Desplanques, J. F. Donoghue, and B. R. Holstein. Unified treatment of the parity violating nuclear-force. *Ann. Phys. (N.Y.)*, 124:449, 1980.
- [17] J Wasem. Lattice qcd calculation of nuclear parity violation. *Phys. Rev. C*, 85:022501, Feb 2012.
- [18] M. Viviani, A. Baroni, L. Girlanda, A. Kievsky, L. E. Marcucci, and R. Schiavilla. Chiral effective field theory analysis of hadronic parity violation in few-nucleon systems. *Phys. Rev. C*, 89:064004, Jun 2014.
- [19] Daniel R. Phillips, Daris Samart, and Carlos Schat. Parity-violating nucleon-nucleon force in the $1/N_c$ expansion. *Phys. Rev. Lett.*, 114:062301, Feb 2015.
- [20] Klaus Blaum, Jens Dilling, and Wilfried Nörtershäuser. Precision atomic physics techniques for nuclear physics with radioactive beams. *Physica Scripta*, 2013(T152):014017, 2013.
- [21] David Gareth Jenkins. Recent advances in nuclear physics through on-line isotope separation. *Nat Phys*, 10(12):909–913, 12 2014.
- [22] D. M. Meekhof, P. Vetter, P. K. Majumder, S. K. Lamoreaux, and E. N. Fortson. Optical-rotation technique used for a high-precision measurement of parity nonconservation in atomic lead. *Phys. Rev. A*, 52:1895, 1995.
- [23] L. Bougas, G. E. Katsoprinakis, W. von Klitzing, J. Sapirstein, and T. P. Rakitzis. Cavity-enhanced parity-nonconserving optical rotation in metastable Xe and Hg. *Phys. Rev. Lett.*, 108:210801, May 2012.
- [24] K. Tsigutkin, D. Dounas-Frazer, A. Family, J. E. Stalnaker, V. V. Yashchuk, and D. Budker. Observation of a large atomic parity violation effect in ytterbium. *Phys. Rev. Lett.*, 103:071601, 2009.
- [25] N. Leefer, L. Bougas, D. Antypas, and D. Budker. Towards a new measurement of parity violation in dysprosium. arXiv: 1412.1245, Dec 2014.

- [26] E. N. Fortson, Y. Pang, and L. Wilets. Nuclear-structure effects in atomic parity nonconservation. *Phys. Rev. Lett.*, 65:2857–2860, Dec 1990.
- [27] S. R. Williams, A. Jayakumar, Ma. R. Hoffman, B. B. Blinov, and E. N. Fortson. Method for measuring the $6S_{1/2} \leftrightarrow 5D_{3/2}$ magnetic-dipole-transition moment in Ba^+ . *Phys. Rev. A*, 88:012515, Jul 2013.
- [28] M. Nuñez Portela, J.E. van den Berg, H. Bekker, O. Böll, E.A. Dijck, G.S. Giri, S. Hoekstra, K. Jungmann, A. Mohanty, C.J.G. Onderwater, B. Santra, S. Schlessler, R.G.E. Timmermans, O.O. Versolato, L.W. Wansbeek, L. Willmann, and H.W. Wilschut. Towards a precise measurement of atomic parity violation in a single Ra^+ ion. *Hyperfine Interactions*, 214(1-3):157–162, 2013.
- [29] D. Antypas and D. S. Elliott. Measurement of a weak transition moment using two-pathway coherent control. *Physical Review A*, 87(4):042505–, 04 2013.
- [30] E. Gomez, S Aubin, G. D. Sprouse, L. A. Orozco, and D. P. DeMille. Measurement method for the nuclear anapole moment of laser-trapped alkali-metal atoms. *Phys. Rev. A*, 75:033418, 2007.
- [31] D. Sheng, L. A. Orozco, and E. Gomez. Preliminary studies for anapole moment measurements in rubidium and francium. *J. Phys. B*, 43:074004, 2010.
- [32] S. B. Cahn, J. Ammon, E. Kirilov, Y. V. Gurevich, D. Murphree, R. Paolino, D. A. Rahmlow, M. G. Kozlov, and D. DeMille. Zeeman-tuned rotational level-crossing spectroscopy in a diatomic free radical. *Phys. Rev. Lett.*, 112:163002, Apr 2014.
- [33] Marie Anne Bouchiat. Linear stark shift in dressed atoms as a signal to measure a nuclear anapole moment with a cold-atom fountain or interferometer. *Phys. Rev. Lett.*, 98:043003, Jan 2007.
- [34] D. R. Dounas-Frazer, K. Tsigutkin, D. English, and D. Budker. Atomic parity violation in $j = 0 \rightarrow 0$ two-photon transitions. *Phys. Rev. A*, 84:023404, 2011.
- [35] M. Roberts, B. V. Stadnik, Y. A. Dzuba, V. V. Flambaum, V. N. Leefer, and D. Budker. Parity-violating interactions of cosmic fields with atoms, molecules, and nuclei: Concepts and calculations for laboratory searches and extracting limits. *Phys. Rev. D*, 90:096005, Nov 2014.
- [36] A. Adare *et al.* (PHENIX Collaboration). Search for dark photons from neutral meson decays in $p + p$ and $d + \text{Au}$ collisions at $\sqrt{s_{NN}} = 200$ GeV. *Phys. Rev. C*, 91:031901, Mar 2015.
- [37] J. P. Lees *et al.* (BaBar Collaboration). Search for a dark photon in e^+e^- collisions at *BaBar*. *Phys. Rev. Lett.*, 113:201801, Nov 2014.

- [38] E. Gomez, L. A. Orozco, A. Pérez Galván, and G. D. Sprouse. Lifetime measurement of the $8s$ level in francium. *Phys. Rev. A*, 71:062504, 2005.
- [39] C. E. Loving and P. G. H. Sandars. On the feasibility of an atomic-beam resonance experiment sensitive to the nuclear-spin-dependent weak neutral current interaction. *J. Phys. B*, 10:2755, 1977.
- [40] D. J. Berkeland and M. G. Boshier. Destabilization of dark states and optical spectroscopy in zeeman-degenerate atomic systems. *Phys. Rev. A*, 65:033413, Feb 2002.
- [41] Nikolay V Vitanov, Thomas Halfmann, Bruce W Shore, and Klaas Bergmann. Laser-induced population transfer by adiabatic passage techniques. *Annual Review of Physical Chemistry*, 52(1):763–809, 2001. PMID: 11326080.
- [42] M Tandecki, J Zhang, R Collister, S Aubin, J A Behr, E Gomez, G Gwinner, L A Orozco, and M R Pearson. Commissioning of the francium trapping facility at triumf by the frpnc collaboration. *Journal of Instrumentation*, 8(12):P12006, 2013.
- [43] M. Tandecki, J. Zhang, S. Aubin, J.A. Behr, R. Collister, E. Gomez, G. Gwinner, H. Heggen, J. Lassen, L.A. Orozco, M.R. Pearson, S. Raeder, and A. Teigelhöfer. Offline trapping of ^{221}Fr in a magneto-optical trap from implantation of an ^{225}Ac ion beam. *Journal of Instrumentation*, 9(10):P10013, Oct 2014.
- [44] C. Monroe, W. Swann, H. Robinson, and C. Wieman. Very cold trapped atoms in a vapor cell. *Phys. Rev. Lett.*, 65:1571, 1990.
- [45] S. Aubin, E. Gomez, L. A. Orozco, and G. D. Sprouse. High efficiency magneto-optical trap for unstable isotopes. *Rev. Sci. Instrum.*, 74:4342, 2003.
- [46] W. L. Kruithof. *Laser trapping of sodium isotopes for a high-precision -decay experiment*. PhD thesis, RIJKSUNIVERSITEIT GRONINGEN, July 2012.
- [47] Seth Aubin. *High Efficiency Francium Trap for Precision Spectroscopy*. PhD thesis, SUNY Stony Brook, 2003.
- [48] J. A. Fedchak, P Cabaay, W. J. Cummings, C. E. Jones, and R. S. Kowalczyk. Silane coatings for laser-driven polarized hydrogen sources and targets. *Nucl. Instr. and Meth. A*, 391(3):405, 1997.
- [49] Andres D. Cimmarusti. *Control protocols for manipulation of ground-state quantum beats in a cavity QED system*. PhD thesis, University of Maryland, 2014.
- [50] D. Melconian, M. Trinczek, A. Gorelov, W. P. Alford, J. A. Behr, J.M. D’Auria, M. Domsbky, U. Giesen, K. P. Jackson, T. B. Swanson, and W. Wong. Release of ^{37}K from catcher foils. *Nucl. Instr. and Meth. A*, 538:93, Feb 2005.

- [51] R. Guckert, X. Zhao, S. G. Crane, A. Hime, W. A. Taylor, D. Tupa, D. J. Vieira, and H. Wollnik. Magneto-optical trapping of radioactive ^{82}Rb atoms. *Phys. Rev. A*, 58, 1998.
- [52] C. de Mauro, R. Calabrese, L. Corradi, A. Dainelli, A. Khanbekyan, E. Mariotti, P. Minguzzi, L. Moi, S. Sanguinetti, G. Stancari, L. Tomassetti, and S. Veronesi. Measurement of diffusion coefficients of francium and rubidium in yttrium based on laser spectroscopy. *Phys. Rev. A*, 78:063415, Dec 2008.
- [53] Timothy Dinneen, Albert Ghiorso, and Harvey Gould. An orthotropic source of thermal atoms. *Rev. Sci. Instrum.*, 67:752, 1996.
- [54] Herbert B. Michaelson. The work function of the elements and its periodicity. *Journal of Applied Physics*, 48:4729–4733, 1977.
- [55] M. J. Dresser. The sahalangmuir equation and its application. *J. Appl. Phys.*, 39:338, 1968.
- [56] J. E. Sansonetti. Spectroscopic data for neutral francium (fri). *Journal of Physical and Chemical Reference Data*, 36:497–507, 2007.
- [57] M. Stephens, R. Rhodes, and C. Wieman. High collection efficiency in a laser trap. *J. Appl. Phys.*, 76:3479, 1994.
- [58] C. B. Alcock, V. P. Itkin, and M. K. Horrigan. Vapour pressure equations for the metallic elements: 298–2500k. *Canadian Metallurgical Quarterly*, 23(3):309, 1984.
- [59] W. Z. Zhao, J. E. Simsarian, L. A. Orozco, and G. D. Sprouse. A computer-based digital feedback control of frequency drift of multiple lasers. *Rev. Sci. Instrum.*, 69:3737, 1998.
- [60] C. Wieman and T. W. Hänsch. Doppler-free laser polarization spectroscopy. *Phys. Rev. Lett.*, 36:1170–1173, May 1976.
- [61] D J McCarron, S A King, and S L Cornish. Modulation transfer spectroscopy in atomic rubidium. *Measurement Science and Technology*, 19(10):105601, 2008.
- [62] Z.-T. Lu, K. L. Corwin, K. R. Vogel, C. E. Wieman, T. P. Dinneen, J. Maddi, and Harvey Gould. Efficient collection of ^{221}Fr into a vapor cell magneto-optical trap. *Phys. Rev. Lett.*, 79:994–997, Aug 1997.
- [63] J. D. Carter and J. D. D. Martin. Energy shifts of rydberg atoms due to patch fields near metal surfaces. *Phys. Rev. A*, 83:032902, Mar 2011.
- [64] T. L. Nicholson, S. L. Campbell, R. B. Hutson, G. E. Marti, B. J. Bloom, R. L. McNally, W. Zhang, M. D. Barrett, M. S. Safronova, G. F. Strouse, W. L. Tew, and J. Ye. Systematic evaluation of an atomic clock at 2 [times] 10⁻¹⁸ total uncertainty. *Nat Commun*, 6, 04 2015.

- [65] Guang Hao Low, Peter F. Herskind, and Isaac L. Chuang. Finite-geometry models of electric field noise from patch potentials in ion traps. *Phys. Rev. A*, 84:053425, Nov 2011.
- [66] Markus Greiner, Immanuel Bloch, Theodor W. Hänsch, and Tilman Esslinger. Magnetic transport of trapped cold atoms over a large distance. *Phys. Rev. A*, 63:031401, Feb 2001.
- [67] T. L. Gustavson, A. P. Chikkatur, A. E. Leanhardt, A. Görlitz, S. Gupta, D. E. Pritchard, and W. Ketterle. Transport of Bose-Einstein Condensates with optical tweezers. *Phys. Rev. Lett.*, 88:020401, Dec 2001.
- [68] Fang Fang and David S. Weiss. Resonator-enhanced optical guiding and trapping of cs atoms. *Opt. Lett.*, 34(2):169–171, Jan 2009.
- [69] T. B. Swanson, D. Asgeirsson, J. A. Behr, A. Gorelov, and D. Melconian. Efficient transfer in a double magneto-optical trap system. *J. Opt. Soc. Am. B*, 15(11):2641–2645, Nov 1998.
- [70] A. Perez Galvan, Phd. thesis.
- [71] A Bohr and V. F. Weisskopf. The influence of nuclear structure on the hyperfine structure of heavy elements. *Phys. Rev.*, 77:94, 1950.
- [72] J. S. Grossman, L. A. Orozco, M. R. Pearson, J. E. Simsarian, G. D. Sprouse, and W. Z. Zhao. Hyperfine anomaly measurements in francium isotopes and the radial distribution of neutrons. *Phys. Rev. Lett.*, 83:935, 1999.
- [73] J. M. Grossman. *Spectroscopy of Trapped Francium*. PhD thesis, SUNY Stony Brook, 2002.
- [74] R. Collister, G. Gwinner, M. Tandecki, J. A. Behr, M. R. Pearson, J. Zhang, L. A. Orozco, S. Aubin, and E. Gomez. Isotope shifts in francium isotopes $^{206-213}\text{Fr}$ and ^{221}Fr . *Phys. Rev. A*, 90, Nov 2014.
- [75] J. Zhang *et al.* (FrPNC collaboration). Hyperfine anomaly in Fr: boundaries of the single particle model. *submitted to PRL*, :, 2015.
- [76] C. Ott, A. Kaldun, P. Raith, K. Meyer, M. Laux, J. Evers, C. H. Keitel, C. H. Greene, and T. Pfeifer. Lorentz meets Fano in spectral line shapes: A universal phase and its laser control. *Science*, 340(6133):716–720, Mar 2013.
- [77] Aaron L. Stancik and Eric B. Brauns. A simple asymmetric lineshape for fitting infrared absorption spectra. *Vibrational Spectroscopy*, 47(1):66 – 69, 2008.
- [78] H. H. Stroke, R. J. Blin-Stoyle, and V. Jaccarino. Configuration mixing and the effects of distributed nuclear magnetization on hyperfine structure in odd- a nuclei. *Phys. Rev.*, 123:1326–1348, Aug 1961.

- [79] S. Büttgenbach. Magnetic hyperfine anomalies. *Hyperfine Interactions*, 20(1):1–64, 1984.
- [80] B. R. Mottelson and S. G. Nilsson. Classification of the nucleonic states in deformed nuclei. *Phys. Rev.*, 99:1615–1617, Sep 1955.
- [81] J. R. Crespo López-Urrutia, P. Beiersdorfer, K. Widmann, B. B. Birkett, A.-M. Mårtensson-Pendrill, and M. G. H. Gustavsson. Nuclear magnetization distribution radii determined by hyperfine transitions in the $1s$ level of H-like ions $^{185}\text{Re}^{74+}$ and $^{187}\text{Re}^{74+}$. *Phys. Rev. A*, 57:879–887, Feb 1998.
- [82] M. G. H. Gustavsson, C. Forssén, and A. M. Mårtensson-Pendrill. Thallium hyperfine anomaly. *Hyperfine Interactions*, 127(1-4):347–352, 2000.
- [83] Ann-Marie Mårtensson-Pendrill. Magnetic moment distributions in Tl nuclei. *Phys. Rev. Lett.*, 74:2184–2187, Mar 1995.
- [84] Roger D. Woods and David S. Saxon. Diffuse surface optical model for nucleon-nuclei scattering. *Phys. Rev.*, 95:577–578, Jul 1954.
- [85] B A Brown (private communication).
- [86] K. M. Lynch, J. Billowes, M. L. Bissell, I. Budinčević, T. E. Cocolios, R. P. De Groote, S. De Schepper, V. N. Fedosseev, K. T. Flanagan, S. Franchoo, R. F. Garcia Ruiz, H. Heylen, B. A. Marsh, G. Neyens, T. J. Procter, R. E. Rossel, S. Rothe, I. Strashnov, H. H. Stroke, and K. D. A. Wendt. Decay-assisted laser spectroscopy of neutron-deficient francium. *Phys. Rev. X*, 4:011055, Mar 2014.
- [87] Jenny E. Rosenthal and G. Breit. The isotope shift in hyperfine structure. *Phys. Rev.*, 41:459–470, Aug 1932.
- [88] M. F. Crawford and A. L. Schawlow. Electron-nuclear potential fields from hyperfine structure. *Phys. Rev.*, 76:1310, 1949.
- [89] H. J. Rosenberg and H. H. Stroke. Effect of a diffuse nuclear charge distribution on the hyperfine-structure interaction. *Phys. Rev. A*, 5:1992–2000, May 1972.
- [90] I. Angeli and K.P. Marinova. Table of experimental nuclear ground state charge radii: An update. *Atomic Data and Nuclear Data Tables*, 99(1):69 – 95, 2013.
- [91] Kris Heyde and John L. Wood. Shape coexistence in atomic nuclei. *Rev. Mod. Phys.*, 83:1467–1521, Nov 2011.
- [92] Pavel Cejnar, Jan Jolie, and Richard F. Casten. Quantum phase transitions in the shapes of atomic nuclei. *Rev. Mod. Phys.*, 82:2155–2212, Aug 2010.

- [93] A. Voss, M. R. Pearson, J. Billowes, F. Buchinger, B. Cheal, J. E. Crawford, A. A. Kwiatkowski, C. D. P. Levy, and O. Shelbaya. First use of high-frequency intensity modulation of narrow-linewidth laser light and its application in determination of $^{206,205,204}\text{Fr}$ ground-state properties. *Phys. Rev. Lett.*, 111:122501, Sep 2013.
- [94] A. Voss, F. Buchinger, B. Cheal, J. E. Crawford, J. Dilling, M. Kortelainen, A. A. Kwiatkowski, A. Leary, C. D. P. Levy, F. Mooshammer, M. L. Ojeda, M. R. Pearson, T. J. Procter, and W. Al Tamimi. Nuclear moments and charge radii of neutron-deficient francium isotopes and isomers. *Phys. Rev. C*, 91:044307, Apr 2015.
- [95] Kenneth S. Krane. *Introductory Nuclear Physics*. John Wiley and Sons, Hoboken, NJ, 1988.
- [96] Richard B. Firestone and Virginia S. Shirley. *Table of Isotopes*. John Wiley and Sons, Hoboken, NJ, 8 edition, 1996.
- [97] Ben R. Mottelson A. Bohr. *Nuclear Structure*, volume II. W. A. Benjamin, Inc, Reading, Massachusetts, 1975.
- [98] C. Ekström, L. Robertsson, and A. Rosén. Nuclear and electronic g-factors of ^{211}Fr , nuclear ground-state spin of ^{207}Fr and the nuclear single-particle structure in the range $^{207-228}\text{Fr}$. *Physica Scripta*, 34(6A):624, 1986.
- [99] J. P. Davidson. *Collective Models of the Nucleus*. Academic Press, New York, 1968.
- [100] V. V. Flambaum and D. W. Murray. Anapole moment and nucleon weak interactions. *Phys. Rev. C*, 56:1641–1644, Sep 1997.
- [101] W. R. Johnson, M. S. Safronova, and U. I. Safronova. Combined effect of coherent Z exchange and the hyperfine interaction in the atomic parity-nonconserving interaction. *Phys. Rev. A*, 67:062106, Jun 2003.
- [102] B. Klos, A. Trzcińska, J. Jastrzebski, T. Czosnyka, M. Kisieliński, P. Lubiński, P. Napiorkowski, L. Pieńkowski, F. J. Hartmann, B. Ketzer, P. Ring, R. Schmidt, T. von Egidy, R. Smolańczuk, S. Wycech, K. Gulda, W. Kurcewicz, E. Widmann, and B. A. Brown. Neutron density distributions from antiprotonic ^{208}Pb and ^{209}Bi atoms. *Phys. Rev. C*, 76:014311, Jul 2007.
- [103] S. Abrahamyan *et al.* Measurement of the neutron radius of ^{208}Pb through parity violation in electron scattering. *Phys. Rev. Lett.*, 108:112502, Mar 2012.
- [104] B. A. Brown. Constraints on the Skyrme equations of state from properties of doubly magic nuclei. *Phys. Rev. Lett.*, 111:232502, Dec 2013.

- [105] C. Tarbert *et al.* (Crystal Ball at MAMI and A2 Collaboration). Neutron skin of ^{208}Pb from coherent pion photoproduction. *Phys. Rev. Lett.*, 112:242502, Jun 2014.
- [106] Tapas Sil, M. Centelles, X. Viñas, and J. Piekarewicz. Atomic parity nonconservation, neutron radii, and effective field theories of nuclei. *Phys. Rev. C*, 71:045502, Apr 2005.
- [107] Adam B. Jones and B. Alex Brown. Two-parameter Fermi function fits to experimental charge and point-proton densities for ^{208}Pb . *Phys. Rev. C*, 90:067304, Dec 2014.
- [108] B. A. Brown, A. Derevianko, and V. V. Flambaum. Calculations of the neutron skin and its effect in atomic parity violation. *Phys. Rev. C*, 79:035501, 2009.
- [109] M. Warda, M. Centelles, X. Viñas, and X. Roca-Maza. Influence of the single-particle structure on the nuclear surface and the neutron skin. *Phys. Rev. C*, 89:064302, Jun 2014.
- [110] E. Gomez, S. Aubin, L. A. Orozco, G. D. Sprouse, E. Iskrenova-Tchoukova, and M. S. Safronova. Nuclear magnetic moment of ^{210}Fr : A combined theoretical and experimental approach. *Phys. Rev. Lett.*, 100:172502, May 2008.
- [111] D. Sheng, J. Zhang, and L. A. Orozco. Sensitivity test of a blue-detuned dipole trap designed for parity non-conservation measurements in fr. *Rev. Sci. Instr.*, 83:043106, 2012.
- [112] D Sheng, J Zhang, and L A Orozco. Rb atoms in a blue-detuned dipole trap: Coherence and ground-state differential ac stark shift. *Phys. Rev. A*, 87:063412, Jun 2013.